A Wide-Band Air-Ground Channel Model

DISSERTATION

zur Erlangung des akademischen Grads eines

DOKTOR-INGENIEURS
(DR.-ING.)

der Fakultät für Elektrotechnik und Informationstechnik der
Technischen Universität Ilmenau
des Freistaats Thüringen

von

Dipl.-Ing. Nicolas Schneckenburger
aus Mainz

Gutachter:	Prof. Dr.-Ing. Giovanni Del Galdo
	Prof. Dr.-Ing. Uwe-Carsten Fiebig
	Prof. David W. Matolak, Ph.D.
Eingereicht am	2. Oktober 2017
Wissenschaftliche Aussprache am	20. Dezember 2017

urn:nbn:de:gbv:ilm1-2017000665

Acknowledgments

For many people pursuing a PhD and writing a dissertation is seen as a strenuous task. I only very seldomly experienced it that way: although there were ups and downs (that is life) I enjoyed the work for almost the entire time. Working on measurement data was often very thrilling: given your signal processing works well, you will always experience the effects of nature at work.

The second reason why I enjoyed my work so much are the people I worked together with over those years.

First of all, my thanks go to my three supervisors:

To Prof. Giovanni del Galdo who was interested in my work from the very beginning. Thank you for all those conference calls and all those ideas you brought up during them.

To Prof. Uwe-Carsten Fiebig for all the support during the last years and his keen interest in how the underlying physics shape the channel. Thank you for all the sketches and figures we drew to understand the channel better.

To Prof. David Matolak who has gone through similar measurements and thus always showed a lot of empathy about the problems connected with measurements. Thank you for those conference calls and knowing all (sic!) references connected with the air-ground (AG) channel.

I also want to mention the three postdocs who had an impeccable influence on my dissertation, in alphabetical order (to avoid bad temper): Dr. Thomas Jost, Dr. Dmitriy Shutin, and Dr. Michael Walter. Without you, this dissertation would not have been what it is now. Thanks to all the motivation you provided during my lows.

I am also very thankful for my group leader, Dr. Michael Schnell, for not only his valuable scientific input, but also for keeping my back clear from all those administrative burdens.

When talking about administrative burdens I have to mention the great administrative staff of the department: Thank you Christina Burger and Jutta Uelner for having so much patience with me.

I also have the pleasure to work with a group of additional great people, not only at the Communications Systems department, but at the entire Institute of Communication and Navigation: especially larger projects like the flight measurements would not have been possible without you. In particular, I want to thank for the work (and time in general) together Dr. Ulrich Epple, Alexandra Filip, Dr. Nico Franzen, Christian Gentner, Dr. Thomas Gräupl, Miguel Bellido Manganell, Daniel Mielke, Dr. Okuary Osechas, Dr. Maria Puyol, Lukas Schalk, Dr. Emanuel Staudinger, and Dr. Thanawat Thiasiriphet.

I also want to mention the extraordinary enjoyable half-year-stay at Stanford University. During my stay I received so many ideas and insights, not only scientifically. For making that stay possible I have to thank Prof. Christoph Günther and Prof. Per Enge. The reason why I enjoyed this stay so much were the great people we met there and worked together with, in particular Dr. Sherman Lo and Dr. Tyler Reid. In that context I also want to thank the people from the FAA APNT working group, especially Dr. Wouter Pelgrum and Dr. Robert Lilley.

The main reason why I actually started pursuing the PhD are probably my parents: Thank you for infusing that curiosity into me and encouraging me to question everything (I know that must have been hard sometimes).

The last, and biggest thanks go out to my wife Johanna and my sons Thomas and Paul. Thank you for all that support! During the last year you were the sole reason I was able to finish the dissertation.

Andechs, October 2017 — Nicolas Schneckenburger

Kurzfassung

Die Flugsicherung in der zivilen Luftfahrt durchgeht aktuell einen Modernisierungsprozess. Im Zuge dieses Prozesses müssen auch die verwendeten Kommunikations-, Navigations-, und Luftraumüberwachungssysteme modernisiert werden. Um neue oder verbesserte Systeme nicht ausschließlich mit Hilfe von teuren Flugkampagnen testen zu müssen, ist ein Kanalmodell des Boden-Luftkanals notwendig. Solch ein Modell erlaubt Tests mit Hilfe von Computersimulationen.

In dieser Arbeit entwerfen wir eine neue Kanalmodellarchitektur für den Boden-Luftkanal. Aufgrund des verwendeten geometrisch-stochastischen Modellierungsansatzes ist das Kanalmodell, im Gegensatz zu älteren Kanalmodellen, in der Lage, die Nichtstationarität des Kanals genau zu reproduzieren. Das Modell verwendet geometrische Modellierungselemente, um die verschiedenen Ausbreitungseffekte abzubilden. Statistische Verteilungen beschreiben die Eigenschaften der Modellierungselemente, z.B. die Verteilung von Reflektoren um die Sendeantenne. Durch das Wählen unterschiedlicher Verteilungen kann die gleiche Modellarchitektur einfach an verschiedene Umgebungen angepasst werden.

Für diese Arbeit wurden zwei Flugmesskampagnen im L-Band in der Nähe des Versuchsflughafen in Oberpfaffenhofen durchgeführt. Im Zuge dieser Dissertation verwenden wir die gewonnenen Messdaten, um die Kanalmodellarchitektur auf die Messumgebung zu parametrisieren (anzupassen). Dafür sind neue Verfahren notwendig. Wir entwickeln einen Algorithmus zur Detektion von Multipfadkomponenten im Messsignal und zum Schätzen der zugehörigen Parameter. Auf Basis dieser Schätzung lokalisieren wir die Reflektoren, welche die detektierten Multipfadkomponenten verursachen.

Die gewonnenen Ergebnisse erlauben einen weitreichenden Erkenntnisgewinn über die Eigenschaften des Boden-Luftkanals und unterstreichen dessen Nichtstationariät. Die Ergebnisse erlauben uns außerdem, ein Kanalmodell zur Parametrisierung der Messumgebung zu erstellen. Die Parametrisierung wird erfolgreich mit

Hilfe verschiedener Messdatensätze validiert. Daher kann das in dieser Dissertation vorgestellte Kanalmodell in Zukunft zur Analyse von Flugsicherungssystemen verwendet werden. Dadurch kann die Anzahl der notwendigen, in der Regel extrem teuren Flugversuche verringert werden.

Abstract

In civil aviation, air-traffic management and with that the underlying communication, navigation, and surveillance (CNS) infrastructure is currently being modernized. To test improved or newly developed terrestrial CNS systems without costly implementations and measurements, computer simulations using an AG channel model are crucial.

In this dissertation we propose an AG channel model for the L-band which - unlike previous proposals - fully captures the statistical non-stationary nature of the channel: we are now able to test the full range of terrestrial CNS systems.

We propose a geometry-based stochastic channel model (GBSCM) architecture for the AG channel. In the GBSCM, geometrical model elements represent the different propagation effects, e.g., reflections off buildings. The model elements and their properties are environment specific and are characterized by statistical distributions: the channel model can be adapted to different environments by choosing the respective statistical distributions.

We conducted two L-band flight trial campaigns in a regional airport environment to investigate the AG channel. Throughout this dissertation we use the collected data to parameterize the channel model architecture. To characterize the geometrical model elements for the parameterization, multipath components (MPCs) in the measured signal need to be detected and their parameters have to be estimated: we propose an algorithm combining super-resolution parameter estimation with a tracking filter. Based on the estimated MPC parameters we propose localizing the reflectors causing these MPCs using a Bayesian method. The presented algorithms may not only be used in AG channel sounding but in any scenario where an accurate MPC parameter tracking and reflector localization is required.

Applying the algorithm to the measurement data demonstrates the non-stationarity of the AG channel. The results also allow us to parameterize the channel model to a regional airport environment. To assess the channel model quality the parame-

terization is successfully validated against measurement data. In consequence, our newly developed channel model is of high value for the computer-based performance analysis of CNS systems: the performance of new or improved CNS systems can now be realistically tested using computer simulations.

Contents

Chapter 1

Introduction

The way we use and manage the airspace is currently undergoing a major modernization process. Two reasons for that process can be identified: first, the continued growth of traditional airspace users, e.g., air transportation or general aviation, over the last decades mandates an increase in terms for operational efficiency.

Second, apart from a higher number of traditional airspace users, a completely new class of aircraft is currently emerging: unmanned aerial vehicles (UAVs) will become a major factor within the next years. The number of UAVs are predicted to grow by a factor of roughly seventeen compared to today's numbers within the next five years [1]. Their seamless integration into the airspace poses a major challenge for the future. The different types of UAVs to be integrated into the airspace range from small recreational UAVs to large cargo or military type UAVs. The two largest programs to push the modernization process of the airspace are Single European Sky ATM Research (SESAR) in Europe or Next Generation Air Transportation System (NextGen) in the US [2], [3].

The changes in the use of the airspace also require changes in the way the airspace is managed. In that context, the communication, navigation, and surveillance (CNS) infrastructure is a key factor, as it has to support more aircraft and thus has to provide better navigation accuracy and higher communication capacity. While the provision of CNS capabilities for manned aircraft is already safety critical, for UAVs operations without absolutely reliable CNS capabilities are not possible. Therefore, the CNS infrastructure is currently undergoing a major innovation process. Legacy systems, some dating back to the middle of the last century, are being replaced or superseded by new and more efficient systems.

On the communication side, the currently used very high frequency (VHF) analog air-ground voice link between pilot and air traffic controller, originally developed in the late 1930s, is planned to be modernized in the near future. The reason for the modernization is twofold: first, the current radio link will soon reach its capacity limit and will not be able to keep pace with the anticipated growth of the air traffic. A further increase of the capacity with the current technology is not possible. Second, the currently ongoing modernization of the complete air traffic management (ATM) infrastructure demands digital communication capabilities between the air and ground. Digital communication systems can be used to exchange flight critical data, e.g., flight trajectories and weather information, as well as supplementary data, e.g., passenger lists. The new communication capability is planned to be provided primarily by a network of ground stations. Satellite communication is planned serve aircraft in areas which cannot be covered by ground links. The designated candidate for the new ground based communication link is the L-band Digital Aeronautical Communication System (LDACS) [4], [5].

On the navigation side, the largest part of the modernization consists of transitioning to global navigation satellite system (GNSS) based navigation, e.g., Global Positioning System (GPS) and Galileo. In combination with augmentation systems or receiver autonomous integrity monitoring (RAIM), GNSS is able to offer a high degree of accuracy, availability, and integrity required to support all phases of the flight. Nevertheless, terrestrial radionavigation systems will still play an important role as alternative positioning, navigation, and timing (APNT) systems in the future navigation infrastructure [6]. APNT systems are used as backup systems in case the primary GNSS based navigation becomes unavailable. An unavailability of GNSS may be due to intentional or unintentional interference or system failures. Thus, terrestrial radionavigation will continue to be an integral component of the future CNS infrastructure. Current US and European plans foresee to continue and expand the operations of distance measuring equipment (DME), a two way ranging system dating back to the 1950s [7]. Also the use of other, more modern aviation radio signals such as LDACS or automatic dependent surveillance - broadcast (ADS-B) are APNT candidate systems.

In the future communication systems will have to provide higher data rates and lower latencies and serve a larger number of users; navigation and surveillance systems will have to guarantee increased positioning accuracy and integrity information. One of the major factors limiting the performance of terrestrial CNS systems are the propagation characteristics for radio waves between ground station and aircraft. While traveling from ground station to aircraft, the communication or navigation signals may be altered or degraded, e.g., by multipath propagation effects or shadowing. Thus, in order develop new or improved CNS solutions a thorough understanding of the air-ground (AG) channel is required.

A general and accurate model of the AG channel is mandatory for the testing and optimization of both modified legacy systems as well as novel systems. An AG channel model allows the analysis of terrestrial CNS systems independently from flight trials which are usually very complex, cost intensive, and require a long lead time. Additionally, the number of flight trajectories, systems or configurations which can be covered by flight trials is limited. Using a channel model, terrestrial CNS systems can be evaluated using computer simulations. Simulations allow the economic and rapid testing of a large variety of systems and configurations. Currently, no accurate general wideband model of AG channel derived from measured data exists.

Contribution of Dissertation

In this dissertation, we propose a channel model of the AG channel for terrestrial CNS systems in the L-band. Using the channel model we are able to realistically simulate the effects of the channel on terrestrial CNS systems.

The contributions of the dissertation can be split up in four parts:

1. Layout of a channel model architecture for the AG channel [8], [9].
2. Development of algorithms to estimate information required to adapt the architecture to a specific environment from measured data [10].
3. Design, implementation, and execution of flight trials to measure the AG channel properties [11].
4. Adaptation of the channel model architecture to a regional airport environment and succesful validation of the channel model against measured data [12].

The presented AG channel model architecture uses a geometry-based stochastic modeling approach. Thus, the AG channel model is efficiently able to describe not only the long term statistical channel properties but also the channel's non-stationarity. If a channel is non-stationary its statistical properties change over time: the statistical description of the channel at a given time instance may be very different from the description at a different time instance. Representing such a behavior using a purely statistical modeling approach usually results in unfeasibly complex channel models. Compared to a purely statistical approach, a geometry-based stochastic channel model (GBSCM) models propagation effects closer to their original physical cause; e.g., a multipath component (MPC) is not modeled as a purely statistical event but as a reflection originating from a specific building.

In Fig. 1.1 we show channel model architecture and the different model elements. The strongest signal component is usually received through the line-of-sight (LoS) path.

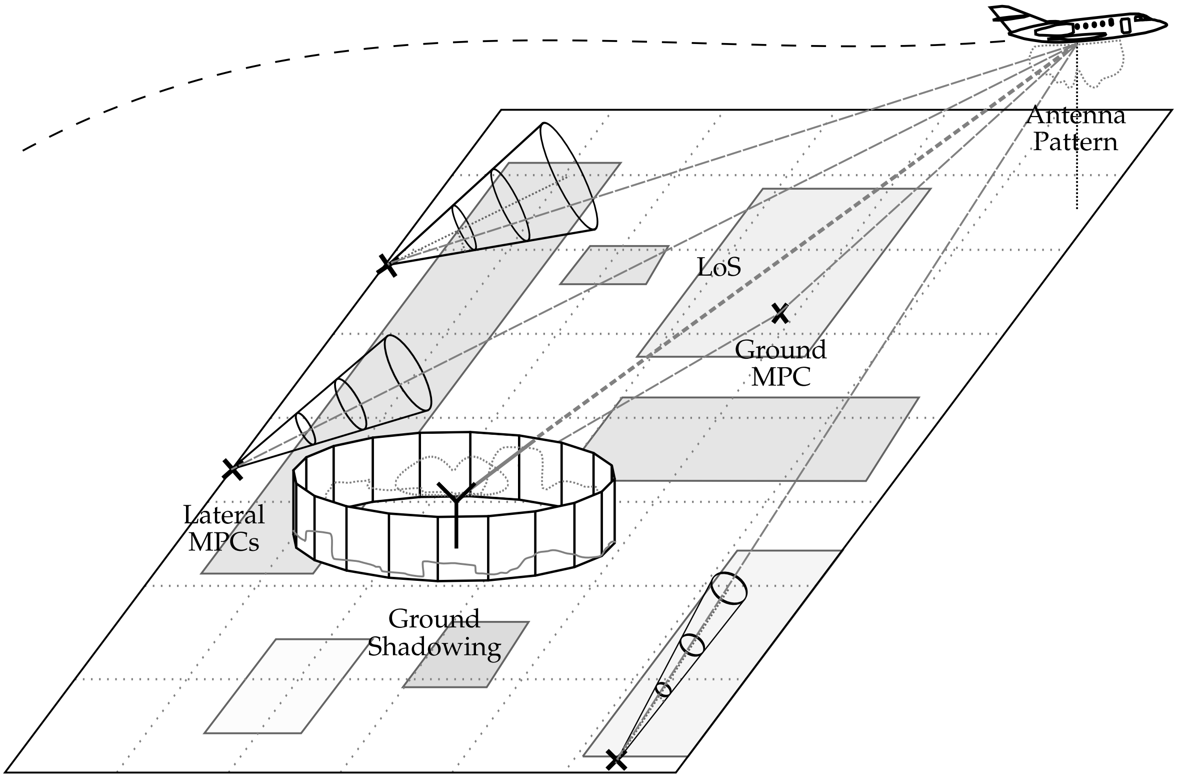

Figure 1.1. *Model elements of the presented channel model.*

The surface component, in the following referred to as ground MPC, is usually caused by a reflection off the ground; the resulting MPCs generally have a small delay relative to the direct LoS propagation path and therefore lead to an attenuation of the latter. MPCs can also be caused by reflections of surrounding buildings or structures; such lateral MPCs cause frequency selective fading and can, depending on the delay of the MPC relative to the LoS path, result in large navigation errors. Other relevant elements are shadowing by terrain or buildings and influence of the involved antennas at ground station and aircraft. Not shown in Fig. 1.1 are diffuse MPCs caused by diffraction, scattering, or reflector clusters.

The channel model architecture can be parameterized, i.e., adapted to a specific environment using the distributions describing the model element properties shown in Fig. 1.1, e.g., how reflectors are distributed. In this dissertation we provide the parameterization for a regional airport environment based on L-band measurements.

Structure of Dissertation

The dissertation is organized as follows.

Chapter 2 provides an overview of the propagation phenomena relevant to terrestrial CNS systems. A special focus is put on multipath propagation and its consequences for communication and navigation receivers. We then provide a comprehensive overview of different approaches to model a channel. The overview includes three modeling techniques: statistical modeling, geometrical modeling, and geometry-based statistical modeling. We also summarize previous models of the AG channel and discuss their shortcomings. The major drawbacks of previous models fall into two classes: first, the models are often fully statistical models. Therefore, in order to minimize the complexity of the model, they do not to capture the non-stationarity of the AG channel; this non-stationarity is especially relevant in the context of navigation systems. Second, previous models are often not derived from flight measured data. Eventually, we derive the requirements on a comprehensive channel model for the analysis of terrestrial CNS systems.

In **Chapter 3** we propose a geometry-based statistical channel model architecture. The architecture covers all relevant propagation effects using the geometrical model elements shown in Fig. 1.1. The model elements are distributed in the environment according to statistical distributions, hence the name GBSCM. Using different parameterizations, i.e., different distributions describing the model element properties, the channel model architecture can adapted to different environments. The geometry-based statistical channel model architecture is well capable to reproduce the non-stationarity of the AG channel.

The parameterization of the channel model to an environment requires information which is generally not trivial to estimate based on measured data, e.g., the positions of reflectors causing MPCs. Thus, in **Chapter 4** we describe how this information can be estimated from measured data. To this end we first describe how the fundamental statistical channel properties can be estimated from measured data. We then propose a MPC parameter estimation and tracking algorithm able to detect the individual MPCs in the measured signal and estimate the associated MPC parameters, e.g., delay. These MPC parameters are then used to localize the reflectors causing detected MPCs using a Bayesian method. Note that the applicability of the presented algorithms goes far beyond the scope of AG measurements: the algorithms may be used in any setting where an accurate estimation of MPC parameters and reflector locations is required.

Chapter 5 is devoted to the flight trials carried out to measure the propagation characteristics of the AG channel in the L-band. The measurements were conducted in a regional airport environment. We start by describing the principal hardware components and waveforms employed during the flight trials. In order to perform a thorough analysis of the channel we require a fully synchronized hardware setup. Thus, we present the synchronization concept and procedures to achieve time synchronization between ground station and aircraft. To be able to assess the fidelity of the measurement system, we also include a discussion of the different errors sources for the measurements. These errors can either be due to the setup itself or interference by aircraft avionics or other systems. The chapter is concluded by an overview of the different flight routes flown throughout the campaign.

In **Chapter 6** we present results generated by applying the previously described algorithms to the measured data. First we show statistical results on the channel properties. These results include the distribution of receive power and classical statistical channel characteristics, e.g., power delay profile (PDP). We also present results on the MPC parameter estimation and tracking algorithm. The results of the reflector localization algorithm illustrate the distribution of reflectors in the environment the measurements were conducted. Thus, the results allow a deep insight in how the environment around the ground station influences the channel.

In **Chapter 7** we propose a parameterization for a regional airport environment for the L-band using geometry-based statistical channel model architecture presented in Chapter 2. We start by discussing how the distributions for the different model elements are derived from the results presented in Chapter 6. The channel model parameterization is successfully validated using three methods: first, a quantitative, statistical validation in which we compare key statistical parameters between measurements and channel model. Second, a qualitative validation in which we compare time series of between measurements and channel model. Third, we validate the channel model using LDACS range measurements: we compare the channel model output against the 2012/2013 LDACS flight trial ranging experiments. Therefore, we show that the channel's effects on a CNS system are accurately reproduced.

In **Chapter 8** we summarize the key contributions of this dissertation.

CHAPTER **2**

CHANNEL MODELING FUNDAMENTALS

Contents

2.1 Overview

The following chapter describes the essentials of channel modeling. We start in Sec. 2.2 with the propagation mechanisms shaping the channel. The channel impacts the performance of the various kinds of communication, navigation, and surveillance (CNS) systems very differently as we show in Sec. 2.3. Different types of channel models are discussed in Sec. 2.4. In Sec. 2.5 we present the basic theory used to analytically describe important features of the channel. This analytical framework is an important basis for the modeling of a channel. The chapter concludes in Sec. 2.6 with an overview of prior work on the air-ground (AG) channel. Herein, we also define the requirements on the comprehensive AG channel model presented in this dissertation.

2.2 Propagation Mechanisms

When shouting while standing within a narrow canyon one is often able to hear one or multiple echoes of his or her own voice. These echoes are caused by sound waves being reflected off the canyon walls: sound waves are able to travel back to the shouting person. Therefore, sound waves may reach the same point via different propagation paths. Each of those propagation paths, depending on where and how often sound waves are reflected, has a different length, and thus also a different delay.

We can make similar considerations about electromagnetic waves as for acoustic waves. The electromagnetic fields used to transmit information propagate according to the Maxwell equations. The electromagnetic fields form a plane wave if one is located in the far field, i.e., at distance from the transmitter larger than the Fraunhofer distance. In that case we can adopt the useful approximation of describing electromagnetic waves as rays [13].

Therefore, radio signals[1] emitted from the transmitter can be visualized to travel to the receiver via multiple propagation paths (rays). The signal delay, i.e., the time it takes for the signal to travel from receiver to transmitter, is linearly related to the propagation path length. The shortest physically possible propagation path is referred to as the line-of-sight (LoS) path[2]. All other propagation paths are termed

[1] In the following by the term signal we understand (wireless) radio signals.

[2] Note that the LoS path is not necessarily the straight line between transmitter and receiver, as signals may travel on a bent path, e.g., due to tropospheric bending. The LoS signal can also not be defined as the signal component with the shortest delay, i.e., the signal component received first, as the LoS signal may be blocked, e.g., by a building.

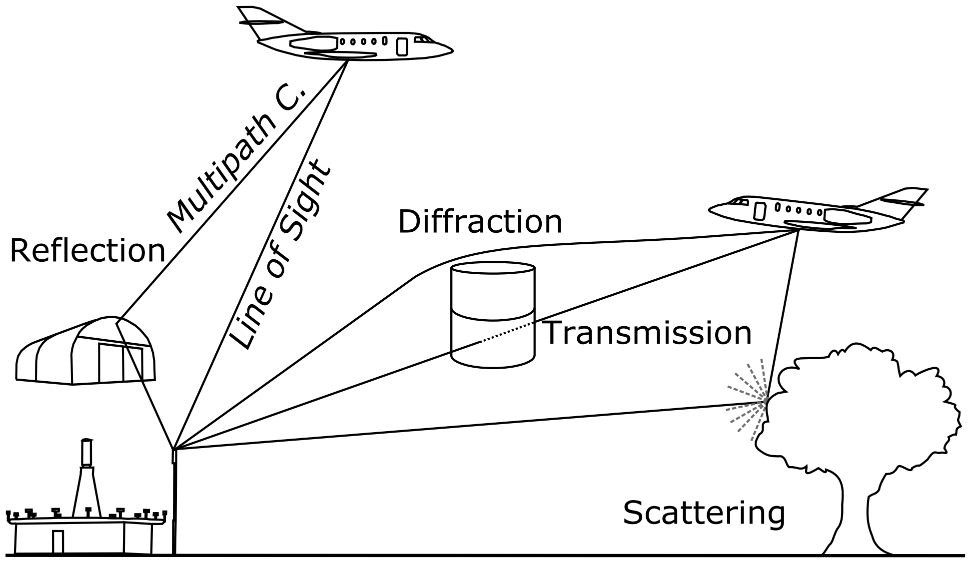

Figure 2.1. *Fundamental propagation mechanisms.*

multipaths. We refer to the signal received through the LoS path as the LoS signal, while signals received through multipaths are called multipath components (MPCs). As shown below, both the LoS signal as well as MPCs can be characterized by the same parameters. Thus, in the following we often do not distinguish between LoS signal and MPCs and term all signals received through any propagation path as MPCs.

The four main propagation mechanisms shaping the channel are shown in Fig. 2.1.

Reflection and refraction: When signals arrive at a smooth border region between two different isotropic media, one part of the signal is reflected while the other part entering the media is refracted. Snell's law states that the angle of incidence, i.e., between the incoming signal and the line perpendicular to the surface, equals the reflection angle, i.e., the angle beteen the outgoing signal and the line perpendicular to the surface [14]. Snell's law also defines how the direction of the refracted signals changes.

The phase and amplitude of reflected and refracted signal depend on the electromagnetic properties of the surface as well as the angle of incidence [15]. For the angle of incidence approaching $90°$ all power of the incoming signal is reflected back. This effect is called total reflection and can be observed when looking at a very large incident angle, i.e., almost in parallel direction, at a glass surface: in that case the glass surface becomes a mirror.

Reflection and refraction do not only appear between gaseous and solid media, but also between two gaseous media. Therefore, in the context of the AG propagation, signals generally do not travel on a straight path through the troposphere. As the troposphere is thinning with increasing altitude, the signals are refracted, i.e., they travel on a slightly bent path [14], [16]. A special case of tropospheric reflection and refraction is ducting: We speak of ducting if signals become trapped in one or more of the tropospere's layers. The signals may be reflected back to earth, or even start bouncing within the borders of tropospheric layers and, thus, follow the curvature of the earth.

Scattering: While signals are reflected off smooth surfaces, in case of a rough surfaces signals are scattered. In that case, signals are scattered in multiple directions (in contrast to being reflected into a single direction as in the case of a reflection). The roughness of a surface is usually characterized using the standard deviation of the surface irregularities relative to the mean height. Whether a surface causes scattering with a specific signal is usually described by Rayleigh roughness criterion which is a function of three parameters: the standard deviation of the surface irregularities, the signal wavelength, and the grazing angle of the signal, i.e., the angle between the incoming signal and the ground surface. For example, given a signal with carrier frequency of $1\,\mathrm{GHz}$ and a grazing angle of $5°$, the standard deviation of the surface irregularities must be at least $2.8\,\mathrm{m}$ to cause significant scattering [14].

We distinguish between three different types of scattering. The scattering type depends on size of the object causing the scattering in relation to the signal wavelength [17]. If an object is small compared to the signal wavelength we speak of Rayleigh scattering. In case of both object and signal wavelength being of similar size Mie scattering results. For objects larger than the signal wavelength we talk of geometric scattering.

Scattering often occurs simultaneously with reflections: depending on the roughness of the surface, part of the signal is reflected in a specific direction, while another part is scattered in multiple directions.

Diffraction: Diffraction directly follows from the Huygens-Fresnel principle how waves enter the space lying behind an obstacle [14]. The result is that signals are bent around edges.

For diffraction to appear, the object causing it must be in the order of a signal wavelength. Diffraction can significantly alter the shape of a signal.

Transmission: When signals pass through different media they are attenuated. The attenuation the signals experience depends on material and signal wavelength. In air signals generally only experience a very minor attenuation. In optically dense media, e.g., concrete walls, signals may be attenuated by tenths of dB per meter [18].

Note that the emitted signal may be subject to an arbitrary combination or repetition of the mechanisms described above. For example, a signal may be reflected off a wall, then scattered off a column, and eventually reflected off a second wall before it reaches the receiver. The concatenation of multiple reflections is often observed. We term the concatenation of multiple reflections as multi-bounce reflections.

Parameters of a Multipath Component (MPC)

In the single input single output (SISO) case, we can characterize an MPC at a given time instance using the following parameters:

- delay τ,
- complex amplitude α,
- Doppler frequency ν, and
- delay-dispersive function κ.

Complex Amplitude

Both power and phase of an MPC are characterized by its complex amplitude α. While traveling through air, the absolute value of the complex MPC amplitude decreases according to the free space path loss (FSPL) [14]. The phase of the complex MPC amplitude depends on the signal wavelength of the carrier frequency and the distance traveled.

The change the complex MPC amplitude experiences during a reflection or scattering depends on the complex reflection coefficient Γ. The reflection coefficient is a function of the material on which the reflection occurs, its electromagnetic properties, its roughness, as well as the angle between the incoming signal and the reflecting surface [15], [19].

Delay

The MPC delay τ describes the time it takes for the signal to travel from the transmitter to the receiver. Assuming straight propagation paths, the MPC delay is completely defined by the underlying geometry. The MPC delay is equal to the distance traveled from the transmitter via its reflections point towards the receiver, divided by the speed of light in air c_{a}.

Doppler Frequency

The MPC Doppler frequency ν is proportional to the rate of change of the MPC delay τ, i.e., its first derivative with respect to time t

$$\nu = \frac{\partial \tau}{\partial t} f_{\mathrm{c}} \tag{2.1}$$

with f_{c} denoting the carrier frequency of the signal.

The MPC Doppler frequency also describes the direction from which the MPC is received. Assuming a fixed ground station and a moving aircraft, we can also interpret the MPC Doppler frequency in a geometrical sense as

$$\nu = \cos(\varphi_v) \frac{|\boldsymbol{v}| f_{\mathrm{c}}}{c_{\mathrm{a}}} \tag{2.2}$$

where φ_v is the angle between the movement direction of the aircraft and the line connecting aircraft and ground station for the LoS path, or in the case of an MPC, its last reflection point. The absolute aircraft speed is denoted by $|\boldsymbol{v}|$.

Delay Dispersive Function

The propagation mechanisms described above can significantly change the shape, i.e., the frequency response, of a signal. We denote the delay-dispersive function the MPC undergoes by $\kappa(\tau, t)$, i.e., for a given carrier frequency a function of the delay τ and continuous time t. The shape of the delay-dispersive function depends on the fundamental propagation mechanisms the MPC has undergone. For example, for the direct LoS signal or a reflection from a smooth surface of large dimensions, the delay-dispersive function may be very similar to a Dirac function, i.e., has a flat spectrum. If an MPC experiences scattering or diffraction on its way to the receiver, the spectrum of the delay-dispersive function may not be flat at all.

Throughout the dissertation we use the term excess MPC delay, excess Doppler frequency, and excess power. By those relative parameters we understand the MPC delay, Doppler frequency, or power relative to the corresponding parameter of the LoS signal.

2.3 Propagation in the Context of Terrestrial Communication, Navigation, and Surveillance Systems

The environment any radio system is operated in strongly influences the performance of the system. In this section we describe how the underlying physics impact

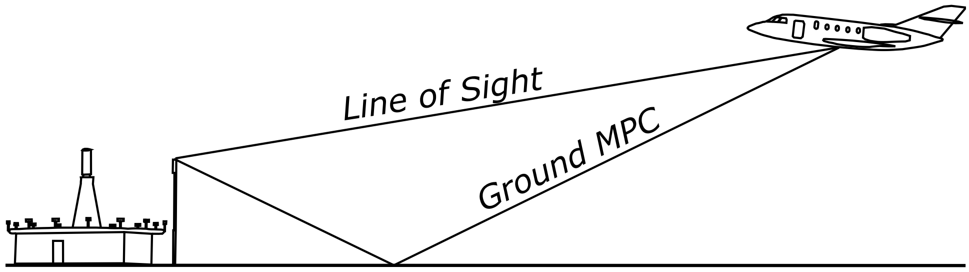

Figure 2.2. *Ground multipath propagation in the AG channel.*

the operation of terrestrial CNS systems. We show that the AG channel significantly affects the performance of CNS systems by two effects: flat fading and frequency selective fading.

In **flat fading** (also known as narrowband or large scale fading) the received signal is attenuated over the full signal bandwidth evenly. Flat fading can be caused by different effects, e.g., multipath propagation, shadowing (the blockage of the LoS signal by a building or terrain), or the directivity of the involved antennas. As described in Sec. 2.3.1 the overlapping of the LoS signal with an MPC caused by a ground reflection can lead to a significant reduction of the receiver performance.

If the signal experiences a different attenuation on different frequencies we speak of **frequency selective fading** (also known as small scale fading). In the AG channel frequency selective fading is predominantly caused by the overlapping of an MPC with the LoS signal. For the fading to become frequency selective, the excess MPC delay has to be at least in the order of the reciprocal system bandwidth. Especially in the context of navigation, as shown in Sec. 2.3.2, frequency selective fading has a significant impact on the receiver performance.

2.3.1 Communication

For decades in civil aviation low bandwidth analog AG communication systems have been employed, e.g., the very high frequency (VHF) voice communication with typical bandwidths of $25\,\mathrm{kHz}$ or $8.33\,\mathrm{kHz}$. Such low bandwidth systems predominantly experience flat fading.

An effect often causing flat fading is the overlaying of the LoS signal with a ground MPC, i.e., a reflection off the ground plane, as illustrated in Fig. 2.2 [20]. Due to superposition of the ground MPC with the LoS signal, the resulting signal may be severely attenuated with respect to the individual LoS signal. The result is fading of the received signal power.

Depending on the depth of the fade the received signal power may vanish in the

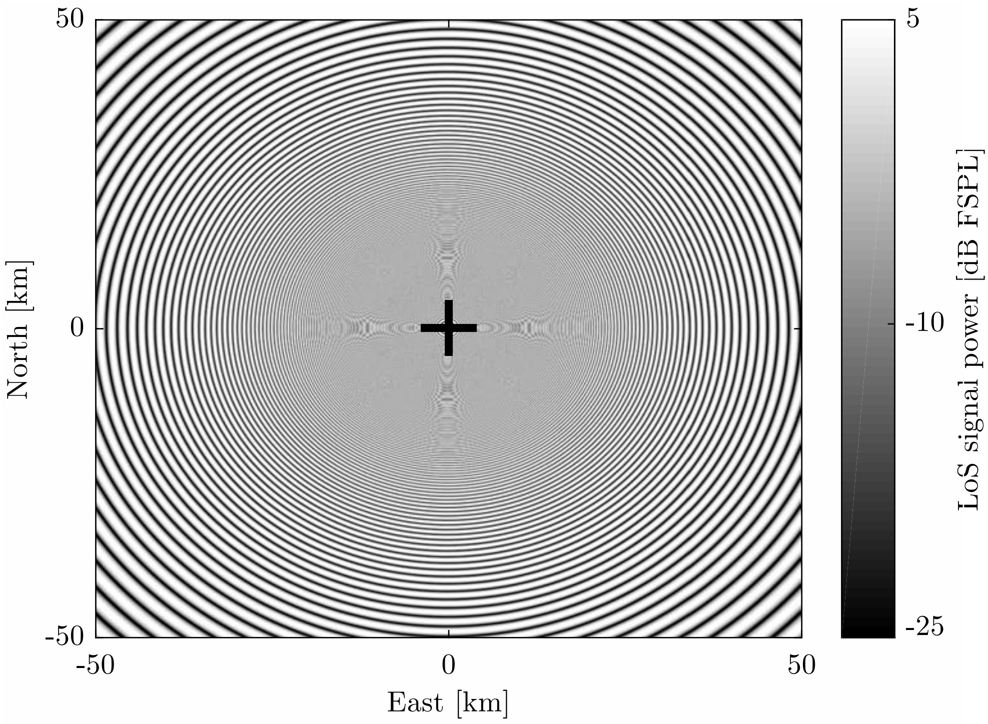

Figure 2.3. *Variation of the received signal power due to ground multipath propagation.*

noise floor. For an analog voice communication system the result is an incomprehensible voice signal. In a digital communication system the bit error ratio (BER) increases until it reaches 0.5: the communication link breaks down and no information can be exchanged.

In Fig. 2.3 the fades of the received signal power due to ground multipath propagation are visualized. For Fig. 2.3 we assume an aircraft flying at a constant altitude of $10\,\mathrm{km}$ above ground level (AGL). The ground station position is marked by a black cross. We normalize the received signal power by FSPL and assume a perfectly reflecting ground surface [14].

From Fig. 2.3, we observe that for an aircraft flying at a constant altitude, the variation of the received signal power occurs in a circular shape. With increasing link distance the distance between two fades decreases. Assuming a straight trajectory, an aircraft experiences longer periods where the received signal is at a very low power level.

A critical situation occurs if the aircraft flies on a circle around the ground station, i.e., continuously stays in an area experiencing fading. In that case the fades of the received signal power can last for a very long time.

Frequency selective fading is relevant in the context of modern wideband aeronautical communication systems, e.g., L-band Digital Aeronautical Communication

System (LDACS). Frequency selective fading causes the communication signal to arrive at the receiver distorted. In general, equalization of the received signal becomes necessary [21]. Depending on the quality of the equalization process the BER can reach an error floor, i.e., even if the signal power is increased, the BER stays constant.

We conclude that in the past mainly flat fading was relevant for the low bandwidth civil communication systems. For the digital civil communication systems currently being introduced also frequency selective fading is highly relevant.

2.3.2 Navigation

As for a communication system, the performance of a navigation system can also be severely influenced by the channel. The figure of merit in the context of navigation is the range estimation error, also referred to as the ranging error.

To estimate its position, the navigation receiver relies on combining ranges to different ground stations of known location. These ranges can be in the form of a true range, e.g., in the case of the two way ranging system distance measuring equipment (DME), or a pseudorange like in Global Positioning System (GPS) [22], [23]. Additional sensors such as barometer, inertial navigation system (INS), or in the case of a VHF omnidirectional range (VOR) angle information often supplement the position estimation [22].

In the DME system the airborne DME interrogates, i.e., sends pulses, to a neighboring ground station [22]. After waiting a fixed delay time $t_{\mathrm{DME,w}}$, the ground station replies to the interrogation using pulses. The true range d is calculated based on the total propagation time $t_{\mathrm{DME,t}}$ as

$$d = \frac{t_{\mathrm{DME,t}} - t_{\mathrm{DME,w}}}{2} c_{\mathrm{a}}. \tag{2.3}$$

In pseudoranging systems, e.g., global navigation satellite system (GNSS) or the proposed LDACS based navigation, the ground station continuously emits a known signal [5], [23]. Based on the time instant at which the signal is received the range to the ground station is estimated. As the exact time of transmission with respect to the system time[3] is unknown at the receiver, the range contains an unknown clock offset and is therefore referred to as a pseudorange [23].

Calculating pseudoranges to four known transmitter locations, e.g., satellites or ground stations, allows the estimation of the own position as well as of the clock

[3] By system time we understand a common time identical to all ground stations.

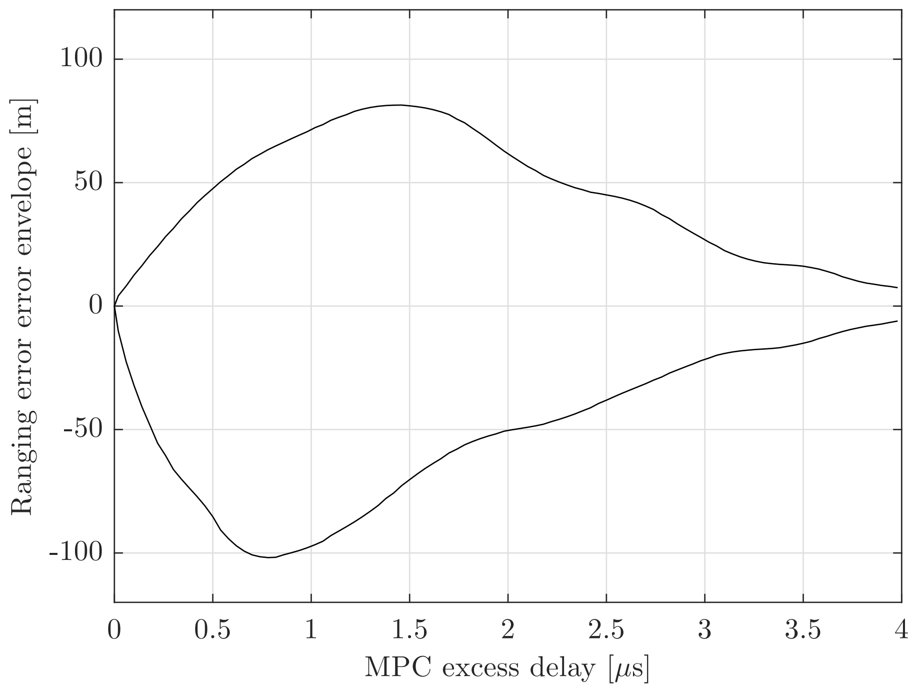

Figure 2.4. *DME multipath error envelope for two-path channel (LoS signal and MPC) based on measured on standard airborne DME signal [24].*

offset at the receiver with respect to the system time. As the degradation on ranging and pseudoranging caused by the channel are identical, we do not distinguish between the two in the following.

Ranging errors can be divided into fast and slowly varying ranging errors. Fast varying ranging errors can in general be well mitigated by tracking or averaging, e.g., a delay-locked loop (DLL), as they usually follow a zero mean distribution [23]. Slowly varying ranging errors are far more critical as they are in a form of a bias rather than a zero-mean error distribution. Such a bias in the ranging is hard to mitigate [24]–[26].

The most typical cause for fast varying ranging errors is a low signal-to-noise-ratio (SNR). The low SNR may be caused by flat fading or a large link distance. The ranging error becomes more and more influenced by the thermal noise. Resulting is a normally distributed ranging error.

Frequency selective fading caused by the overlapping of the LoS signal with one or more MPCs is known to cause both slowly and fast varying ranging errors. As an example Fig. 2.4 shows the ranging error envelope generated using an airborne DME signal. The MPC power relative to the LoS signal power in Fig. 2.4 is $-6\,\mathrm{dB}$.

From Fig. 2.4, we observe a dependency of the ranging error on the excess MPC delay: small ranging errors exist for very short excess MPC delays $< 100\,\mathrm{ns}$. The largest ranging errors are observed between $250\,\mathrm{ns}$ and $2\,\mu\mathrm{s}$. For larger excess MPC delays the ranging error decreases again. The ranging error scales with the excess MPC power (not shown in Fig. 2.4), i.e., increasing the excess MPC power also increases the ranging error. Error envelopes for different systems look similar in its shape, but depending on the system bandwidth, waveform, and receiver algorithm, the errors may scale up and down.

Assuming a fixed excess MPC delay and power, the ranging error oscillates between the upper and lower curve in Fig. 2.4 with the excess MPC Doppler frequency. Thus, the excess MPC Doppler frequency determines whether the ranging error is slowly or fast varying. In both cases the resulting ranging error may not be distributed with zero mean, i.e., will be in the form of a bias. While fast varying ranging errors can be averaged out, slowly varying MPCs, especially MPCs with a long lifetime, are hard to mitigate. For averaging out such ranging errors, the averaging duration would have to be chosen unrealistically long in order to mitigate the error.

Both flat and frequency selective fading usually exist at the same time in the AG channel. Large ranging errors can occur if the LoS signal is strongly attenuated by flat fading, while at the same time a MPC at the critical excess MPC delay exists. In that case the excess MPC power of a typically weak MPC increases. The resulting ranging error also increases. The corner case of that situation is if the MPC power becomes higher than the LoS signal power. In that case the ranging error can grow to very high values as an MPC might be mistaken for the LoS signal.

2.3.3 Surveillance

There are currently several systems for surveillance in civil aviation. The most relevant systems in the L-band are automatic dependent surveillance - broadcast (ADS-B), secondary surveillance radar (SSR), and primary surveillance radar (PSR) [27].

In ADS-B a transponder continuously broadcasts its position in the L-band to both the ground and other aircraft using pulse position modulation (PPM). For the position calculation the aircraft usually relies on its onboard navigation systems. Therefore, ADS-B functions like a communication system. The channel degrades the ADS-B performance in the same way as described in Sec. 2.3.1.

In SSR the ground station interrogates the aircraft, which replies using PPM. Using a directional antenna both the range to the aircraft as well as the angle under which the aircraft is seen at the ground station can be estimated. Multipath propagation affects the ranging and angle estimation error similarly as the navigation systems described in Sec. 2.3.2. In SSR supplementary information like the aircraft identification and altitude is transmitted. The communication functionality of SSR experiences the degradation as a communication system described in Sec. 2.3.1.

The PSR is a conventional radar. A strong signal is transmitted from the ground station towards the aircraft. Aircraft are localized using the reflected signal. The main advantage of the PSR is that no equipment is required onboard the aircraft. The performance of the PSR is influenced in similar fashion by the channel as a navigation system as discussed in Sec. 2.3.2.

2.4 Channel Modeling

In the previous section we described the impact of the channel on terrestrial CNS systems. It is unfeasible to conduct flight trials every time a new or improved system is to be tested. Thus, starting in the early 1960's first models of the AG channel were developed.

Existing channel models can be divided into three types [28]: deterministic channel models, statistical channel models, and geometry-based stochastic channel models. The different types are discussed in Sec. 2.4.1 through Sec. 2.4.3.

2.4.1 Deterministic Channel Modeling

Deterministic or physical channel models aim to reproduce the theoretical physical propagation mechanisms. These deterministic models usually require a detailed knowledge about the environment transmitter and receiver are located in. The knowledge often consists of a detailed building plan of the environment, e.g., of an airport. Such a building plan includes information about the location of buildings or objects. Additionally, the building plan provides information about the materials the buildings or objects are composed of. The propagation characteristics are then computed based on the physical propagation mechanisms. Depending on the acceptable complexity, the simulations take into account some or all of the propagation mechanisms described in Sec. 2.1 and shown in Fig. 2.1.

The propagation mechanisms can be modeled using two approaches [29]. The full wave approach aims to solve the Maxwell equations directly. In contrast to that, the geometrical theory of diffraction (GTD) approach approximates planar electromagnetic waves as rays. Hence they are often commonly referred to as ray tracers.

A major drawback of deterministic channel models is that their output is not necessarily identical to what measurements would provide. This is due to simplifications of deterministic channel models. These simplifications, in turn, are required to keep the computational complexity in acceptable limits. Nevertheless, determin-

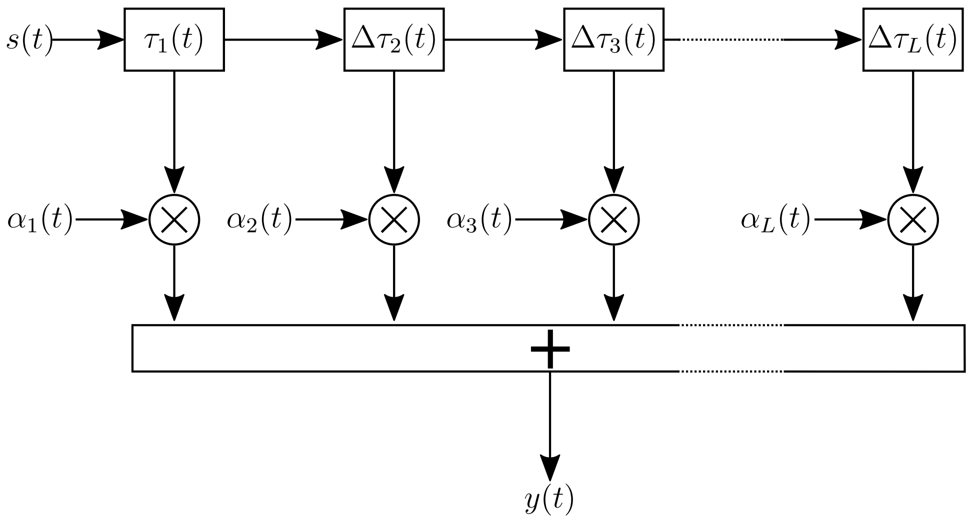

Figure 2.5. *Graphical representation of a tapped delay line model.*

istic channel models are often used to obtain an approximation of the channel if setting up a measurement campaign is not possible or unfeasible.

2.4.2 Statistical Channel Modeling

Most of the past and current channel models are statistical channel models. Hereby, the channel is described as a statistical process without any reference to the underlying geometry. Statistical channel models provide a simple, yet powerful way to describe different environments.

Fig. 2.5 shows the general form of the most commonly used realization of a statistical channel model, the tapped delay line model.

The channel consists of $L\left(t\right)$ taps, each representing one or the vector sum of multiple MPCs. Each tap is delayed by the delay $\tau_l\left(t\right)$ and multiplied by the complex weight $\alpha_l\left(t\right)$.

The additional delay of each MPC $\Delta\tau_k(t)$ in Fig. 2.5 is given as

$$\Delta\tau_k(t) = \tau_k(t) - \sum_{l=1}^{k-1} \tau_l(t). \tag{2.4}$$

In a statistical channel model both the MPC delays and complex weights as well as the number of taps follow a statistical distribution, e.g., Rice and Rayleigh distributions are typical for the complex weights.

We can differentiate between stationary and non-stationary channel models - see Sec. 2.5 for a definition of stationarity . If stationarity is assumed the distributions of MPC delays, complex weights, and number of MPCs do not change over time. Due to the simplicity, stationary channel models are currently predominantly used in the field of statistical channel modeling: the channel is described using a linear time-invariant model. Nevertheless, in recent years more interest has been focused on modeling non-stationary channels [30], [31].

Early channel models were stationary narrowband channel models describing only flat fading, i.e., distribution of the receive power. The narrowband assumption applied to Fig. 2.5 means that only one tap exists. Apart from the simplicity, the measurement data required for such channel models could already be recorded with hardware available back then. Additionally, single tap channel models were usually sufficient for the narrowband CNS systems employed at those times. Nevertheless, the applicability of narrowband statistical channel models in the context of navigation has always been limited. The main reason is that narrowband channel models do not consider frequency selective effects caused by MPCs, the major cause for the most critical ranging errors.

As the typical bandwidth of communication systems grew over decades narrowband channel models are proving less applicable to the new systems. The necessity arose to model the frequency selective fading of a channel. The resulting models are wideband channel models with multiple taps. Again, both MPC delays and complex weights are drawn from statistical distribution.

A major drawback of statistical channels is that modeling non-stationary channels using solely statistical distributions is very complex. The complexity, however, can be reduced if the underlying geometry is considered, as it is the case for geometry-based stochastic channel model (GBSCM) described in the following.

2.4.3 Geometry-Based Stochastic Channel Modeling

GBSCMs arose as a hybrid between deterministic and statistical channel models and combine the advantages of both [28], [32], [33]. Their main advantage over purely statistical channel models is that they are more suited to model non-stationary channels. Compared to deterministic channel models, the simulations using GBSCMs are usually significantly less computationally complex than simulations using deterministic channel models.

A typical approach in GBSCM is to use geometrical model elements, e.g., reflectors or scatterers, and to place these model elements in the environment to be investigated, in our case an airport. Usually, the locations of model elements follow a statistical distribution. Once the model elements are placed, their influence on the channel only depend on the position of receiver and transmitter. The evolution of MPC parameters, e.g., MPC delay, are a direct result of the geometry. As model elements are statistically distributed, different realizations of the same channel can be rapidly generated and employed for testing different systems or scenarios.

There are two ways to derive the statistical distributions for the model elements. The first is to derive the statistical distributions based on the underling geometry. For example, if driving through a canyon, reflectors may be located on walls on both sides of the road. In this dissertation however, we will base the distributions on measurement data, e.g., as done in [32], [33].

2.5 Channel Description

In the previous section, we describe different ways to model a channel. We now focus on methods of describing and characterizing channels using standard values.

Early channel descriptions used a narrowband approach in which only flat fading is is modeled, i.e., in terms of statistics the receive power. As the bandwidth of systems increased over decades the narrowband description of the channel turned out to be insufficient to model the performance of new systems. The necessity arose to consider wideband channels and to take its frequency selective fading into account. The underlying theory to describe channels was first developed by Bello in his seminal work [34]. Bello's considerations still build the basis for the description of channels and various channel model types.

In Fig. 2.6 an overview of the functions introduced by Bello is given. The deterministic and statistical description of channels using so called system functions derived by Bello is discussed in Sec. 2.5.1 and Sec. 2.5.2, respectively.

2.5.1 Deterministic Channel Description

Bello introduces four kernel functions shown in Fig. 2.6 (left side) to describe a time-variant channel. The different functions describe the identical channel and can be transformed into each other according to Fig. 2.6.

The starting point of any channel description is the time-variant impulse response $h(\tau, t)$ describing the relation between the received signal $\boldsymbol{y}(t)$ and the transmit signal $s(t)$

$$\boldsymbol{y}(t) = \int_{-\infty}^{\infty} h(\tau, t)\, s(t-\tau)\, \mathrm{d}\tau + \psi(t), \tag{2.5}$$

where $\psi(t)$ represents additive noise. The time-variant impulse response allows us to analyze the evolution of MPC delays τ over time t.

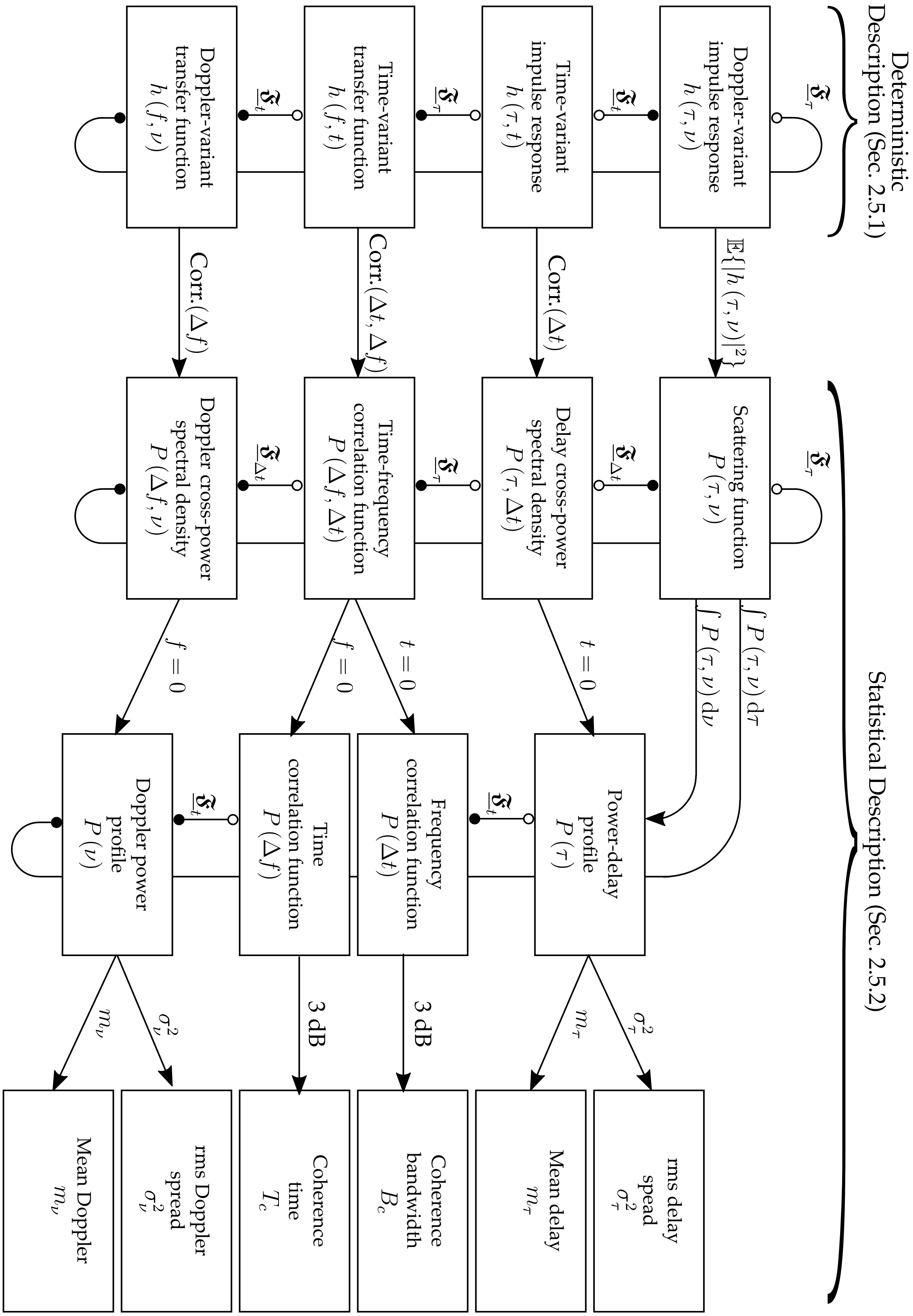

Figure 2.6. *System functions of the time-variant WSSUS channel (based on [35]).*

The Doppler-variant impulse response is calculated as

$$h(\tau,\nu) = \int_{-\infty}^{\infty} h(\tau,t)\exp(-\mathrm{j}2\pi\nu t)\,\mathrm{d}t \tag{2.6}$$

and shows the delay τ and Doppler frequency ν of the MPCs.

The time-variant transfer function

$$h(f,t) = \int_{-\infty}^{\infty} h(\tau,t)\exp(-\mathrm{j}2\pi f\tau)\,\mathrm{d}\tau \tag{2.7}$$

provides information about the change of the signal spectrum $h(f)$ over time t.

The Doppler-variant transfer function

$$h(f,\nu) = \int_{-\infty}^{\infty} h(f,\nu)\exp(-\mathrm{j}2\pi ft)\,\mathrm{d}t \tag{2.8}$$

gives describes how quickly the signal spectrum $h(f)$ changes using the Doppler frequency ν.

2.5.2 Statistical Channel Description

The autocorrelation functions between the deterministic functions introduced in Sec. 2.5.1 build the basis for the statistical description of a channel:

$$P(\tau_1,\tau_2,t_1,t_2) = \mathbb{E}\{h(\tau_1,t_1)\,h^*(\tau_2,t_2)\}, \tag{2.9}$$

$$P(\tau_1,\tau_2,\nu_1,\nu_2) = \mathbb{E}\{h(\tau_1,\nu_1)\,h^*(\tau_2,\nu_2)\}, \tag{2.10}$$

$$P(f_1,f_2,t_1,t_2) = \mathbb{E}\{h(f_1,t_1)\,h^*(f_2,t_2)\}, \text{and} \tag{2.11}$$

$$P(f_1,f_2,\nu_1,\nu_2) = \mathbb{E}\{h(f_1,\nu_1)\,h^*(f_2,\nu_2)\}. \tag{2.12}$$

Generally the correlation functions are four-dimensional. However, as we show below the number of variables can be reduced to two if two assumptions are fulfilled.

Wide-Sense Stationarity (WSS)

In statistics a stationary process is a stochastic process whose first and second order moment, e.g., mean and variance, are independent from the time [36]. In general no real world channel is stationary in the strict sense. But we can weaken the term stationary by assuming stationarity in a wide-sense. By a wide-sense stationary (WSS) channel we understand a channel whose fading statistics do not depend on the absolute time, but only on the time difference[14]. Thus the fading characteristics neither depend on the absolute time t_1 and t_2 but only on the time difference $\Delta t = t_2 - t_1$. Hence, the number of variables in (2.9) through (2.12) can be reduced by one. The delay-Doppler autocorrelation function becomes

$$P(\tau_1, \tau_2, \nu_1, \nu_2) \underset{\text{WSS}}{=} P(\tau_1, \tau_2, \Delta\nu) \,. \tag{2.13}$$

Uncorrelated Scattering (US)

Uncorrelated scattering (US) means that the scattering occuring in the channel is uncorrelated [14]. That means a scatterer with delay τ_1 is uncorrelated from a scatterer with different delay τ_2. Using the US assumption the number of variables in (2.9) through (2.12) can be reduced. We can write the delay-Doppler autocorrelation function as

$$P(\tau_1, \tau_2, \nu_1, \nu_2) \underset{\text{US}}{=} P(\Delta\tau, \nu_1, \nu_2) \tag{2.14}$$

with the delay difference $\Delta\tau = \tau_2 - \tau_1$.

Wide-Sense Stationary Uncorrelated Scattering (WSSUS)

Using the assumptions of WSS and US, in short the WSSUS assumption, we obtain the statistical description of the channel shown in Fig. 2.6 (right side): the correlation functions now only depend on two input variables

Of great importance in the context of channel modeling is the **scattering function** $P(\tau, \nu)$. The scattering function describes the expected receive power at a certain delay τ and Doppler frequency ν.

The functions shown in Fig. 2.6 are often marginalized to obtain a more compact characterization of the statistical channel properties. The two most commonly used marginals are presented in the following:

The **power delay profile (PDP)** $P(\tau)$ describes the receive power distribution over the delay τ. In both communication and navigation the power-delay profile is a key figure allowing for an elementary performance analysis of a system using the channel. For example, if a significant part of the power is received at the delay τ most critical for a specific navigation system, e.g., around $800\,\mathrm{ns}$ for DME as shown in Fig. 2.4, large ranging errors are to be expected.

Both **mean delay** m_τ and **root-mean-square (rms) delay spread** σ_τ^2 can be directly calculated from the power delay profile (PDP) $P(\tau)$ resulting in

$$m_\tau = \frac{\int_0^\infty \tau P(\tau)\,d\tau}{\int_0^\infty P(\tau)\,d\tau} \text{and} \tag{2.15}$$

$$\sigma_\tau^2 = \frac{\int_0^\infty (m_\tau - \tau)^2 P(\tau)\,d\tau}{\int_0^\infty P(\tau)\,d\tau}. \tag{2.16}$$

Both parameters are widely used to describe the dispersiveness of the channel in a very compact form. The mean delay m_τ provides information at which delay the power is concentrated. The rms delay spread σ_τ^2 describes how the receive power spreads around the mean delay m_τ.

The **Doppler power profile (DPP)** $P(\nu)$ describes the receive power distribution over the Doppler frequency ν. If the channel exhibits all its power on the LoS signal Doppler frequency, ranging errors due to MPCs are more difficult to mitigate as described in Sec. 2.3.2.

Similarly as for the PDP, we can use the Doppler power profile (DPP) to calculate the **mean Doppler frequency** m_ν and **rms Doppler spread** σ_ν^2 as

$$m_\nu = \frac{\int_{-\infty}^\infty \nu P(\nu)\,d\nu}{\int_{-\infty}^\infty P(\nu)\,d\nu} \text{and} \tag{2.17}$$

$$\sigma_\nu^2 = \frac{\int_{-\infty}^\infty (m_\nu - \nu)^2 P(\nu)\,d\nu}{\int_{-\infty}^\infty P(\nu)\,d\nu}. \tag{2.18}$$

Again, both mean Doppler frequency m_ν and rms Doppler spread σ_ν^2 allow for a very compact description of the channel's statistical properties.

2.6 Air-Ground Channel Modeling - Prior Work

The prior work on the AG channel has been predominantly conducted in the field of communications. We can divide the previous work in two categories: flight trial measurements and theoretical analyses. Flight trial channel measurements often resulted in statistical analyses or channel models. Theoretical analyses based on considerations of the underlying geometry both resulted in deterministic and statistical descriptions or channel models.

2.6.1 Channel Measurements

We can classify previous measurements by the frequency band they were conducted in. As this dissertation is concerned with the L-band AG channel we focus on measurements in that frequency band in the following. For a more comprehensive overview including other frequency bands refer to [37], [38]. Examples for measurements in VHF- and C-band are [39]–[42] and [43]–[50], respectively.

Tab. 2.1 gives an overview of previous measurements conducted in the L-band.

While early L-band measurements were narrowband measurements using a continuous wave (CW) signal, the transition to wideband measurements over time becomes obvious in Tab. 2.1.

Narrowband L-band measurements were conducted by Painter in 1973 using an aircraft [51]. The publication is focused on the variation of the receive power due to ground multipath propagation. Measurements are taken at $f_\mathrm{c} = 1463\,\mathrm{MHz}$ over calm ocean, swamp, and cultivated fields. A two-ray channel model developed in the paper is validated against the measurements. The authors conclude that even the presented simple channel model allows for an accurate prediction of the receive power.

J. R. Child also analyzes the effects of ground multipath propagation in the context of coverage prediction for a communication system [52]. Measurements using a variety of jet and turboprop aircraft are conducted at $f_\mathrm{c} = 900\,\mathrm{MHz}$ confirm the well-known slow variation of the receive power. Child also proposes a method to predict coverage based on panoramic photographs taken from the ground station site. It is concluded that with the help of photographs one is able to predict the coverage accurately within 'a few percent'.

The transition to wideband AG measurements is made in [53], [54]. Measurements using an mid-size business jet are conducted at $f_\mathrm{c} = 1500\,\mathrm{MHz}$ with a bandwidth of $10\,\mathrm{MHz}$ in a desert environment. Due to a tracking parabolic ground antenna multipath propagation is significantly reduced. Nevertheless, both ground and additional MPCs are detected. The statistical analysis of the measurement data includes receive power and phase, PDP as well as rms delay spread and mean delay. The authors conclude that the channel can be modeled by a 3-ray channel model: LoS path, ground MPC, and second MPC, caused by bounces off the surrounding foothills and mountains. The ground MPC has a power between 70% to 96% relative to the LoS signal power. Its MPC parameters are calculated based on the underlying geometry. The second MPC with a power between 2% to 8% relative to the LoS signal power is modeled as a zero mean circularly-symmetric complex normal distribution.

In [55] measurements for low-altitude operations are conducted at $f_\mathrm{c} = 2\,\mathrm{GHz}$ with a bandwidth of $80\,\mathrm{MHz}$. Statistics of the receive power, PDP, mean delay, rms delay spread, and MPC counts are presented. Using a four element antenna array an analysis of achievable diversity gain is performed.

Year	Carr. Freq. f_c	Bandw.	Outcome	Ref.
1973	1463 MHz	CW	Statistical analysis (rx power) 2-path model for receive power	[51]
1985	900 MHz	CW	Statistical analysis (rx power) Coverage prediction based on photographs	[52]
2002	1500 MHz	10 MHz	Statistical analysis (rx power & phase, PDP, delay spread) 3-path model	[53], [54]
2003	2 GHz	80 MHz	Statistical analysis (rx power, PDP, mean delay, delay spread, MPC counts) Diversity analysis	[55]
2011	1800 MHz	50 MHz	Statistical analysis (PDP, delay spread, MPC counts) Diversity analysis	[56]
2011	2 GHz	CW	Statistical analysis (path loss) Path loss model	[57]
2011	1100 MHz	500 kHz	Ranging error analysis of DME and ADS-B	[58]–[61]
2011	2 GHz	CW	Diversity Analysis	[62], [63]
2011	915 MHz	10 MHz	Statistical analysis (rx power and delay spreads) Diversity analysis	[64]
2013	970 MHz	5 MHz	Statistical analysis (rx power, delay spread, K-factor, spatial correlation) Wideband channel model	[65]–[69]

Table 2.1. *Previous L-band measurements conducted for the AG channel.*

The author of [53] conducts multiple input multiple output (MIMO) measurements using a helicopter at $f_\mathrm{c} = 1800\,\mathrm{MHz}$ with a bandwidth of $50\,\mathrm{MHz}$ in [56]. A statistical analysis using PDP is performed. The PDPs from the different antennas are compared with each other. Additionally, the achievable diversity gain is analyzed.

In [57] a unmanned aerial vehicle (UAV) is used to study the receive power in an urban environment at $f_\mathrm{c} = 2\,\mathrm{GHz}$. The measurements deal with a blockage of the LoS signal by buildings, caused by the low elevation angles at which the airship is seen under at the ground station, as well as fading due to MPCs. A channel model is developed to predict the receive power.

The group of authors from [57] conducts single input multiple output (SIMO) measurements using an airship at $f_\mathrm{c} = 2\,\mathrm{GHz}$ [62], [63]. For two environments, urban and wooded, the achievable diversity gains are investigated for low elevation angles.

In [64] an UAV is employed for MIMO L-band measurements at $f_\mathrm{c} = 915\,\mathrm{MHz}$ with a bandwidth of $10\,\mathrm{MHz}$. The altitude of the UAV is $200\,\mathrm{m}$ and its maximum range to the ground receiver is less than a kilometer. The statistical analysis of the measurement data includes distributions of receive power and rms delay spreads. Additionally the spatial correlation of the channel is analyzed.

The most comprehensive AG channel measurements so far are described in [65]–[69]. During the measurements the propagation conditions are investigated at $f_\mathrm{c} = 970\,\mathrm{MHz}$ using a bandwidth of $5\,\mathrm{MHz}$ in a variety of different environments, e.g., fresh and salt water, hilly, mountainous, urban, and suburban, using a jet aircraft. The publications present a very thorough statistical evaluation of the measurement data including the statistics of receive power, rms delay spread, K-factor, and spatial correlation. Wideband statistical channel models for the different environments are presented. Apart from the LoS path, the channel model includes a specular ground reflection, which MPC parameters are calculated based on the underlying geometry. Additional MPCs represent reflection from other objects, e.g., buildings or terrain features. The MPC parameters of those MPCs are statistically distributed. The number of additional MPC depends on the environment.

Worth noting in the context of measurements are the flight trials conducted at Ohio University [58]–[61]. It is debatable whether these measurements can be seen as channel measurements in a strict sense, as they measure the ranging error using DME and ADS-B signals. Yet they offer very detailed insight into the effects of the AG channel on ranging and terrestrial navigation systems in general. It is confirmed that the LoS can be attenuated by tenths of dB due to ground multipath propagation. The authors show that the time-variance of the channel is able to cause bias like ranging errors existing for several minutes. Such errors cannot be mitigated by methods such as averaging or tracking.

2.6.2 Theoretical Channel Analyses

The AG channel has also been analyzed using theoretical considerations. The advantage of such analyses is that they do not require cost intensive flight trials. Additionally, the resulting simulations and channel models are easy to adapt to different frequency bands. The major drawback of channel models based solely on theory is that they may not fully reflect the reality, as the underlying assumptions are usually simplifications of the reality. In the worst case the assumptions may even be wrong. In the following we only discuss the analyses most relevant in the context of L-band channel modeling. For a more complete summary the reader is referred to [37], [38].

An often cited theoretical work about the AG channel was published by Bello. Within [70] analytic expressions for the correlation functions are derived based on the underlying geometry. While going into mathematical depth in the publication, Bello does not provide an easily usable channel model able to be used directly for simulations.

In [71] a tapped-delay line model is proposed for different phases of the flight. The channel model has been widely used in literature for simulating AG communication links. Although some references to earlier channel measurements are made, the parameters are mostly derived using theoretical considerations and/or scientific guesses. While initially developed for the VHF-band, an extension to the L-band exists [72]. However, like the original channel model, the L-band extension is also based on theoretical considerations. For both channel models, a validation using measurement data is not provided.

Further theoretical analyses of the AG channel resulting in statistic or deterministic models have been published in [73]–[77].

2.6.3 Shortcomings of Previous Channel Models

Currently there exists no comprehensive wideband channel model based on and validated by measurement data which is suitable for testing the full range of CNS systems.

Being focused on communication systems previous channel models based on measurement data are statistical channel models. They are not suitable to describe the non-stationarity of the AG channel sufficiently for navigation systems: while being able to model fast varying ranging errors caused by short-lived MPCs well, current channel models are not able to reproduce slowly varying ranging errors, e.g., caused by long-lived MPCs. However, these slowly varying ranging errors are most critical in the navigation context as these errors are hard to mitigate.

Deterministic channel models considering underlying geometry are theoretically able to capture the non-stationary nature of the AG channel. Nevertheless, these channel models have two major drawbacks. First, it is hard to estimate in which way they are able to represent the reality of AG channel. Second, due to the complex simulations required for deterministic channel models, deterministic channel models are not suited for rapid testing for various flight situations, environments and system parameters. Thus, it is impossible to simulate a large number of flight hours necessary to investigate rare events, i.e., errors which only occur with a very low probability. Such rare errors are highly relevant for a safety critical environment such as civil aviation where the correct functioning of systems has to be guaranteed to down very small probabilities, e.g., 10^{-7}.

We are able to conclude the requirements on a channel model suitable to test all CNS systems in the L-band as follows. The AG channel model we propose should...

1. ...be able to capture the non-stationary nature of the AG channel. Especially slowly varying ranging errors need to be representable by the channel model.

2. ...allow for the computationally efficient simulation of different flight situations and system parameters.

3. ...be based on and validated by flight trial measurement data.

As described in Chapter 3 we model the channel using a GBSCM. We show throughout this dissertation, particularly in Chapter 7, that a GBSCM is well suitable to fulfill the first two requirements. Basis for the validation of the channel model is measurement data collected during the flight trials described in Chapter 5.

2.7 Summary

In this chapter we analyze the current state of the art of modeling the AG channel. To this end we first discuss the fundamental propagation effects shaping channel and characterize their influence on terrestrial CNS systems. Following is a brief overview of different ways to describe channels. Based on a literature research we derive the requirements on a channel model able to asses the performance of the full range of terrestrial CNS systems.

CHAPTER 3

CHANNEL MODEL ARCHITECTURE

Contents

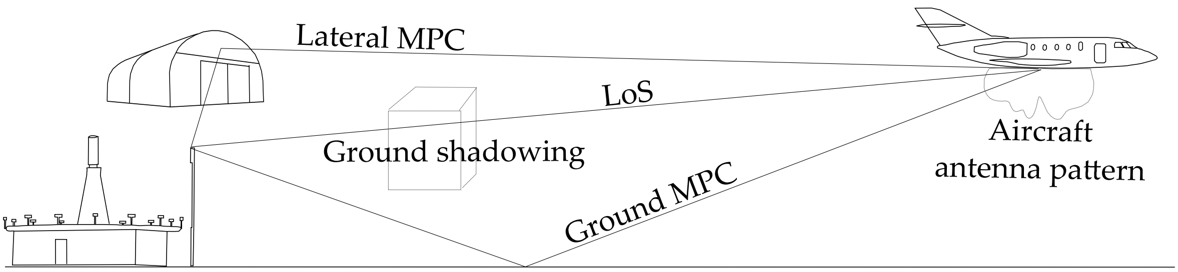

Figure 3.1. *Relevant propagation effects in the AG channel.*

3.1 Overview

The previous chapter focused on channel modeling in general and on previous approaches of modeling the air-ground (AG) channel. We also discussed shortcomings of existing models. In this chapter we propose a new approach of modeling the AG channel. To this end, in Sec. 3.2 we start by discussing the relevant propagation effects an AG channel model has to cover. Based on the knowledge on the propagation effects in Sec. 3.3 we propose an architecture for modeling the AG channel using a geometrical-based stochastic approach. We present both the channel model architecture as well as individual model elements of the proposed geometry-based stochastic channel model (GBSCM). Based on the channel model architecture, we can use different parameterizations to model different environments. Later in this dissertation we present a parameterization for a regional airport environment. In Sec. 3.4 we outline how a parameterization for a specific environment is derived: we discuss what information is required, i.e., what kind of information has to be obtained.

Content of this chapter has been published in [8] and submitted for publication to [9].

3.2 Propagation Effects in the Air-Ground Channel

In Fig. 3.1 we show the main propagation effects of the AG channel relevant for terrestrial communication, navigation, and surveillance (CNS) systems. The most dominant propagation component is the line-of-sight (LoS) signal: it has usually a significantly higher power than the other signals caused by multipath propagation. We can distinguish between multipath related and non-multipath related effects. The multipath propagation related effects are

- **Ground multipath component (MPC)** is an MPC with a usually short delay, mostly caused by a reflection off the ground surface. As the delay is usually significantly smaller than the reciprocal signal bandwidth, the delay can generally not be resolved by the receiver: thus, ground MPCs often cause flat fading and, therefore, an attenuation of the LoS signal. Ground multipath propagation can limit the coverage of a communication system or increase ranging errors in a terrestrial navigation system.

- **Lateral MPC** is an MPC with a longer delay attributable to reflections of buildings, large structures, vegetation, or terrain. Due to the usually long delay relative to the reciprocal signal bandwidth of lateral MPCs, these components cause frequency selective fading: a the signal in a part of the frequency band is attenuated. Lateral MPCs are the main driver for ranging errors in terrestrial navigation systems as described in Chapter 2.
- **Diffuse MPCs** are predominantly caused by clusters of reflectors or scattering. We model diffuse MPCs using a colored noise term.

The non-multipath related effects are

- **Antennas** at the ground and aircraft (including effects of the airframe) alter the measured signal power and phase depending on the angle of departure and arrival, respectively.
- **Ground shadowing** describes the blockage of the LoS path by a building or terrain mostly in the vicinity of the ground station.

These two effects can lead to an attenuation of the LoS signal.

In this section we describe how each effect can be modeled in a GBSCM.

3.3 Channel Model Architecture and Elements

We start in Sec. 3.3.1 by presenting the general architecture of the proposed GBSCM for the AG channel. In Sec. 3.3.2 we outline the how simulations using the channel model are conducted. The section concludes with a discussion of the different model elements in Sec. 3.3.3 to Sec. 3.3.8.

3.3.1 Architecture Overview

The model architecture uses a geometry-based stochastic approach: we draw the model element's properties, e.g., location of a reflector, from statistical distributions. These distributions are derived from measurement data. We call the entirety of the

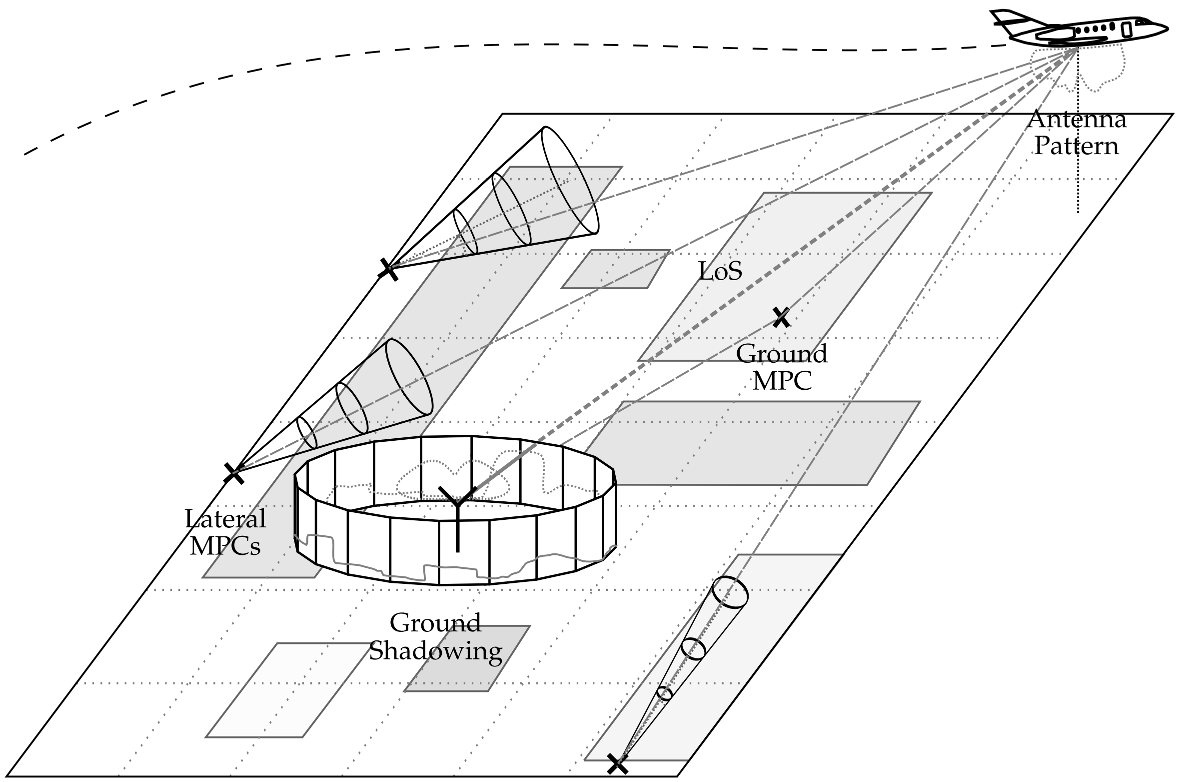

Figure 3.2. *Proposed GBSCM approach for the AG channel.*

statistical distributions describing all properties of a model element as a parameterization. A parameterization is thus environment specific: different parameterizations allow us to use the same architecture to model different environments.

We talk of a realization of the channel model if we draw values for all model elements, e.g., positions of reflectors, from the corresponding distributions. After that the properties remain fixed. Apart from noise, the channel is deterministic: the channel impulse response (CIR) is solely a function of the aircraft position.

Fig. 3.2 shows the proposed architecture of the channel model. The general idea is to model the propagation channel as a sum of plane waves. The waves present different propagation effects, such as LoS propagation, ground multipath propagation, and lateral multipath propagation, described in Sec. 3.3.3 through Sec. 3.3.5. To model the channel we use the concept of the double-directional mobile radio channel [78] .

Propagation paths are weighted by an antenna radiation pattern at the aircraft and an antenna radiation pattern ground station described in Sec. 3.3.6. Additionally, the LoS path may be blocked by the effect of ground shadowing as outlined in Sec. 3.3.7. The colored noise component described in Sec. 3.3.8 models diffuse MPCs.

3.3.2 Simulation Chain

The simulation chain of the channel model shown in Fig. 3.3 can be divided into three steps.

To **initialize** the channel model a parameterization for an environment is required. This parameterization includes all required statistical distributions describing model element properties and other information, e.g., information about the antennas. From the distributions describing the model element properties a realization of the channel model is generated: we draw the properties of ground MPC, the lateral MPCs, and diffuse MPCs, e.g., location of ground reflecting areas or the power associated with each reflector. After the initialization the channel model is fully defined: the channel characteristics are - apart from thermal noise - only a function of the aircraft position and attitude.

In the next step the **CIRs** is generated. To this end, we first calculate the aircraft position and attitude for every time instance for which the channel is to be simulated. The positions and attitudes are interpolated based on the aircraft trajectory defined by the user. Given aircraft position and attitude, the geometrical nature of the channel model allows the calculation the MPC properties for every time instance: these properties include the MPC parameters, i.e., delay, Doppler frequency, and complex weight, and the gains of the involved antennas. For reflectors representing lateral MPCs we additionally check if the aircraft is seen within the cone associated with the reflector, i.e., if a lateral MPC is received from the reflector.

In the **application** phase we convolve the CIRs with the desired transmit signal. This transmit signal may be a channel sounding signal to reproduce the channel sounding experiments, or the signal of a terrestrial CNS system. The generated receive signal is then analyzed: possible characteristics of interest are channel properties, e.g., power delay profile (PDP) or delay spreads, or CNS system performance characteristics, e.g., bit error ratio (BER) or ranging errors.

3.3.3 Line-of-Sight Signal

The LoS path is the direct propagation path between the ground station and the aircraft. Most of the time the majority of power is received through the LoS signal. The received power of the LoS signal follows free space path loss (FSPL) conditions (if not influenced by any of the effects described below). However, for large link distances we have to consider the divergence of the reflected rays due to the curvature of the earth as well as diffration effects. Both lead to a reduction of the received power [14], [79].

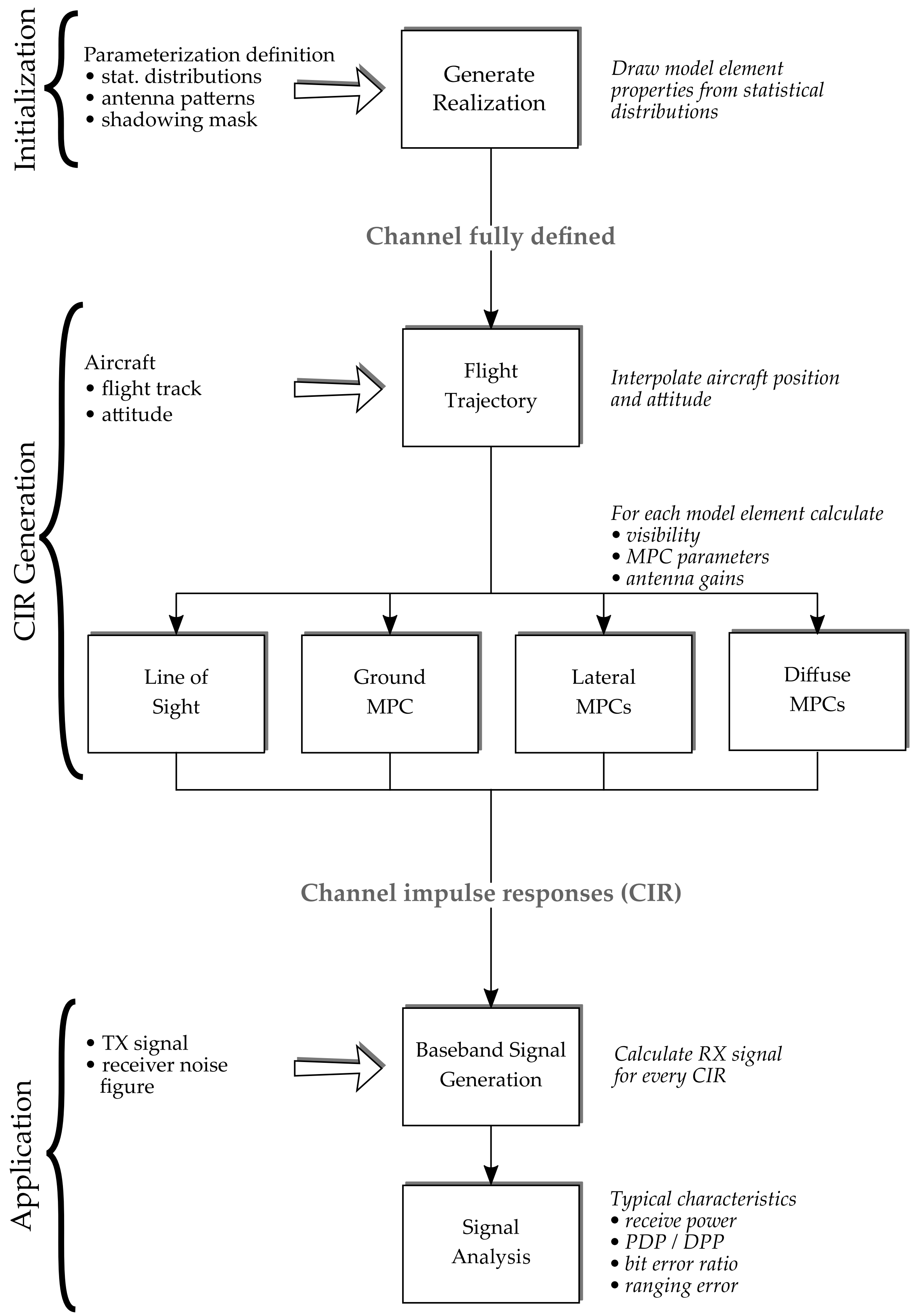

Figure 3.3. *Simulation chain of the channel model.*

For navigation applications, the bending of the electromagnetic waves due to the troposphere's composition leads to a slight overestimation of the range [14]. The increasing speed of light for higher layers of the troposphere has the opposite effect, as it cause ranges to be estimated too short. Methods exist to predict and to compensate the effects of the troposphere [11], [16].

3.3.4 Ground Multipath Component

Ground multipath propagation originates from a reflection off the ground surface with (for most practical link distances) a short excess delay, i.e., delay relative to the delay of the LoS signal; the phase of the (received) ground multipath component varies in a different way compared to the phase of the (received) LoS signal while the aircraft moves. The superposition of both signal components results in a fading of the received LoS signal - see Sec. 2.3.1. However, measurements have shown that the ground MPC is not always present or exhibits only weak power levels [20]. The ground MPC may be attenuated relative to FSPL due to a poorly reflecting ground surface (given the current angle of incidence, ground material, and roughness) or a shadowing of the ground component, e.g., by a building or terrain features.

Proposed Modeling

We propose modeling ground multipath propagation by characterization of reflecting areas on the ground. A ground MPC is received if the ground reflection point lies in such a reflecting area. The ground reflection point is defined as the specular reflection point on the ground surface. The location of the ground reflection point depends on both ground station antenna height above ground and aircraft position. We assume horizontally aligned reflecting areas, i.e., the reflecting areas lie in the same plane as the ground surface around the ground antenna. Thus, once the reflecting areas are defined, the interaction of the ground MPC with the LoS component, and the resulting attenuation or amplification of the latter, follows directly from the underlying geometry.

We characterize the reflecting areas by the following properties. The values for the different properties are drawn from statistical distributions. Note that all of those properties strongly depend on the environment a ground station is set up in.

- **Coverage ratio:** We define the coverage ratio as the ratio between the sum of all reflecting area sizes and the overall area size around the ground station.
- **Size:** We model the size of a reflecting area statistically.

- **Shape:** The reflecting areas (such as a runway, a parking area, a taxiing area) are of different shape. We also model the distribution of the shape statistically.

- **Material:** The ground station environment is usually composed of a mix of different types of surfaces. Their electro-magnetic properties such as conductivity and permitivity have been extensively investigated in the past and are modeled by estimates based upon known material constant values, which are selected as mean values of a random distribution [15], [19].

- **Material Roughness:** The roughness has an influence on how much power is scattered in all directions rather than reflected in the direction defined by the law of reflection [14]. As often done in literature the variation of the surface irregularities relative to the mean height is modeled using a normal distribution, characterized by the standard deviation. Given material roughness the reflected power can be approximated [19]. We model the standard deviation of the surface irregularities using a statistical distribution, i.e., each reflecting area has a different standard deviation of the surface irregularities relative to the mean height.

For the derivation of the distributions describing ground reflecting area properties we would ideally like to estimate the complex weight of the ground MPC. Unfortunately, in measurements the ground MPC and LoS signal can usually not be separated, i.e., their MPC parameters cannot be estimated individually: a separation is not possible due to the small excess delay of the ground MPC with respect to the resolution of the received signal. Therefore, from the measurement we are not able to directly obtain information about the ground reflection coefficient.

However, a different approach is possible: we derive the distributions reflecting area properties based on ground surface information of the environment to be modeled. In our case we use land usage data, satellite imagery, and a digital elevation model (DEM) of the ground station surrounding. We are then able to validate the chosen distributions against the measured received LoS signal power.

3.3.5 Lateral Multipath Components

By lateral MPCs we mean signal components that originate from reflections outside the two-dimensional plane defined by the LoS path and the ground MPC. In most cases lateral MPCs are attributable to large structures such as buildings, vegetation, or terrain; unlike the ground MPC, lateral MPCs usually have a relatively large excess delay: lateral MPCs lead to frequency selective fading and may cause large

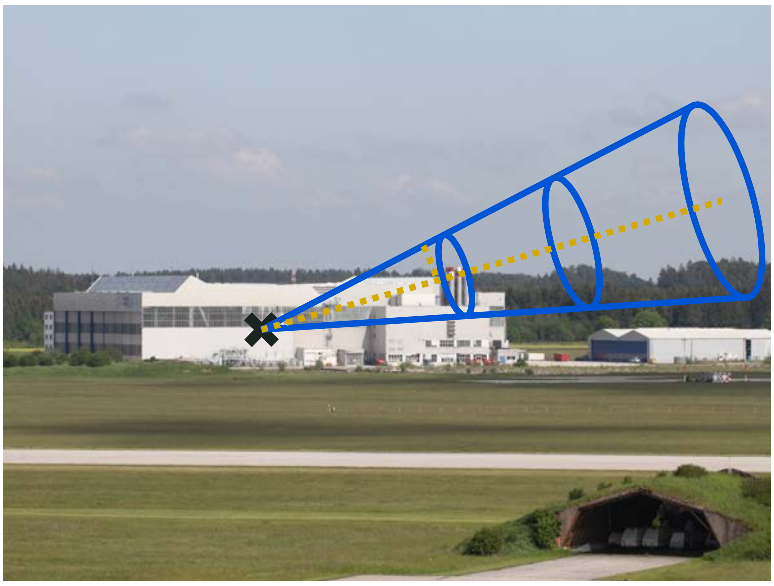

Figure 3.4. *Illustration of modeling lateral MPCs as point reflectors.*

range estimation errors for terrestrial navigation systems, e.g., distance measuring equipment (DME) [25].

Proposed Modeling

It can be observed that lateral MPCs with similar MPC parameters only appear within specific sections of the flight; if the aircraft returns to the approximately same location, MPCs with similar MPC parameters will be observed again. We therefore propose representing lateral components by point reflectors. The visibility of a reflector is defined by a cone shaped opening as shown in Fig. 3.4 [33]. Thus, the number of visible lateral MPCs and their MPC parameters is a function of the aircraft position. A reflector can be described by the following properties:

- **Location $\boldsymbol{r}$:** The location of a reflector defines the delay of the MPC it represents: it is equal to the distance traveled from ground station via the reflector to the aircraft, divided by the speed of light.
- **Opening direction $[\theta_\mathrm{d}, \phi_\mathrm{d}]^\mathrm{T}$:** The opening direction is the direction of the cone's axis of symmetry. The opening direction is characterized by an azimuth and elevation angle, θ_d and ϕ_d, taken with respect to the reflector location - see Sec. 7.2.3.
- **Opening width ω:** The opening angle describes how far the cone opens relative to the cone's axis of symmetry.
- **Complex weight α:** The complex weight of a reflector is described by a statistical

process. Depending on aircraft and reflector position, the power is additionally altered according to FSPL and antenna gains.

The derivation of the distributions describing the above properties requires an analysis of the reflectors causing the observed lateral MPCs: this analysis includes both MPC parameters and locations of the reflectors. To model the complex weight of a reflector, we have to estimate the reflectors' complex amplitude for each time step of the reflectors' visibility. Additionally, for the geometrical modeling we have to know the location of each reflector.

3.3.6 Antennas

The ground and airborne antennas have a significant influence on the received power level and, thus, are taken into account in the proposed modeling approach. While the gain of the ground antenna exhibits only small variations for typical link geometries, the gain of the aircraft antenna experiences rapid and strong variations depending on the aircraft attitude: fades exceeding $10\,\mathrm{dB}$ for a duration of more than $20\,\mathrm{s}$ were observed while the aircraft was performing banking maneuvers [11]. Under unfavorable circumstances the LoS signal might be attenuated, while at the same time an MPC is amplified. The resulting propagation conditions are very challenging for terrestrial CNS systems. As an example for a typical aircraft antenna in Fig. 3.5 we show the radiation pattern of the CNS antenna used during the flight trials. Note however, that this pattern may significantly change once the antenna is mounted on the aircraft - see App. B.

Due to the geometrical nature of the channel model, the inclusion of antenna effects is straight forward. The antenna's radiation pattern may only describe received amplitude but can also include information about the phase as well. If the locations of aircraft and reflector relative to the location of the ground station are known, the gain of the ground antenna can be directly calculated for all propagation paths. For the calculation of the airborne antenna gain the aircraft attitude, i.e., yaw, pitch, and roll, is additionally required.

For the channel model parameterization presented in this dissertation we measured the radiation patterns of the involved antennas in an anechoic chamber without the aircraft. Nevertheless, also the aircraft pattern, i.e., antenna radiation pattern including effects by the airframe, can be included if available.

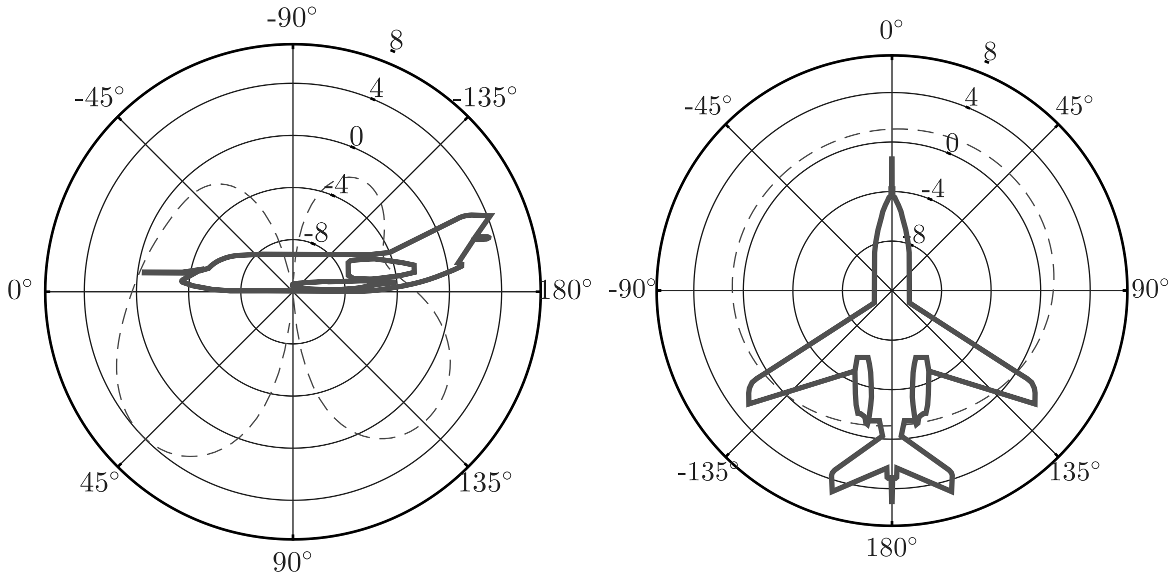

Figure 3.5. *Measured gain pattern of the aircraft antenna (without aircraft). The cut in azimuthal direction is at an elevation angle of* $5°$.

3.3.7 Ground Shadowing

Ground shadowing is understood as the blockage of the LoS signal by surrounding structures, vegetation or terrain. Ground shadowing usually causes a strong attenuation or even full blockage of the LoS path.

Ground shadowing has been observed to severely degrade the ranging performance, as it can lead to strong attenuation of the LoS signal for a long duration. The degradation can be especially severe for aircraft flying at low elevation angles relative to the ground facility, a typical scenario when using terrestrial radionavigation. As a result, a lateral MPC may be received with a higher power than the LoS signal power [25]. Herein, the LoS is strongly attenuated by vegetation, while a lateral MPC exists originating from a hangar: the LoS signal is received at a lower power than the lateral MPC for over a minute. The result is a strongly degraded DME performance, i.e., errors exceeding $150\,\mathrm{m}$.

Proposed Modeling

We propose modeling ground shadowing by an azimuth-elevation mask. An example for such a mask is shown in Fig. 3.6. The brightness in Fig. 3.6 describes the attenuation of the LoS signal. Thus, for any aircraft location the LoS signal attenuation can be directly calculated.

The elevation mask can be derived by different means: we may derive the elevation mask using received LoS signal power directly. Such measurements require

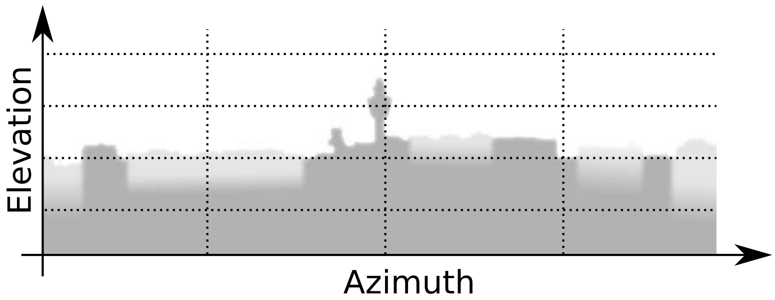

Figure 3.6. *Azimuth-elevation mask describing the attenuation of the LoS signal.*

the aircraft to be seen under a low elevation angles from the ground station for a long duration: the aircraft needs to be either very far away from the ground station, or fly at a very low altitude. Therefore, two alternatives to measurements are proposed [80]. First we can rely on DEM data. Knowing the location of ground station and aircraft we can calculate blockage of the LoS path. We chose a second approach based on image processing techniques. Using a calibrated panorama image taken from the ground station location we can estimate at which elevation and azimuth angles the LoS path is shadowed. However, for the parameterization presented in this dissertation ground shadowing does not play a role as the antenna is located highly elevated above ground.

3.3.8 Diffuse Multipath Components

Diffuse MPCs are caused by clusters of reflectors, multi-bounce reflections, diffraction, or scattering. Thus, diffuse MPCs can usually not be modeled as a single reflector. As their power level is generally significantly lower than the power levels of other types of MPCs, their influence on the performance of CNS systems is usually small to non-existent.

Proposed Modeling

We propose modeling diffuse MPCs as a geometry-based stoachstic process: the decay of the power over the delay is described by an exponential function. The distribution of the power over the Doppler frequency is defined by the aircraft position and speed relative to the ground station.

3.4 Required Information

In Tab. 3.1 we summarize the information required to derive a parameterization of the channel model. The table shows both the required information as well as the resulting propagation effect.

The LoS signal power is modeled to follow FSPL. The LoS signal delay depends on the geometrical distance between ground station and aircraft as well as the path bending due to the troposphere. Both MPC parameters are defined if the ground station and the aircraft position are known. Additionally, meteorological information is used to improve the prediction of the bending due to troposphere. The distribution of the LoS signal power and delay have to be estimated from the measurement data in order to validate the modeling approach against the measurements.

We validate the ground MPC modeling approach using the measured LoS signal power. For the derivation of the property distributions for the ground reflecting areas we rely on land usage data, satellite imagery, and a DEM of the ground station surrounding. To calculate delay and complex weight of the ground MPC we have to know the aircraft position and ground antenna height above ground.

For the geometrical modeling of the lateral MPCs it is mandatory to estimate the location of reflectors causing MPCs. Given the location of a reflector (including the height relative to GS antenna) and aircraft position, the distributions for the reflector properties, e.g., opening direction or angle, can be directly derived. Additionally, we have to estimate complex weight and its evolution over time for each reflector.

To model the effects of the antenna we require the antenna radiation patterns. Given the aircraft position and attitude, i.e., yaw, pitch, and roll, as well as the antenna radiation patterns, the gain of the involved antennas can directly be calculated.

To include shadowing effects in the model we use a panoramic shadowing mask (taken at the ground station location) to predict blockage of the LoS signal. The panoramic image has to be calibrated, i.e., we are able to map an aircraft position directly on a pixel in the image. A second method to generate such a mask might be based on an DEM. Using the measured received power we define angular segments in which the LoS signal is strongly attenuated.

To analyze the diffuse MPCs we have to calculate the residual received signal, i.e., the signal after all specular MPCs are removed. Thus, we have to estimate the delay, Doppler frequency, and complex weight for both LoS signal and all detectable MPCs.

The validation of the complete model is performed in two parts. In a quantita-

Model Element	Effect	Information
Line of sight signal	• LoS delay & complex amplitude	• Aircraft position & velocity • Ground station position • Meteorological information
Ground MPC	• Ground MPC delay & complex amplitude	• Aircraft position & velocity • Ground station position & height • Ground surface information
Lateral MPCs	• MPC delay & complex amplitude	• Aircraft position & velocity • Ground station position & height • Building or terrain map
Antenna patterns	• (Complex) antenna gains	• Aircraft position & attitude • Antenna patterns
Ground shadowing	• Attenuation	• Aircraft position • Ground station panorama • DEM
Colored noise	• Residual signal, PSD	• Aircraft position & velocity

Table 3.1. *Required information for the derivation of a channel model parameterization.*

tive validation we compare the measured statistical characteristics against the statistical characteristics of the channel model. In this dissertation we use the statistics of the LoS signal power, PDP, and Doppler power profile (DPP), as well as Delay and Doppler spread for validation. The second part of the validation is done in a qualitative manner: we compare the LoS and MPC parameter evolution over time between measurement and model for selected segments of the flight.

3.5 Summary

In this chapter we present a GBSCM architecture to model the AG channel. The channel model architecture uses geometrical model elements to represent the different propagation effects, e.g., reflections off buildings. The model elements and their properties are environment specific and are characterized by statistical distributions: this approach enables to parameterize the channel model, i.e., to adapt it, to different environments or frequency bands by choosing the respective statistical distributions.

Due to the geometrical nature of the proposed architecture we are able to accurately model the non-stationarity of the AG channel - a factor especially relevant for navigation systems. Additionally, due to the geometrical modeling approach we are not only limited to modeling single input single output (SISO) channels, but the channel model architecture is also well suited for multiple input multiple output (MIMO) channels.

Overall, we have presented a versatile AG channel model architecture which may be applied to a wide range of environments and frequencies.

CHAPTER 4

CHANNEL PARAMETER ESTIMATION

Contents

4.1 Overview

In Chapter 3 we presented the framework for a geometry-based stochastic channel model (GBSCM) of the air-ground (AG) channel. We also discussed the required information to parameterize the channel model architecture to a specific environment. As we base the channel model on measurement data, we have to estimate the following information from measurement data:

1. the statistical channel description parameters, e.g., a set of power delay profiles (PDPs) a flight scenario - see Sec. 4.4;

2. the propagation paths and the evolution of the associated multipath component (MPC) parameters, i.e., delay, Doppler frequency, and complex weight - see Sec. 4.5;

3. the locations of reflectors causing MPCs - see Sec. 4.6.

The above information can be estimated from the channel sounding experiments described in Chapter 5.

The basis for the estimation is the signal model described in Sec. 4.2: the system model describes how a periodic channel sounding signal emitted from a ground station is altered by the multipath channel. We assume that the channel impulse response consists of a superposition of plane waves [33], [81], [82].

Before the above information can be estimated, the interference in the measured signal is detected during the preprocessing described in Sec. 4.3. We also shift the measured signal in time and frequency by the line-of-sight (LoS) signal delay and Doppler frequency. The shifting improves the MPC parameter estimation discussed in Sec. 4.5 and simplifies the data processing.

The methods developed in this chapter are applied to measurement data discussed in Chapter 5. Results of that application are presented in Chapter 6. These results also build the basis for the parameterization of the channel model proposed in Chapter 7.

Content of this chapter has been published in [11], [83] and submitted for publication to [10].

4.2 Signal Model

In this section we define the fundamental signal model which describes how the multipath channel transforms a transmitted signal. We also provide the mathematical basis on how an individual MPC is non-linearly parameterized by the delay τ

and Doppler frequency ν. As the Doppler frequency ν we understand the negative change rate of the delay τ over time multiplied by the carrier frequency f_c. Therefore, the Doppler frequency ν is proportional to the first derivative of the delay τ with respect to time. The signal model builds the basis for any of the following estimation methods.

We employ a multipath channel model where the channel impulse response (CIR) at continuous delay τ and time t consists of the superposition of plane waves[1], each representing an MPC [33], [81]:

$$h(\tau, t) = \sum_{l=1}^{\infty} \alpha_l(t) \kappa_l \left(\tau - \tau_l\left(t\right)\right), \tag{4.1}$$

where $\alpha_l(t)$ represents the complex weight of MPC l and $\tau_l\left(t\right)$ its delay. The delay-dispersive function the l-th MPC is subjected to is denoted by $\kappa_l\left(\tau\right)$. The shape of $\kappa_l\left(\tau\right)$ depends on the fundamental propagation phenomena the l-th MPC has undergone. For example, for the direct LoS path or a reflection from a flat surface of large dimensions, $\kappa_l\left(\tau\right)$ may be very similar to a Dirac function. If an MPC experiences scattering or diffraction on its way to the receiver, the spectrum of $\kappa_l\left(\tau\right)$ may not be flat at all.

To investigate the propagation conditions that can be described by the model in (4.1) we use channel sounding. In channel sounding the transmit signal consists of the periodic repetition of a known time-discrete transmit sequence of duration T_{sym}. We assume in the following that I repetitions of the transmit sequence are combined into a block b. During the block duration we assume the MPC parameters to be constant and the channel to fulfill the wide-sense stationary uncorrelated scattering (WSSUS) assumption. The discrete measured signal $\boldsymbol{y}_{\mathrm{mod},b}$ for block b according to (4.1) is given as

$$\boldsymbol{y}_{\mathrm{mod},b} = \sum_{l=1}^{\infty} \alpha_{b,l} \boldsymbol{c}^I(\tau_{b,l}, \nu_{b,l}) * \tilde{\boldsymbol{\kappa}}_{b,l} + \boldsymbol{\psi}_{\mathrm{w},b}, \tag{4.2}$$

where $\alpha_{b,l}$ represents the complex weight of MPC l. The vector $\boldsymbol{c}^I(\tau, \nu) \in \mathbb{C}^{IN \times 1}$ consists of I repetitions of the time sampled transmit signal $\boldsymbol{c}$, non-linearly parameterized by the delay τ and Doppler frequency ν. The Doppler frequency ν describes the change of the delay τ during a block b. As described each path signal is distorted by $\kappa_{b,l}\left(\tau\right)$. We denote the time discrete impulse response of $\kappa_{b,l}\left(\tau\right)$ as $\tilde{\boldsymbol{\kappa}}_{b,l}$. The additive white noise is represented by $\boldsymbol{\psi}_{\mathrm{w},b} \in \mathbb{C}^{N \times 1}$ which follows a circularly-symmetric complex zero mean normal distribution, i.e., $\boldsymbol{\psi}_{\mathrm{w},b} \sim \mathcal{CN}(0, \mathbb{I}_{IN}\sigma_{\mathrm{n}}^2)$.

[1] Note, that in reality an infinite number of possible connections between a transmitter and receiver exist. As this assumption is not practical we limit the number of propagation paths later in this section.

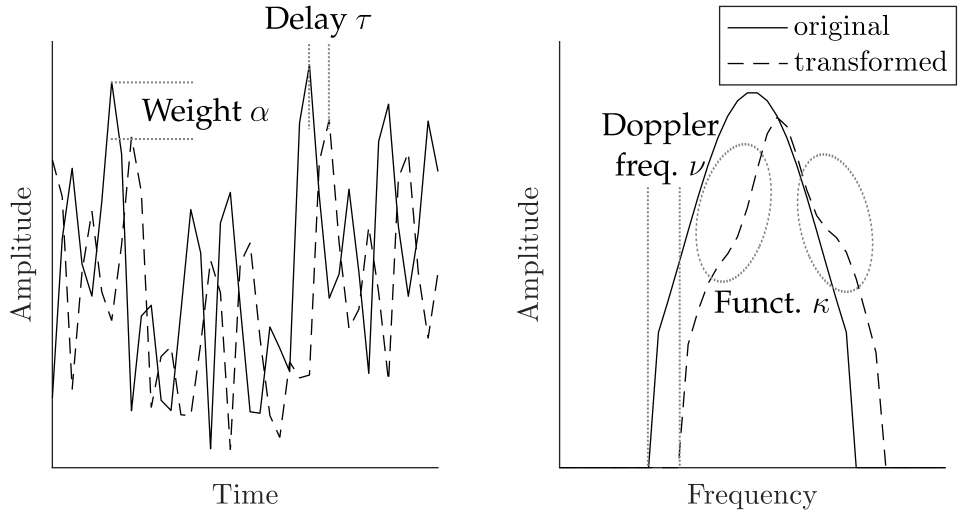

Figure 4.1. *Visualization of the signal transformation in time and frequency domain.*

In Fig. 4.1 we visualize the transformation a signal may undergo. The complex weight α scales the signal. While the delay τ shifts the signal in the time domain, the Doppler frequency ν shifts the signal in the frequency domain. The delay-dispersive function κ changes the shape of the signal itself (more apparent in the frequency domain but also visible in the time domain).

Unfortunately, due to its complexity, (4.2) cannot be directly used as basis for the detection of MPCs and estimation of its parameters from measurements. Therefore, the following simplifications are often made in literature. These simplifications are in general only valid for narrowband signals [81].

First, we have to limit the MPC number to an integer number L (sparsity assumption). Second, the arbitrary form of $\tilde{\boldsymbol{\kappa}}_{b,l}$ cannot be parametrically estimated, therefore we simplify $\tilde{\boldsymbol{\kappa}}_{b,l}$ to be a Dirac function.

Hence, the simplified model can be written as

$$\boldsymbol{y}_b = \sum_{l=1}^{L} \alpha_{b,l} \boldsymbol{c}^I(\tau_{b,l}, \nu_{b,l}) + \boldsymbol{\psi}_b. \tag{4.3}$$

The simplifications result in a model mismatch between (4.2) and (4.3). Thus, if we subtract all MPCs from the measured signal

$$\boldsymbol{\psi}_b = \boldsymbol{y}_b - \sum_{l=1}^{L} \alpha_{b,l} \boldsymbol{c}^I(\tau_{b,l}, \nu_{b,l}), \tag{4.4}$$

the residual signal (or short residuum) consists of the colored noise $\boldsymbol{\psi}_b$, which contains of the complex white noise $\boldsymbol{\psi}_{\mathrm{w},b}$ and an additional term due to the model mismatch. We assume the colored noise to be distributed as a circularly-symmetric complex normal distribution with covariance $\underline{\boldsymbol{\Sigma}}_{\psi\psi}$, i.e., $\boldsymbol{\psi}_b \sim \mathcal{CN}(0, \underline{\boldsymbol{\Sigma}}_{\psi\psi})$. A second motivation for introducing the colored noise $\boldsymbol{\psi}_b$ are effects associated with measurements of limited bandwidth: In measurements with a limited bandwidth, it is impossible to detect all MPCs existing in the measured signal. MPCs with very similar parameters (which often appear as clusters of MPCs) may be only detected as a single MPC. MPCs of low power comparable to the noise floor may not be detected at all. These undetected MPCs will also be part of the colored noise $\boldsymbol{\psi}_b$.

In literature the colored noise $\boldsymbol{\psi}_b$, often referred to as dense multipath component (DMC), is modeled in various ways [84]–[86], e.g., using single or multiple exponential functions over the delay τ or an autoregressive (AR) process. In contrast to that, we model the colored noise $\boldsymbol{\psi}_b$ in the frequency domain using a two-dimensional moving average process as described in Sec. 4.5.3.

For notational convenience we define the following vectors containing the parameters of all L MPCs. For block b the complex weights of the MPCs are denoted as $\boldsymbol{\alpha}_b = [\alpha_{b,1}, \ldots, \alpha_{b,L}]^{\mathrm{T}}$, the delays as $\boldsymbol{\tau}_b = [\tau_{b,1}, \ldots, \tau_{b,L}]^{\mathrm{T}}$, and the Doppler frequencies as $\boldsymbol{\nu}_b = [\nu_{b,1}, \ldots, \nu_{b,L}]^{\mathrm{T}}$. The matrix $\underline{\boldsymbol{C}}(\boldsymbol{\tau}_b, \boldsymbol{\nu}_b) \in \mathbb{C}^{IN \times L}$ includes the signals of all MPCs and is defined as

$$\underline{\boldsymbol{C}}(\boldsymbol{\tau}_b, \boldsymbol{\nu}_b) = \left[\boldsymbol{c}^I(\tau_{b,1}, \nu_{b,1}), \ldots, \boldsymbol{c}^I(\tau_{b,L}, \nu_{b,L})\right]. \tag{4.5}$$

Using the definitions above we rewrite (4.3) as

$$\boldsymbol{y}_b = \underline{\boldsymbol{C}}(\boldsymbol{\tau}_b, \boldsymbol{\nu}_b)\boldsymbol{\alpha}_b + \boldsymbol{\psi}_b. \tag{4.6}$$

For the identification of MPCs and estimation of their parameters, in addition to the multipath model in (4.6), we require a mathematical description of how the parameters in (4.6) alter a block of I repetitions of the transmit sequence $\boldsymbol{c}^I$. The parameterization by the weight α_b only constitutes a simple multiplication. In contrast delay τ_b and Doppler frequency ν_b alter a block non-linearly.

The block of I repetitions of the transformed transmit sequence period $\boldsymbol{c}^I(\tau, \nu) \in \mathbb{C}^{IN \times 1}$ can be expressed as

$$\boldsymbol{c}^I(\tau, \nu) = \begin{bmatrix} \boldsymbol{c}\left(\tau^1\right) \\ \vdots \\ \boldsymbol{c}\left(\tau^I\right) \end{bmatrix} \odot \exp\{\mathrm{j}2\pi T_{\mathrm{s}} \left[0, \ldots, NI\right]^{\mathrm{T}} \nu\}, \tag{4.7}$$

where $\boldsymbol{c}\left(\tau^i\right)$ denotes the time domain transmit sequence shifted by the delay τ^i with

$$\boldsymbol{c}\left(\tau^i\right) = \underline{\boldsymbol{\mathfrak{F}}}_N^{\mathrm{H}} \left(\underline{\boldsymbol{\mathfrak{F}}}_N \boldsymbol{s} \odot \exp\{-\mathrm{j}\frac{2\pi}{NT_{\mathrm{s}}} \left[0, .., N\right]^{\mathrm{T}} \tau^i\}\right). \tag{4.8}$$

Hereby, $\underline{\mathfrak{F}}_N$ and $\underline{\mathfrak{F}}_N^{\mathrm{H}}$ represent the discrete Fourier transform (DFT) and inverse DFT matrices of size N. In case of a non-zero Doppler frequency ν, each repetition of the transmit sequence arrives at the receiver shifted by a different delay τ^i. The changing delay τ^i compensates the effect of the aircraft movement within a block:

$$\tau^i(\tau, \nu) = \tau - \frac{T_{\mathrm{s}} N}{f_{\mathrm{c}}} \nu \left(\frac{I-1}{2} - i \right). \tag{4.9}$$

4.3 Preprocessing

During the preprocessing two actions are performed: first, we detect parts in the measured signal $\boldsymbol{y}_b$ corrupted by interference. The interference can be mainly attributed to the onboard distance measuring equipment (DME). Second, the measured signal $\boldsymbol{y}_b$ is shifted in time and frequency by the LoS signal delay τ_{LoS} and Doppler frequency ν_{LoS}.

4.3.1 Detection of DME Interference

The onboard DME is transmitting at a maximum power of $60\,\mathrm{dBm}$ with a duty cycle of roughly 3%. While transmitting, the onboard DME drives the receiver low noise amplifier (LNA) into saturation (co-site interference). Instances of the transmit sequence affected by DME interference manifest themselves by a significant increase (several tens of dB) of the noise floor. Thus, those instances of the transmit sequence are not considered for the calculation of the statistical channel description and MPC parameter estimation described in Sec. 4.5.2 and Sec. 4.5.2, respectively.

To detect instances of the transmit sequence which are subjected to interference we first estimate the noise floor for each instance. To this end, we estimate the time-variant impulse response of the measured signal $\boldsymbol{y}_b$. We reshape $\boldsymbol{y}_b$ into a $(N \times I)$ matrix and apply a column-wise DFT[2] resulting in $\underline{\boldsymbol{Y}}_b^{f,t}$

$$\underline{\boldsymbol{Y}}_b^{f,t} = \underline{\mathfrak{F}}_N \mathrm{vec}_{N \times I}^{-1}\{\boldsymbol{y}_b\}. \tag{4.10}$$

We then perform an element-wise division by the frequency domain calibration signal, $\underline{\mathfrak{F}}_N \boldsymbol{c}$

$$\underline{\boldsymbol{H}}_b^{f,t} = \underline{\boldsymbol{Y}}_b^{f,t} \oslash \left(\underline{\mathfrak{F}}_N \boldsymbol{c} \otimes \mathbb{1}_I^{\mathrm{T}} \right) \tag{4.11}$$

[2] By applying a DFT we assume periodicity of the signal. Although the measured signal is not periodic, only very minor distortions are observed due to the signals non-periodicity when applying the DFT. Thus, we forego the utilization of a tapering window.

resulting in the time-variant transfer function $\underline{\boldsymbol{H}}_b^{f,t}$. The time-variant impulse response is calculated by an inverse DFT along the first dimension of the time-variant transfer function $\underline{\boldsymbol{H}}_b^{f,t}$:

$$\underline{\boldsymbol{H}}_b^{\tau,f} = \underline{\mathfrak{F}}_N^{\mathrm{H}} \underline{\boldsymbol{H}}_b^{f,t}. \tag{4.12}$$

Each column of $\underline{\boldsymbol{H}}_b^{\tau,t}$ contains the impulse response of the channel for a different time t. Each row n of $\underline{\boldsymbol{H}}_b^{\tau,t}$ corresponds to a delay $\tau_n = nT_{\mathrm{s}}$. We assume that the time-variant impulse response consists only of noise for large delay indices $(\tau_n - \tau_{\mathrm{LoS}}) > 50\,\mathrm{km}/c_{\mathrm{a}}$. This assumption can be easily verified by a visual inspection of measurement data. The noise floor for each column, $\sigma_b^2 \in \mathbb{C}^{1\times I}$ is calculated as the column-wise mean power of all elements corresponding to a delay index in the set Γ_n

$$\Gamma_n = \{n \in \{0,..,N-1\} : 50\,\mathrm{km} < (\tau_n - \tau_{\mathrm{LoS}})\,c_{\mathrm{a}} < 100\,\mathrm{km}\}. \tag{4.13}$$

With no interference present, i.e., under the assumption that all elements in $\underline{\boldsymbol{H}}_b^{\tau,t}$ corresponding to a delay index $\tau_n \in \Gamma_n$ being complex circularly symmetric normally distributed, the elements in σ_b^2 follow a chi squared distribution with $2\langle\Gamma_n\rangle$ degrees of freedom. A visual inspection of the measurement data shows that in most cases the assumption is valid and the chi squared distribution provides a decent fit. We detect an instance of the channel sounding sequence i being distorted by interference, if its noise floor is outside the 99.9% quantile of the chi squared distribution. Let ${\chi^2_{2\langle\Gamma_n\rangle}}^{-1}(x)$ be the cumulative distribution function (CDF) of σ_b^2 describing the distribution of the elements in σ_b^2, i.e., a chi squared distribution with $2\langle\Gamma_n\rangle$ degrees of freedom. The set of interference free instances of the transmit sequence is denoted by $\Gamma_{\tau,b}$.

$$\Gamma_{\tau,b} = \{i \in \{1,..,I\} : \sigma_{b,i}^2 < {\chi^2_{2\langle\Gamma_n\rangle}}^{-1}(0.999)\}. \tag{4.14}$$

4.3.2 Shifting to LoS Signal Delay and Doppler Frequency

The main motivation for shifting the measured signal $\boldsymbol{y}_b$ to the LoS signal delay and Doppler frequency is to limit the variability of the MPC parameters: the parameters of the different MPCs usually change in a similar manner as those associated with the LoS signal. A limited variability of the MPC parameters improves the parameter estimation described in Sec. 4.5. Additionally, the shifting simplifies the processing of the measured signal: all MPC parameters are automatically taken relative to those of the LoS signal.

To shift a block $\boldsymbol{y}_b$ of the measured signal we use the system function defined in (4.7). However, while in the parameter estimation the system function is applied to I repetitions of the transmit sequence, for the preprocessing we apply the same function on a block of the measured signal $\boldsymbol{y}_b$. We shift the measured signal in time by the negative LoS signal delay $-\tau_{\mathrm{LoS,b}}$ and in frequency by the negative LoS signal Doppler frequency $-\nu_{\mathrm{LoS,b}}$. The values for $\tau_{\mathrm{LoS,b}}$ and $\nu_{\mathrm{LoS,b}}$ are as we later explain in Sec. 5.2.4 based on Global Positioning System (GPS) and inertial measurements. We denote the block of measured signal $\boldsymbol{y}_b$ shifted to LoS signal delay $-\tau_{\mathrm{LoS,b}}$ and LoS signal Doppler frequency $-\nu_{\mathrm{LoS,b}}$ as $\tilde{\boldsymbol{y}}_b$.

4.4 Statistical Channel Description

For the characterization of the AG channel and for the validation of the channel model presented in Chapter 7 we require a statistical channel description. In Sec. 2.5.2 we discuss the theoretical basis for such a statistical description - see Fig. 2.6.

If working with measurement data, the estimation of the statistical channel properties is not as straightforward as in theory: therefore, in this section we describe how we estimate the main statistical channel description parameters from a block b of the preprocessed measured signal $\tilde{\boldsymbol{y}}_b$. In the following we have to keep in mind that the calculation of the statistical channel description parameters involves taking the expected value. We realize the expectation operation by averaging over multiple blocks b. We base our calculations on the time-variant channel impulse response $\underline{\boldsymbol{H}}_b^{f,t}$ - see Sec. 4.3. In the following the set of $\Gamma_{\tau,b}$ denotes the interference free instances of the transmit sequence as calculated in Sec. 4.3.

4.4.1 Power Delay Profile (PDP)

The PDP P_b^τ provides the average power over delay of the CIR. Let $\boldsymbol{x}_{\Gamma_{\tau,b}} \in \mathbb{R}^{\langle\Gamma_{\tau,b}\rangle\times 1}$ denote a indictator vector with ones at the positions of indices contained in $\Gamma_{\tau,b}$ and the rest zeros. Thus, $\boldsymbol{x}_{\Gamma_{\tau,b}}$ is a vector indicating which column in $\underline{\boldsymbol{H}}_b^{\tau,t}$ is influenced by interference. The PDP P_b^τ for block b is calculated the row-wise sum of the time-variant impulse response power $|\underline{\boldsymbol{H}}_b^{\tau,t}|^2$.

$$P_b^\tau = \frac{1}{\langle\Gamma_{\tau,b}\rangle}|\underline{\boldsymbol{H}}_b^{\tau,t}|^2\boldsymbol{x}_{\Gamma_{\tau,b}}. \tag{4.15}$$

Thus, we only consider instances of the transmit sequence which are not influenced by onboard DME interference.

4.4.2 Doppler Power Profile (DPP)

The distribution of the power over Doppler frequency is described by the Doppler power profile (DPP) P_b^{ν}. For the calculation of the DPP we first calculate the scattering function $\underline{\boldsymbol{P}}_b^{\tau,\nu}$ of block b of the channel.

The Doppler-variant impulse response $\underline{\boldsymbol{H}}_b^{\tau,\nu}$ is obtained by a DFT along the second dimension of the time-variant impulse response $\underline{\boldsymbol{H}}_b^{\tau,t}$:

$$\underline{\boldsymbol{H}}_b^{\tau,\nu} = \underline{\boldsymbol{H}}_b^{\tau,t} \underline{\boldsymbol{\mathfrak{F}}}_I^{\mathrm{T}}. \tag{4.16}$$

We estimate the scattering function $\underline{\boldsymbol{P}}_b^{\tau,\nu}$ for a single block as

$$\underline{\boldsymbol{P}}_b^{\tau,\nu} = |\underline{\boldsymbol{H}}_b^{\tau,\nu}|^2. \tag{4.17}$$

Due to interference of the onboard DME, the noise power between consecutive instances of the transmit sequence varies. The interference degrades the estimation of the scattering function $\underline{\boldsymbol{P}}_b^{\tau,\nu}$ and can be mitigated up to a certain extent by considering only delay indices τ_n, i.e., rows of $\underline{\boldsymbol{P}}_b^{\tau,\nu}$, which exhibit a significant signal to interference power for the calculation of the DPP. A visual inspection shows, that no significant MPCs with a delay exceed the corresponding distance of $5\,\mathrm{km}$. Therefore, the set of the delay indices $\Gamma_{\tau,b}$ to be considered for the calculation of the DPP is

$$\Gamma_{\tau,b} = \{n \in \{0, .., N-1\} : 0\,\mathrm{km} < \tau_n c_{\mathrm{a}} < 5\,\mathrm{km}\}\,. \tag{4.18}$$

Let again $\boldsymbol{x}_{\Gamma_{\tau,b}} \in \mathbb{R}^{\langle \Gamma_{\tau,b} \rangle \times 1}$ denote an indicator vector with ones at the positions of indices contained in $\Gamma_{\tau,b}$ and the rest zeros. Thus, $\boldsymbol{x}_{\Gamma_{\tau,b}}$ is a vector indicating rows in $\underline{\boldsymbol{P}}_b^{\tau,\nu}$ which contain a signal other than noise. The DPP P_b^{ν} is calculated as

$$P_b^{\nu} = \frac{1}{\langle \Gamma_{\tau,b} \rangle} \underline{\boldsymbol{P}}_b^{\tau,\nu\mathrm{T}} \boldsymbol{x}_{\Gamma_{\tau,b}}. \tag{4.19}$$

4.4.3 Parameters of the Delay-dispersive Channel

Mean delay, delay spread, mean Doppler and Doppler spread are standard measures to describe the dispersiveness of the channel.

The mean delay $m_{\tau,b}$ of block b's PDP P_b is calculated as

$$m_{\tau,b} = \frac{\left(P_b^{\tau} \odot [0, .., N-1]^{\mathrm{T}}\, T_{\mathrm{s}}\right)^{\mathrm{T}} \boldsymbol{x}_{\tau,b}}{\left(P_b^{\tau}\right)^{\mathrm{T}} \boldsymbol{x}_{\tau,b}} \tag{4.20}$$

and the squared delay spread $\sigma_{\tau,b}^2$ as

$$\sigma_{\tau,b}^2 = \frac{\left(P_b^{\tau} \odot \left([0, .., N-1]^{\mathrm{T}}\, T_{\mathrm{s}}\right)^2\right)^{\mathrm{T}} \boldsymbol{x}_{\tau,b}}{\left(P_b^{\tau}\right)^{\mathrm{T}} \boldsymbol{x}_{\tau,b}} - m_{\tau,b}^2. \tag{4.21}$$

By using the thresholding vector $\boldsymbol{x}_{\tau,b} \in \mathbb{R}^{N\times 1}$ we only consider elements significantly high above the noise floor. The vector $\boldsymbol{x}_{\tau,b}$ is all zeros, except for positions where the values of PDP P_b^τ are outside the 99% quantile of the noise floor.

4.5 MPC Parameter Estimation & Tracking

The goal of the proposed parameter estimation and tracking algorithm is to identify dominant MPCs, estimate, and track their parameters. The estimated MPC parameters build the basis for the localization of reflectors in Sec. 4.6.

To estimate and track the MPC parameters we combine super-resolution parameter estimation with an information filter. For block b the MPC parameter vector $\boldsymbol{\xi}_b$ to be estimated is defined as

$$\boldsymbol{\xi}_b = \left[\boldsymbol{\tau}_b^{\mathrm{T}}, \boldsymbol{\nu}_b^{\mathrm{T}}, \log|\boldsymbol{\alpha}_b|^{\mathrm{T}}, \arg\left(\boldsymbol{\alpha}_b\right)^{\mathrm{T}}\right]^{\mathrm{T}}. \tag{4.22}$$

Note that in $\boldsymbol{\xi}_b$ we separate the complex weights $\boldsymbol{\alpha}_b$ into amplitude and phase and take the logarithm of the amplitude vector $\boldsymbol{\alpha}_b$ according to [84]. According to (4.6), the estimation of the MPC parameters $\boldsymbol{\xi}_b$ is performed block-wise based on the preprocessed signal $\tilde{\boldsymbol{y}}_b$.

Fig. 4.2 shows the block diagram of the parameter estimation and tracking algorithm. We observe the two integral parts: on the right side the parameter estimation, responsible for the estimation of $\boldsymbol{\xi}_b$ and for finding new MPCs; on the left side the information filter responsible for tracking and smoothing the estimated parameters $\boldsymbol{\xi}_b$.

The MPC parameters $\boldsymbol{\xi}_b$ are maximum likelihood (ML) estimated based on the preprocessed signal. Using the estimated colored noise $\underline{\boldsymbol{\Psi}}_b^{\tau,\nu}$ we derive a power threshold for the detection of new MPCs. If the power of a newly detected MPC exceeds this threshold the MPC is considered for the parameter estimation. New MPCs are added to the model as long as MPCs with a power exceeding the threshold exist.

The estimated MPC parameters are filtered in an information filter. The information filter smooths the MPC parameter estimates by assuming a linear dynamical system model, i.e., the information filter exploits the correlations of the MPC parameters over the time. The filtering of the MPC parameter estimates requires information about the quality of the estimation, i.e., the expected error between the MPC parameter estimate and the true parameter. This information is provided by the Fisher information matrix $\underline{\mathfrak{J}}_b$. Additionally, the information filter also estimates

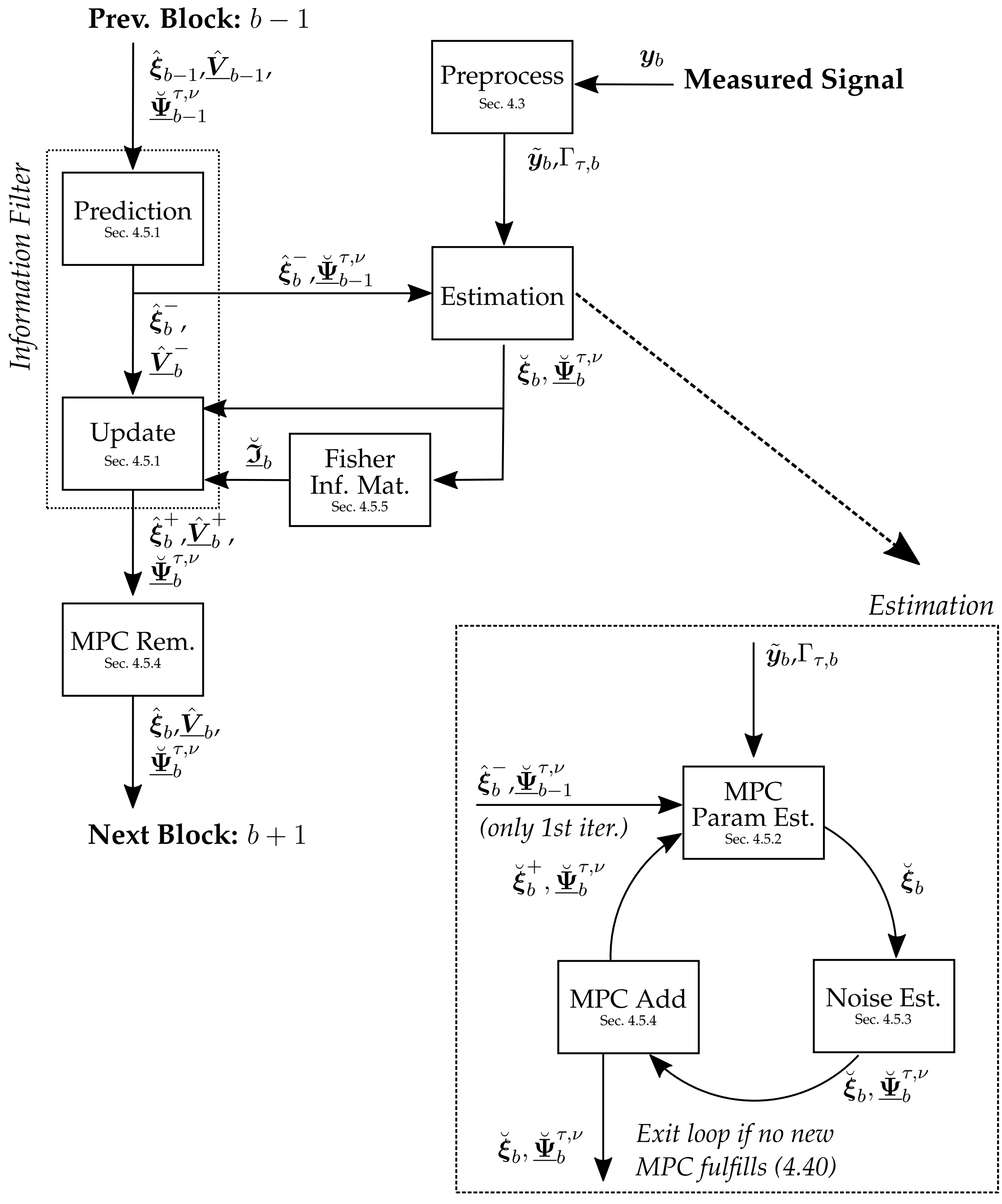

Figure 4.2. *Block diagram of the parameter estimation and tracking algorithm.*

the error variance $\underline{\boldsymbol{V}}_b$ of the filtered MPC parameters and predicts the MPC parameters for the next block $b + 1$.

MPCs which have a low power are removed after the update step in the information filter. An MPC is removed from the model if its power is below a threshold calculated based on the colored noise.

In order to maintain conciseness we limit ourselves to the description of the single input single output (SISO) case. Nevertheless, the extension of the algorithm to the multiple input multiple output (MIMO) case is straight forward. The general structure of the algorithm remains unchanged.

4.5.1 Parameter Tracking

The tracking algorithm is realized by an information filter, sometimes also referred to as *inverse covariance filter* [87]. Our motivation to include an information filter is twofold: first, the combination of information filter and ML parameter estimation allows us identify the parameter estimates $\breve{\boldsymbol{\xi}}_b$ across time which belong to the same physical signal path, which otherwise would be independent. We are thus able to analyze the evolution of MPCs over time. Second, the information filter increases the reliability of the MPC parameter estimates, as it exploits the inherent temporal coherence of the paths by applying smoothing. Accurate parameter estimates are a requirement for the localization of reflectors described in Sec. 4.6.

Compared to a Kalman filter, an information filter uses the same assumptions and delivers identical results. However, due to a different formulation of the filter equations, it directly uses the Fisher information matrix $\breve{\underline{\mathfrak{J}}}_b$ as input rather than its inverse, as the Kalman filter does. As a consequence, the estimation is numerically more robust as the inversion of the Fisher information matrix can cause numerical problems for an ill conditioned Fisher information matrix, e.g., if highly correlated MPCs with similar parameters exist.

The information filter assumes a time discrete linear dynamical system model based on a homogeneous first order Markov chain: the current true value of the parameter $\boldsymbol{\xi}_b$, usually referred to as the state, only depends on the previous state $\boldsymbol{\xi}_{b-1}$ via a transition matrix $\underline{\boldsymbol{F}}$, and additive state noise of covariance $\underline{\boldsymbol{Q}}$. For both matrices $\underline{\boldsymbol{F}}$ and $\underline{\boldsymbol{Q}}$ we assume no correlation between the individual MPCs, i.e., $\underline{\boldsymbol{F}} = \mathbb{I}_L \otimes \underline{\boldsymbol{F}}_1$ and $\underline{\boldsymbol{Q}} = \mathbb{I}_L \otimes \underline{\boldsymbol{Q}}_1$. The information filter performs a sequential Bayesian estimation for the state vector $\hat{\boldsymbol{\xi}}_b$ and its error covariance matrix $\underline{\hat{\boldsymbol{V}}}_b$. The Bayesian estimation uses the ML parameter estimate $\breve{\boldsymbol{\xi}}_b$, the Fisher information matrix $\breve{\underline{\mathfrak{J}}}_b$, the previous state $\hat{\boldsymbol{\xi}}_{b-1}$, and the error covariance matrix $\underline{\hat{\boldsymbol{V}}}_{b-1}$ as input.

The equations for the information filter are given as [87]

$$\begin{aligned}
&\text{Prediction:} && \\
&\hat{\boldsymbol{\xi}}_b^- &= \quad& \underline{\boldsymbol{F}}\hat{\boldsymbol{\xi}}_{b-1} && (4.23)\\
&\underline{\boldsymbol{V}}_b^- &= \quad& \underline{\boldsymbol{F}}\underline{\boldsymbol{V}}_{b-1}\underline{\boldsymbol{F}}^{\mathrm{T}} + \underline{\boldsymbol{Q}} && (4.24)\\
&\text{Update:} && \\
&\underline{\boldsymbol{V}}_b^+ &= \quad& \left[\left(\underline{\boldsymbol{V}}_b^-\right)^{-1} + \underline{\boldsymbol{M}}^{\mathrm{T}}\breve{\underline{\boldsymbol{\mathfrak{J}}}}_b\underline{\boldsymbol{M}}\right]^{-1} && (4.25)\\
&\underline{\boldsymbol{K}}_b &= \quad& \underline{\boldsymbol{V}}_b^+\underline{\boldsymbol{M}}^{\mathrm{T}}\breve{\underline{\boldsymbol{\mathfrak{J}}}}_b && (4.26)\\
&\hat{\boldsymbol{\xi}}_b^+ &= \quad& \hat{\boldsymbol{\xi}}_b^- + \underline{\boldsymbol{K}}_b^+\left(\breve{\boldsymbol{\xi}}_b - \underline{\boldsymbol{M}}\hat{\boldsymbol{\xi}}_b^-\right). && (4.27)
\end{aligned}$$

The observation model $\underline{\boldsymbol{M}} = \mathbb{I}_{4L}$ describes the relation between measurement $\breve{\boldsymbol{\xi}}_b$ and state $\hat{\boldsymbol{\xi}}_b$. The Kalman gain is denoted by $\underline{\boldsymbol{K}}_b$.

For the transition matrix $\underline{\boldsymbol{F}}_1$ we have to consider the dependency between Doppler frequency ν, delay τ, and phase $\arg(\alpha)$ of an MPC. Both the derivative of the delay τ and phase $\arg(\alpha)$ are proportional to the Doppler frequency ν. Thus, the transition matrix $\underline{\boldsymbol{F}}_1$ is an identity matrix plus off-diagonal elements connecting Doppler frequency ν, delay τ, and phase $\arg(\alpha)$.

We assume a random walk for both the Doppler frequency ν and the logarithmic amplitude $\log|\alpha|$, i.e., their evolution over time is only driven by the state noise characterized by the state covariance matrix $\underline{\boldsymbol{Q}}$. Similarly to the transition matrix $\underline{\boldsymbol{F}}$, for the state covariance matrix $\underline{\boldsymbol{Q}}$ we also have to consider the relation between Doppler frequency ν, delay τ, and phase $\arg(\alpha)$ [87]. The individual elements in $\underline{\boldsymbol{Q}}_1$, e.g., the state noise of the Doppler frequency ν, are chosen taking into account the flight dynamics.

Note that the number of tracked MPCs changes as described in Sec. 4.5.4, i.e., if L changes, the dimension of the error covariance matrix $\underline{\boldsymbol{V}}_b$ has to be adjusted.

Role of Preprocessing

As described in Sec. 4.3 we shift the measured signal $\boldsymbol{y}_b$ by the LoS signal delay τ_{LoS} and LoS signal Doppler frequency ν_{LoS}. The shifting reduces the variability of the MPC parameters delay τ and Doppler frequency ν. Both the estimated LoS signal delay $\breve{\tau}_{\mathrm{LoS}}$ and LoS signal Doppler frequency $\breve{\nu}_{\mathrm{LoS}}$ after correction are zero on average. Thus, the evolution of both parameters can be described using a random walk, the underlying assumption of the information filter.

4.5.2 MPC Parameter Estimation

The goal of the parameter estimation is to find the ML estimate for the MPC parameters $\breve{\boldsymbol{\xi}}_b$. To this end we minimize the mean squared error (MSE) between the preprocessed measured signal $\tilde{\boldsymbol{y}}_b$ and the theoretical signal $\boldsymbol{y}_{\mathrm{mod},b}$ based on the signal model (4.6):

$$\breve{\boldsymbol{\xi}}_b = \arg\min_{\boldsymbol{\xi}} \left(\tilde{\boldsymbol{y}}_b - \boldsymbol{y}_b\right)^{\mathrm{H}} \underline{\boldsymbol{\Sigma}}_{\psi\psi}^{-1} \left(\tilde{\boldsymbol{y}}_b - \boldsymbol{y}_b\right). \tag{4.28}$$

For the minimization, all instances of the transmit sequence in $\tilde{\boldsymbol{y}}_b$ affected by interference are discarded.

The minimization is initialized with the previously detected MPC parameters. For the first iteration, as shown in Fig. 4.2 (right side), we use the predicted state vector $\hat{\boldsymbol{\xi}}_b^-$ of the information filter. For all following iterations we use $\breve{\boldsymbol{\xi}}_b^+$ which contains the result of the previous ML estimation $\breve{\boldsymbol{\xi}}_b$ and the MPC parameters of MPCs which were newly detected according to Sec. 4.5.4.

The minimization is performed using the bound optimization by quadratic approximation (BOBYQA) algorithm [88]. The BOBYQA algorithm is chosen for two reasons: first, it is derivative free. An investigation on the presented measured data has shown that derivative free minimization algorithms exhibit more stability. Second, it is bound constrained: the maximum deviation from its initialization a parameter can have after the minimization can be set. Thus, if a previously tracked MPC does not exist anymore, it is removed from the model. Without a bound constrained algorithm, the minimization may "jump" to an MPC with similar MPC parameters.

4.5.3 Colored Noise Estimation

We model the residuum, i.e., the remaining measured signal after all detectable MPCs have been subtracted, using the colored noise term $\boldsymbol{\psi}_b$ as defined in (4.4). By colored noise we mean that the noise variance is a function of delay τ and Doppler frequency ν. We assume the time-frequency correlation function $\underline{\boldsymbol{P}}_{\psi,b}^{f,t}$ of colored noise to be a two dimensional moving average process. Note that the following definitions only stand under the assumption that the channel pertains the WSSUS properties for a sufficient time.

For one block, the colored noise $\boldsymbol{\psi}_b$ is defined as

$$\boldsymbol{\psi}_b = \tilde{\boldsymbol{y}}_b - \underline{\boldsymbol{C}}(\boldsymbol{\tau}_b, \boldsymbol{\nu}_b)\boldsymbol{\alpha}_b. \tag{4.29}$$

First, we calculate the Doppler-variant impulse response of the colored noise $\boldsymbol{\psi}_b$.

Therefore, we reshape $\boldsymbol{\psi}_b$ into a $(N \times I)$ matrix and apply a column-wise DFT resulting in $\underline{\boldsymbol{\psi}}_b^{f,t}$ with

$$\underline{\boldsymbol{\psi}}_b^{f,t} = \underline{\mathfrak{F}}_N \mathrm{vec}_{N\times I}^{-1}\{\boldsymbol{\psi}_b\}. \tag{4.30}$$

We then perform an element-wise division by the frequency domain calibration signal, $\underline{\mathfrak{F}}_N \boldsymbol{c}$

$$\underline{\boldsymbol{H}}_{\psi,b}^{f,t} = \underline{\boldsymbol{\psi}}_b^{f,t} \oslash \left(\underline{\mathfrak{F}}_N \boldsymbol{c} \otimes \mathbb{1}_I^{\mathrm{T}}\right) \tag{4.31}$$

resulting in the time-variant transfer function $\underline{\boldsymbol{H}}_{\psi,b}^{f,t}$. Again, $\oslash$ denotes the element-wise division. The Doppler variant impulse response $\underline{\boldsymbol{H}}_{\psi,b}^{\tau,\nu}$ is obtained by an inverse DFT along the first, and a DFT along the second dimension of the time-variant transfer function $\underline{\boldsymbol{H}}_{\psi,b}^{f,t}$:

$$\underline{\boldsymbol{H}}_{\psi,b}^{\tau,\nu} = \underline{\mathfrak{F}}_N^{\mathrm{H}} \underline{\boldsymbol{H}}_{\psi,b}^{f,t} \underline{\mathfrak{F}}_I^{\mathrm{T}}. \tag{4.32}$$

The scattering function $\underline{\boldsymbol{P}}_{\psi,b}^{\tau,\nu}$ is estimated as[3]

$$\underline{\boldsymbol{P}}_{\psi,b}^{\tau,\nu} = |\underline{\boldsymbol{H}}_{\psi,b}^{\tau,\nu}|^2. \tag{4.33}$$

Fig. 4.3a shows a typical realization of the scattering function $\underline{\boldsymbol{P}}_{\psi,b}^{\tau,\nu}$ calculated from the colored noise $\boldsymbol{\psi}_b$ of the measured signal. Within $\underline{\boldsymbol{P}}_{\psi,b}^{\tau,\nu}$ previously undetected MPCs as well as effects due to the model mismatch discussed in (4.2) are visible.

The colored noise is modeled using a two-dimensional moving average process: Therefore, we assume that the time-frequency correlation function of the colored noise $\underline{\breve{\boldsymbol{\Psi}}}_b^{\tau,\nu}$ can be expressed by filter coefficients of a finite impulse response filter. For the estimation of the filter coefficients we first calculate the time-frequency correlation function $\underline{\boldsymbol{P}}_{\psi,b}^{f,t}$ of the colored noise $\boldsymbol{\psi}_b$ as

$$\underline{\boldsymbol{P}}_{\psi,b}^{f,t} = \underline{\mathfrak{F}}_N \underline{\boldsymbol{P}}_{\psi,b}^{\tau,\nu} \underline{\mathfrak{F}}_I^{\mathrm{H}^{\mathrm{T}}}. \tag{4.34}$$

Next, we estimate the time-frequency correlation function of the moving average process using the Blackman-Tukey transformation [89]. Let the vector $\boldsymbol{w}_{\mathrm{BM}}(n) \in \mathbb{R}^{n\times 1}$ denote the Blackman window of length n. The length of the windows used in the Blackman-Tukey transformation in frequency n_{BM}^f and time domain n_{BM}^t, is defined by the relative Blackman window length Δ_{BM} as

$$n_{\mathrm{BM}}^f = \lceil \Delta_{\mathrm{BM}} N \rceil \text{ and } n_{\mathrm{BM}}^t = \lceil \Delta_{\mathrm{BM}} I \rceil. \tag{4.35}$$

In other words, Δ_{BM} is the ratio of the dimensions of $\underline{\boldsymbol{P}}_{\psi,b}^{f,t}$ and Blackman-window length. Appending zeros evenly before the first and after the last element of the

[3] The calculation of $\underline{\boldsymbol{P}}_{\psi,b}^{\tau,\nu}$ involves taking the expected value of $|\underline{\boldsymbol{H}}_{\psi,b}^{\tau,\nu}|^2$. However, as we only have one representation of $|\underline{\boldsymbol{H}}_{\psi,b}^{\tau,\nu}|^2$ we omit the expectation operation and use the $|\underline{\boldsymbol{H}}_{\psi,b}^{\tau,\nu}|^2$ as the best available estimate. In the literature, the scattering function estimated in such a way is also termed *instant scattering function* or *squared spreading function*.

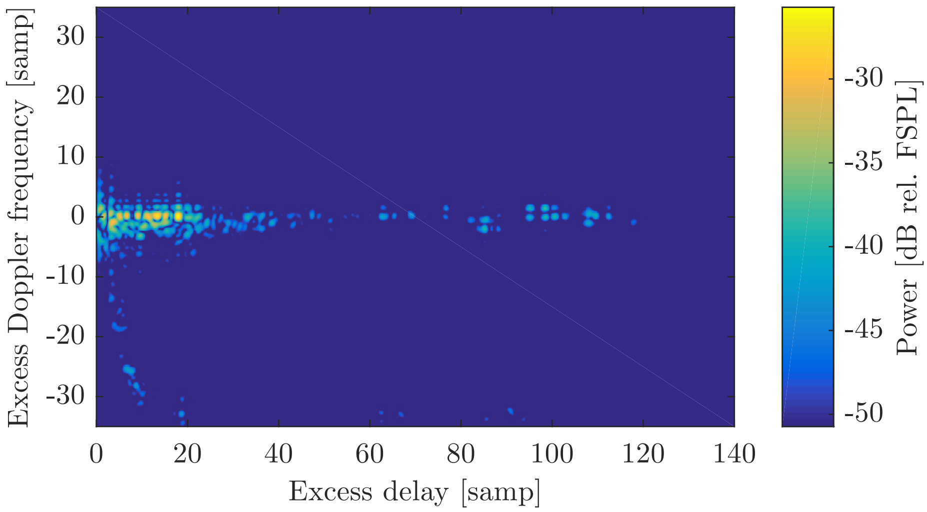

(a) *Scattering function* $\underline{\boldsymbol{P}}_{\psi,b}^{\tau,\nu}$

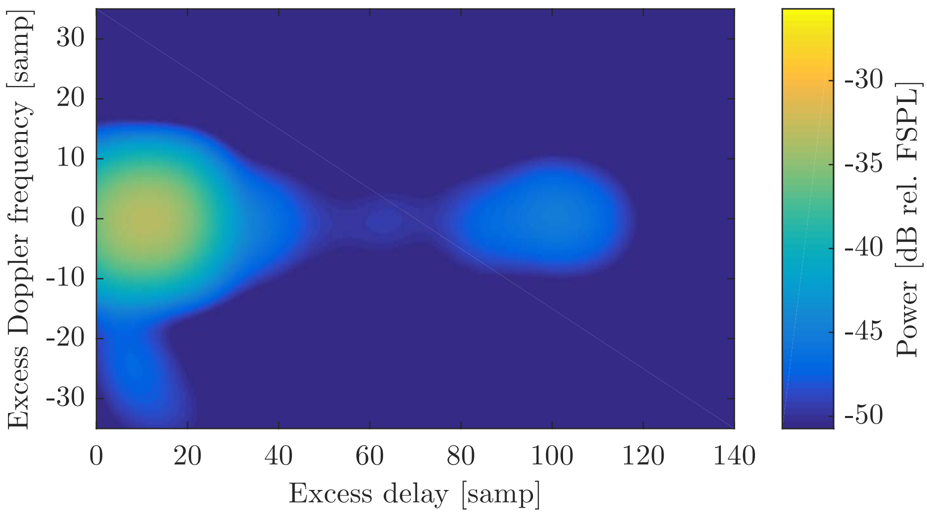

(b) *Est. colored noise scattering function* $\breve{\underline{\boldsymbol{\Psi}}}_{b}^{\tau,\nu}$

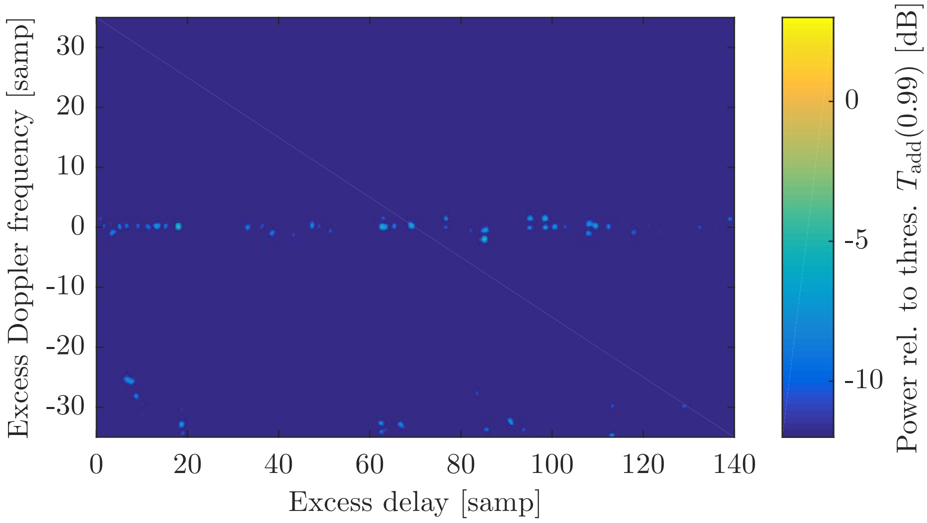

(c) *Detection matrix* $\underline{\boldsymbol{D}}_{b}^{\tau,\nu}$

Figure 4.3. *Modeling of the colored noise and detection of new MPCs. Delay τ and Doppler frequency ν are normalized by physical delay and Doppler frequency resolution.*

windows $\boldsymbol{w}_{\mathrm{BM}}\left(n^f_{\mathrm{BM}}\right)$ and $\boldsymbol{w}_{\mathrm{BM}}\left(n^t_{\mathrm{BM}}\right)$ results in the vectors $\tilde{\boldsymbol{w}}^f_{\mathrm{BM}} \in \mathbb{R}^{N\times 1}$ and $\tilde{\boldsymbol{w}}^t_{\mathrm{BM}} \in \mathbb{R}^{I\times 1}$.

The filtered time-frequency correlation function of the colored noise $\underline{\breve{\boldsymbol{\Psi}}}^{f,t}_b$ is calculated as

$$\underline{\breve{\boldsymbol{\Psi}}}^{f,t}_b = \underline{\boldsymbol{P}}^{f,t}_{\psi,b} \odot \left(\tilde{\boldsymbol{w}}^f_{\mathrm{BM}}(\tilde{\boldsymbol{w}}^t_{\mathrm{BM}})^{\mathrm{T}}\right). \tag{4.36}$$

The colored noise scattering function $\underline{\breve{\boldsymbol{\Psi}}}^{\tau,\nu}_b$ is obtained by

$$\underline{\breve{\boldsymbol{\Psi}}}^{\tau,\nu}_b = \underline{\boldsymbol{\mathfrak{F}}}^{\mathrm{H}}_N \underline{\breve{\boldsymbol{\Psi}}}^{f,t}_b \underline{\boldsymbol{\mathfrak{F}}}^{\mathrm{T}}_I. \tag{4.37}$$

A typical example of the estimated colored noise scattering function $\underline{\breve{\boldsymbol{\Psi}}}^{\tau,\nu}_b$ based on measured signal is shown in Fig. 4.3b. The relative Blackman-window length Δ_{BM} controls how much the scattering function $\underline{\boldsymbol{P}}^{\tau,\nu}_{\psi,b}$ is smoothed by the filtering. The desired effect of the smoothing is to remove the peaks of the scattering function $\underline{\boldsymbol{P}}^{\tau,\nu}_{\psi,b}$, i.e., specular MPCs, while maintaining the dense MPCs, e.g., clusters of MPCs.

We choose Δ_{BM} heuristically such that the majority of the power of $\underline{\boldsymbol{P}}^{f,t}_{\psi,b}$ is contained within the window. A typical value for the relative Blackman-window length Δ_{BM} for the considered measured data is $\Delta_{\mathrm{BM}} = \frac{1}{8}$.

4.5.4 Model Order Adjustments

As indicated in Fig. 4.2 (right side), MPCs may be added after the MPC parameter and colored noise estimation step. The model order may be decreased after the update step of the information filter. The algorithm allows the number of currently tracked MPCs to change arbitrarily during the processing of one block b, e.g., several MPCs may be added or removed.

For both removal and detection of MPCs we rely on a one sided statistical hypothesis test in which we compare the MPC power against the colored noise power at the respective MPC parameter pairs (τ, ν). The reason for comparing the power of an MPC against colored noise (rather than white noise) is to avoid detecting MPCs within clusters of MPCs. Such MPCs are usually not resolvable given the limited bandwidth of the transmit sequence.

Path Detection

New MPCs are added one by one to the model. The loop of adding new MPCs, estimating their parameters, and recalculating the colored noise is visualized in Fig. 4.2 (right side). The loop is continued until there are no undetected MPCs left.

For the detection of new MPCs we calculate an interpolated version of the scattering function $\underline{\boldsymbol{P}}^{\tau,\nu}_{\psi,b}$ as defined in (4.33). Previously undetected MPCs show up in the residuum as illustrated in Fig. 4.3a.

We aim to detect only MPCs which have a significantly higher power than the noise floor. In other words, they must have a significantly high signal-to-noise-ratio (SNR), such that they are unlikely be the result of the colored noise. The criteria is to add MPCs only if their power is outside the Q_{add} quantile of the underlying noise.

Let us assume that the colored noise $\boldsymbol{\psi}_b$ is zero-mean circularly-symmetric complex normally distributed. Then individual elements $P^{\tau,\nu}_b(\tau,\nu)$ of the scattering function $\underline{\boldsymbol{P}}^{\tau,\nu}_{\psi,b}$ are the squared amplitude of that distribution. Thus, $P^{\tau,\nu}_b(\tau,\nu)$ follows an exponential distribution $P^{\tau,\nu}_b(\tau,\nu)\sim\frac{1}{\sigma^2_{\text{n}}(\tau,\nu)}\exp(-\frac{x}{\sigma^2_{\text{n}}(\tau,\nu)})$. The noise variance $\sigma^2_{\text{n}}(\tau,\nu)$ depends on the colored noise power at the MPC parameter pair (τ,ν).

Normalizing the scattering function $\underline{\boldsymbol{P}}^{\tau,\nu}_{\psi,b}$ by the colored noise scattering function $\underline{\breve{\boldsymbol{\Psi}}}^{\tau,\nu}_b$ results in the detection matrix $\underline{\boldsymbol{D}}^{\tau,\nu}_b$

$$\underline{\boldsymbol{D}}^{\tau,\nu}_b = \underline{\boldsymbol{P}}^{\tau,\nu}_{\psi,b} \oslash \underline{\breve{\boldsymbol{\Psi}}}^{\tau,\nu}_b. \tag{4.38}$$

Due to the normalization, all elements in $\underline{\boldsymbol{D}}^{\tau,\nu}_b$ follow an exponential distribution $D^{\tau,\nu}_b(\tau,\nu)\sim\exp(-x)$. The maximum value $D^{\tau,\nu}_{b,\text{max}}$ of the detection matrix $\underline{\boldsymbol{D}}^{\tau,\nu}_b$ is distributed according to the Gumbel distribution shown in Fig. 4.4 [90]

$$D^{\tau,\nu}_{b,\text{max}}\sim e^{-x+\log(NI)-e^{-x+\log(NI)}}. \tag{4.39}$$

Using (4.39) we can setup a one-sided hypothesis test to check whether the current maximum $D^{\tau,\nu}_{b,\text{max}}$ is most likely caused by noise or may represent an MPC. The threshold $\mathrm{t}_{\text{add}}(Q_{\text{add}})$ for the Q_{add}-quantile of $D^{\tau,\nu}_{b,\text{max}}$ is calculated as

$$\mathrm{t}_{\text{add}}(Q_{\text{add}}) = \log(NI) - \log(-\log Q_{\text{add}}). \tag{4.40}$$

An example is given in Fig. 4.4: if $D^{\tau,\nu}_{b,\text{max}}$ exceeds $\mathrm{t}_{\text{add}}(99\%)$ the probability that the maximum is caused by noise is 1% or smaller. We add new MPCs until there are no MPC parameter pairs (τ,ν) left for which the maximum of the detection matrix $\underline{\boldsymbol{D}}^{\tau,\nu}_b$ exceeds the threshold $\mathrm{t}_{\text{add}}(99\%)$.

Fig. 4.3c shows the detection matrix $D^{\tau,\nu}_{b,\text{max}}$ calculated from the data presented in Fig. 4.3a and Sec. 4.3b. The interpolation (by oversampling) allows to obtain a better initialization of the MPC parameter pair (τ,ν). In Fig. 4.3c no MPC exists exceeding the threshold $\mathrm{t}_{\text{add}}(99\%)$.

The above method also works for the first block of measured data, i.e., $b=1$, during the initialization where no previously tracked MPCs exist: starting with the first detectable MPC, we add MPCs one by one.

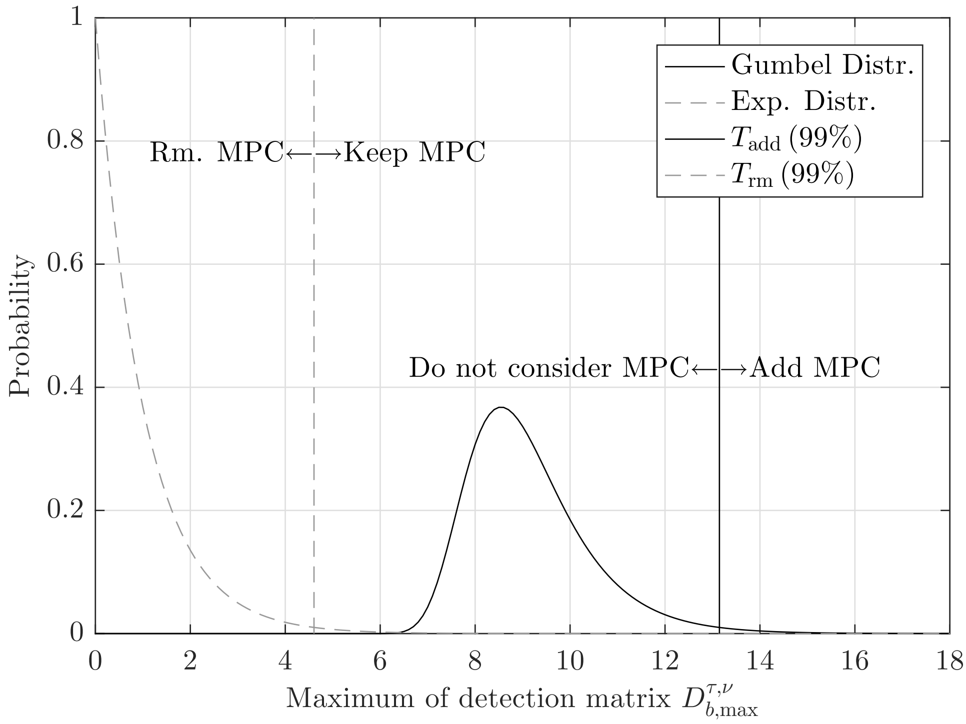

Figure 4.4. *Hypothesis tests to detect new and remove existing MPCs.*

Path Removal

MPCs are removed after the update-step of the information filter as visualized in Fig. 4.2. We remove an MPC if its power is within the Q_{rm} noise quantile of the probability density function (PDF) of the scattering function $\underline{\boldsymbol{P}}^{\tau,\nu}_{\psi,b}$.

Assuming the input signal is circularly-symmetric complex normal distributed, the elements in the scattering function $\underline{\boldsymbol{P}}^{\tau,\nu}_{\psi,b}$ follow an exponential distribution. An MPC is removed, if its estimated power $|\hat{\boldsymbol{\alpha}}_l|^2$, normalized by the estimated colored noise power at the corresponding MPC parameter pair (τ, ν), is below the threshold $\mathrm{t}_{\mathrm{rm}}\left(Q_{\mathrm{rm}}\right)$, where

$$\mathrm{t}_{\mathrm{rm}}\left(Q_{\mathrm{rm}}\right) = -\log\left(1 - Q_{\mathrm{rm}}\right). \tag{4.41}$$

The hypothesis test for the removal of MPCs is visualized in Fig. 4.4.

4.5.5 Calculation of Fisher Information Matrix

To include the ML estimated MPC parameters $\underline{\breve{\mathfrak{I}}}_b$ in the information filter as measurement, the inverse of the covariance matrix needs to be characterized. Because the MPC parameters $\underline{\breve{\mathfrak{I}}}_b$ are estimated using ML, we use the Fisher information matrix $\underline{\breve{\mathfrak{I}}}_b$ in the information filter.

Using the definitions above, the element (i, j) of the Fisher information matrix $\breve{\underline{\mathfrak{I}}}$ is calculated as [91]

$$[\underline{\mathfrak{I}}_b]_{ij} = 2\mathrm{Re}\left\{ \frac{\partial \boldsymbol{\alpha}_b^{\mathrm{H}} \underline{\boldsymbol{C}}^{\mathrm{H}}(\boldsymbol{\tau}_b, \boldsymbol{\nu}_b)}{\partial \xi_{i,l}} \underline{\boldsymbol{\Sigma}}^{-1} \frac{\partial \underline{\boldsymbol{C}}(\boldsymbol{\tau}_b, \boldsymbol{\nu}_b)\boldsymbol{\alpha}}{\partial \xi_{j,l}} \right\} \tag{4.42}$$

where $\xi_{i,l}$ and $\xi_{j,l}$ denote i-th and j-th MPC parameter, e.g., delay τ or Doppler frequency ν, of MPC l. Thus, for the calculation of Fisher information matrix, $\underline{\mathfrak{I}}_b$ the partial derivatives of the signal parameterization described in (4.7) have to be taken.

Note that the Fisher information matrix should be calculated using the true MPC parameters $\boldsymbol{\xi}_b$. Nevertheless, as those are not available, we use the output of the ML estimator $\breve{\boldsymbol{\xi}}_b$ as best estimate. The resulting matrix is known as the stochastic Fisher information matrix [92]. The stochastic Fisher information matrix calculated in that way is denoted by $\breve{\underline{\mathfrak{I}}}_b$. For the covariance matrix $\breve{\underline{\boldsymbol{\Sigma}}}_b$ we can either assume a white noise or calculate it based on the colored noise component $\breve{\underline{\boldsymbol{\Psi}}}_b^{\tau,\nu}$ estimated in Sec. 4.5.3.

4.6 Localization Algorithm

In this section we describe how the location of a physical reflector on the ground can be estimated, given the output of the parameter estimation from Sec. 4.5.

The general idea behind the algorithm can be illustrated as follows. If we know the aircraft location $\boldsymbol{d}_b$ and speed vector $\boldsymbol{v}_b$ at the time corresponding to block index b and only consider single-bounce reflections, points of equal delay τ lie on an ellipsoid while points of constant Doppler frequency ν lie on a cone detailed in App. C. Thus, for one snapshot, the estimated MPC delay τ and Doppler frequency ν define an ellipsoid and cone, respectively. Intersecting these two surfaces with the ground plane results in an ellipse and hyperbola, each defining points on the ground on which a reflection would cause MPCs with delay τ and Doppler frequency ν, respectively. Reflectors on the ground causing MPCs with delay τ and Doppler frequency ν lie on the intersection points of those two curves[4]. Hereby, only one intersection is the true location of the reflector. We term other intersections as ambiguities.

The above method, applied in the context of reflector localization, has been outlined in [26]. In our investigations, calculating "hard locations" in such a way has

[4] According to Bezout's theorem, two quadratic curves in general position can have up to $\Pi = 4$ intersections [93]. In the special case that two quadratic curves were identical, then there would be an infinite number of intersections. As this case occurs with probability 0, we do not consider it in the following.

shown poor localization accuracy, as we are not able to average over multiple blocks b, especially in the presence of ambiguities.

To increase the localization accuracy, in this contribution we extend the method presented in [26] to calculate the PDF, i.e., a "soft location", of the reflector location for each block b and MPC. The PDFs of the same MPC can be averaged over the full duration an MPC is visible. Due to averaging, the locations of reflectors may be calculated with significantly higher accuracy. Additionally, averaging usually mitigates problems arising from ambiguities. Usually, intersection points which do not represent a real reflector location change the locations with a moving aircraft while true reflector location remains fixed. Therefore, at the true location of the reflector the PDF of each block b "adds up", while at other location it averages out.

4.6.1 Fundmentals

The accuracy of the reflector localization depends on how well the MPC parameters delay $\hat{\tau}_{b,l}$ and Doppler frequency $\hat{\nu}_{b,l}$ are estimated: their erroneous estimation may significantly degrade the localization accuracy or render it completely non functional.

Fig. 4.5 shows the principle of how the probability of an MPC being caused by a single-bounce reflection at location $\boldsymbol{g}$ is calculated.

Although the methods described below can be generalized to higher dimensions, for better readability in the following we limit ourselves to the two-dimensional case; we assume that all reflectors are located on the ground plane at a height of $-h_{\mathrm{GS}}$ relative to the location of the ground antenna[5]. The vector $\boldsymbol{g} = [g_{\mathrm{E}}, g_{\mathrm{N}}, -h_{\mathrm{GS}}]^{\mathrm{T}}$ denotes the location in a local, ground station centered east-north-up (ENU) coordinate system (i.e., the ground station is located at $[0, 0, 0]^{\mathrm{T}}$).

As shown in Fig. 4.5, we assume for a block b and MPC index l the parameter measurements to be distributed as a two dimensional normal distribution, i.e., $p_{\mathrm{P}b,l}(\boldsymbol{\mu}) \sim \mathcal{N}(\hat{\boldsymbol{\mu}}_{b,l}, \hat{\underline{\boldsymbol{\Sigma}}}_{b,l})$ with $\boldsymbol{\mu} = [\tau, \nu]^{\mathrm{T}}$. The normal distribution has mean $\hat{\boldsymbol{\mu}}_{b,l} = [\hat{\tau}_{b,l}, \hat{\nu}_{b,l}]^{\mathrm{T}}$ and covariance matrix $\hat{\underline{\boldsymbol{\Sigma}}}_{b,l}$. The smoothed delay and Doppler frequency estimates provided by the information filter are denoted as $\hat{\tau}_{b,l}$ and $\hat{\nu}_{b,l}$. The covariance matrix of both parameters is represented by $\hat{\underline{\boldsymbol{\Sigma}}}_{b,l}$. The goal is to transform the PDF $p_{\mathrm{P}b,l}(\boldsymbol{\mu})$ from the parameter domain into a Cartesian domain and calculate $p_{\mathrm{C}b,l}(\boldsymbol{g})$. Hereby, $p_{\mathrm{C}b,l}(\boldsymbol{g})$ denotes the probability that the current MPC with the pa-

[5] Therefore, we assume a "flat earth model". Although the method described above can easily extended to a curved earth model, this extension is associated with a significantly higher computational complexity as calculations have to be conducted in three dimensions. As the results between the curved and flat earth assumption are expected to be very similar we use the latter.

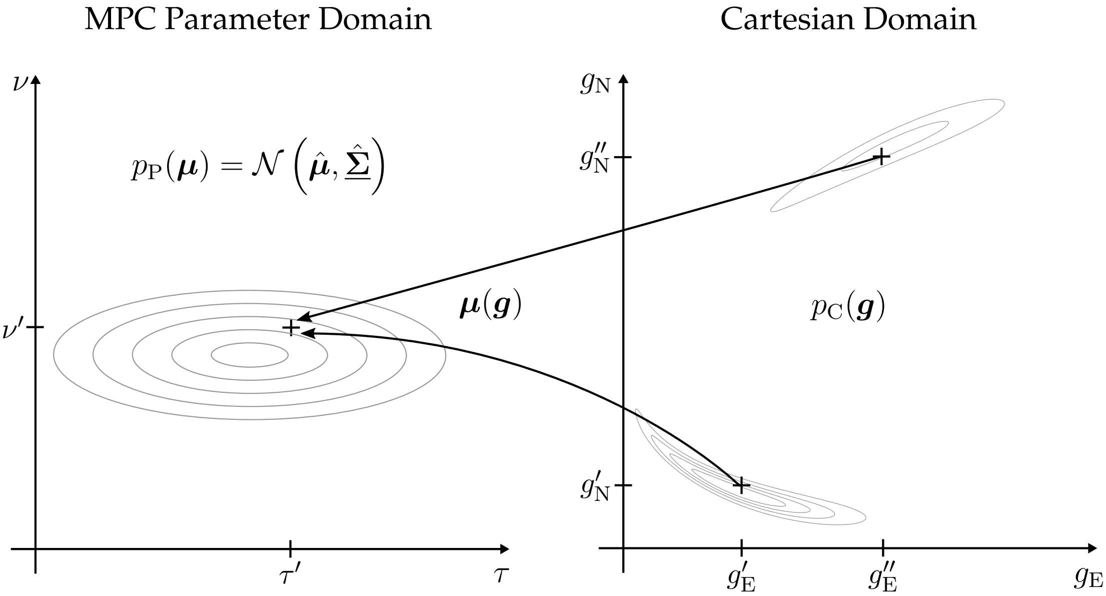

Figure 4.5. *Principle of the reflector localization. One point in the MPC domain can cause more than one PDF in the Cartesian domain. The uncertainty is modeled as a bivariate distribution in the MPC parameter domain which translates into a highly distorted distribution in the Cartesian domain.*

rameters $\hat{\boldsymbol{\mu}}_{b,l}$ and $\underline{\hat{\Sigma}}_{b,l}$ is caused by a single bounce reflection of a reflector located at location $\boldsymbol{g}$.

The function $\boldsymbol{\mu}(\boldsymbol{g})$ connecting the parameter with the Cartesian domain, i.e., relating the probability at location $\boldsymbol{g}$ to the MPC parameter vector $\boldsymbol{\mu}$ is

$$\boldsymbol{\mu}(\boldsymbol{g}) = \begin{bmatrix} \tau\left(\boldsymbol{g}\right) \\ \nu\left(\boldsymbol{g}\right) \end{bmatrix}. \tag{4.43}$$

The delay τ given as a function of reflector location $\boldsymbol{g}$ is

$$\tau\left(\boldsymbol{g}\right) = \frac{\|\boldsymbol{g}\| + \|\boldsymbol{g} - \boldsymbol{d}_b\|}{c_{\mathrm{a}}}. \tag{4.44}$$

Similarly, the Doppler frequency ν as a function of reflector location $\boldsymbol{g}$ is calculated as

$$\nu\left(\boldsymbol{g}\right) = \frac{\left(\boldsymbol{g} - \boldsymbol{d}_b\right)^{\mathrm{T}} \cdot \boldsymbol{v}_b}{\|\boldsymbol{g} - \boldsymbol{d}_b\| c_{\mathrm{a}}} f_{\mathrm{c}}, \tag{4.45}$$

where c_{a} denotes the speed of light in air.

Note that $\boldsymbol{\mu}(\boldsymbol{g})$ is generally not a bijective function, i.e., one point in the parameter domain $\boldsymbol{\mu}$ may map to up to multiple points in the Cartesian domain, normally one or two as visualized in Fig. 4.5.

4.6.2 Reflector Location Probability Density Function (PDF)

The PDF $p_{\mathrm{C}b,l}\left(\boldsymbol{g}\right)$ in the Cartesian domain can be calculated as [36], [94]

$$p_{\mathrm{C}b,l}\left(\boldsymbol{g}\right) = \frac{1}{\Pi} p_{\mathrm{P}b,l}\left(\boldsymbol{\mu}(\boldsymbol{g})\right) \Upsilon\left(\boldsymbol{g}\right). \tag{4.46}$$

Hereby, Π denotes the number of intersections between the shapes defined by the delay τ and Doppler frequency ν. $\Upsilon\left(\boldsymbol{g}\right)$ denotes the Jacobian of $\boldsymbol{\mu}(\boldsymbol{g})$ which normalizes $p_{\mathrm{P}b,l}\left(\boldsymbol{\mu}(\boldsymbol{g})\right)$

$$\Upsilon\left(\boldsymbol{g}\right) = \det \begin{pmatrix} \frac{\tau(\boldsymbol{g})}{\partial g_{\mathrm{E}}} & \frac{\tau(\boldsymbol{g})}{\partial g_{\mathrm{N}}} \\ \frac{\nu(\boldsymbol{g})}{\partial g_{\mathrm{E}}} & \frac{\nu(\boldsymbol{g})}{\partial g_{\mathrm{N}}} \end{pmatrix}. \tag{4.47}$$

It is important that $\Upsilon\left(\boldsymbol{g}\right)$ is not a constant but rather a non-linear function changing the probabilities for each point $\boldsymbol{g}$ differently. Normalized by $\Upsilon\left(\boldsymbol{g}\right)$, the resulting PDF $p_{\mathrm{C}b,l}\left(\boldsymbol{g}\right)$ integrates to one, i.e.,

$$\int\int p_{\mathrm{C}b,l}\left(\boldsymbol{g}\right) dg_{\mathrm{E}} dg_{\mathrm{N}} = 1. \tag{4.48}$$

The derivation of the Jacobian is described in App. D.

Assume $U_u = \left\{\left(b_1, l_1\right), \ldots, \left(b_{\langle U_u\rangle}, l_{\langle U_u\rangle}\right)\right\}$ describes the set of block and MPC index pairs of an MPC u tracked over $\langle U_u\rangle$ blocks. The averaged PDF is calculated as

$$p_{\mathrm{C}u}\left(\boldsymbol{g}\right) = \sum_{U_u} \frac{1}{\langle U_u\rangle} p_{\mathrm{C}b,l}\left(\boldsymbol{g}\right). \tag{4.49}$$

We assume the maximum of the averaged PDF $p_{\mathrm{C}u}\left(\boldsymbol{g}\right)$ to be the true location of the reflector causing the MPC u.

4.7 Summary

In this chapter we derive algorithms to estimate the information required to adapt the channel model to an environment. The main contributions are twofold:
firstly, we propose an algorithm that allows detecting MPCs in a measured signal and estimate their MPC parameters. To this end, we combine a super-resolution parameter estimation with an information filter. The information filter allows to improve the parameter estimation performance significantly. Thus, the presented algorithm is specifically useful for measurements in a high noise environment or scenarios where a very accurate parameter estimation performance is required.
Secondly, we propose a Bayesian localization algorithm for reflectors based on their estimated MPC parameters. As the localization does not require (electronically) steerable antennas, the algorithm can essentially be applied to any measurement

were a sufficiently accurate ground truth is available.
While the algorithms presented in this chapter are designed for AG channel sounding experiments, the applicability of the algorithms reaches beyond the AG related application.

Chapter 5

Flight Trial Setup

Contents

5.1 Overview

Up to this point the contribution of this dissertation is of theoretical nature: in Chapter 3 we proposed a new channel model architecture for the air-ground (AG) channel. The methods to estimate the information required to parameterize the channel model are described in Chapter 4. These methods are intended to be applied on flight trial measurement data.

Obtaining this measurement data is not a trivial task, both from a technical and regulatory standpoint. In this chapter we present the channel sounding setup to obtain this data by means of flight trials. In Sec. 5.2, we focus on the design of the flight trials: we describe the key hardware components, the channel sounding signal, and the procedures required to execute the measurements. The flight routes flown in November 2013 are presented in Sec. 5.3.

We use the acquired measurement data to characterize the channel in Chapter 6. The measurement data also builds the basis for the parameterization of the channel model in Chapter 7.

Content of this chapter has been published in [11], [95].

5.2 Measurement System

In the following sections, we describe the system used for the measurement of the AG radio channel. In Sec. 5.2.1 we focus on the employed hardware components. The channel sounding signal is introduced in Sec. 5.2.2. In Sec. 5.2.3 procedures to achieve time synchronization between ground station and aircraft are described. To investigate the properties of the AG radio channel with respect to ranging, we require a precise reference for the distance between ground station and aircraft. The calculation of this reference distance is explained in Sec. 5.2.4. In Sec. 5.2.5 we describe the factors which contribute errors to the measurements. In Sec. 5.2.6 we discuss the different types of interference received during the measurements.

5.2.1 Hardware Setup

The setup for the measurement of the AG radio channel is composed of a ground based transmitter, located in a van, and a receiver, installed in one of the research aircraft of the DLR, namely the Falcon 20E (D-CMET) shown in Fig. 5.1.

The transmitter hardware is mostly setup in a van, with the only exception of the high power amplifier (HPA) and ground antenna being located on the rooftop

Figure 5.1. *Aircraft carrying the receiver.*

Figure 5.2. *Transmitter surroundings as seen from the transmit antenna's point of view. Each image shows a* 180° *segment of the full* 360° *panorama shot.*

of a neighboring building at $23\,\mathrm{m}$ above ground level (AGL) ($652\,\mathrm{m}$ above mean sea level (AMSL)). On the rooftop, the HPA is connected to the ground antenna by a $15\,\mathrm{m}$ cable. During flight testing, the van is parked in front of the building on which HPA and ground antenna are located. The HPA on the rooftop is connected to the van in via a $75\,\mathrm{m}$ cable. A mobile setup is necessary to position the transmitter near the aircraft for pre-flight calibration of the measurement equipment - see Sec. 5.2.3. The position of the transmit antenna is fixed and is precisely measured using Global Positioning System (GPS) with centimeter accuracy via post-processing [96]. During calibration, the transmit antenna is disconnected from the rest of the ground station hardware. In Fig. 5.2, we show the area surrounding the transmit antenna in a $360°$ panorama view:

the runway of the neighboring Oberpfaffenhofen airport (EDMO) is clearly visible. The environment around the transmit antenna mimics well a regional airport environment: it includes large and small hangar buildings, as well as civil infrastructure, such as office buildings, and large open spaces of either grassy or concrete

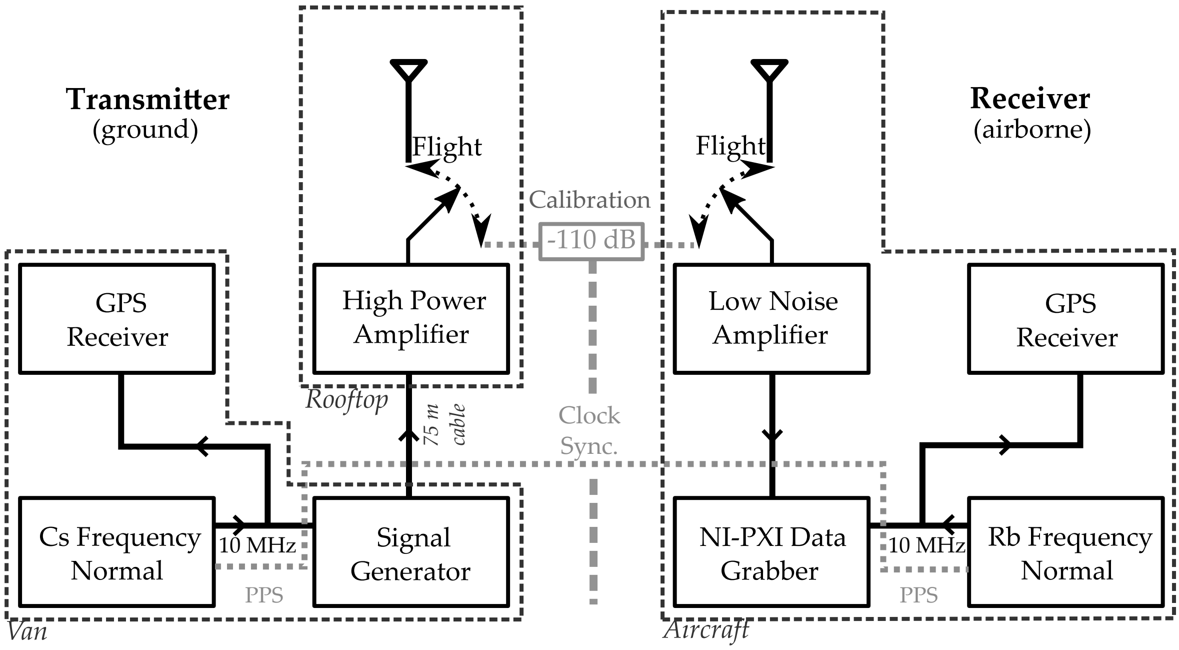

Figure 5.3. *Hardware setup for the transmitter, located on ground, and the airborne receiver. The dotted blue lines denote the cable configuration during calibration and clock synchronization.*

surface. As transmit antenna we employ an L-band aircraft communication blade antenna, manufactured by Sensor Systems (S65-5366-715) with vertical polarization.

The block diagram of the transmitter hardware setup is depicted in Fig. 5.3 (left side). The cesium (Cs) frequency normal (or frequency standard), an Agilent 5071A acts as common oscillator for the ground station hardware that consists of the GPS receiver, a signal generator and the high power amplifier as shown in Fig. 5.3. In order to monitor the clock drift of the Cs frequency normal to GPS time during the measurements, we employ a high precision multi-frequency global navigation satellite system (GNSS) receiver (Septentrio PolaRx4TR PRO). The transmitted sounding sequence is generated using an arbitrary waveform generator (AWG) from Rohde & Schwarz (SMBV100A) and amplified by a custom built HPA.

The block diagram of the receiver components is also depicted in Fig. 5.3 (right side). A rubidium (Rb) frequency normal (Spectratime SRO100) acts a the common oscillator for all onboard devices. Due to its superior stability, a Cs frequency normal would be also preferred in the airplane. Unfortunately, no Cs frequency normal was available at the time when the receiver hardware was certified for the flight trials. Therefore, due to legal restrictions it could not be used during the measurements. However, the lower stability of the Rb frequency normal is not a problem as its drift can be well monitored using GPS as described in Sec. 5.2.3. For receiving the signal, we employ the same type of antenna as for transmitting: the vertically polarized aircraft L-band communication antenna from Sensor Systems (S65-5366-715) located on the bottom of the fuselage facing downwards.

The signal received by the antenna is first pre-filtered and then amplified using a custom built low noise amplifier (LNA) with $35\,\mathrm{dB}$ gain. Afterwards, the signal can be attenuated using a step attenuator in order to use the full dynamic range of the analogue-to-digital-converter (ADC). The resulting signal is recorded by a data grabber that is realized on a National Instruments PXIe platform [97]. The device downconverts the measured signal to the baseband, samples it, and stores the samples on an array of solid state drives (SSDs). The entire PXIe system uses the $10\,\mathrm{MHz}$ output of the Rb frequency normal as reference frequency. The onboard multi-frequency GNSS receiver (Septentrio PolaRx2e) serves two tasks. First, its post-processed measurements are taken as reference or the aircraft position. Second, similarly to the transmitter, the GNSS receiver monitors the drift of the Rb frequency normal with respect to GPS time.

The ground and airborne crew stay in contact using satellite phone connection. Before the installation of hardware in an aircraft a lengthy certification process is required by German law.

5.2.2 Channel Sounding Signal

The channel sounding signal used in the measurements is a multitone signal [82]. In its structure it is similar to an orthogonal frequency division multiplexing (OFDM) signal with constant subcarrier amplitude, but pseudo-random, non-discrete phases of each subcarrier, and no cyclic prefix. The inverse discrete Fourier transform (IDFT) size is $N_{\text{fft}} = 12800$ with $N_c = 5120$ subcarriers being used by the channel sounding signal[1]. The phases of the subcarriers are chosen as Newman phases according to [98]. Thus, the frequency domain transmit signal $\underline{\mathfrak{F}}\boldsymbol{s}$ of one period of the channel sounding signal can be expressed as a vector

$$\underline{\mathfrak{F}}\boldsymbol{s} = \left[\underbrace{0,..,0}_{\text{length}7680/2}, e^{j\pi\frac{([0,..,N_c-1])^2}{N_c}}, \underbrace{0,..,0}_{\text{length}7680/2} \right]^{\mathrm{T}} \tag{5.1}$$

where each element represents a sample and N_c defines the number of used subcarriers. The transmit signal $\underline{\mathfrak{F}}\boldsymbol{s}$ is then converted to the time domain using a N_{fft} point IDFT resulting in $\boldsymbol{s}$. The time domain signal $\boldsymbol{s}$ is stored on the AWG for transmission. Fig. 5.4 shows the time and frequency domain signal of the channel sounding

[1] The oversampling of a factor of 2.5, i.e., using 7680 guard carriers, is necessary due to compatibility reasons.

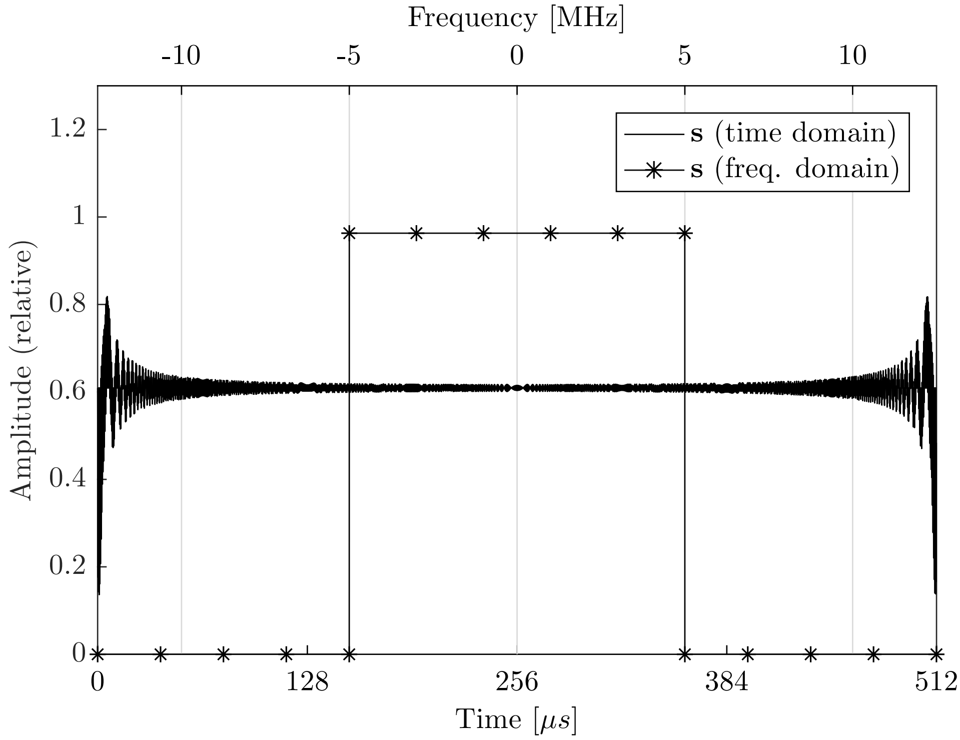

Figure 5.4. *Oversampled time and frequency domain representation $\boldsymbol{s}$ and $\underline{\mathfrak{F}}\boldsymbol{s}$ of the channel sounding signal.*

signal. The resulting transmit signal $\boldsymbol{s}$ exhibits a low peak-to-average-power-ratio (PAPR) of $2.6\,\mathrm{dB}$. Therefore, the power amplifier can be used effectively with a small required backoff (headroom) to prevent operation in the non-linear domain. Tab. 5.1 summarizes the key parameters of the sounding signal. The time period of the transmit signal is set to $t_{\mathrm{symb}} = 512\,\mu\mathrm{s}$, determining both the maximum resolvable Doppler frequency, $f_{\mathrm{d,max}} = (2t_{\mathrm{symb}})^{-1}$, as well as the maximum range, $d_{\mathrm{max}} = t_{\mathrm{symb}}\, c_{\mathrm{a}}$, which can be resolved without ambiguities. The value for the theoretically resolvable Doppler frequency is well above $760\,\mathrm{Hz}$, the maximum value experienced during the measurements. Similarly, the maximum resolvable range is significantly higher than the corresponding experienced maximum multipath component (MPC) delay.

To be able to measure the propagation characteristics of the channel up to the radio horizon, we assume the signal must be detectable at a maximum distance of $400\,\mathrm{km}$. With a transmit power of $37\,\mathrm{dBm}$ at the HPA output and $2\,\mathrm{dBi}$ gains for the receive and transmit antennas, the signal is received at $-110\,\mathrm{dBm}$ assuming free space path loss (FSPL) for $400\,\mathrm{km}$ distance. Integrated over one transmit symbol ($t_{\mathrm{symb}} = 512\,\mu\mathrm{s}$), the signal-to-noise-ratio (SNR) after correlation over the thermal

Table 5.1. *Channel sounding signal key parameters*

Parameter	Value
Carrier frequency (f_c)	$970\,\mathrm{MHz}$
Signal bandwidth ($\Delta \mathrm{f}_{\mathrm{BW}}$)	$10\,\mathrm{MHz}$
Transmit power (@ HPA output)	$37\,\mathrm{dBm}$
Used subcarriers (N_c)	5120
AWG IDFT size (N_{fft})	12800
Symbol duration (t_{symb})	$512\,\mu\mathrm{s}$
Range resolution (d_{res})	$30\,\mathrm{m}$
Max. resolvable range (d_{max})	$153\,\mathrm{km}$
Max. resolvable freq. ($f_{\mathrm{d,max}}$)	$977\,\mathrm{Hz}$

noise floor is $31\,\mathrm{dB}$ using the realistic assumption of a system noise temperature of $300\,\mathrm{K}$.

5.2.3 Measurement Procedures

The characterization of the AG radio channel is based on the channel transfer function. In this section, we explain how we calibrate the measurement system to be able to estimate the transfer function. The calibration allows us to compensate time-invariant contributions caused by the measurement hardware, e.g., distortions by the analog hardware. We further describe the time synchronization between ground station and aircraft, which is mandatory to investigate the impact of the propagation channel on ranging.

Calibration

In order to compensate the influence of the hardware components on the recorded signal, a calibration is performed prior to the actual channel sounding measurement. We define calibration to be the estimation of the transfer function of the entire hardware setup, including receiver and transmitter hardware except the antennas. Hereby, the impact of both the transmitter and receiver hardware, as well as the clock offset at the moment of calibration, are inherently taken into account. The calibration signal is measured like a regular channel measurement, with the only difference that the receiver and transmitter clocks are synchronized by cable and the transmitter is directly connected to the receiver by their antenna cables using a $110\,\mathrm{dB}$ attenuator, as depicted in Fig. 5.3.

At the receiver side, after downconversion and ADC, the baseband transfer function of the hardware setup (including the attenuator) can be expressed as

$$\boldsymbol{h}_{\mathrm{HW},f} = \boldsymbol{c}_f \oslash \underline{\boldsymbol{\mathfrak{F}}}\boldsymbol{s}, \tag{5.2}$$

where $\boldsymbol{c}_f$ is the discrete Fourier transform (DFT) of the recorded calibration signal $\boldsymbol{c}$. The element-wise division is denoted by $\oslash$.

Measurement Principle

The channel transfer function $\boldsymbol{h}_f$ between the transmitter and receiver can be estimated as [82]

$$\boldsymbol{h}_f = \boldsymbol{y}_f \oslash \boldsymbol{c}_f\,, \tag{5.3}$$

where $\boldsymbol{y}_f$ denotes the DFT of the received time domain signal $\boldsymbol{y}$. Hereby, the DFT of the previously measured calibration signal $\boldsymbol{c}_f$ accounts for all imperfections of the hardware setup, e.g distortions by the analog hardware. Note that the calibration measurement does not take the characteristics of the antennas into account. As the antennas cause only a very minor additional propagation delay due to their size, we neglect their influence on the measured signal in terms of ranging. In terms of received power, we treat the antennas as part of the channel.

Time Synchronization

To measure the absolute propagation delay of the individual MPCs, the ground station and aircraft have to rely on a common time reference. If a time drift between the ground station and aircraft clocks occurs, the measured channel impulse response will exhibit a propagation independent time variant shift in terms of the delay. During the calibration, i.e., before the start of the measurement, the frequency normals are synchronized as described in Sec. 5.2.3 and visualized in Fig. 5.3. Additionally, to verify the employed time synchronization method, the frequency normals are compared immediately after each measurement flight. To synchronize the ground and airborne frequency normals during the calibration, we connect the pulse per second (PPS) output signal of the Cs frequency normal to the PPS input of the Rb normal located in the aircraft. This connection allows the Rb frequency normal to adjust to the more stable Cs oscillator. The synchronization of the frequency normals is visually verified using an oscilloscope.

During the measurement, both frequency normals drift apart from each other. Hereby, the main contributor is a random walk of the frequency normals, especially for the less stable Rb frequency normal. Additionally, the flight dynamics and cabin environment, i.e., change of gravitational field, magnetic field, acceleration, vibrations, and temperature are responsible for an additional change of the frequency as described in [99]. These effects are mostly random and cannot be deterministically predicted. The changes in frequency of the two frequency normals integrate over flight time, thus resulting in time-variant additive delay, common for all propagation paths. However, this delay can be monitored by relating the output of the frequency normals against a common time reference which is observable at both the ground station and aircraft. In our campaign we use GPS time for this purpose. More specifically, the GPS receivers are not only used for positioning but additionally as timing reference, as for a position solution also the receivers clock offset to the GPS time is estimated. As the GPS receivers make use of the $10\,\mathrm{MHz}$ output of the frequency normals, the change in the estimated receiver clock offset of each position solution allows monitoring the frequencies of both, the ground based Cs and airborne Rb frequency normal. Therefore, the drift caused by the changes in frequency of the two frequency normals can be estimated. In order to increase the precision, the GPS measurements are post-processed. The post-processed real time kinematic (RTK) solution, calculated using the software Novatel GrafNav [99], has an estimated accuracy for the clock offset calculation of $230\,\mathrm{ps}$ ($7\,\mathrm{cm}/c_\mathrm{a}$) for both ground and airborne frequency normals.

The clock corrections are always related to the time of calibration t_cal, at which we define the frequency normals as synchronized. Therefore, the clock offset $\tau_\mathrm{RT}(t)$ between the ground station and aircraft can be expressed as

$$\tau_\mathrm{RT}(t) = (\tau_\mathrm{R}(t) - \tau_\mathrm{R}(t_\mathrm{cal})) - (\tau_\mathrm{T}(t) - \tau_\mathrm{T}(t_\mathrm{cal})). \tag{5.4}$$

The knowledge of the clock offset allows a post-processing based synchronization of the measurement setup for the entire duration of the measurement.

In Fig. 5.5, we show the offset of the ground station and aircraft clocks to GPS time for the flight conducted on November 14th 2013 - see Sec. 5.3. The x-axis shows time relative to the takeoff time t_cal as reference. From Fig. 5.5 the higher stability of the ground station's Cs frequency normal, compared to the Rb frequency normal at the receiver site becomes obvious. This may be explained by, first of all, the higher stability of the Cs over the Rb frequency normal, and second, the less severe vibration and acceleration the Cs frequency normal on ground is exposed to, compared to the Rb frequency normal located in the flying aircraft. Note that over the duration

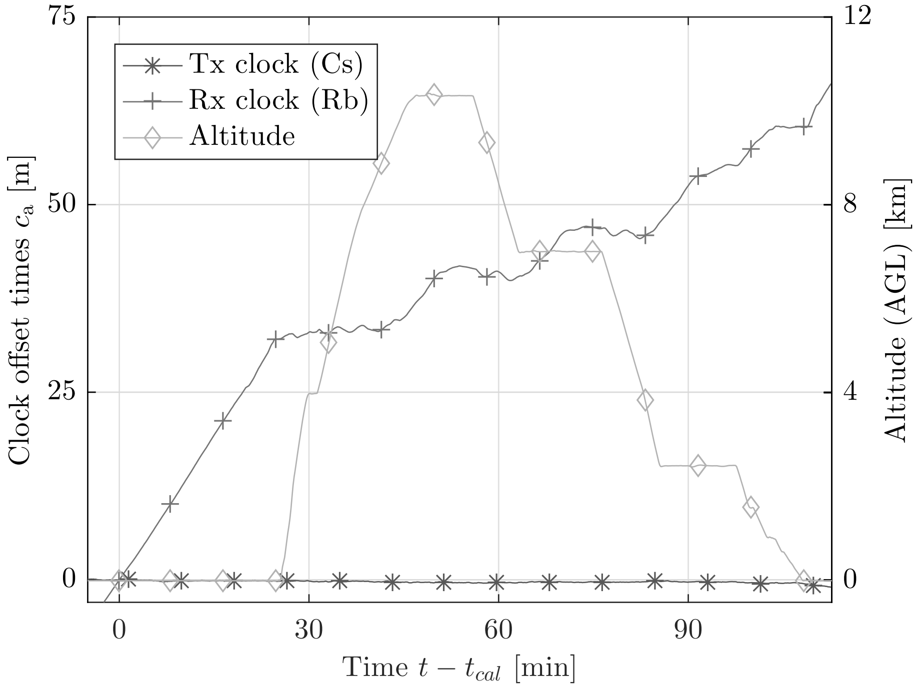

Figure 5.5. *Clock offset to GPS time of the ground station and aircraft clock referenced to the calibration time instant* t_{cal} *for the flight conducted on November 14th 2013.*

of the flight, an offset of approximately $100\,\mathrm{ns}$, corresponding to a distance of $30\,\mathrm{m}$, is observed at the receiver side. The Cs frequency normal exhibits no significant drift compared to GPS time. Additionally, a strong correlation between the flight pattern and the clock offset of the airborne Rb frequency normal can be observed. Due to the aircraft altitude information in Fig. 5.5, we are able to identify significant flight events, such as takeoff, and landing - see Fig. 5.10 for comparison. All events have an impact on the clock drift of the airborne frequency normal. While the aircraft is on ground, the drift is relatively linear, yet after takeoff the linearity is lost. This behavior can be explained by the physical influences on the frequency normal [99]. A detailed investigation of these effects on the frequency normal is left outside the scope of the paper.

With the employed measurement setup, we are not able to determine the accuracy of the GPS solution exactly. Nevertheless, it is possible to check the plausibility of the estimated accuracy of the GPS solution of $7\,\mathrm{cm}/c_{\mathrm{a}}$ and provide some degree of verification for synchronization between ground station and aircraft.

As described above, we perform a calibration before the flight. Additionally, there is another measurement immediately after landing. Both times the receiver is directly connected to the transmitter via cable as shown in Fig. 5.3. Comparing the calibration measurement with the measurement after the flight exhibits a time shift due to the relative frequency offset of the ground station and aircraft frequency normals. Therefore, using the clock corrections, allows a check of the accuracy of the system's time synchronization. A qualitative evaluation for all scenarios shows a maximum time synchronization error of about $0.6\,\mathrm{ns}$, relating to a maximum distance of approximately $0.2\,\mathrm{m}$. Note, however, that this value includes only the errors due to time synchronization and no other influences, e.g., imperfect determination of the transmit and receive antenna position for the range measurement as described in Sec. 5.2.5.

5.2.4 Reference Range Calculation

The range is defined as the geometrical distance between the antennas of the aircraft and the ground station. As we discussed in Chapter 2 for terrestrial radionavigation systems the ranging error, i.e., the difference between the estimated and true range, is of great interest. For the calculation of the ranging error a reference range is required. This reference range is based on GPS position measurements. For the calculation of the aircraft position, two effects have to be compensated for: the difference in position of the GPS antenna and the L-band measurement antenna onboard the aircraft, and the effect of the troposphere on the signal propagation.

Antenna Position Correction

The post-processed GPS solution provides only the position of the GPS antenna. Therefore, the relative position of the GPS antenna on the aircraft to the L-band receive antenna needs to be considered. Fig. 5.6 shows the locations of the two antennas on the aircraft. Due to the different positions of the antennas, the path length $\|\boldsymbol{d}_{\mathrm{GPS}}\|$ calculated based on the GPS positions differs from the propagation path length $\|\boldsymbol{d}_{\mathrm{ANT}}\|$ between the receive and transmit antenna. Hereby, $\|\cdot\|$ denotes the Euclidean norm. The corresponding bias $\|\boldsymbol{d}_{\mathrm{ANT}}\| - \|\boldsymbol{d}_{\mathrm{GPS}}\|$ depends on the position and attitude of the aircraft, i.e., yaw, pitch, and roll angles. This bias can be corrected using the data recorded by the aircraft inertial navigation system (INS). Therefore, we determine the vector $\boldsymbol{d}_{\mathrm{AC}}$ pointing from the GPS antenna to the measurement antenna in the aircraft's local coordinate system on ground before the measurement flight. Rotating this vector by yaw φ_{Y}, pitch φ_{P}, and roll angle φ_{R},

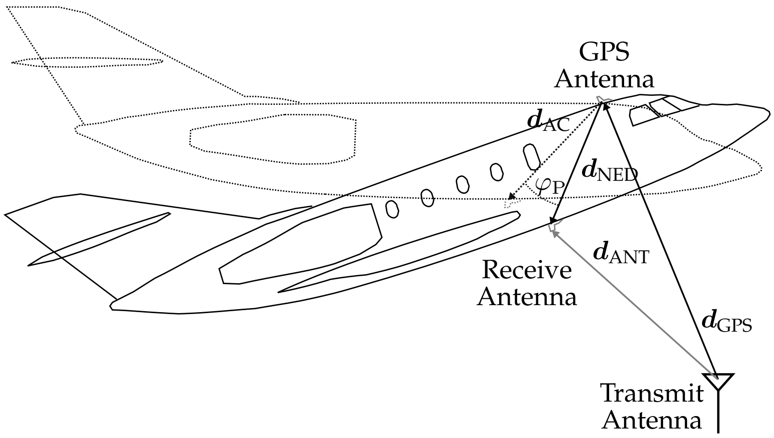

Figure 5.6. *Visualization of the antenna position correction. For simplicity we show the 2D case for a significant pitch angle* φ_{P}*.*

given by the INS measurements, allows conversion of the vector $\boldsymbol{d}_{\mathrm{AC}}$ into a local north-east-down (NED) coordinate system, resulting in $\boldsymbol{d}_{\mathrm{NED}}$

$$\boldsymbol{d}_{\mathrm{NED}} = \begin{bmatrix} \cos\varphi_{\mathrm{Y}} & -\sin\varphi_{\mathrm{Y}} & 0 \\ \sin\varphi_{\mathrm{Y}} & \cos\varphi_{\mathrm{Y}} & 0 \\ 0 & 0 & 1 \end{bmatrix} \times \begin{bmatrix} \cos\varphi_{\mathrm{P}} & 0 & \sin\varphi_{\mathrm{P}} \\ 0 & 1 & 0 \\ -\sin\varphi_{\mathrm{P}} & 0 & \cos\varphi_{\mathrm{P}} \end{bmatrix} \times \begin{bmatrix} 1 & 0 & 0 \\ 0 & \cos\varphi_{\mathrm{R}} & -\sin\varphi_{\mathrm{R}} \\ 0 & \sin\varphi_{\mathrm{R}} & \cos\varphi_{\mathrm{R}} \end{bmatrix} \boldsymbol{d}_{\mathrm{AC}}. \tag{5.5}$$

Converting $\boldsymbol{d}_{\mathrm{NED}}$, with respect to the reference point $\boldsymbol{d}_{\mathrm{GPS}}$, to a global metric coordinate system, such as earth-centered earth-fixed (ECEF) [100], allows a calculation of $\boldsymbol{d}_{\mathrm{ANT}}$.

Compensation of the Tropospheric Delay

Another error source that has a significant impact on ranging is the troposphere. The troposphere introduces a bias on the estimation of the line-of-sight (LoS) path length, depending on the link distance and the elevation angle, at which the aircraft is seen from the ground station site.

With increasing altitude, the thinning air leads to a change of the air's refractive index: the speed of propagation increases compared to the speed of light near ground which is usually slightly smaller than the speed of light in vacuum. The increase of the speed of light has two major consequences which can lead to significant errors in the path length estimation. First, assume a constant speed of light at the value valid at ground level. The path length estimation error is as large as $35\,\mathrm{m}$

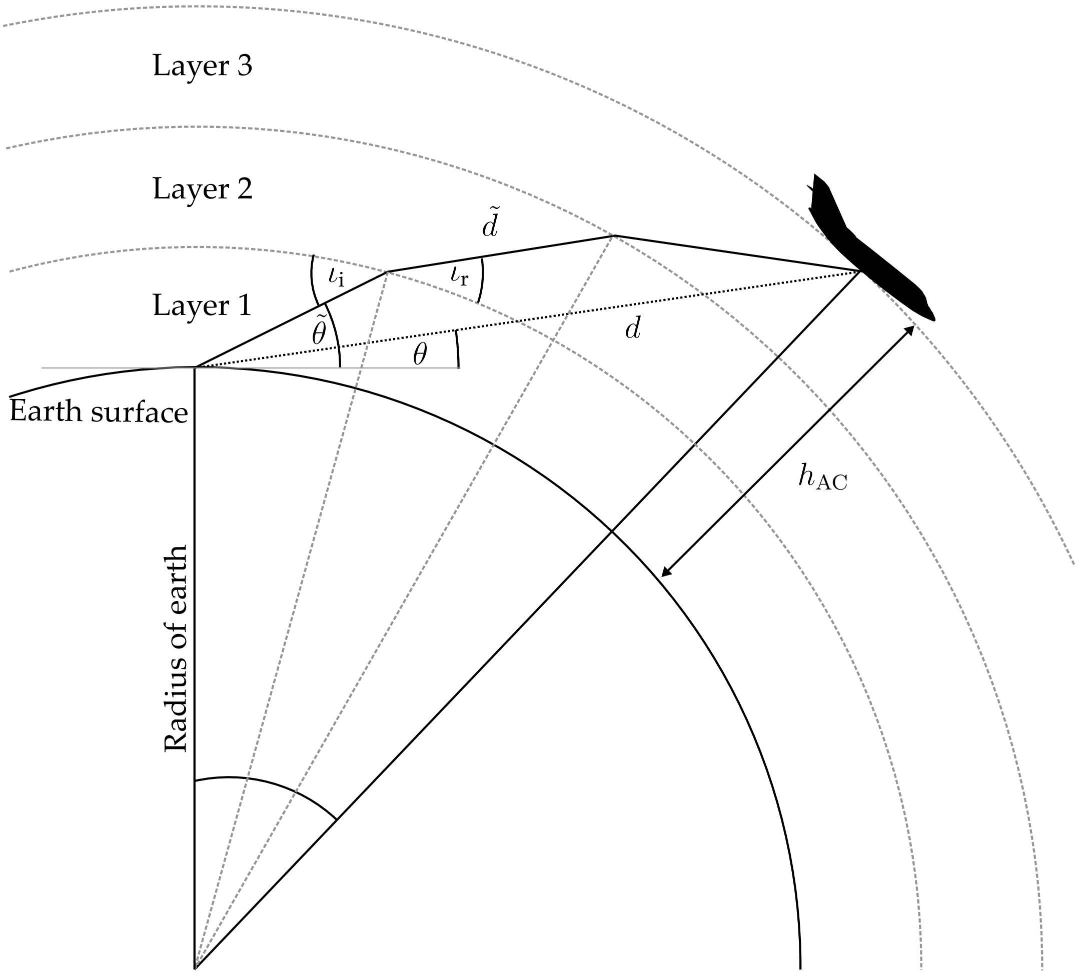

Figure 5.7. *Millman model of the troposphere. The number of layers used for the correction of the troposphere is significantly higher as the depicted three layers (about 100 layers).*

for an aircraft traveling at $10\,\mathrm{km}$ AMSL at a distance of $350\,\mathrm{km}$ to the ground station at $652\,\mathrm{m}$ AMSL. Second, the decreasing refractivity of consecutive layers in the troposphere bends the electromagnetic wave. Therefore the path length increases leading to a positive bias compared to the geometrical LoS distance. For an aircraft at $10\,\mathrm{km}$ AMSL at a distance of $350\,\mathrm{km}$ the resulting bias is about $2\,\mathrm{m}$.

Both effects can be corrected by applying a model for the troposphere. For the correction we use the model and formulas derived in [16]. Hereby, the troposphere is divided into layers as visualized in Fig. 5.7. We observe, that the length of the bent path $\tilde{d}$ is longer than the direct path length d. This is due to the refraction occurring at the layer boundaries, i.e., the angle of incidence ι_i is different to the refraction angle ι_r. The relation between the two angles is described by Snell's law and depends on the refractivity of each layer. The refractivity of each layer depends on the air pressure and the relative humidity. We use meteorological data collected by the air-

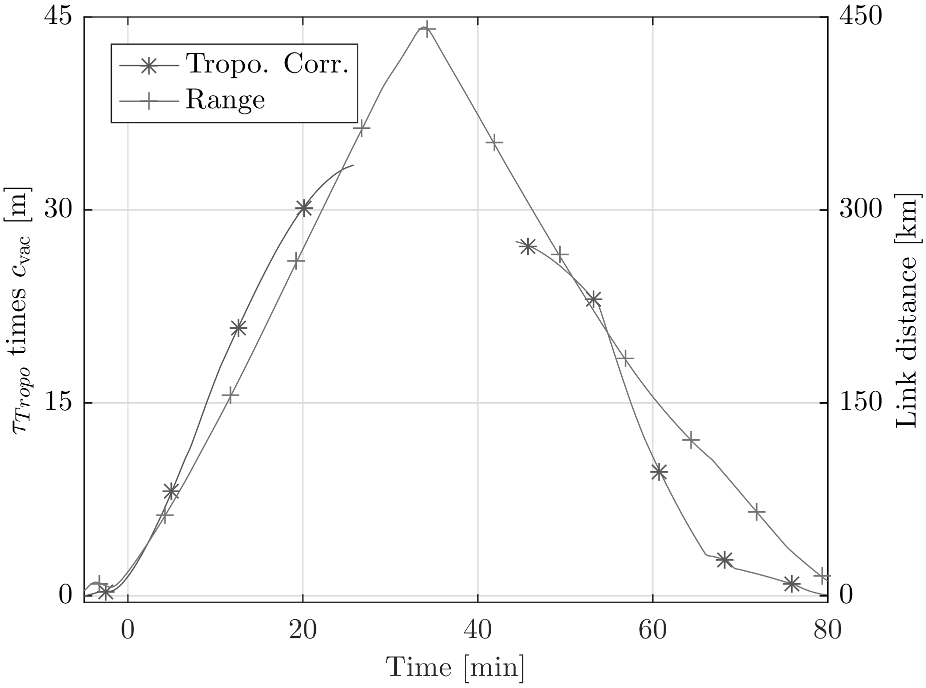

Figure 5.8. *Tropsphere correction for the flight conducted on November 20th 2013 (part 2). During the time between* 25 *and* 45 min *a correction cannot be calculated as the aircraft is behind the radio horizon.*

craft's measurement system to take the relative humidity at different altitudes into account. Due to the refraction of the signal the geometrical elevation angle θ the aircraft is seen under is different to the angle the signal leaves the ground antenna $\tilde{\theta}$ to reach the aircraft.

We define the additional delay due to the troposphere as

$$\tau_{\text{Tropo}} = \tau_{\text{bent}} - \tau_{\text{straight}} \tag{5.6}$$

where τ_{bent} defines the propagation time for the bent path assuming a variable propagation speed calculated using [16] and the propagation time for the direct path τ_{straight} where we assume a speed of propagation in vacuum.

Fig. 5.8 shows the troposphere correction for the flight conducted on November 20th 2013 (part 2) - see Sec. 5.3. The correction mitigates the error caused by assuming a constant speed of light for the range calculation (speed of light at sea level). The different correction values for the outward and return flight are due to the lower altitude on the way back (compare Fig. 5.14).

Table 5.2. *Error contributions degrading the measurement system's performance (A: aircraft, G: ground station)*

Error description	**Loc.**	**Error** (std)
Random errors		
GPS time	A	$^{7\,\mathrm{cm}}/_{c_\mathrm{a}}$
GPS time	G	$^{7\,\mathrm{cm}}/_{c_\mathrm{a}}$
GPS pos.	A	10 cm
L-band ant. pos.	A	50 cm
Systematic errors		
Tx ant. pos.	G	10 cm
Calibration	A/G	10 cm

5.2.5 Approximation of the Overall Measurement Error

In the following, we identify the major error contributions which degrade the setup's accuracy with respect to range measurements. Tab. 5.2 gives an estimate of the errors expected from each contribution. Please note that each number should be seen as an educated guess rather than an exactly measurable figure. Nevertheless, the list allows us to check the plausibility of the results presented in Chapter 6.

The accuracy of the GPS position and time solution in the measurement influences the monitoring of both the ground and airborne frequency standard as well as the ground truth for the aircraft position. It therefore contributes to three different error sources. The GPS raw data is processed using NovAtel GrafNav [96]. As part of the processing the standard deviation of the three dimensional position and time solution solution is estimated. The average standard deviation of the three error sources is given in Tab. 5.2.

For the estimation of the L-band antenna position based on the GPS antenna onboard the aircraft, we measured the vector connecting both antennas $\boldsymbol{d}_{\mathrm{AC}}$. The vector $\boldsymbol{d}_{\mathrm{AC}}$ contains a systematic error that is randomized by possibly erroneous INS measurements for the yaw, pitch and roll angles.

As the location of the transmit antenna is fixed, its position can be very precisely measured over a long time down to millimeter accuracy using a post processed GPS solution. However, it is impossible to setup the L-band antenna in a way that its phase center is at exactly the same position as the phase center of the GPS antenna. Thus, a bias is introduced. Another systematic error is caused by the calibration process. Several cable connectors have to be disconnected and reconnected during the calibration process. Possibly imperfect connections may introduce a systematic error here. An error introduced by receiver noise during the calibration is negligible due to the high SNR.

From the very rough approximation in Tab. 5.2 we conclude that a ranging typical error due to the setup is expected to be below $60\,\mathrm{cm}$. Note however, that this value does not include model errors for the correction of the troposphere. The tropospheric error depends on the composition of the different air layers in the troposphere and their properties, e.g., pressure, temperature, and water content. As the exact modeling of this highly complex system is beyond the scope of the paper, we treat the remaining error after application of the troposphere correction as part of the range estimation error that is part of the channel.

5.2.6 Interference

The channel sounding is performed in the lower L-band between frequencies of $965\,\mathrm{MHz}$ and $975\,\mathrm{MHz}$. Although, no other civil users are assigned to the band, interfering signals were experienced during the measurements. The interference sources can be divided into two categories:

The first category consists of onboard equipment which can act as an interferer. Despite operating in a different frequency range, these systems introduce electromagnetic wideband interference. The most critical example is the onboard distance measuring equipment (DME) transponder. It operates in the frequency band from 1025 to $1150\,\mathrm{MHz}$ and has a typical maximum transmit power of up to $60\,\mathrm{dBm}$ ($1\,\mathrm{kW}$) [22]. The channel sounding signal is received with a power level between -60 to $-105\,\mathrm{dBm}$. Despite the large frequency separation, the high transmit power of the onboard DME usually saturates the receiver's LNA as the input low noise bandpass filter cannot completely suppress the out of band radiation caused by the DME. Fig. 5.9 shows a typical example for the DME wideband interference on the channel sounding signal. The DME signal has a very low duty cycle of about 3% leading to a corruption of only a small part of the measured data that can be easily detected as described in Sec. 4.3.

The second category of interferers is the same frequency for transmissions as the measurements. These interferers might be of military origin, e.g., Joint Tactical Information Distribution System (JTIDS) [22]. A closer investigation of such interferers is difficult as their origin is normally unknown. Nevertheless, a basic characterization of the in-band interferers can be done using data collected during all flights. Most of the observed interfering signals occupy a bandwidth smaller than $15\,\mathrm{kHz}$ and their total power is typically more than $10\,\mathrm{dB}$ below the channel sounding signal's receive

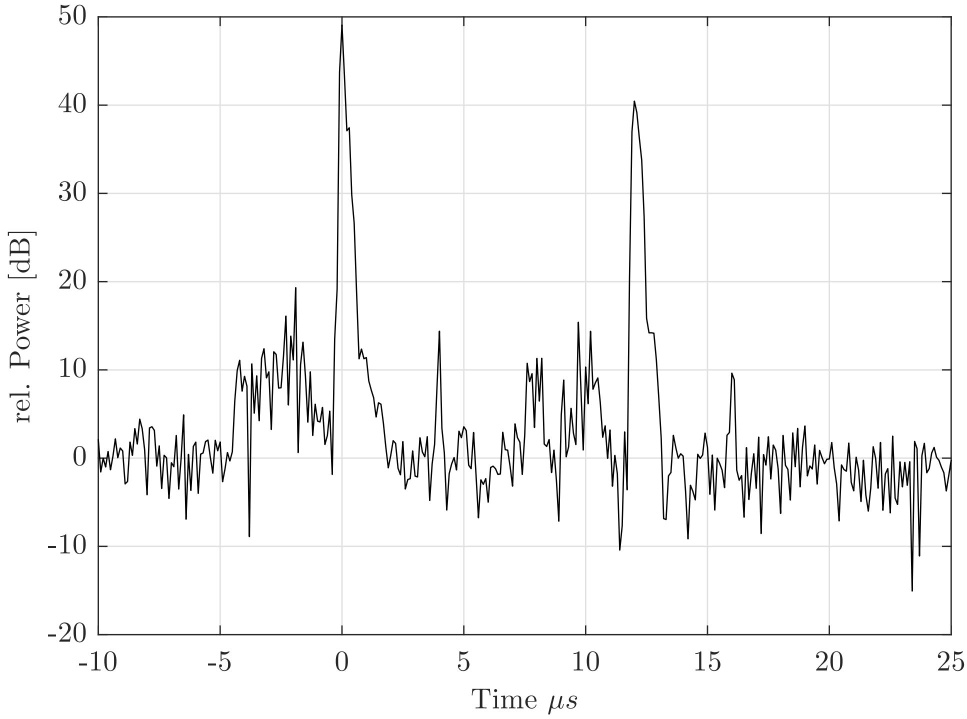

Figure 5.9. *Typical DME wideband interference. The power is normalized to the channel sounding signal power. The spacing between the two pulses is* 12 µs *which matches the DME pulse spacing for in the X channel.*

power. Due to the low power and the high correlation gain of the channel sounding sequence, we deem their influence on the channel measurements as negligible.

5.3 Flight Routes

In this section we describe the different flight routes used for measuring the AG channel in November 2013. Hereby, we focus on flights during which a 10 MHz channel sounding sequence was emitted from the ground station. During the measurements two flights were conducted on November 14th and 20th. The total flight time is 3:31 h. The flight tracks and range-altitude plots of the flights are shown in Fig. 5.11 through Fig. 5.11. The position of the ground station is marked by a cyan cross.

Apart from 10 MHz measurements, six other flights were conducted using different variations of an L-band Digital Aeronautical Communication System (LDACS) communication signal. Those flights took place in November of 2012 and 2013 and are described in [101]–[104]. Parts of the LDACS measurement data is used in Chapter 7 for the validation of the channel model proposed in this dissertation.

Flight 1: November 14th 2013

The aircraft flies around the ground station at a link distance of up to $50\,\mathrm{km}$. Each orbit is done at altitude levels from $3\,\mathrm{km}$ to $9\,\mathrm{km}$ AMSL. The altitude transitions between the orbits are executed on circular trajectories in the north-west of the ground station.

Flight 2: November 20th 2013 - Part 1

Three missed approaches are flown at very low altitudes of $30\,\mathrm{m}$ to $330\,\mathrm{m}$ AGL. Hereby, we experience very strong banking angles of up to $45°$.

Flight 2: November 20th 2013 - Part 2

The aircraft ascends to cruising altitude and accelerates to cruising speed flying on a straight northward course. The course is held until the ground station disappears behind the radio horizon. At a distance as of $450\,\mathrm{km}$ the aircraft turns around and returns to the ground station. During the first half of the cruise the aircraft's altitude is $11\,\mathrm{km}$, whereas on the way back it travels at $9\,\mathrm{km}$ AMSL. At at distance of $200\,\mathrm{km}$ the aircraft begins its final descend towards the airport. Due to the large distance, the aircraft is usually seen at a very low elevation angle from the ground station.

5.3.1 Flight 1: November 14th 2013

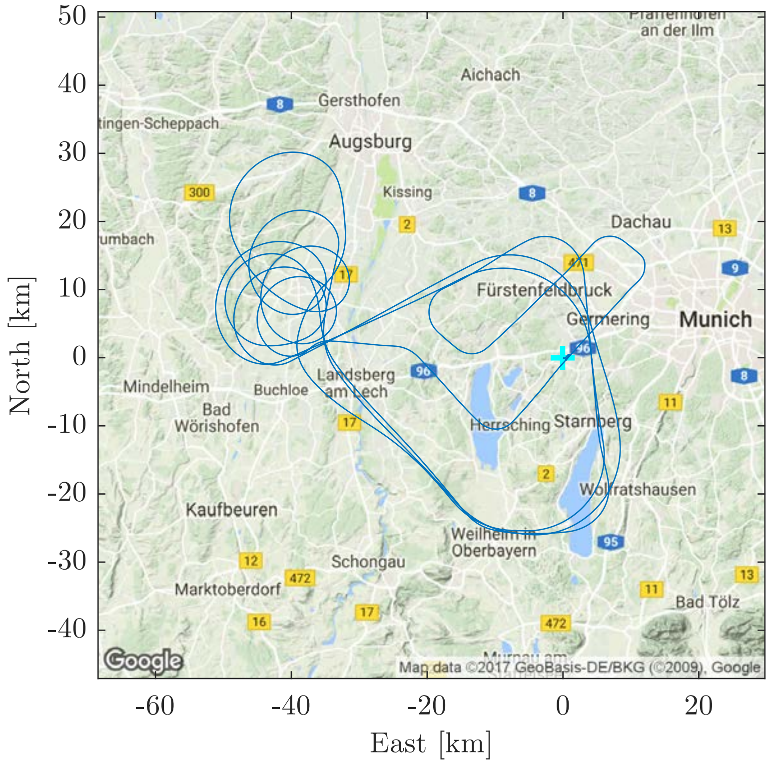

Figure 5.10. *Flight route on the November 14th 2013.* ©*Google*

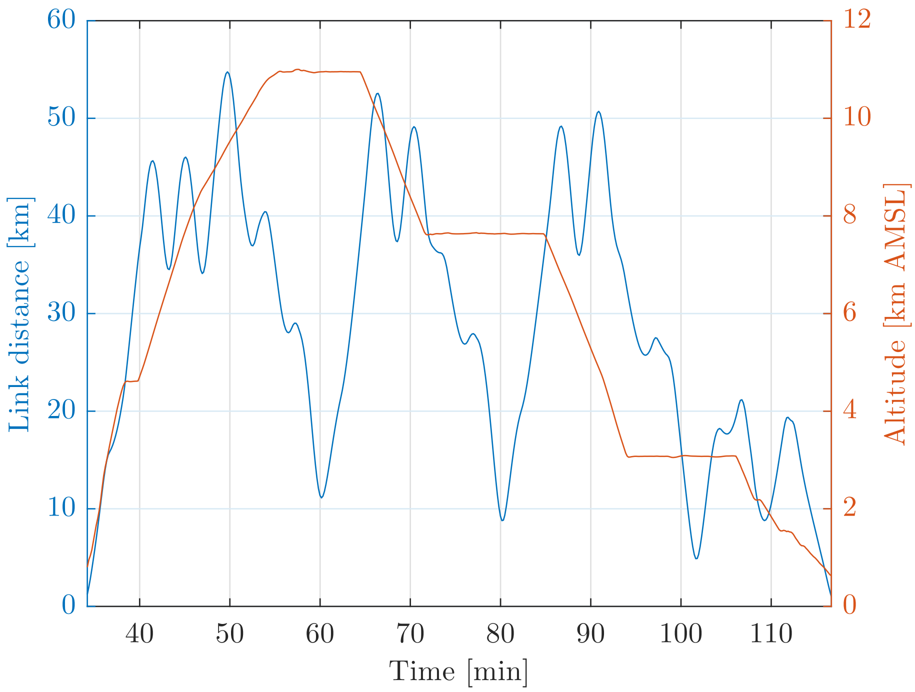

Figure 5.11. *Flight route on the November 14th 2013.*

5.3.2 Flight 2: November 20th 2013 - Part 1

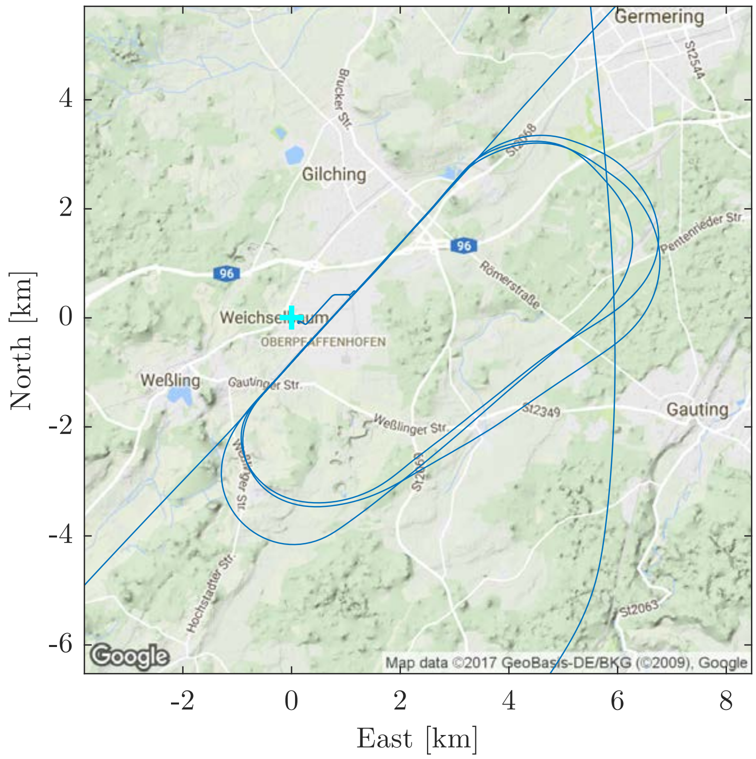

Figure 5.12. *Flight route on the November 20th 2013 (1st part).* ©Google

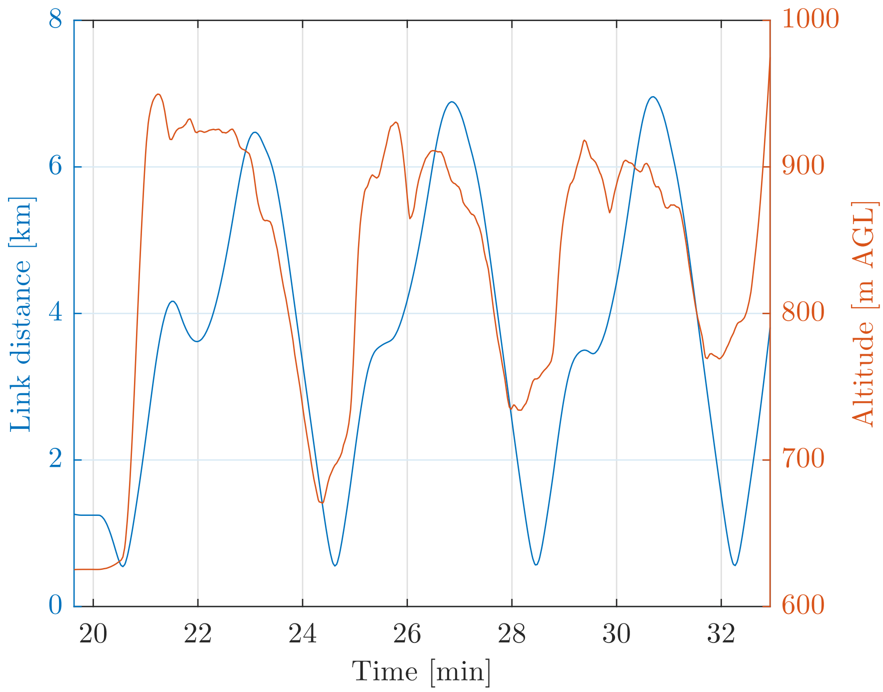

Figure 5.13. *Flight route on the November 20th 2013 (1st part).*

5.3.3 Flight 2: November 20th 2013 - Part 2

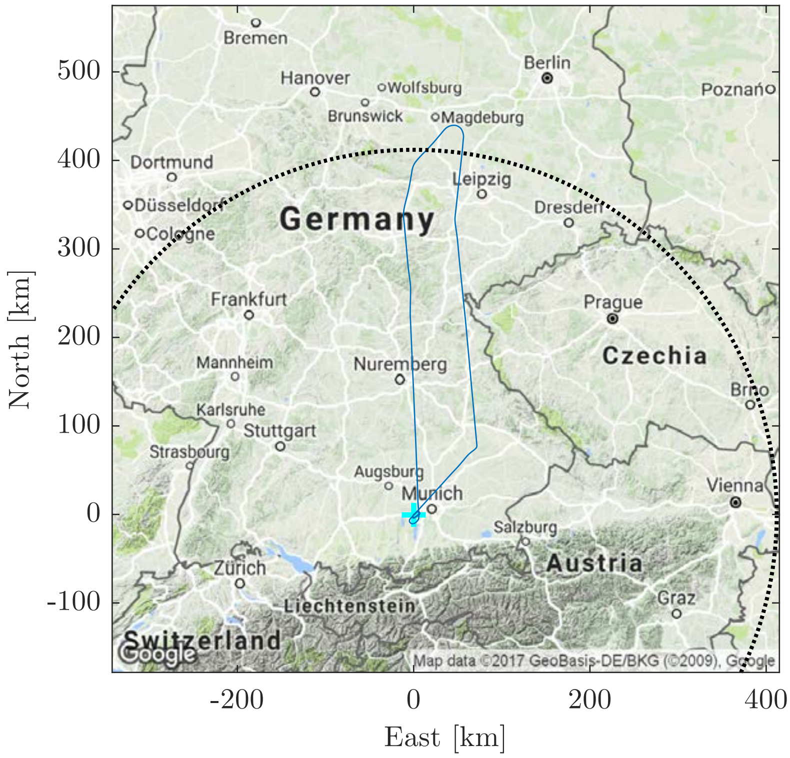

Figure 5.14. *Flight route on the November 20th 2013 (2nd part). The radio horizon (aircraft altitude of* 10 km*) is marked in black. ©Google*

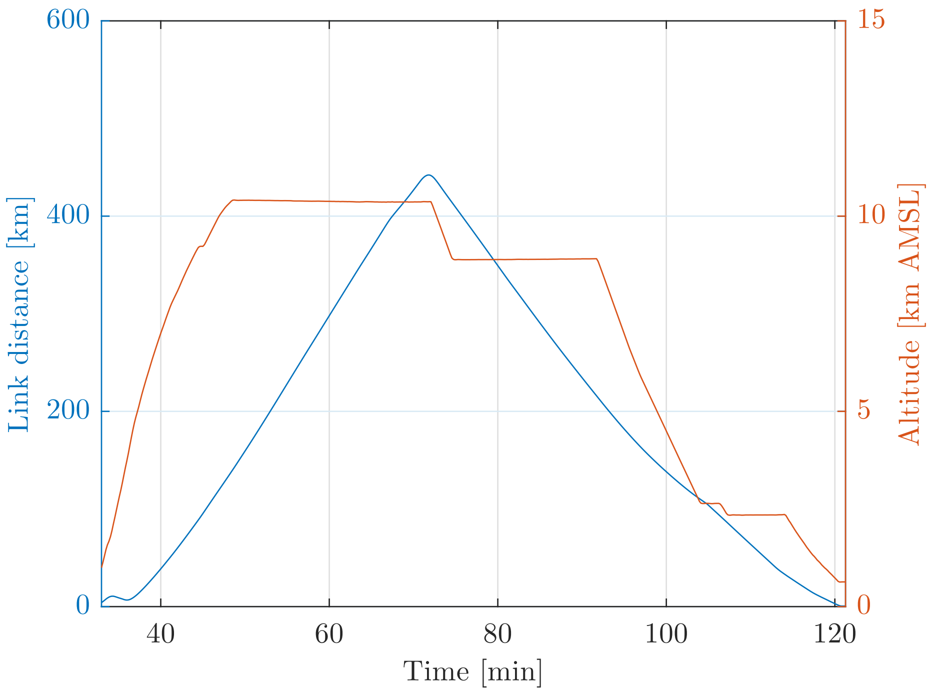

Figure 5.15. *Flight route on the November 20th 2013 (2nd part).*

5.4 Summary

In this chapter we present details on the channel sounding flight experiments conducted as part of this dissertation. We discuss the employed hardware setup, synchronization concept, calibration procedures, and investigated flight patterns.

The main challenge when designing the setup is to guarantee time synchronization between ground station and aircraft. This synchronization is required as we aim to investigate also navigation systems where absolute path lengths matter (in communication systems taking the MPC parameters relative to the LoS signal parameters is usually sufficient). The synchronization is achieved by relating both atomic clocks to an absolute time basis, in our case GPS time. The method is able to provide sub-nanosecond accuracy when using a post-processed GPS solution. As we can relate each recorded sample to GPS time, we are able to determine the exact time offset between each sample of the calibration and measurement. This allows the calculation of absolute propagation path lengths. Note that using high-end GNSS receivers, i.e., multi-frequency, multi-constellation, the same method can essentially be used to provide real-time synchronization between a geographically separated stations down to a few nanoseconds.

Another challenge is the determination of a precise ground truth: using an INS the exact position of the antenna used for channel sounding can be calculated. The effects of the troposphere can be well mitigated using a model from literature.

A regulatory challenge is the hardware certification process of the setup into the aircraft. This process has to be finished weeks before the flight trials. After the certification is completed the setup cannot be altered anymore. Conservative and stringent time planning is mandatory for the success of flight trials.

Overall we can conclude that the setup is suitable for investigating both multipath structure and absolute propagation time of the radio signals in the AG channel. The presented measurement system allows to setup to be used also for other frequency bands with only minor modifications in all kind of different environments. The achieved accuracy of the synchronization and the ground truth also is well suited for measurements with higher bandwidths.

CHAPTER 6

MEASUREMENT RESULTS

Contents

6.1 Overview

In Chapter 4 we described algorithms to analyze the propagation characteristics of the air-ground (AG) channel. In this chapter we apply these algorithms to the channel sounding data collected as described in Chapter 5. We start by providing using results on the line-of-sight (LoS) signal power in Sec. 6.3. We then present results on the statistical properties of the channel in Sec. 6.4, the estimation of the multipath component (MPC) parameters in Sec. 6.5, and the localization of the reflectors causing MPCs in Sec. 6.6. Results presented in this chapter are then used in Chapter 7 for the parameterization of the channel model to an regional airport environment.

In the following we use a block size of $I = 125$. Hence, the channel and MPC parameters are estimated with a rate of $15.625\,\mathrm{Hz}$. During one block the link distance changes on average by $7.3\,\mathrm{m}$ or 24 multiples of the wavelength. The estimation rate also defines the physical Doppler frequency resolution of $15.625\,\mathrm{Hz}$. We assume the channel to be stationary over the duration of the block.

Parts of the results in this chapter have been published in [11], [20] and submitted for publication to [10].

6.2 Definition of Flight Scenarios

The propagation characteristics of the AG channel strongly depend on the underlying geometry, i.e., aircraft altitude, speed, and distance to the ground station. From the total measurement duration of 3:31 h we select three scenarios to be representative for the different phases of the flight shown in Fig. 6.1. The selection of those three scenarios allows the analysis of the AG channel in the dependence of the underlying geometry:

The three scenarios are:

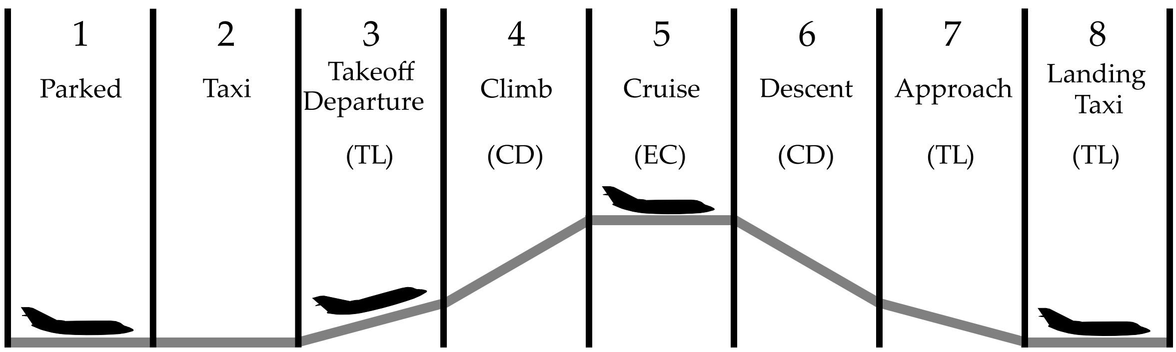

Figure 6.1. *Phases of flight according to [105].*

Table 6.1. *Parameters of the investigated flight scenarios*

Scenario	TL	CD	EC
Duration [min]	15	44	16
Rx-Tx dist. [km]	$0.5 - 7.3$	$20 - 80$	$80 - 250$
mean	4	37	186
Speed [m/s]	$63 - 106$	$127 - 222$	$192 - 235$
mean	88	171	214
Altitude [m/km]	$30 - 315$	$3 - 9$	$8 - 10.4$
mean	186	6.4	9.7
	[m] AGL	[km] AMSL	[km] AMSL

- *Takeoff & landing (TL):* We simulate takeoff, approach, and landing by flying three missed approaches at low altitudes of $30\,\mathrm{m}$ to $330\,\mathrm{m}$ above ground level (AGL). Each missed approach is followed two steep $180°$ turns (banking angles of up to $45°$) - see flight 2 (part 1) Sec. 5.12. We additionally consider the take takeoff and landing from flight 1 into account - see Sec. 5.10.

- *Climb & descent (CD):* The aircraft ascends and descends at distances of up to $50\,\mathrm{km}$ at altitude levels from $3\,\mathrm{km}$ to $9\,\mathrm{km}$ above mean sea level (AMSL). The flight segments for this scenario are mainly taken from flight 1 - see Sec. 5.10. Two shorter segments from flight 2 (part 2) are also considered.

- *Enroute cruise (EC):* The aircraft travels at a large distance from the ground station at normal cruising speed. During the first half of the trip the aircraft's altitude is $10.4\,\mathrm{km}$, whereas on the way back it travels at $8.9\,\mathrm{km}$ AMSL. The flight segments of the EC scenario are taken from flight 2 (part 2) described in Sec. 5.14.

The key flight parameters for each scenario are summarized in Tab. 6.1.

6.3 Line-of-Sight Signal Power

In the following we provide results on the LoS signal power. By the LoS signal power we understand the power received in the first delay bin: in most situations the signal in the first delay bin does not only consist of the LoS signal, but also, due to its short excess delay relative to the reciprocal of the signal bandwidth, the ground MPC.

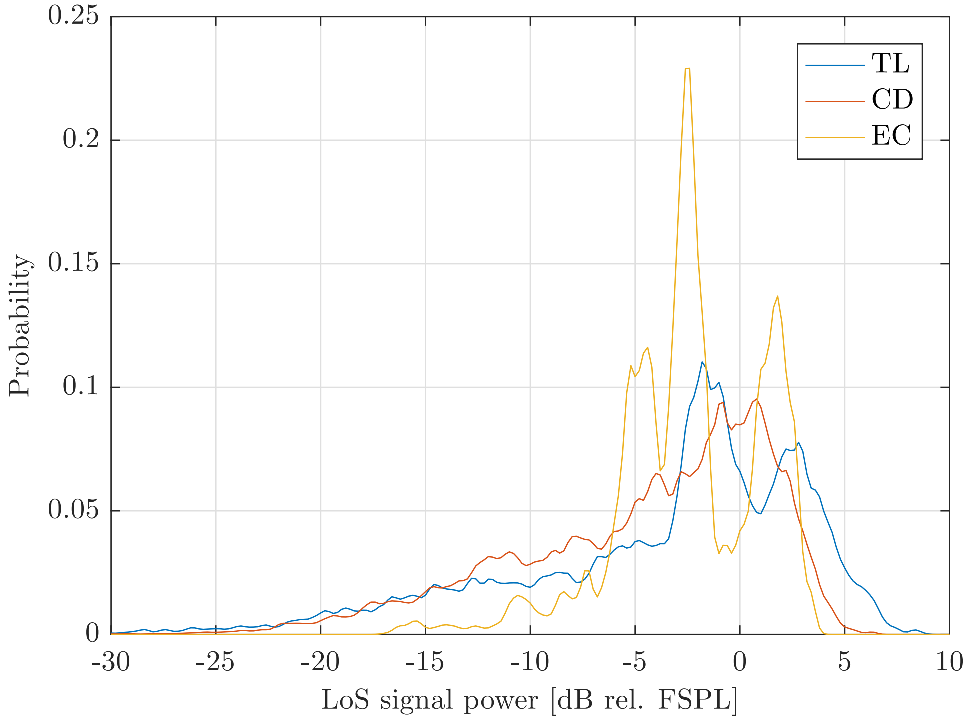

Figure 6.2. *Distribution of the LoS signal power for the three scenarios.*

We start by analyzing the statistical distribution of the LoS signal power in Sec. 6.3.1. The non-stationarity of the AG becomes apparent when we inspect the LoS signal power as a function of the aircraft position in Sec. 6.3.2.

6.3.1 Statistical Distribution

In Fig. 6.2 we show the distribution of the LoS power for the three scenarios. Although being normalized to free space path loss (FSPL), the LoS signal power experiences variations which are mainly caused by two effects.

First, due to the ground reflection described in Sec. 3.3.4: depending on the power of the MPC, the LoS signal can be amplified by $6\,\mathrm{dB}$ or strongly attenuated: maximum fades exceeding an attenuation of $20\,\mathrm{dB}$ are observed, which matches results from other flight trials [59], [67].

Second, the variation of the LoS signal power may be caused by the involved antennas as well as effects due to the airframe as discussed in Sec. 3.3.6 and Sec. B. The antennas themselves are monopoles mounted on a ground plane and have maximum gains of about $4\,\mathrm{dBi}$ - see Fig. 3.5. When the aircraft is banking, the combined gain of both antennas may significantly vary, e.g., more than $10\,\mathrm{dB}$. The airframe may influence the received power due to shadowing, e.g., by a wing during turns, or reflections off parts of the fuselage. As the influence by the airframe and antenna patterns are usually hard to separate, they are often considered jointly as a so called aircraft pattern [106], [107]. Analyzing the locations at which a strong attenuation of the LoS signal appears, show that both effects mentioned above can individually cause attenuation of the LoS signal exceeding $20\,\mathrm{dB}$.

The maximum LoS signal power of $8.8\,\mathrm{dB}$ (relative to FSPL), $6.4\,\mathrm{dB}$, and $4.2\,\mathrm{dB}$ for the scenarios is reasonable considering the maximum antenna gains and a $6\,\mathrm{dB}$ amplification due to ground multipath propagation.

Comparing the results for the three scenarios shows that during the TL the highest variation of the LoS signal power of $23\,\mathrm{dB}$ (90% percentile) is observed. A large part of this variation is attributed to the aircraft pattern: in the TL scenario the aircraft experiences large banking angles; therefore, the elevation angle under which the airborne antenna sees the ground station changes. The result is a strongly varying LoS signal power, as the antenna gain is very sensitive to changes in the angle of arrival. Additionally, the large banking angles introduce shadowing by the airframe.

The CD scenario shows also a high variability of the LoS signal power of about $20\,\mathrm{dB}$ (90% percentile). Hereby, the fading of the LoS signal path can be attributed, mainly to ground multipath and the aircraft patterns.

The LoS signal power variation of $10\,\mathrm{dB}$ (90% percentile) in the EC scenario can be attributed to two effects: firstly, ground multipath propagation leads to variations in the power of the LoS signal. Compared to the other scenarios, due the larger link distance, the resulting geometry leads to fades which last significantly longer in the EC scenario[1]. Secondly, we observe that the LoS signal is received at two distinct power levels. As the aircraft antenna has a different gain in the aircraft's forward and backward movement direction, the two power levels represent the aircraft flying away and towards the ground station.

6.3.2 Non-Stationarity

In the following we analyze the LoS signal power as a function of the aircraft position. The presented results allow us to investigate the effects of ground multipath propagation. The aircraft position is first expressed geographically. Additionally, we investigate the LoS signal power against the angle the aircraft is seen from the ground station.

[1]This fact is important to note, as it is not visible from the statistical distributions shown in Fig. 6.2.

Geographical Position

In Fig. 6.3 we plot the LoS signal power against the aircraft position [20]. To minimize the effects of the airborne antenna we exclude flight situations where the aircraft is turning steeply.

From Fig. 6.3 we notice that the ground MPC is not always present: when the aircraft is flying on a trajectory straight north a periodic variation of the LoS signal power can be observed. This variation is a clear indicator of the presence of one ground MPC and the resulting the 2-ray effect. However, on a similar straight trajectory in the northeast of the ground station no variation of the power is observed. No ground MPC is present: the ground MPC may either be shadowed, e.g., by a building, or is of very weak power, e.g., due to a poorly reflecting ground surface.

Apart from the periodic variation of the LoS signal power, a second effect can be observed: when the aircraft is flying on an orbit around the ground station fades may last for a long duration. A part of the LoS signal attenuation can most likely be attributed to ground multipath propagation - see Sec. 2.3.1. However, as we show in App. B, the aircraft pattern adds another significant contribution to the fading. Unfortunately, an approximation of the degree each of the two effects contribute to the fading is not possible with the available data.

Angular Position

In Fig. 6.4 we show LoS power against the aircraft position in the angular domain[2] (as seen from the ground station). The LoS signal power is color coded using the same coding as in Fig. 6.3.

Similarly to Fig. 6.3, Fig. 6.4 visualizes the non-stationarity of the channel: fades of the LoS power may last for a long duration. Periodic fades of the LoS signal power due to ground multipath propagation or aircraft pattern can be observed. Due to the ground antenna being located on top of a high building no ground shadowing appears (except for the aircraft disappearing behind the radio horizon - marked using an ‘H’).

6.4 Multipath Channel Statistics

In this section we present statistical results describing the multipath structure of the AG channel: results on the distribution of the power delay profile (PDP) in Sec. 6.4.1,

[2] For details on the generation of the calibrated panorama image refer to App. E.

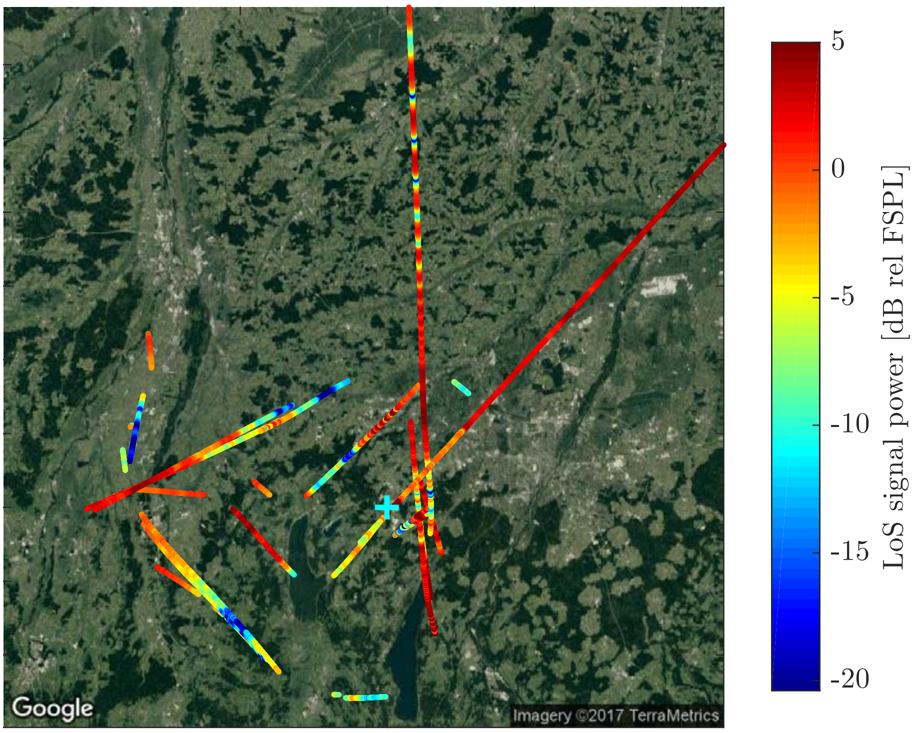

Figure 6.3. *LoS signal power against the geographical aircraft position. ©Google*

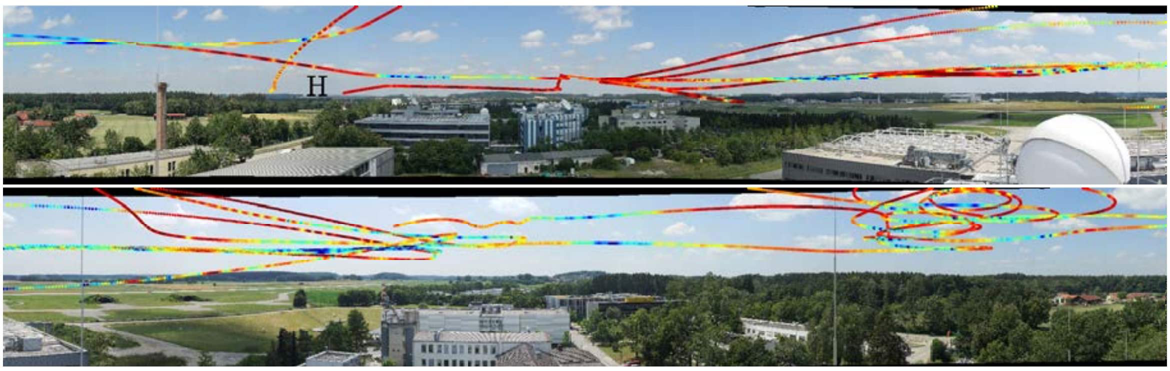

Figure 6.4. *LoS signal power versus aircraft position in the angular domain (as seen from the ground station antenna). The top shows the northern, the bottom the southern hemisphere.*

of the Doppler power profile (DPP) in Sec. 6.4.2, and of the root-mean-square (rms) delay spread in Sec. 6.4.3.

6.4.1 Power Delay Profile

In Fig. 6.5 we show the distribution of the power over the excess delay (relative to the LoS signal delay τ_{LoS}), i.e., the distribution of the PDPs, for the three scenarios. The plots are generated by using all PDPs measured during one scenario: based on the selected PDPs we estimate the distribution of the power in each delay bin using a Gaussian kernel smoother [108]. The probability in Fig. 6.5 is color coded using a logarithmic scale. The received power is normalized to FSPL.

We can make the following observations: with an increasing link distance, a decreasing number of different MPCs is received. However, the remaining individual MPCs become more distinct and have a higher probability. With increasing distance the variation of the elevation angle, under which the aircraft is seen by the ground station, becomes smaller. The result is a smaller variation of the geometry, i.e., reflectors causing MPC stay in view for a longer time. As the Doppler frequency is proportional to the derivative of the delay, a large distance results in MPCs with small excess Doppler frequencies as shown in Sec. 6.4.2.

In the TL scenario the signal power distribution indicates the existence of numerous propagation paths, both distinct and diffuse. The most likely explanation is the small link distance causing the continuously changing geometrical relations under which the ground antenna and its surroundings are seen. Compared to the other scenarios, the power decays the slowest: at an excess delay of $4\,\mu\mathrm{s}$ the power is still significantly above the noise floor which might result from a higher signal-to-noise-ratio (SNR) due to the smaller distance.

In the CD scenario we observe more MPCs but fewer distinct ones. Compared to the EC scenario the distribution is more spread. A larger spread means that the channel's multipath structure exhibits larger variations which may be explained by the more rapid changes of the geometry compared to the EC scenario.

In the EC scenario, only distinct peaks can be seen. The sharp peaks indicate that each path is visible for a long time period. However, it is important to note that the higher noise level may shadow weaker MPCs.

6.4.2 Doppler Power Profile

In Fig. 6.6 we show the distribution of the power over the excess Doppler frequency (relative to the Doppler frequency of the LoS signal ν_{LoS}), i.e., the distribution of the

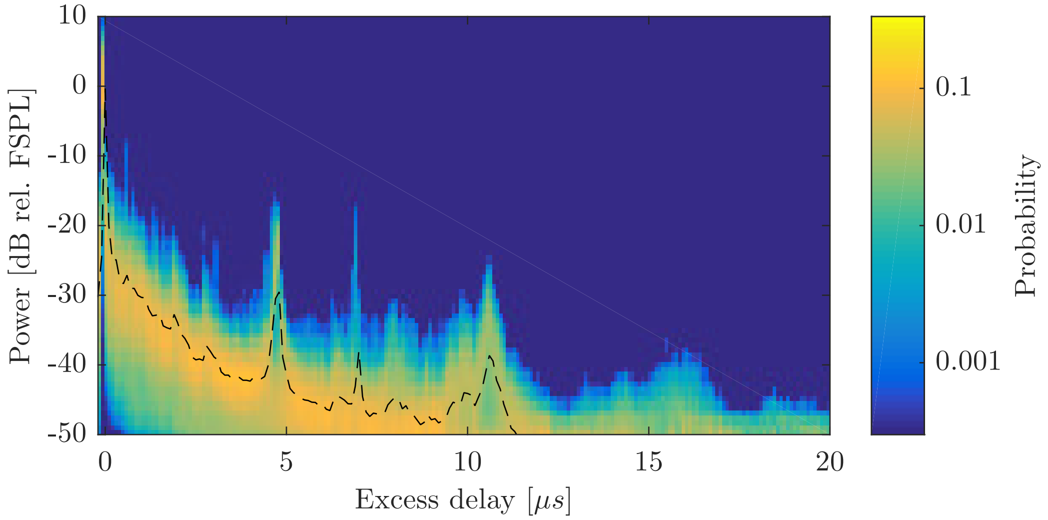

(a) *Takeoff & landing (TL)*

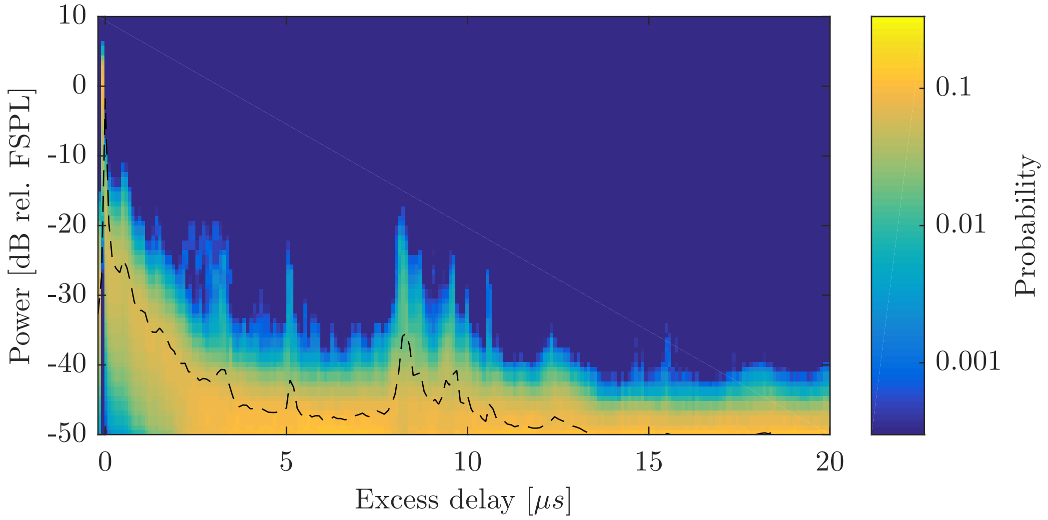

(b) *Climb & descent (CD)*

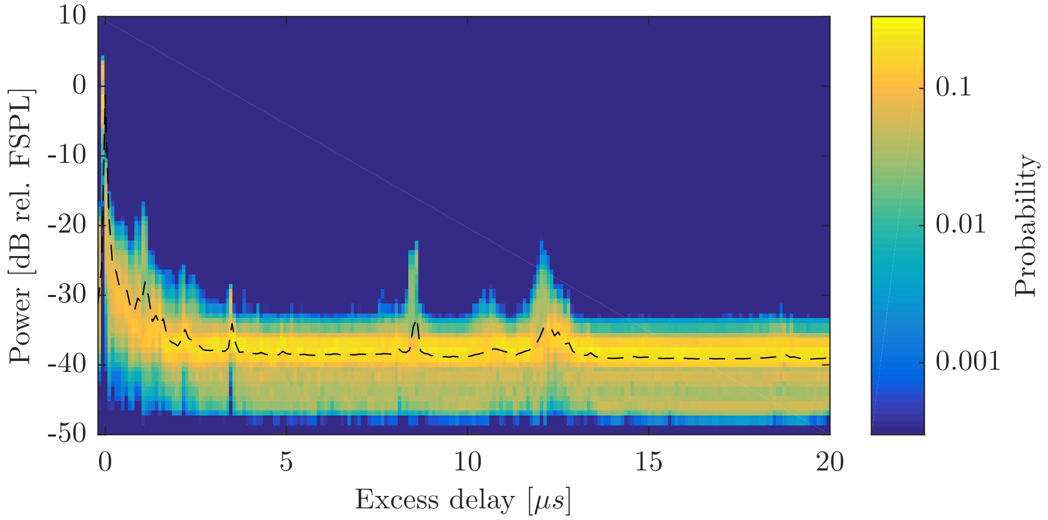

(c) *Enroute cruise (EC)*

Figure 6.5. *PDP for the investigated scenarios.*

Table 6.2. *rms delay spreads for the investigated scenarios.*

Scenario	EC	CD	TL
Mean [ns]	613	413	315
Median [ns]	526	322	242
Max [ns]	3198	3508	1517
Std. dev. [ns]	348	290	243

DPPs, for three scenarios. The Doppler frequency of a MPC describes the angle from which the MPC is received (relative to the aircraft movement direction and speed). As for Fig. 6.5, the probability is color coded using a logarithmic scale. The received power is normalized to FSPL.

From Fig. 6.6 the following observations are made:

For an aircraft flying in close proximity of the ground station, as in the TL scenario, a significant contribution of power on Doppler frequencies other than the one of the LoS signal is observed, and therefore, components are received from all directions. This result is intuitive, as the aircraft flies at very close distance to the ground station's scattering environment. Thus, the aircraft observes the reflectors under a variety of different angles of arrival. The maximum excess Doppler of $580\,\mathrm{Hz}$ matches well to the largest possible excess Doppler frequency of $660\,\mathrm{Hz}$, determined by the maximum speed of the aircraft of $105\,\mathrm{m/s}$.

In the CD scenario, the power is mostly received at the same Doppler frequency as the LoS signal.

In the EC scenario, all propagation paths arrive with the same Doppler frequency as the LoS signal. Equivalently, we can conclude that MPCs are seen under the same angle of arrival as the LoS path as they originate most probably from objects in the direct surrounding of the ground antenna. This conclusion can be later verified in Sec. 6.6 using the reflector localization algorithm.

6.4.3 Mean Delay and Delay Spread

The rms delay spread is a standard measure to describe the dispersiveness of a channel. In Fig. 6.7 we show the distribution of the rms delay spread for each scenario. The mean, median, maximum, and standard deviation of the rms delay spread is summarized in Tab. 6.2. For the calculation of the results we only consider signal components exceeding the 99% noise quantile as described in Sec. 4.4.3

The presented results confirm the observations from the PDP results in Fig. 6.5:

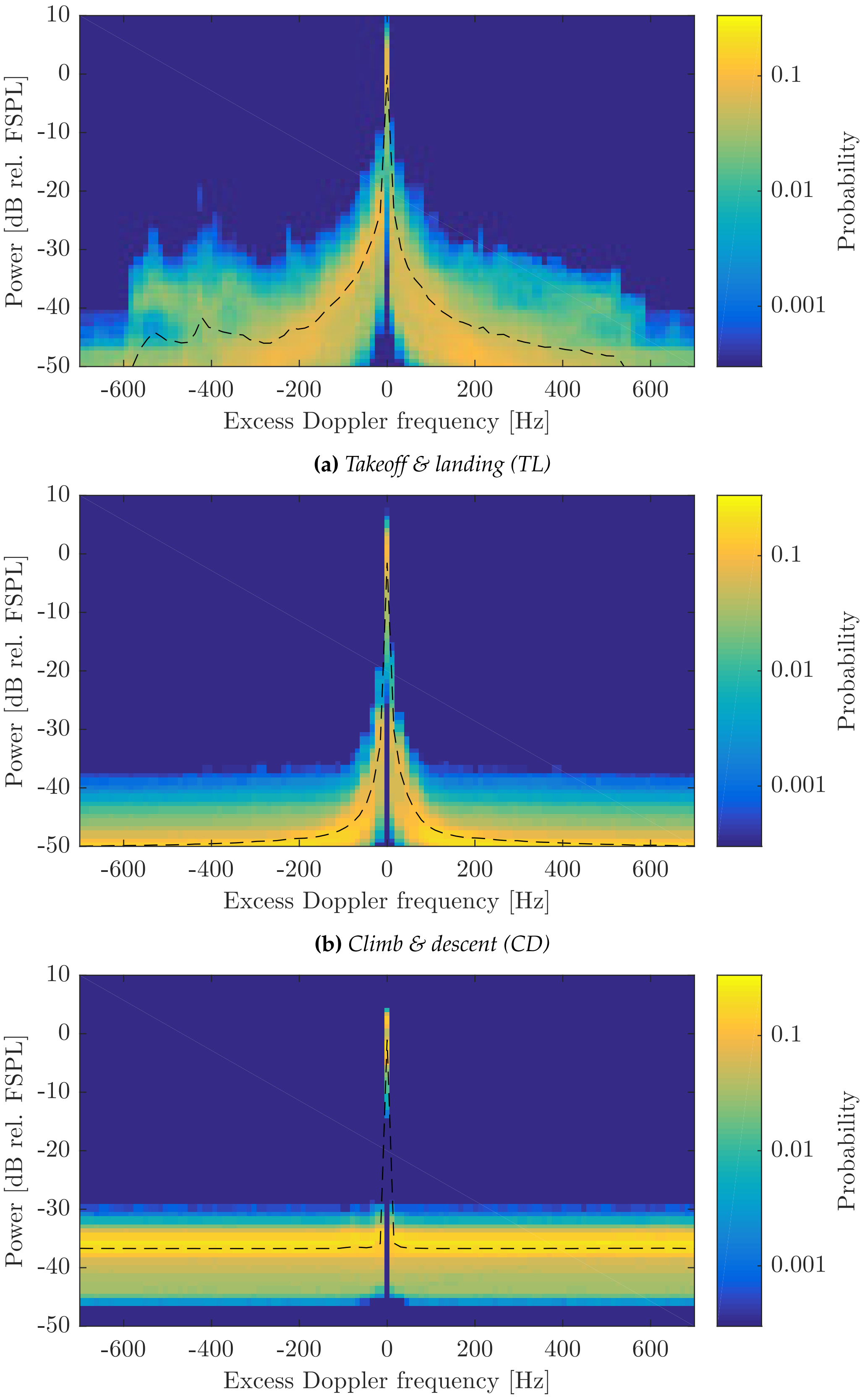

(a) *Takeoff & landing (TL)*

(b) *Climb & descent (CD)*

(c) *Enroute cruise (EC)*

Figure 6.6. *DPP for the investigated scenarios.*

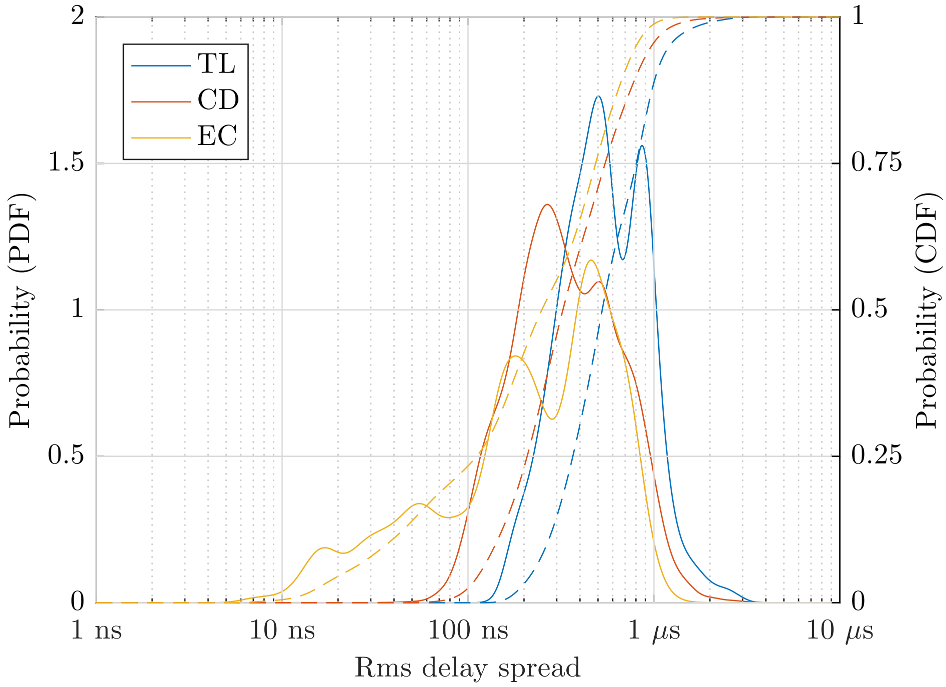

Figure 6.7. *PDF (solid line) and CDF (dashed line) of rms delay spread for the investigated scenarios.*

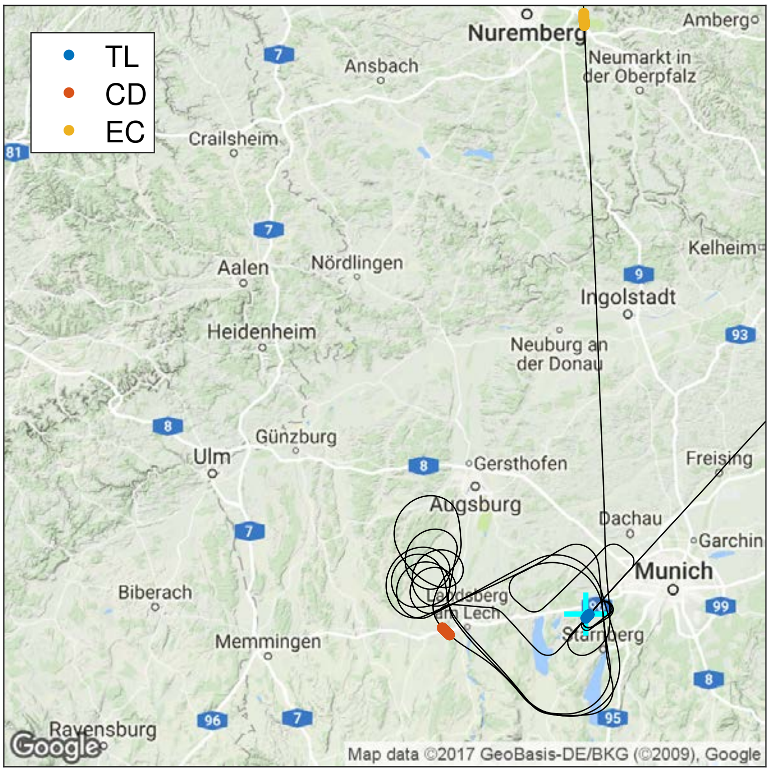

Figure 6.8. *Flight segments analyzed to generate the results in Fig. 6.9 and Fig. 6.10 (map dimensions* 250 km × 250 km*). ©Google*

for a increasing link distance the power of the MPC decreases. Thus, also the rms delay spread decreases. Nevertheless, part of the decrease of the rms delay spread may also be attributed to the decreasing SNR: MPCs may be shadowed by the rising noise floor

6.5 Multipath Component Parameter Estimation Algorithm

In the last section, we described the key statistical properties of the AG channel. These statistical properties allow a quantitative characterization of the channel. In this section, we proceed to a qualitative characterization, analyzing the variations of the AG channel over a shorter duration. To this end we show the results of the parameter estimation for the three scenarios: the results demonstrate the performance of the MPC parameter estimation algorithm described in Sec. 4.5.

For the parameter estimation, the noise quantile thresholds for adding and removing MPCs are set to $Q_{\mathrm{add}} = Q_{\mathrm{rm}} = 0.99$. State variances in $\underline{\boldsymbol{Q}}$ are chosen heuristically according to the flight dynamics experienced during the flight.

For the generation of the results presented in the following the flight segments shown in Fig. 6.8 are used. Each $15\,\mathrm{s}$ segment is chosen as a representative example of the three scenarios defined Sec. 6.2. We mark the ground station location by a cyan cross.

In Fig. 6.9 and Fig. 6.10 we present results of the MPC parameter estimation algorithm (output of the information filter). The power relative to FSPL is color coded.

From both Fig. 6.9 and Fig. 6.10 we observe the time variant behavior of the channel becomes apparent: the parameters of the existing MPCs exhibit a strong correlation over time. Each of the MPCs, visible as a horizontal line can be associated with a reflecting object, e.g., a building, using the reflector localization algorithm.

6.5.1 Power

In all scenarios the LoS signal, i.e., the signal in the LoS delay bin, is clearly the most powerful signal. This result is in line with the results presented in Sec. 6.4.

Comparing the results for the scenarios in Fig. 6.9 the increasing speed of channel variations for an increasing link distance become apparent: in the EC scenario the propagation conditions remain very stable: the power $|\alpha|^2$ of the MPCs are almost constant. However, with a decreasing link distance these power variations occur

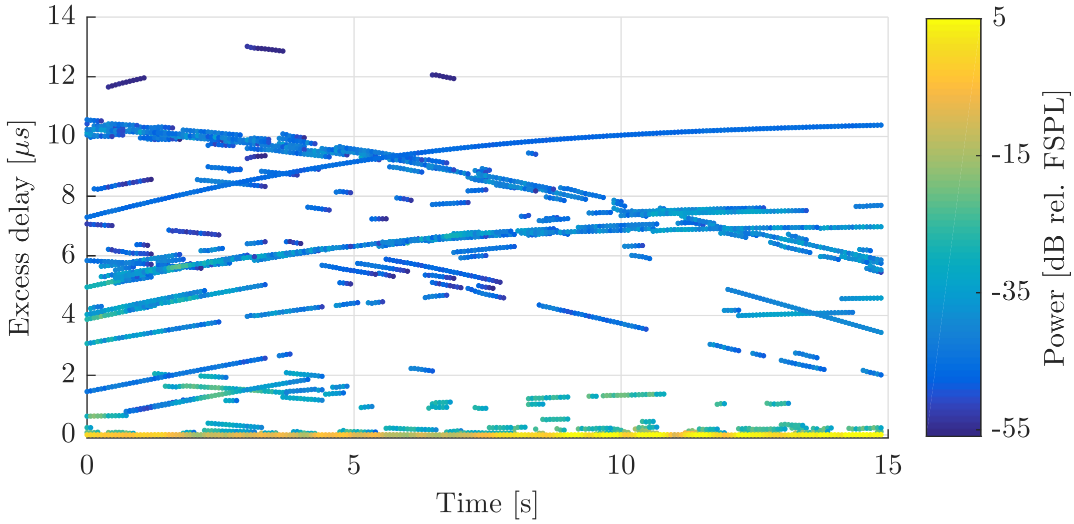

(a) *Takeoff & landing (TL)*

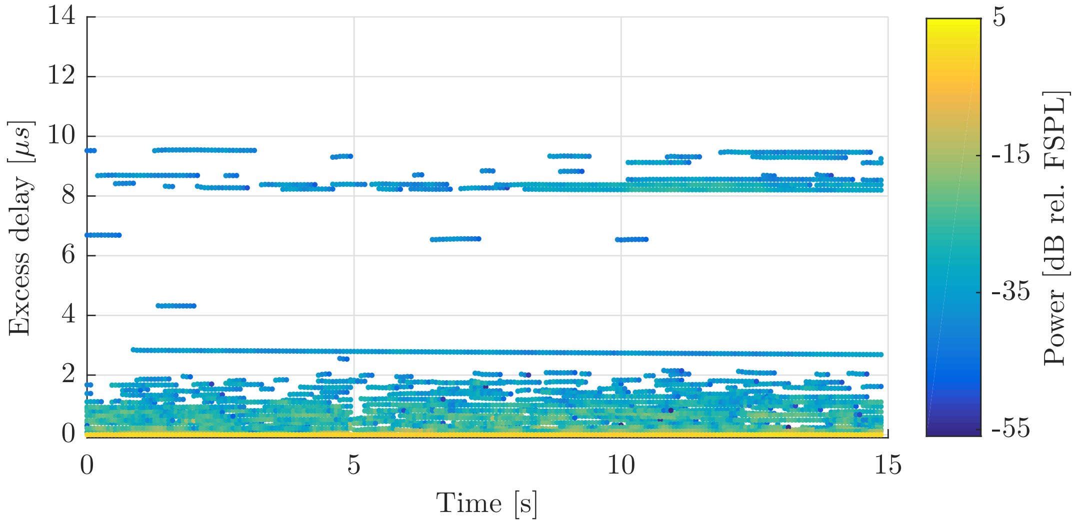

(b) *Climb & descent (CD)*

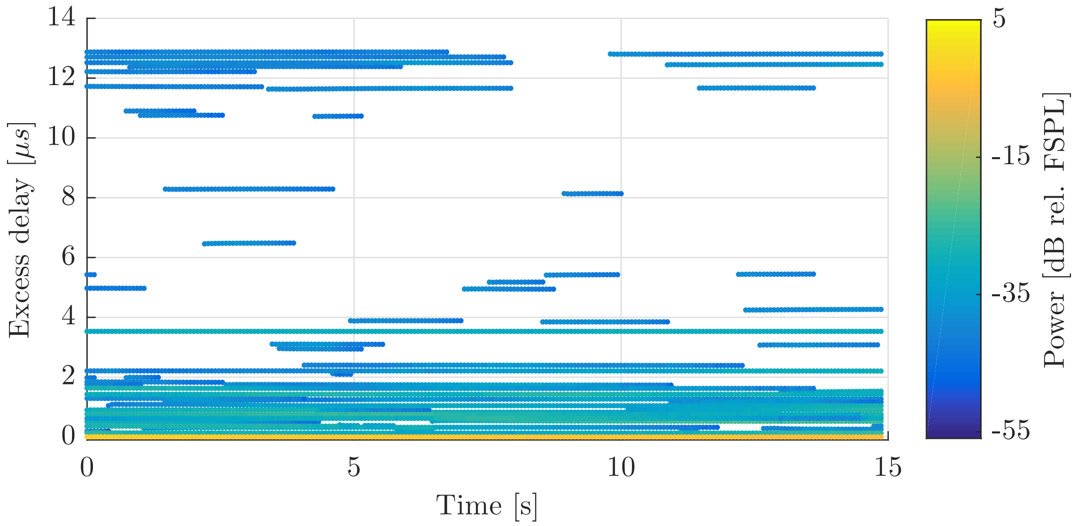

(c) *Enroute cruise (EC)*

Figure 6.9. *Estimated excess delay of the detected MPC.*

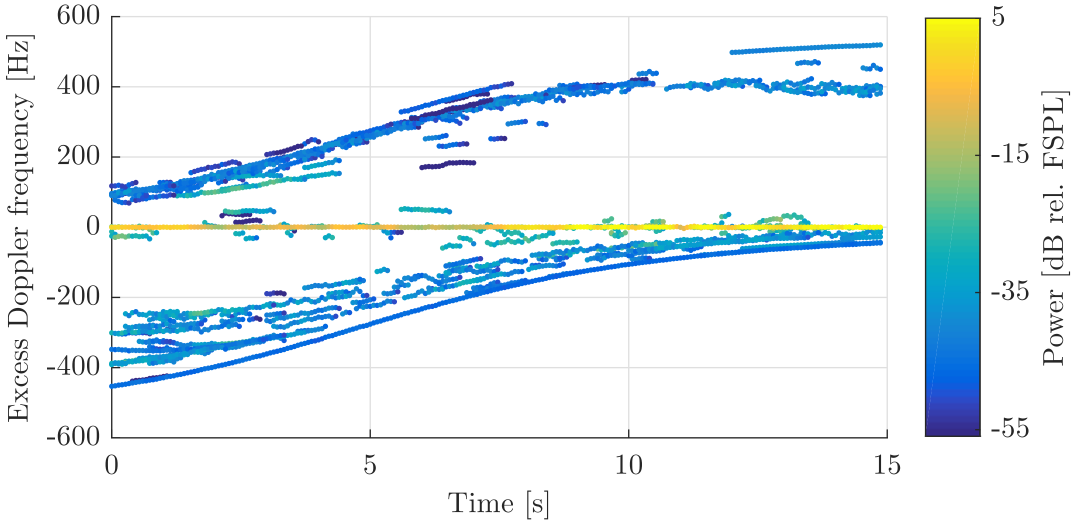

(a) *Takeoff & landing (TL)*

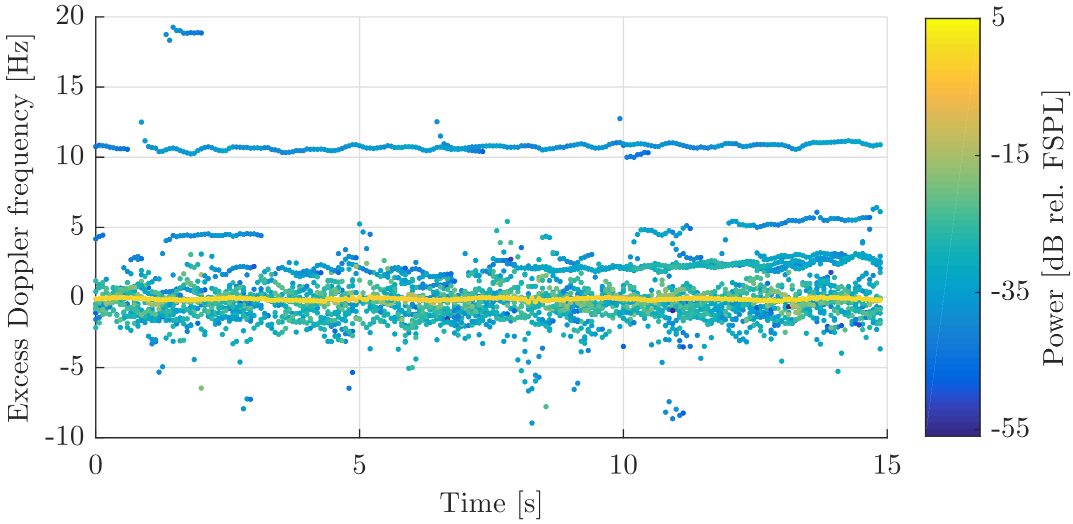

(b) *Climb & descent (CD)*

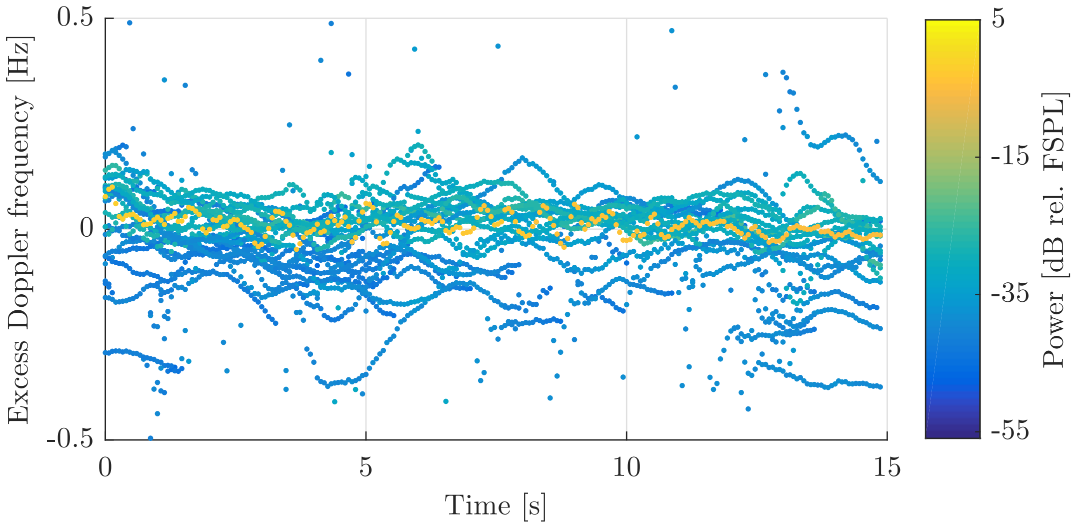

(c) *Enroute cruise (EC)*

Figure 6.10. *Estimated excess Doppler frequency of the detected MPC.*

more rapidly: in both the CD and TL scenario the power $|\alpha|^2$ of an MPC may change by more than $20\,\mathrm{dB}$ within a second.

This increasing variation of the power $|\alpha|^2$ can be explained as follows: as we will later show in Sec. 6.6, reflectors causing MPCs are almost exclusively located in the near surrounding of the ground station, i.e., less than $5\,\mathrm{km}$ away from the ground station. If the aircraft is traveling at a large distance, the reflection point on the reflecting object moves slowly: thus, the power variations associated with the unevenness of an object also occur slowly. When the aircraft gets closer to the ground station the reflection point moves faster on the reflecting surface resulting in a faster power variation.

6.5.2 Delay Estimation

The excess delay also experiences faster variations for a decreasing link distance. While in the EC scenario the excess delay of each MPC remains almost constant, in the TL scenario the excess delay changes rapidly: changes of the excess delay in the order of $50\,\mathrm{ns\,s^{-1}}$ are not unusual.

The more rapid variations of the excess delay are again a result of the geometry: as shown later in Sec. 6.6 the reflectors causing MPCs are located in the close surrounding of the ground station. If the aircraft is far away, both the distance to the reflector and to the ground station change in an almost identical fashion. Thus, the excess delay of an MPC (relative to the LoS signal delay τ_{LoS}) only changes slowly. However, for an aircraft traveling in the close surrounding of the ground station, as in the TL scenario, the geometry is very different: one reflector might be located behind the aircraft while the ground station is located in front of the aircraft. While the distance to the reflector is increasing, the distance to the ground station decreases. Thus, also the excess delay of the MPC changes completely differently.

6.5.3 Doppler Frequency Estimation

The differences for the three scenarios in terms of the MPCs' excess Doppler frequencies become apparent when observing the scaling of the y-axis. In the TL scenario the maximum excess Doppler frequency is $520\,\mathrm{Hz}$. In comparison, in the EC all MPCs have essentially the same excess Doppler frequency. These results are in line with the results presented in Sec. 6.4.2. However, due to the super-resolution property of the parameter estimation algorithm we are able to analyze Doppler frequencies much more accurately: we are able to resolve the Doppler frequency down to a fraction of a Hertz. This resolution is far more accurate than the physical resolution of the signal of $15.6\,\mathrm{Hz}$ used for the generation of Sec. 6.4.2.

The increasing similarity in terms of the MPC excess Doppler frequencies for an increasing distance can be explained similarly as above in Sec. 6.4.2: seen from far away, reflectors causing MPCs are seen under almost the identical angle as the ground station. Thus, the MPCs' Doppler frequencies is also very similar to the LoS signal Doppler frequency ν_{LoS}.

6.6 Localization Algorithm

We now use those estimated MPC parameters in the reflector localization algorithm described in Sec. 4.6.

For every MPC u we calculate one reflector location PDF $p_{\mathrm{C}u}\left(\boldsymbol{g}\right)$. We first use a coarse grid of $25\,\mathrm{m}$ to calculate the support of the reflector location PDF $p_{\mathrm{C}u}\left(\boldsymbol{g}\right)$. The actual reflector location PDF $p_{\mathrm{C}u}\left(\boldsymbol{g}\right)$ is then calculated on a finer grid using a grid size of roughly $50\,\mathrm{cm}$. The result is then re-integrated back to a larger grid.

During the analyzed measurements, due to its altitude, the ground antenna is higher than all possible reflectors. Thus, the majority of MPCs is most likely caused by double-bounce reflections with one of the reflections being a reflection off the ground plane. However, due to the underlying geometry (usually small height of the ground station over the ground plane compared to the distance between reflector and ground station), the first reflection only adds a very small delay to the total MPC delay. Thus, in the vast majority of cases, the assumption of a single bounce reflection only leads to insignificant errors.

In following we only show lateral MPCs. The ground MPCs, due to their short delay τ relative to the reciprocal of the signal bandwidth can generally not be detected by the MPC parameter estimation. Thus, the origin of ground MPCs cannot be localized.

Results on single reflector PDFs are presented in Sec. 7.2.3; for a statistical description of the reflector locations refer to Sec. 7.2.3.

6.6.1 Single Reflector Probability Density Function

In Fig. 6.11 we show results on the localization of typical reflectors.

For each reflector we show both the satellite image as well as a photograph taken from the ground antenna location. The PDF indicating the location of the reflector is color coded covering a range of $20\,\mathrm{dB}$. We normalize the color coding to the max-

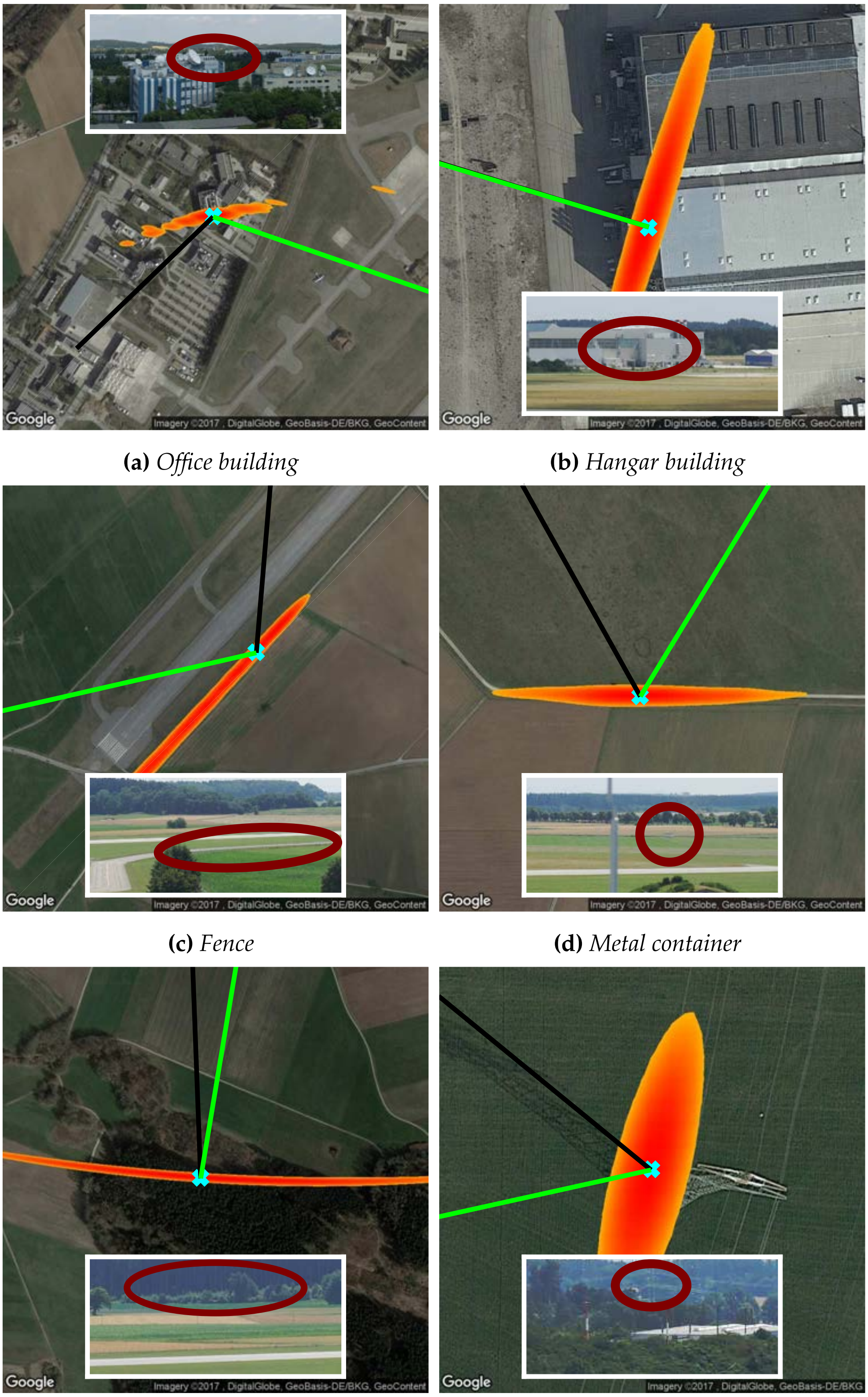

(a) *Office building* **(b)** *Hangar building*

(c) *Fence* **(d)** *Metal container*

(e) *Trees* **(f)** *Power line*

Figure 6.11. *Exemplary results of the reflector localization algorithm. ©Google*

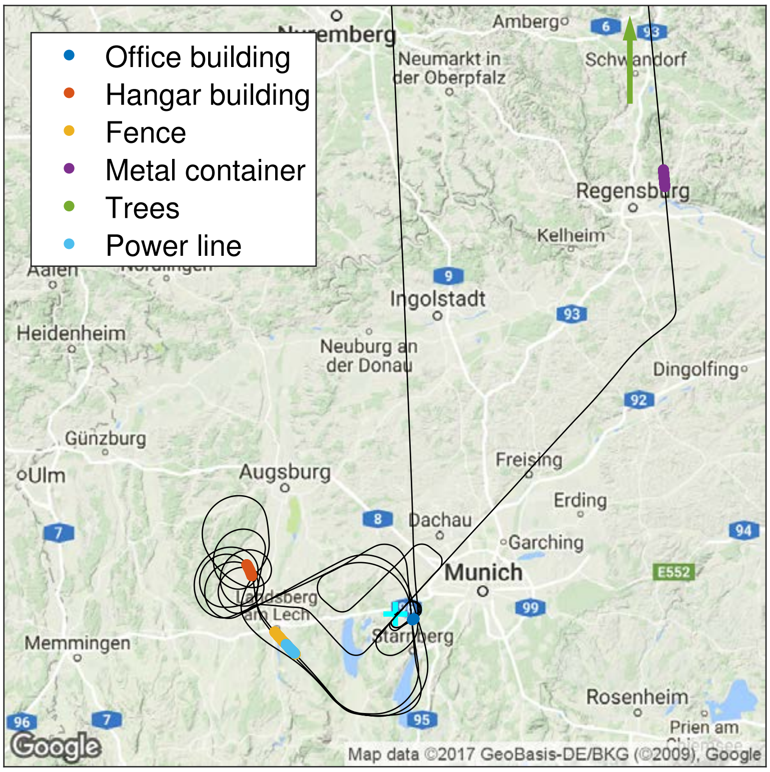

Figure 6.12. *Aircraft location from which the reflectors shown in Fig. 6.11 are seen (Map size* $250\,\mathrm{km} \times 250\,\mathrm{km}$*). ©Google*

imum of each PDF. The black line indicates the direction from the reflector to the ground station, the green line the direction from the reflector to the aircraft. The aircraft locations from which the reflectors are seen are shown in Fig. 6.12. In Fig. 6.12 we mark the ground station locationby a cyan cross.

Overall we observe that the localization algorithm proposed in Sec. 4.6 is able to accurately estimate the location of the reflector causing an MPC: for the shown reflectors the law of reflection is obeyed: the angle of incidence equals the reflection angle.

Most MPCs are caused by nearby office buildings around the ground station, e.g., such as the one shown in Fig. 6.11a. While the MPC is received the aircraft is flying at an altitude of $250\,\mathrm{m}$. The power of these close-by reflectors is usually higher than for reflector located at larger distances to the ground station. Fig. 6.11a demonstrates the benefits of averaging the estimated reflector location PDFs: some of the individual reflector location PDFs are slightly off the building. Nevertheless, the averaged reflector location PDF shows the correct location of the reflector.

Reflections are also often received from the large hangar buildings in the east of the ground station at a distance of 1.5 to $2\,\mathrm{km}$, e.g., as shown in Fig. 6.11b. Due to the large dimensions of the hangars the corresponding MPCs are visible for a long time.

The existence of fences in the ground station environment manifests itself by long lasting MPCs: the MPC caused by the fence shown in Fig. 6.11c is visible for over $30\,\mathrm{s}$. The PDF is spread over the lower half of the fence due to the movement of the reflection point along the fence.

A different type of reflector is shown in Fig. 6.11d: a small metal container causes an MPC received at the aircraft for more than $10\,\mathrm{min}$ while the aircraft is traveling on a straight trajectory towards the ground station. The result in Fig. 6.11d shows that even small objects, if placed at the right location and the right angle towards the ground station, can have a long lasting effect on the channel.

Another effect often observed is the scattering of the transmit signal by trees as shown in Fig. 6.11e. The relevant flight segment is not shown in Fig. 6.12 as it is $50\,\mathrm{km}$ further north. MPCs from forest edges often exist but are generally of a very low power $> -45\,\mathrm{dB}$ (relative to FSPL).

Rarely reflectors may also be far away from the ground station: the high-voltage transmission tower depicted in Fig. 6.11f is located $3.7\,\mathrm{km}$ away from the ground station. However, such reflections from far away objects are not observed often - see Sec. 7.2.3.

6.6.2 Distribution of Reflectors

In the following, we present results on the distribution of reflectors. Fig. 6.13 visualizes the probability of an MPC being received from a certain reflector location for the three scenarios defined in Sec. 6.2.

The ground station location is marked by a cyan cross. For the generation of Fig. 6.13, we use a Gaussian kernel smoother to estimate the distribution of the maxima of $p_{\mathrm{C}u}(\boldsymbol{g})$, calculated for all MPCs detected during the corresponding scenario [108].

From the results shown in Fig. 6.13 some general remarks can be made: in the vast majority of cases, the estimated reflector locations fall on or very close to buildings, fences, or terrain features, such as smaller hills or clusters of trees. Occasions where MPCs are estimated to originate from open areas, i.e., areas without obstacles, are very rare - see Sec. 7.2.3. It can therefore be concluded that the presented algorithm is able to identify the locations of relevant reflectors with a high fidelity. The few cases where the algorithm does not provide a physically meaningful output can most likely be attributed to multi-bounce reflections, a poor parameter estimation performance, or the ambiguous reflector location PDF.

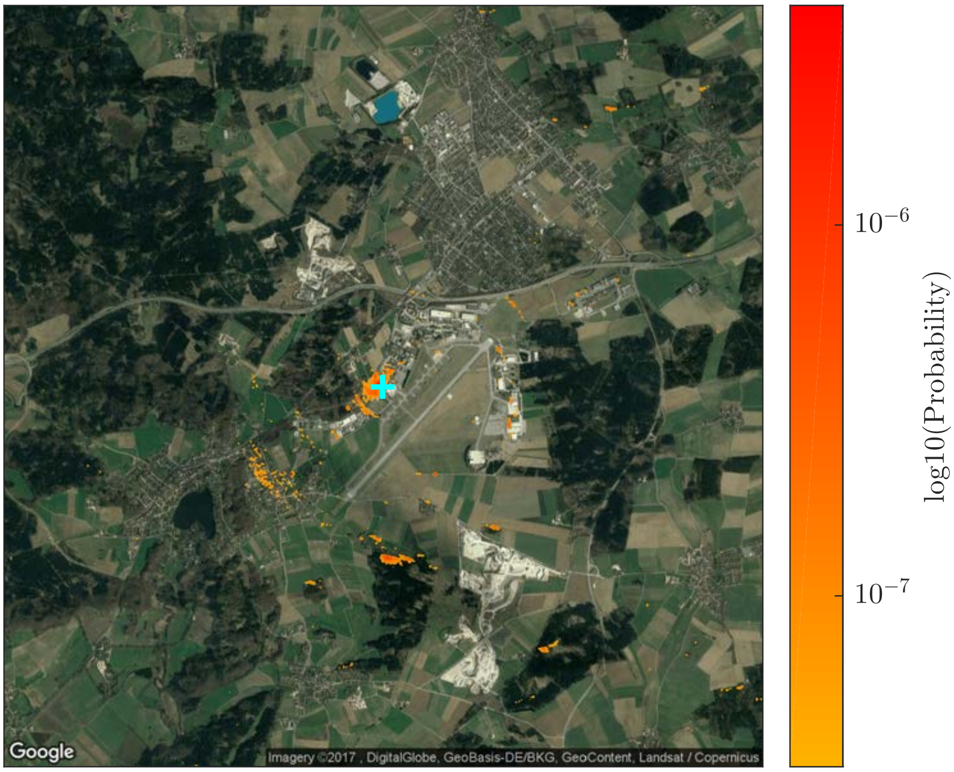

(a) *Takeoff & landing (TL)*

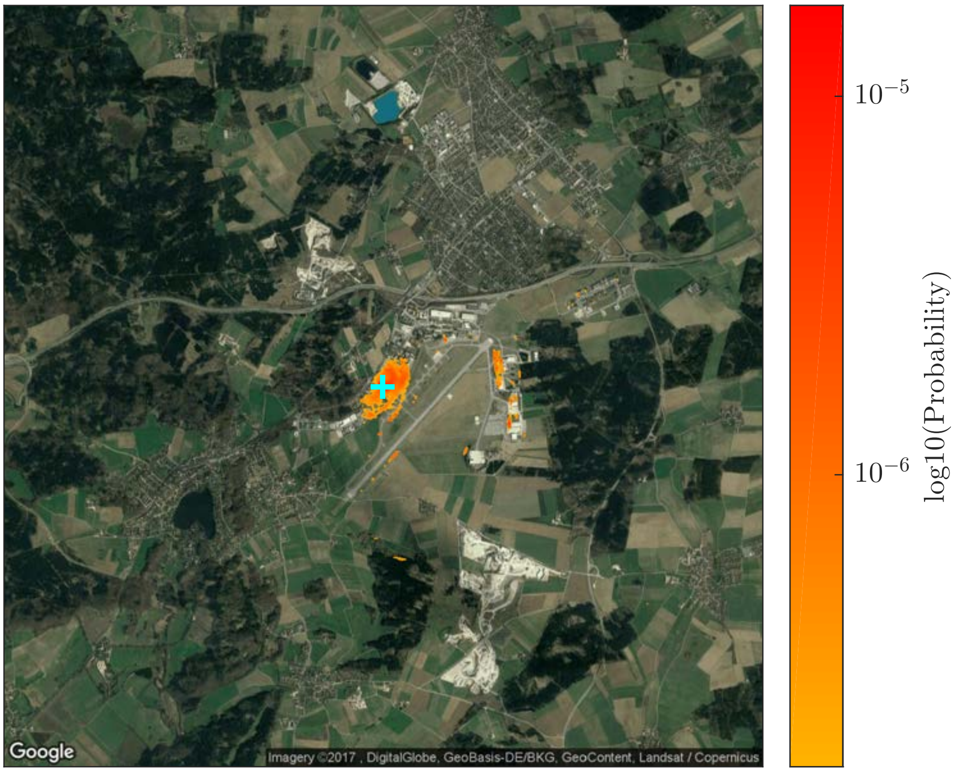

(b) *Climb & descent (CD)*

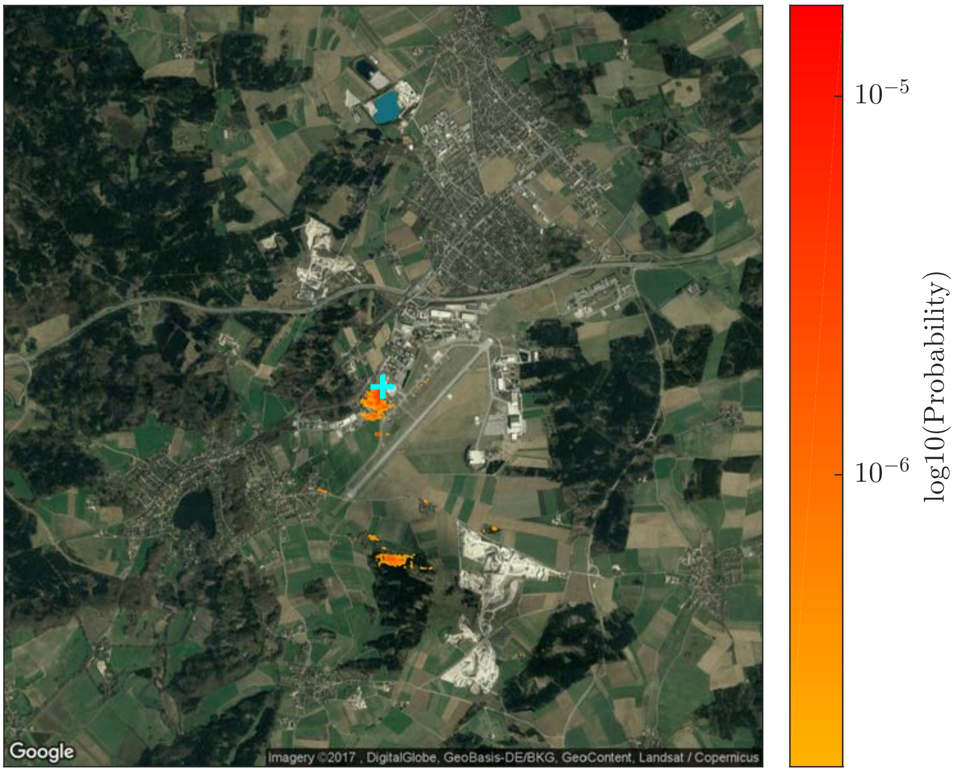

(c) *Enroute cruise (EC)*

Figure 6.13. *Distribution of the reflectors for the three scenarios (Map size* $8\,\mathrm{km} \times 8\,\mathrm{km}$*). ©Google*

For all scenarios the majority of MPCs is received from the direct surrounding of the ground station. We also observe that the aircraft trajectories in the scenarios have a strong influence on the origin of the received MPCs.

In the TL scenario the aircraft is flying in the direct surrounding of the ground station at a low altitude. The locations of the reflectors are spread over the entire map.

In large parts of the CD scenario the aircraft flies westwards of the ground station. Apart from reflectors in the direct surrounding of the ground station, the dominant reflectors originate from the hangar buildings east of the ground station. Additionally, we observe also the effect of the two fences $1\,\mathrm{km}$ south of the ground station.

In the EC scenario the aircraft travels in the northward direction of the ground station at cruising altitude. Apart reflectors in the direct surrounding, reflectors causing MPCs are almost exclusively located south of the ground station. This concentration is, as we will show in Sec. 7.2.3, a result of the fact that during the measurements mostly backscattering is observed: reflectors mostly reflect signals back into the direction of the ground station. Thus, if the aircraft flies in the north of the ground station it will mostly receive MPCs caused by reflectors from the south of the ground station. The typical reflectors in this scenario are trees and isolated buildings.

6.7 Summary

In this chapter we present results characterizing the AG channel. The results are obtained by applying the algorithms described in Chapter 4 to the measured data collected during the flight trials described in Chapter 5.

The first result is that the developed algorithms are well adapted to the measured data collected during the flight trials: the effects of interference - especially the strong interference by the onboard distance measuring equipment (DME) - can be well mitigated.

The acquired results offer a deep insight on the properties of the AG channel: we learn about both the statistical characteristics of the channel and its non-stationarity. We observe that certain propagation characteristics may persist for seconds or even minutes - a behavior very unusual for most other prominent channels, e.g., cell phone communication channels. The non-stationarity is caused by the fact that the propagation characteristics of the channel are almost exclusively defined by the direct surrounding of the ground station: for an aircraft traveling at a large link distance the angles under which the ground station and its surroundings are seen do not change significantly over time; therefore, also the propagation characteristics experience only minor changes.

The ability to localize the reflectors causing MPCs provides a deep understanding of the channel: we are able to investigate how the measured channel is connected to the underlying environment. Therefore, we are now able to not only model the channel more accurately but also identify specifics about an airport environment able to cause challenges for a terrestrial communication, navigation, and surveillance (CNS) system.

CHAPTER 7

CHANNEL MODEL PARAMETERIZATION FOR A REGIONAL AIRPORT

Contents

7.1 Overview

In Sec. 7.2, we use the channel model architecture presented in Chapter 3 to derive an L-band channel model parameterization for a regional airport environment. This parameterization includes all model element property distributions defined in Chapter 3. The channel model parameterization is based on the measured data collected at Oberpfaffenhofen Airport (EDMO) in 2013 - see Chapter 5.

The validation is performed using three methods: first, in a quantitative, statistical manner in Sec. 7.3.1. Second, in Sec. 7.3.2 we present a qualitative validation using time-series of the measured signal and the signal generated using the model. Third, we validate the channel model against flight trial ranging experiments in Sec. 7.3.3.

7.2 Derivation of the Parameterization

In the following we derive a regional airport parameterization for the channel model. To this end, we go through all model elements defined in Chapter 3 and derive the associated distributions. We base each of the distributions on results from the channel sounding experiments described in Chapter 5. The regional airport channel model parameterization is summarized in App. A.

7.2.1 Line of Sight Signal

We propose modeling the line-of-sight (LoS) signal power to follow free space path loss (FSPL). The phase of the LoS signal depends on the propagation path length and the signal wavelength. Additionally, if complex antenna radiation patterns are available, the LoS signal phase is a function of both angle of departure and arrival.

If the absolute length of the LoS path is of interest, as it may be for the analysis of navigation systems, we have to consider the bending of electromagnetic waves due to the troposphere described in Sec. 5.2.4. We propose modeling effects due to the troposphere using an established method from literature [16].

In Fig. 7.1 we show the range estimation error (ranging error), i.e., the estimated model range minus the range based on Global Positioning System (GPS) - see Sec. 5.2.4, with and without compensation of the troposphere for the three scenarios.

We observe that for the takeoff & landing (TL) scenario (due to the short link distance) a correction of the tropospheric effects is not required: both the compensated

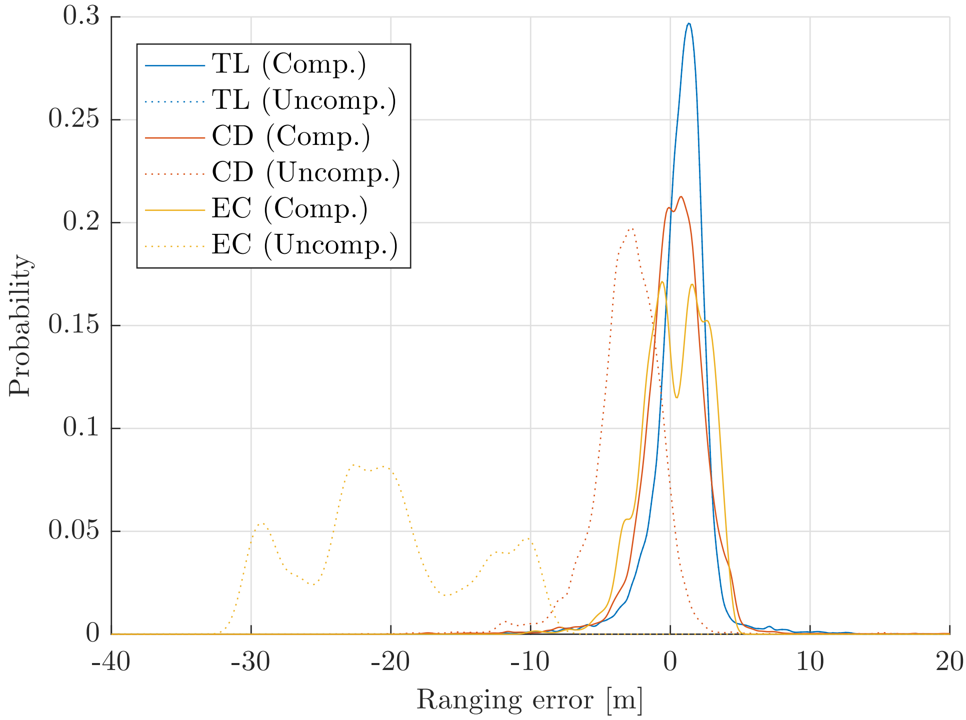

Figure 7.1. *Residual delay estimation error with and without tropospheric correction.*

and uncompensated delay estimation errors are identical. However, for an increasing link distance the effects of the troposphere become more visible: in the climb & descent (CD) scenario (average link distance: $37\,\mathrm{km}$) a bias of $3\,\mathrm{m}$ remains if the tropospheric effects are not compensated for. For the enroute cruise (EC) scenario (average link distance: $180\,\mathrm{km}$) the bias grows to $25\,\mathrm{m}$.

If the tropospheric effects are compensated the remaining bias is $1\,\mathrm{m}$ or less for all three scenarios. This error is within the inaccuracy of the measurement setup described in Sec. 5.2.5. The most likely explanation for the high remaining bias in the TL scenario is the blockage of the LoS path by the aircraft fuselage during steep turns. This attenuation of the LoS signal increases the relative power of multipath components (MPCs) and thus their impact on the range estimation.

Note that in the channel model the effect of the troposphere is modeled not only for the LoS path, but also for all other MPCs using the method described in [16].

7.2.2 Ground Multipath Component

We propose modeling ground multipath propagation by characterization of reflecting areas on the ground. A ground MPC is received if the ground reflection point lies in such a reflecting area. We calculate the location of the ground reflection point as the specular reflection point on the ground surface [14]. The location of the ground reflection point depends on both ground antenna height and aircraft position. We assume horizontally aligned reflecting areas. Thus, once the reflecting areas are defined, the interaction of the ground MPC with the LoS signal, and the resulting attenuation or amplification of the latter, follows directly from the underlying geometry.

We define the coverage ratio $r_{\mathrm{G,cov}}$ as the ratio between the sum of all reflecting area sizes and the overall area size around the ground station. For the regional airport environment, based on the measured data, we approximate that $r_{\mathrm{G,cov}} = 50\%$ of the ground station surrounding is covered by reflecting areas.

We characterize the reflecting areas using different properties. We derive the distribution of the area properties based on ground surface information of the environment to be modeled. In our case we use land usage data, satellite imagery, and a digital elevation model (DEM) of the ground station surroundings.

Shape

The reflecting areas (such as a runway, a parking area, a taxiing area) are of different shape. For simplicity we model all reflecting areas as rectangles of size $l_{\mathrm{G},1} \times l_{\mathrm{G},2}$. We use a normal distribution to describe the logarithmic aspect ratio of each rectangle

$$p\left(\log \frac{l_{\mathrm{G},1}}{l_{\mathrm{G},2}}\right) \sim \mathcal{N}\left(0, \zeta_{\mathrm{G,AR}} = 0.1\right). \tag{7.1}$$

Thus, reflecting areas are all of rectangular shape each with a different aspect ratio.

Size

The airport environment we are modeling consists predominantly of large open areas of either grassy or concrete surface. Thus, also the reflecting areas in the channel model are large: We model the size $l_{\mathrm{G},1} \times l_{\mathrm{G},2}$ as an exponential distribution

$$p\left(l_{\mathrm{G},1} l_{\mathrm{G},1}\right) \sim \mathcal{E}\left(\zeta_{\mathrm{G},s} = 0.01\,\mathrm{km}^2\right). \tag{7.2}$$

That means, the average size of $p\left(l_{\mathrm{G},2} l_{\mathrm{G},1}\right)$ corresponds to a square of $30\,\mathrm{m} \times 30\,\mathrm{m}$.

Material

The ground station environment is usually composed of a mix of different types of surfaces. Their electromagnetic properties such as conductivity and permittivity have been extensively investigated in the past [15], [19] and are modeled by statistical distributions. The ground station environment consists mainly of grassy areas,

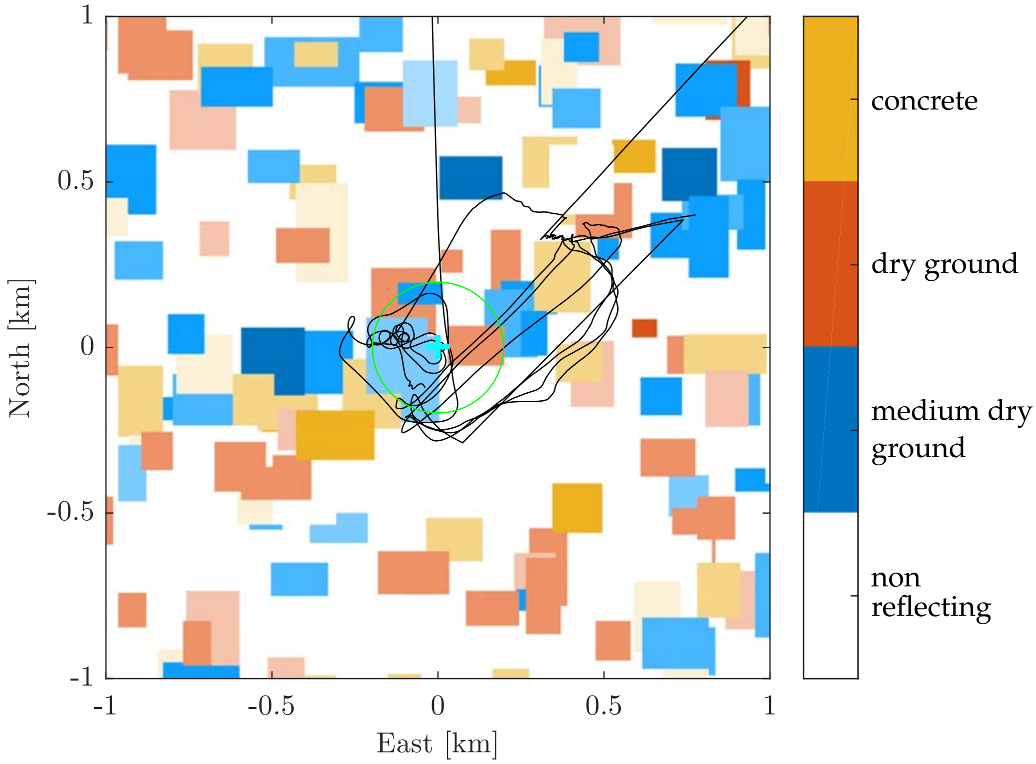

Figure 7.2. *Example for a ground reflecting area realization in the channel model.*

fields, forests, and concrete. Therefore, we assume that the reflecting areas consists of equal parts of *medium dry ground*, *dry ground*, and *concrete* as defined in [15].

Roughness

The roughness of an area has an influence on how much power is scattered in all directions rather than reflected in the direction defined by the law of reflection [14]. We describe the roughness by the standard deviation $\sigma_{\mathrm{G,r}}$ of the surface height about the local surface mean. Given $\sigma_{\mathrm{G,r}}$ the reflected power can be approximated [19]. We model the standard deviation of the surface height using an exponential distribution

$$p\left(\sigma_{\mathrm{G,r}}\right) \sim \mathcal{E}\left(\zeta_{\mathrm{G,r}} = 0.1\,\mathrm{m}\right). \tag{7.3}$$

The mean of 0.1 has been found to provide a good approximation in similar scenarios [67].

Fig. 7.2 shows one realization of the ground reflecting areas for the above property distributions. The different colors in Fig. 7.2 represent different ground surface materials. The lightness of the areas indicates the standard deviation $\sigma_{\mathrm{G,r}}$ of the surface height about the local surface mean: with increasing roughness surfaces become lighter. The black line indicates the track of the ground reflection point for the conducted channel sounding flights. The green line shows the track of a hypothetical flying a circle around the ground station at $5\,\mathrm{km}$ above ground level (AGL) at a distance of $50\,\mathrm{km}$.

7.2.3 Lateral Multipath Component

In this section, we derive the statistical distributions describing the lateral MPCs. For the derivation of the statistical distributions we use information from approximately 130.000 individual reflectors.

Throughout this section we use the following notation:

- The estimated position of reflector k in an east-north-up (ENU) coordinate system is denoted by the vector $\boldsymbol{r}_k = [r_{k,\mathrm{E}}, r_{k,\mathrm{N}}, r_{k,\mathrm{U}}]^{\mathrm{T}} \in \mathbb{R}^{3\times 1}$.
- $M_k \in \mathbb{N}$ denotes the number of channel sounding blocks in which the MPC caused by reflector k is detected. Thus, M_k is equal to the duration the MPC is received divided by the block duration T_{sym} - see Sec. 4.2.
- The vector $\hat{\boldsymbol{\alpha}}_k = [\hat{\alpha}_{k,1}, .., \hat{\alpha}_{k,M_k}]^{\mathrm{T}} \in \mathbb{R}^{M_k\times 1}$ denotes the estimated complex weights associated with reflector k.
- The vectors $\hat{\boldsymbol{\phi}}_k = \left[\hat{\phi}_{k,1}, .., \hat{\phi}_{k,M_k}\right]^{\mathrm{T}} \in \mathbb{R}^{M_k\times 1}$ and $\hat{\boldsymbol{\theta}}_k = \left[\hat{\theta}_{k,1}, .., \hat{\theta}_{k,M_k}\right]^{\mathrm{T}} \in \mathbb{R}^{M_k\times 1}$ denote the azimuth and elevation the aircraft is seen from the reflector k while an MPC from the reflector k is received.
- The elevation the aircraft is seen from the ground station while an MPC from reflector k is received is denoted as $\hat{\theta}_{\mathrm{GS},k} = \left[\hat{\theta}_{\mathrm{GS},k,1}, .., \hat{\theta}_{\mathrm{GS},k,M_k}\right]^{\mathrm{T}} \in \mathbb{R}^{M_k\times 1}$.

Number of Reflectors

The number of reflectors $\zeta_{N_{\mathrm{ref}}}$ we distribute in the channel model is a key property of the channel model parameterization: $\zeta_{N_{\mathrm{ref}}}$ defines how many MPCs are received. As described in Sec. 7.3.2, we adjust the $\zeta_{N_{\mathrm{ref}}}$ such that the average number of reflectors detected during the measurements matches the number of reflectors seen during channel model simulations. An analysis of different flight segments show that $\zeta_{N_{\mathrm{ref}}} = 3.8 \cdot 10^4$ provides a good match.

Opening Direction

The opening direction is the axis of symmetry of the cone used to model a reflector. We divide the opening direction in an azimuthal and elevational direction, $\hat{\phi}_{\mathrm{d},k}$ and $\hat{\theta}_{\mathrm{d},k}$, respectively.

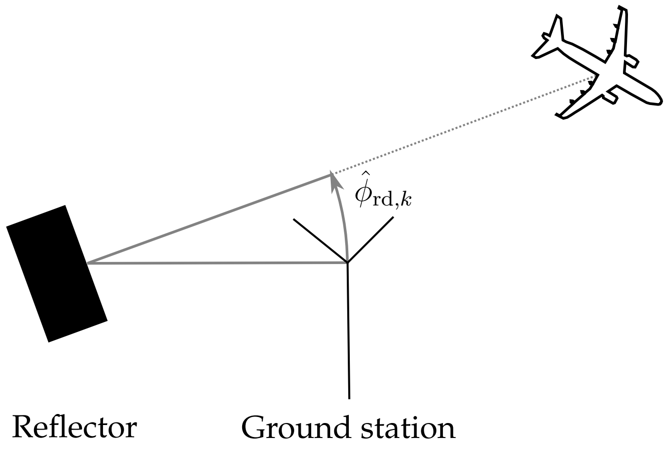

Figure 7.3. *Visualization of the relative opening direction* $\hat{\phi}_{\mathrm{rd},k}$.

Azimuth For the purpose of modeling we calculate the azimuthal opening direction relative to the direction the ground station is seen under as visualized in Fig. 7.3 as

$$\phi_{\mathrm{rd},k} = \hat{\phi}_{\mathrm{d},k} - \tan_2^{-1}\left(-r_{k,\mathrm{N}}, -r_{k,\mathrm{E}}\right). \tag{7.4}$$

Thus, $\hat{\phi}_{\mathrm{rd},k} = 0$ means that aircraft, ground station, and reflector lie on a line while an MPC is received from the reflector.

In Fig. 7.4 we show the distribution of the relative azimuthal opening direction $p\left(\hat{\phi}_{\mathrm{rd}}\right)$. The estimated distribution of $p\left(\hat{\phi}_{\mathrm{rd}}\right)$ is symmetrical around $0°$, i.e., most MPCs are reflected back towards the ground station. This effect, in literature referred to as backscattering, was also observed in previous measurements and simulations [109], [110]. Simple ray-tracing simulations indicate that the narrow distribution shown in Fig. 7.4 are most likely caused by the underlying geometry - see App. F.

The distribution of $p\left(\phi_{\mathrm{rd}}\right)$ is modeled using a exponential distribution $\mathcal{L}$ centered at $0°$, i.e., two exponential distributions mirrored around the y-axis,

$$p\left(\phi_{\mathrm{rd}}\right) \sim \mathcal{E}\left(0, \zeta_{\phi_{\mathrm{rd}},\mathrm{b}} = 0.57\right). \tag{7.5}$$

Note that due to the 2π periodicity of the angle ϕ_{rd}, we wrap the tails of the distribution around in order to make the distribution cyclic.

Elevation The derivation of the distribution for the elevational opening direction $p\left(\theta_{\mathrm{d}}\right)$ is more cumbersome as for the azimuthal direction $p\left(\phi_{\mathrm{d}}\right)$. The complication is caused by the fact that during the measurements the aircraft is only seen under very specific elevation angles from the ground station: the estimated distribution of elevation angles is strongly dependent on the measured flight trajectory T. The aircraft

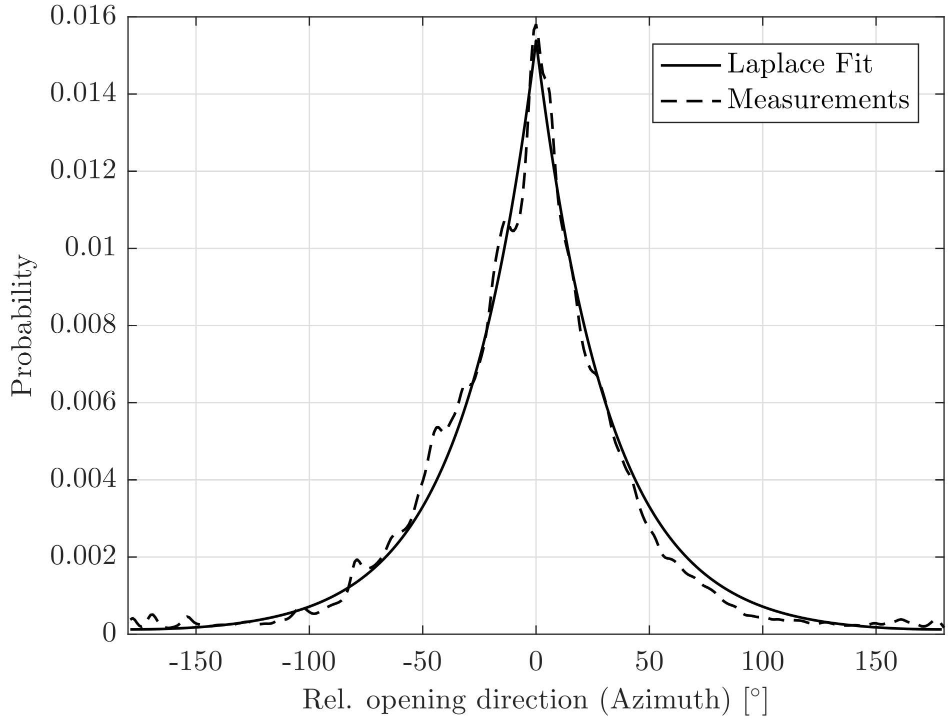

Figure 7.4. *Distribution of the relative azimuthal opening angle* $\phi_{\mathrm{rd},k}$.

is mainly flying at positions where it is seen under very low elevation angles from both ground station and reflectors. In contrast, the azimuth angles ϕ the aircraft is seen from the ground station is approximately uniformly distributed from 0 to 2π.

Fig. 7.5 (left *y*-axis) shows two estimated distributions: first, the distribution of the elevation angle the aircraft is seen from the ground station $p\left(\hat{\theta}_{\mathrm{GS}}|T\right)$ during the entire flight. Second, the distribution of the elevation angle the aircraft is seen from all detected reflectors $p\left(\hat{\theta}|T\right)$. We use the notation of a conditional distribution to underline the dependence on the flight track T. For the calculation of the first distribution $p\left(\hat{\theta}_{\mathrm{GS}}|T\right)$ every location of the aircraft flight track is only considered once. In contrast, for the second distribution $p\left(\hat{\theta}|T\right)$ every location is weighted by the number of MPCs received while the aircraft is at said location.

We now aim to investigate the distribution of the elevational opening direction $p\left(\theta\right)$ independently from the flight track T. By applying Bayes law we write

$$\frac{p\left(T|\hat{\theta}\right)p\left(\hat{\theta}\right)}{p\left(T|\hat{\theta}_{\mathrm{GS}}\right)p\left(\hat{\theta}_{\mathrm{GS}}\right)} = \frac{p\left(\hat{\theta}|T\right)p\left(T\right)}{p\left(\hat{\theta}_{\mathrm{GS}}|T\right)p\left(T\right)}. \tag{7.6}$$

Let us assume that all reflectors are located in the close surroundings of the ground station: the distance between ground station and reflector is in most cases small

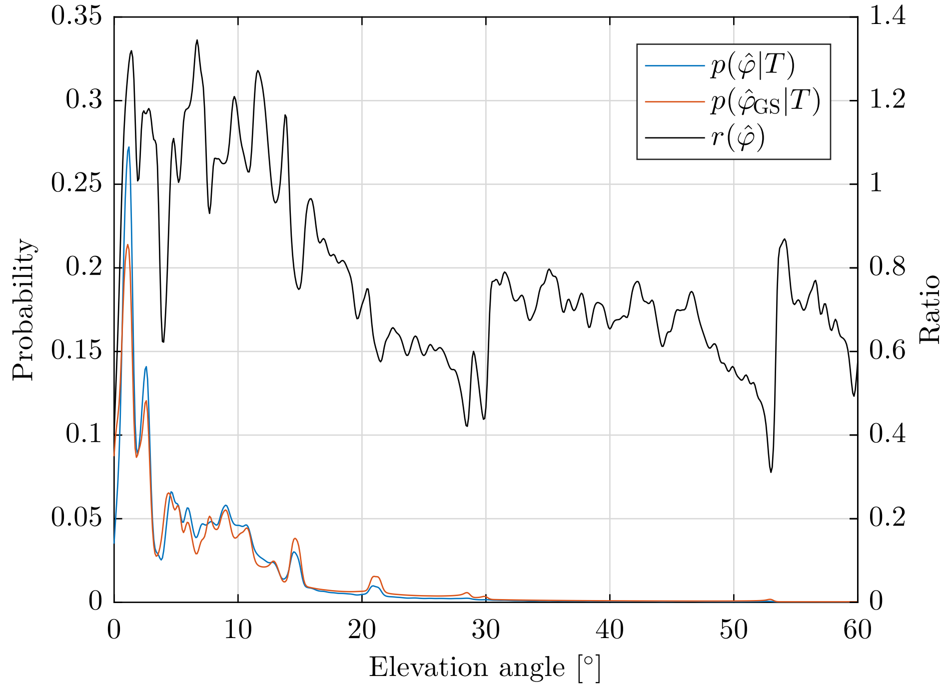

Figure 7.5. *Distribution of the elevation angle the aircraft is seen from both ground station and reflector positions.*

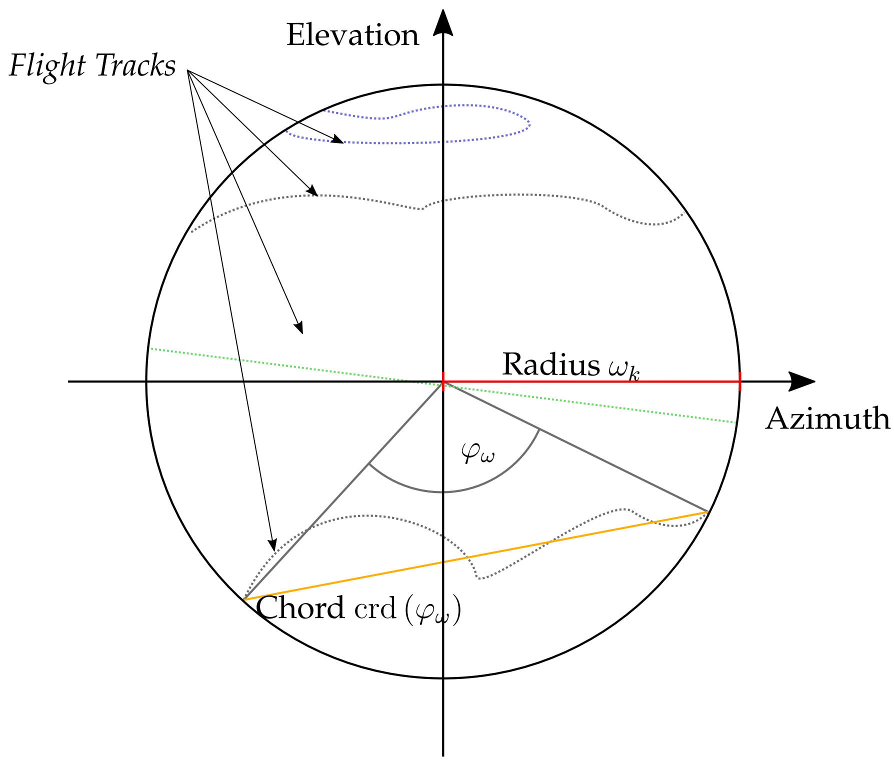

Figure 7.6. *Illustration of the opening width calculation: the figure illustrates different flight tracks as seen from the reflector position.*

relative to the link distance: the elevation angles the aircraft is seen from the ground station, θ_{GS}, and reflector, θ, are almost identical: it follows that

$$p\left(T|\hat{\theta}\right) \approx p\left(T|\hat{\theta}_{\mathrm{GS}}\right). \tag{7.7}$$

Using the simplification from (7.7), we are able to rewrite (7.6) as

$$r\left(\hat{\theta}\right) := \frac{p\left(\hat{\theta}\right)}{p\left(\hat{\theta}_{\mathrm{GS}}\right)} = \frac{p\left(\hat{\theta}|T\right)}{p\left(\hat{\theta}_{\mathrm{GS}}|T\right)}. \tag{7.8}$$

The ratio $r\left(\hat{\theta}\right)$ is proportional to the number of reflectors seen by the aircraft under a certain elevation angle θ: if a dominant elevation angle θ' exist under which the aircraft is seen from a large number of reflectors, there is a peak in the ratio $r\left(\theta\right)$ at that angle θ'. Consequently, reflectors with an elevational opening direction θ'_{d} are more likely than reflectors with other opening directions.

Analyzing the measured ratio $r\left(\hat{\theta}\right)$ in Fig. 7.5 we observe that the ratio $r\left(\hat{\theta}\right)$ is approximately constant [1]. If the ratio $r\left(\theta\right)$ is constant, we can model the distribution of elevational opening directions $p\left(\theta_{\mathrm{d}}\right)$ as uniform distribution $\mathcal{U}$ between $\zeta_{\theta_{\mathrm{d}},\mathrm{l}} = 0$ and $\zeta_{\theta_{\mathrm{d}},\mathrm{u}} = \frac{\pi}{2}$

$$p\left(\theta_{\mathrm{d}}\right) \sim \mathcal{U}\left(\zeta_{\theta_{\mathrm{d}},\mathrm{l}} = 0, \zeta_{\theta_{\mathrm{d}},\mathrm{u}} = \frac{\pi}{2}\right). \tag{7.9}$$

Opening Width

In this section, we describe how the distribution of the opening widths $p\left(\omega\right)$ can be derived from the measured data. Seen from the reflector position the opening width defines a circle centered at $\left[\phi_{\mathrm{d},k}, \theta_{\mathrm{d},k}\right]^{\mathrm{T}}$ as visualized in Fig. 7.6. The radius of the circle equals the opening width ω_k. If the aircraft traverses on a straight path through the circle and its center as shown by the green track in Fig. 7.6, the estimation of the opening width $\hat{\omega}_k$ is straightforward: it is the Euclidean distance between the first and last two-dimensional angle the aircraft is seen under

$$\hat{\omega}_k = \sqrt{\left(\hat{\phi}_{k,1} - \hat{\phi}_{k,M_k}\right)^2 + \left(\hat{\theta}_{k,1} - \hat{\theta}_{k,M_k}\right)^2}. \tag{7.10}$$

In reality the aircraft will most likely traverse through the circle neither on a straight path nor through the center, e.g., blue or grey tracks. We will thus underestimate the opening width $\hat{\omega}_k$ in most cases if we use (7.10).

[1] Although the true ratio $r\left(\theta\right)$ may not be perfectly constant, with the available measurement it is unfeasible to determine the exact shape of $r\left(\theta\right)$. Thus, the assumption of a constant ratio $r\left(\theta\right)$ is reasonable. For more exact determination ratio $r\left(\theta\right)$ more flight trials, especially with trajectories where the aircraft is seen at higher elevation angles from the ground station, would be required.

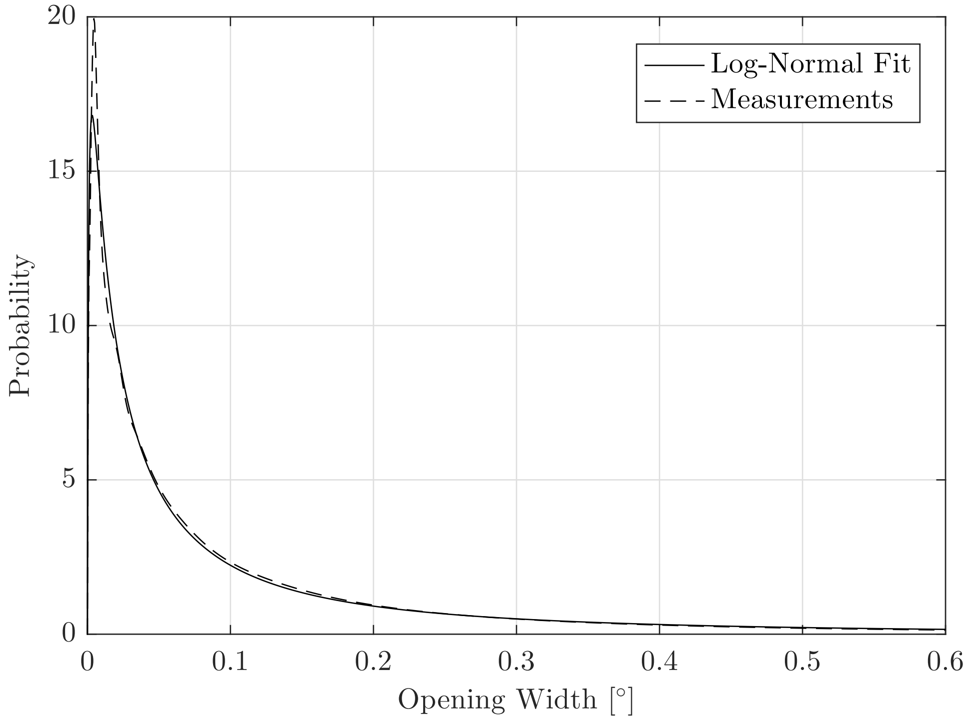

Figure 7.7. *Measured and modeled distributions of the opening width ω.*

Nevertheless, we are able to estimate the opening width $\hat{\omega}_k$ based on the measured data as described below: as visualized in Fig. 7.6, each aircraft trajectory "through the circle" defines a chord $\mathrm{crd}\left(\varphi_\omega\right)$ (orange line). The length of the chord is given as

$$\mathrm{crd}\left(\varphi_\omega\right) = 2\omega \sin\frac{\varphi_\omega}{2}. \tag{7.11}$$

Assume that the angle φ_ω describing the chord is uniformly distributed, i.e., $p\left(\varphi_\omega\right) \sim \mathcal{U}\left(0, 2\pi\right)$: the average chord length can be calculated as

$$\begin{aligned} \mathbb{E}\left\{\mathrm{crd}\left(\varphi_\omega\right)\right\} &= \int_0^{2\pi} \frac{1}{2\pi} 2\omega_k \sin\frac{\varphi_\omega}{2}\,\mathrm{d}\varphi_\omega \\ &= \frac{4\omega_k}{\pi}. \end{aligned} \tag{7.12}$$

Using (7.12) we are able to translate a chord length $\mathrm{crd}\left(\varphi_\omega\right)_k$ estimated from the measurements data into an opening width ω_k.

The opening width ω_k is thus calculated as

$$\hat{\omega}_k = \frac{\pi}{4} \max_{i,j} \sqrt{\left(\hat{\phi}_{k,i} - \hat{\phi}_{k,j}\right)^2 + \left(\hat{\theta}_{k,i} - \hat{\theta}_{k,j}\right)^2},\, i,j = 1,..,M_k. \tag{7.13}$$

The estimated distribution of the opening width $p\left(\hat{\omega}\right)$ is shown in Fig. 7.7. We observe that most reflectors have a narrow opening width $\omega < 0.1°$. Nevertheless, due to a small number of reflectors with large opening widths ω, the mean opening width is $0.7°$. These reflectors have a significant influence on the channel, as due to their large opening width ω, they cause MPC visible for a long duration. To model the distribution $p(\omega)$ we chose a log-normal distribution

$$p(\omega) \sim \log\mathcal{N}\left(\zeta_{\omega,\mu} = -7.15, \zeta_{\omega,\sigma} = 1.77\right). \tag{7.14}$$

The log-normal distribution $\log\mathcal{N}$ is chosen over other distributions as it provides also a good match for the tails of the estimated distribution $p(\hat{\omega})$, i.e., reflectors with large opening widths ω. The drawback is a slight mismatch between the modeled and estimated distribution at smaller opening widths ω around $0.1°$.

Location

This section deals with modeling the reflector location distribution $p(\boldsymbol{r})$. The goal is to model the distribution of positions $p(\boldsymbol{r})$ as simple as possible while still maintaining a good match to the measured distribution $p(\hat{\boldsymbol{r}})$.

In the following we assume that all reflectors are located in the same plane, e.g., their altitude relative the ground station antenna is constant. Furthermore, we model the originally then two-dimensional location using by an one-dimensional distribution $p(r)$, i.e., the distribution of the distance between ground station and reflector. We refer to the distance between ground station and reflector k as the one-dimensional reflector location r_k. Later we show how the one-dimensional reflector location can be transformed back into the two-dimensional location required in the channel model.

In Fig. 7.8 we show the estimated distribution of the one-dimensional reflector location $p(\hat{r})$. Fig. 7.8 demonstrates that most reflectors are located within a short distance to the ground station. This result is intuitive as the closer a building is, the more "angular space" it occupies: For example, if a $100\,\mathrm{m}$ wide building is located at a distance of $10\,\mathrm{m}$ to the ground station, it occupies roughly $160°$. If the same building is located at a distance of $1\,\mathrm{km}$, it occupies only in $5°$.

Nevertheless, as both the results in Sec. 6.6 and Fig. 7.8 show, additional clusters of reflectors exist at larger distances to the ground station. Each cluster is usually caused by a group of buildings or trees. Furthermore, there exist isolated reflectors caused by small isolated single objects, e.g., a metal container on an open field.

We thus propose modeling the one-dimensional reflector location distribution $p(r)$ using three groups of reflectors. Each reflector group is associated with a different distribution:

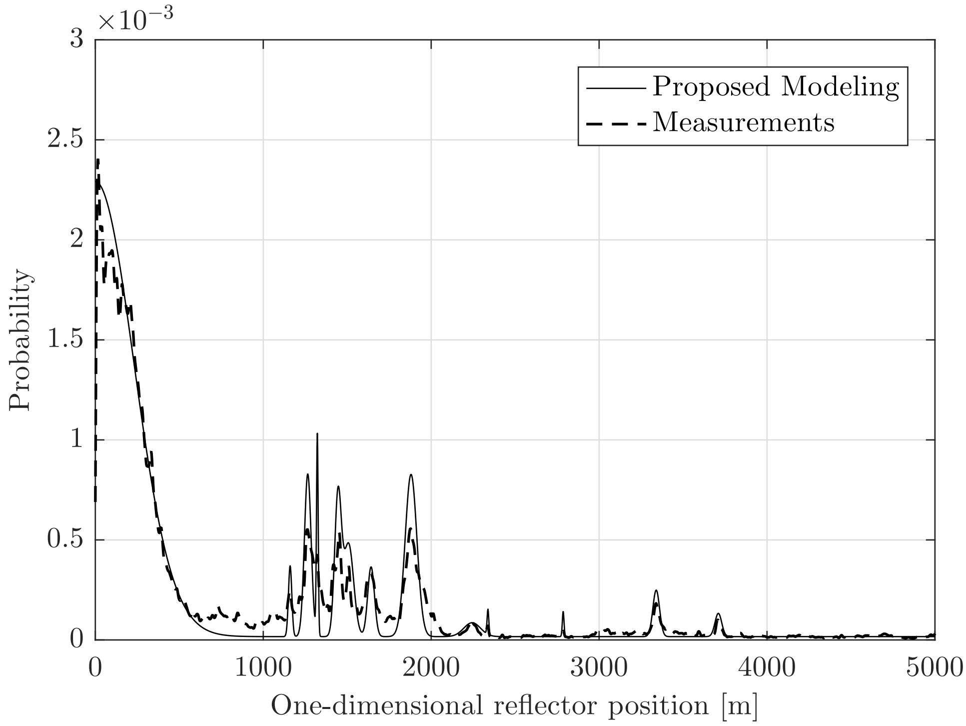

Figure 7.8. *Distribution of the one-dimensional reflector location, i.e., the distance between ground station and reflector.*

Close reflectors: The distribution of reflectors in the direct surrounding of the ground station is modeled using a half normal distribution

$$p_1\left(r\right) \sim \left|\mathcal{N}\right| \left(\zeta_{r,1,\sigma}^2 = \left(213\,\mathrm{m}\right)^2\right). \tag{7.15}$$

Cluster reflectors: We model the distribution of reflectors appearing in clusters using a Gaussian mixture model as

$$p_2\left(r\right) \sim \frac{1}{\zeta_{r,2,N}} \sum_{i=1}^{\zeta_{r,2,N}} \mathcal{N}\left(\zeta_{r,2,\mu_i}, \zeta_{r,2,\sigma_i}^2\right). \tag{7.16}$$

Mean and standard deviation are distributed as $p\left(\zeta_{r,2,\mu}\right) \sim \mathcal{U}\left(500\,\mathrm{m}, 2\,\mathrm{km}\right)$ and $p\left(\zeta_{r,2,\sigma}\right) \sim \mathcal{U}\left(1\,\mathrm{m}, 50\,\mathrm{m}\right)$. The number of clusters is $\zeta_{r,2,N} = 6$.

Isolated reflectors: An uniform distribution is used to model the distribution of isolated reflectors

$$p_3\left(r\right) \sim \mathcal{U}\left(\zeta_{r,3,\mathrm{l}} = 0\,\mathrm{km}, \zeta_{r,3,\mathrm{u}} = 4\,\mathrm{km}\right). \tag{7.17}$$

Each distribution is weighted by the factors $\zeta_{r,w1} = 0.65$, $\zeta_{r,w2} = 0.25$, and $\zeta_{r,w3} = 0.1$.

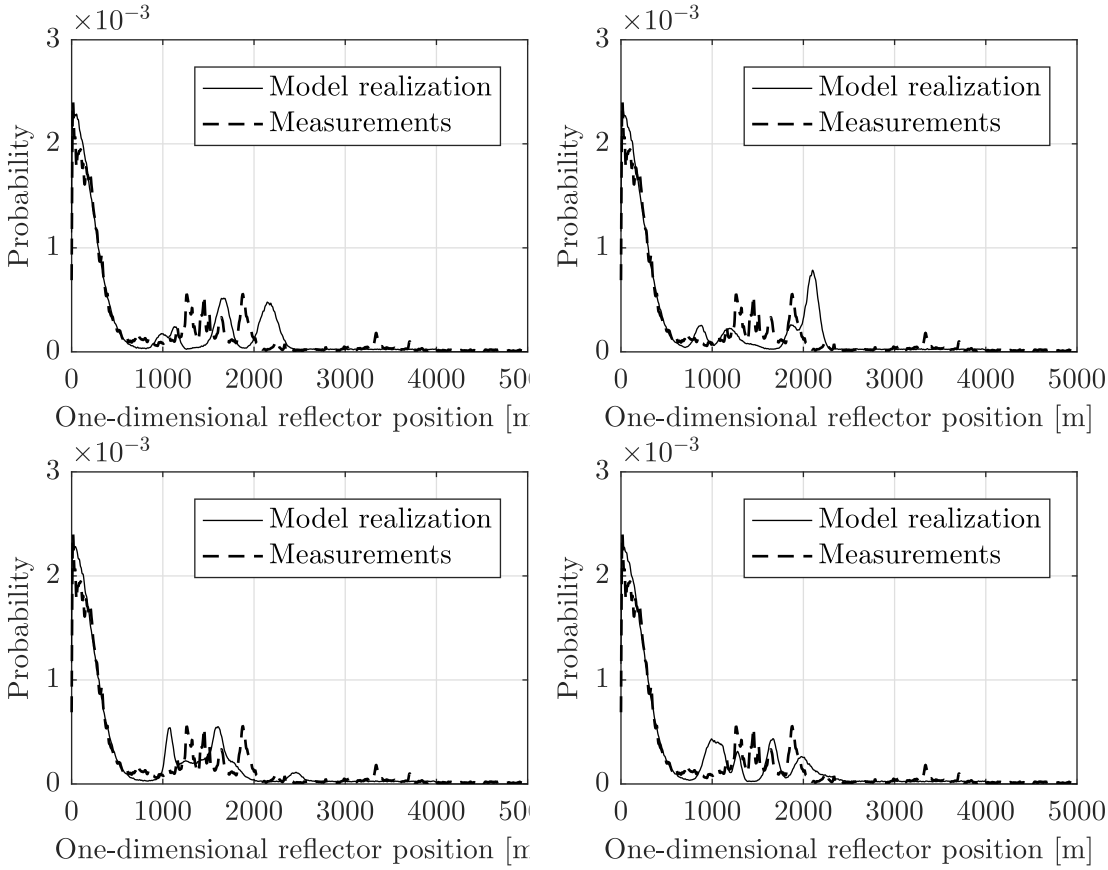

Figure 7.9. *Four channel model realizations of the distribution of the one-dimensional reflector location.*

These factors can be derived from the distribution shown in Fig. 7.8. The distribution for the one-dimensional reflector location is

$$p(r) = \zeta_{r,w1} p_1(r) + \zeta_{r,w2} p_2(r) + \zeta_{r,w3} p_3(r) \quad \text{with} \quad \sum_{i=1}^{3} \zeta_{r,wi} = 1. \tag{7.18}$$

In Fig. 7.9 we show four realizations of the one-dimensional location distribution $p(r)$ using the distributions presented above.

Two Dimensional Reflector Location The two-dimensional reflector location $\boldsymbol{r}'$ is calculated from the one-dimensional reflector location r' (drawn from $p(r)$) as follows:

- Close and isolated reflectors, described by $p_1(r)$ and $p_3(r)$, are uniformly distributed around the ground station on the circle defined by r', i.e.,

$$\boldsymbol{r}' = r' \left[\cos\varphi', \sin\varphi'\right]^{\mathrm{T}} \text{ with } \varphi \sim \mathcal{U}(0, 2\pi). \tag{7.19}$$

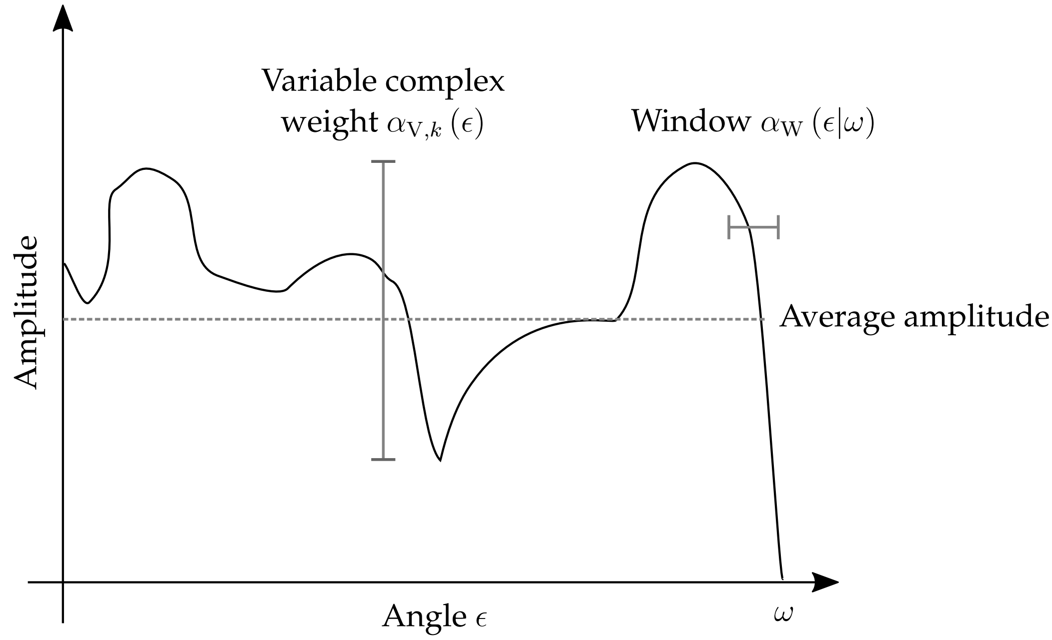

Figure 7.10. *Impact of the three processes used for modeling the complex weight of a reflector.*

- The cluster reflectors are distributed as follows: for each cluster we first calculate the cluster mean $\boldsymbol{\zeta}'_{r,2,\mu}$ from $\zeta_{r,2,\mu}$ as

$$\boldsymbol{\zeta}'_{r,2,\mu} = \zeta'_{r,2,\mu} \left[\cos\varphi', \sin\varphi'\right]^{\mathrm{T}} \text{ with } \varphi \sim \mathcal{U}\left(0, 2\pi\right). \tag{7.20}$$

  The reflectors belonging to each cluster are distributed around the cluster mean $\boldsymbol{\zeta}'_{r,2,\mu}$ by a two-dimensional normal distribution

$$\boldsymbol{r}' = \boldsymbol{\zeta}'_{r,2,\mu} + \left(r' - \zeta'_{r,2,\mu}\right) \left[\cos\varphi', \sin\varphi'\right]^{\mathrm{T}} \text{ with } \varphi \sim \mathcal{U}\left(0, 2\pi\right). \tag{7.21}$$

Complex Weight

We model the complex weight $\alpha_k(\epsilon)$ relative to FSPL to be a function of the angle ϵ: the angle ϵ is calculated as the Euclidean distance between the elevation and azimuth the aircraft is currently seen under and the cones opening direction

$$\epsilon = \sqrt{\left(\phi_{\mathrm{d},k} - \phi_k\right)^2 + \left(\theta_{\mathrm{d},k} - \theta_k\right)^2}. \tag{7.22}$$

Thus, the complex weight is rotationally symmetrical around the center of the cone.

The complex weight $\alpha_k(\epsilon, r)$ is calculated as the product of the three processes depicted in Fig. 7.10

$$\alpha_k(\epsilon) = \alpha_{\mathrm{A},k}\alpha_{\mathrm{V},k}(\epsilon)\,\alpha_{\mathrm{W}}(\epsilon|\omega). \tag{7.23}$$

- The **average amplitude term** $\alpha_{\mathrm{A},k}$ defines the mean amplitude of the MPC associated with reflector k.

- The **variable complex weight term** $\alpha_{\mathrm{V},k}(\epsilon)$ characterizes the complex weight of the MPC as a function of the angle ϵ.

- The **window term** $\alpha_{\mathrm{W}}(\epsilon,\omega)$ defines the drop of the MPC amplitude at the edges of the cone of width ω.

Average Amplitude We propose modeling the distribution $p(\alpha_{\mathrm{A}}|r)$ of the average MPC amplitude as the product of two terms

$$p(\alpha_{\mathrm{A}}|r) \sim p(\alpha_{\mathrm{An}})\,\bar{\alpha}_{\mathrm{A}}(r)\,. \tag{7.24}$$

- The distance dependent mean of the average MPC amplitude is described by $\bar{\alpha}_{\mathrm{A}}(r)$. Thus, $\bar{\alpha}_{\mathrm{A}}(r)$ describes how the mean amplitude of a large number of reflectors at distance r' differs from the mean amplitude of a large number of reflectors at distance r''.

- The distribution around the distance dependent mean is characterized by the distribution $p(\alpha_{\mathrm{An}})$., Thus, $p(\alpha_{\mathrm{An}})$ describes how the amplitude of a large number of reflectors all located at a fixed distance r' varies.

Distance Dependent Mean of Average Amplitude To investigate the distance dependent mean of the average amplitude $\bar{\alpha}_{\mathrm{A}}(r)$ we calculate the average MPC amplitude $\hat{\alpha}_{\mathrm{A},k}$ associated with each reflector as

$$\hat{\alpha}_{\mathrm{A},k} = \frac{1}{M_k}\sum_{m=1}^{M_k}|\hat{\boldsymbol{\alpha}}_{k,m}|. \tag{7.25}$$

Fig. 7.11 shows the mean and standard deviation of the average amplitude $\hat{\alpha}_{\mathrm{A}}$ against the distance between reflector and ground station r. We observe a strong dependence of both mean and standard deviation of the average MPC amplitude on the distance between ground station and reflector: for an increasing distance between ground station and reflector, the standard deviation of the mean decreases.

We model the mean of the average MPC amplitude $\bar{\alpha}_{\mathrm{A}}(r)$ using an exponential function

$$\bar{\alpha}_{\mathrm{A}}(r) = c_{\alpha_{\mathrm{A}},1} + \zeta_{\bar{\alpha}_{\mathrm{A}},2}\exp\left\{-\frac{r}{\zeta_{\bar{\alpha}_{\mathrm{A}},3}}\right\}. \tag{7.26}$$

The coefficients in (7.26) are least squares (LS) estimated based on the measured data as $\zeta_{\bar{\alpha}_{\mathrm{A}},1} = 0.017$, $\zeta_{\bar{\alpha}_{\mathrm{A}},2} = 0.148$, and $\zeta_{\bar{\alpha}_{\mathrm{A}},3} = 61.1\,\mathrm{m}$. The result of the fitted function is shown Fig. 7.11.

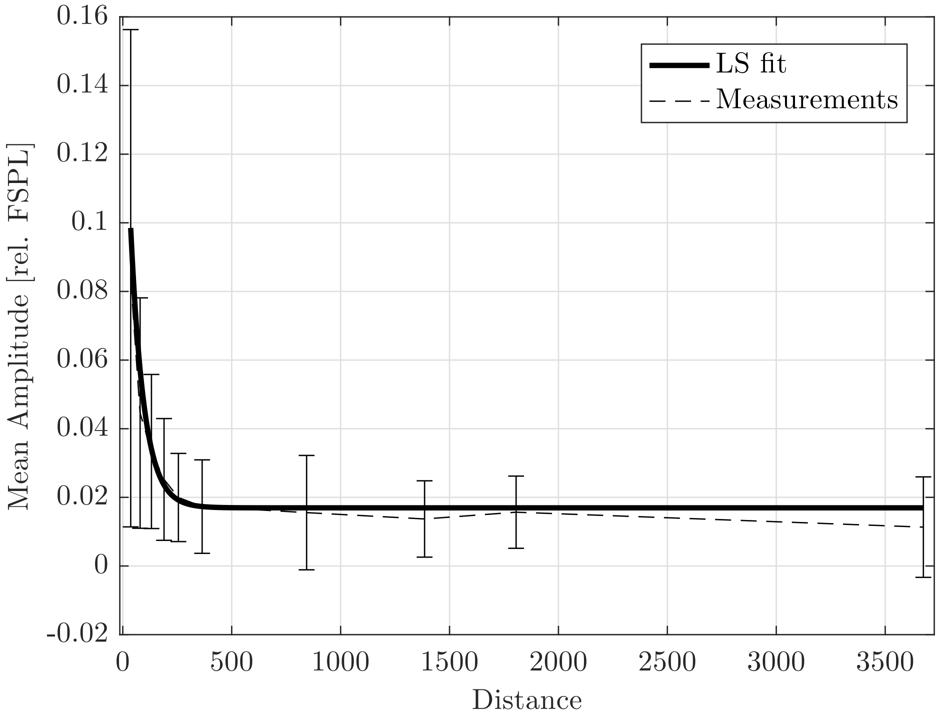

Figure 7.11. *Mean of average reflector amplitude $\bar{\alpha}_{\mathrm{A}}$ as a function of the distance r.*

Average Amplitude Distribution As illustrated by the error bars in Fig. 7.11, for a given distance between ground station and reflector r', the average MPC amplitude varies around the distance dependent mean $\bar{\alpha}_{\mathrm{A}}(r')$. We are now concerned with that variation of the average MPC amplitude around the mean $\bar{\alpha}_{\mathrm{A}}(r)$. To characterize the distribution of that variation we normalize the average MPC amplitudes by the mean $\bar{\alpha}_{\mathrm{A}}(r)$

$$\hat{\alpha}_{\mathrm{An},k} = \frac{\hat{\alpha}_{\mathrm{A},k}}{\bar{\alpha}_{\mathrm{A}}(r_k)}. \tag{7.27}$$

Fig. 7.11 shows distribution of the normalized average MPC amplitude $p(\hat{\alpha}_{\mathrm{An}})$. We model the distribution of the normalized average amplitude $p(\alpha_{\mathrm{An}})$ using a log-normal distribution

$$p(\alpha_{\mathrm{An}}) \sim \log\mathcal{N}\left(\zeta_{\alpha_{\mathrm{An}},\mu} = -0.23, \zeta_{\alpha_{\mathrm{An}},\sigma} = 0.69\right). \tag{7.28}$$

Therefore, the distribution of the average MPC amplitude $p(\alpha_{\mathrm{A}}|r)$ is given as

$$p(\alpha_{\mathrm{A}}|r) \sim \log\mathcal{N}\left(\zeta_{\alpha_{\mathrm{An}},\mu}, \zeta_{\alpha_{\mathrm{An}},\sigma}\right)\bar{\alpha}_{\mathrm{A}}(r). \tag{7.29}$$

Complex Weight Variation In the following we investigate the variation of the complex weight of the MPC associated with a reflector. Modeling the variation as a function of the angle ϵ accounts for the physical observation that, apart from thermal

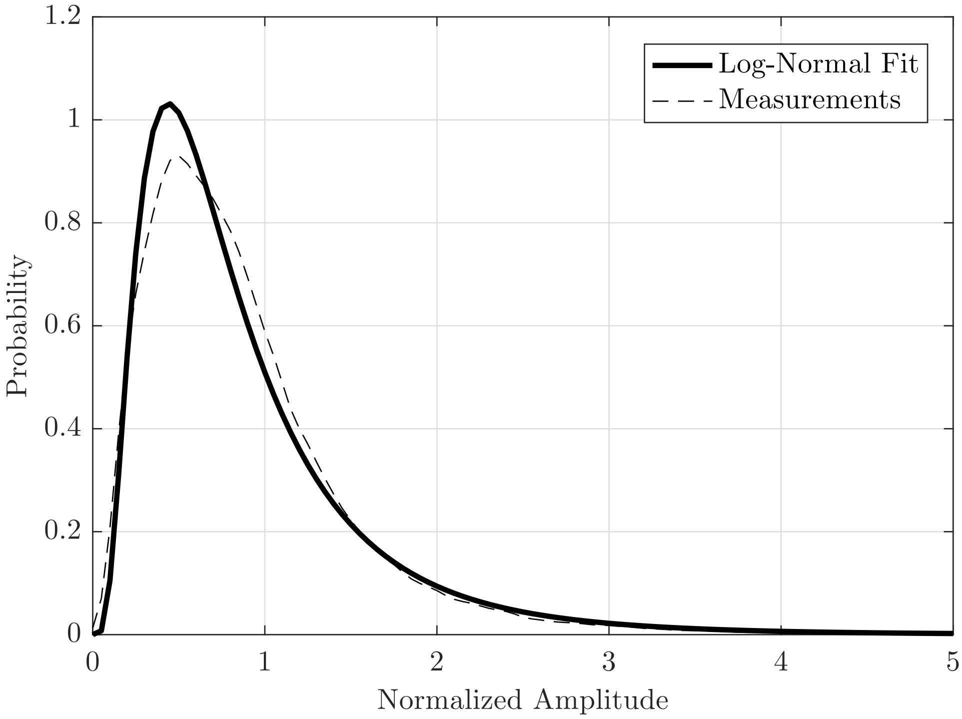

Figure 7.12. *Distribution of the normalized average reflector amplitude* $p\left(\hat{\alpha}_{\mathrm{An}}\right)$.

noise, the channel does not change if the aircraft is not moving, e.g., as possible for an airship or a helicopter.

For the analysis of the MPC's complex weight variation we normalize the complex weight of each MPC by its average amplitude

$$\hat{\boldsymbol{\alpha}}_{\mathrm{V},k} = \frac{\hat{\boldsymbol{\alpha}}_k}{\hat{\alpha}_{\mathrm{A},k}}. \tag{7.30}$$

In Fig. 7.13 we show the amplitude and phase of an MPC's complex weight $\hat{\boldsymbol{\alpha}}_{\mathrm{V},k}\left(\epsilon\right)$. We observe a correlation of amplitude and phase over the angle ϵ.

As illustrated in Fig. 7.14 we propose modeling the MPC's complex weight $\alpha_{\mathrm{V}}\left(\epsilon\right)$ as the sum of two random variables [33]

$$\alpha_{\mathrm{V},k}\left(\epsilon\right) = \alpha_{\mathrm{V,c},k} + \alpha_{\mathrm{V,ar},k}\left(\epsilon\right). \tag{7.31}$$

The variable $\alpha_{\mathrm{V,c},k}$ describes the mean of $\alpha_{\mathrm{V},k}\left(\epsilon\right)$ and $\alpha_{\mathrm{V,ar}}\left(\epsilon\right)$ the variation over the angle ϵ. The amplitude of $\alpha_{\mathrm{V,c}}$ is '1' and its phase is uniformly distributed

$$\alpha_{\mathrm{V,c}} = e^{\mathrm{j}\arg\left(\alpha_{\mathrm{V,c}}\right)} \quad \text{with} \quad \arg\left(\alpha_{\mathrm{V,c}}\right) \sim \mathcal{U}\left(0, 2\pi\right). \tag{7.32}$$

The random variable $\alpha_{\mathrm{V,ar}}\left(\epsilon\right)$ is drawn from an autoregressive (AR) process.

For the modeling of $\alpha_{\mathrm{V},k}\left(\epsilon\right)$ we require the following information from the measured data:

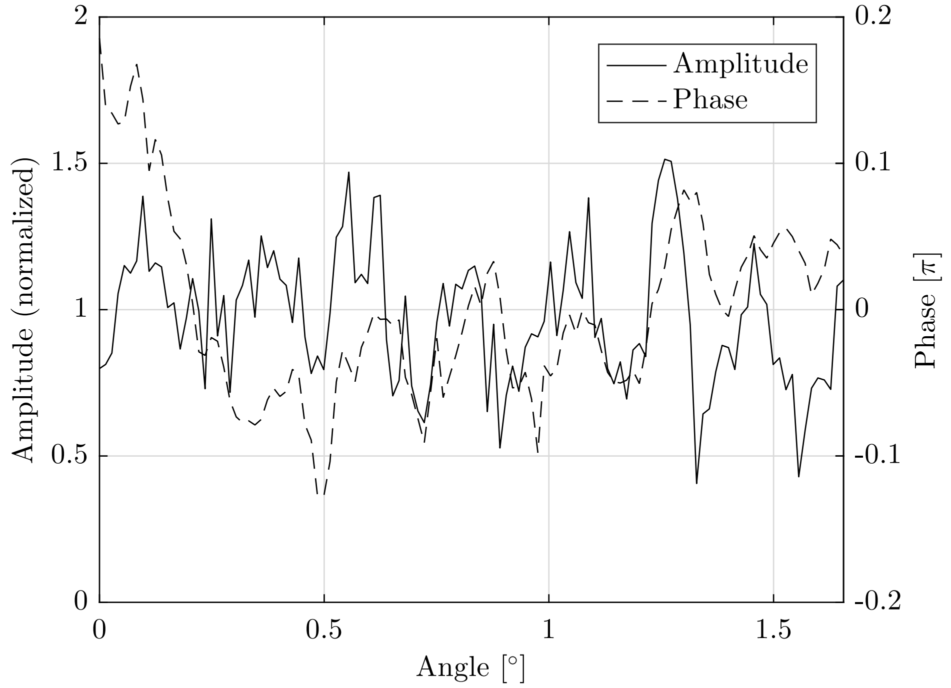

Figure 7.13. *Distribution of the amplitude, normalized by the mean amplitude of the reflector.*

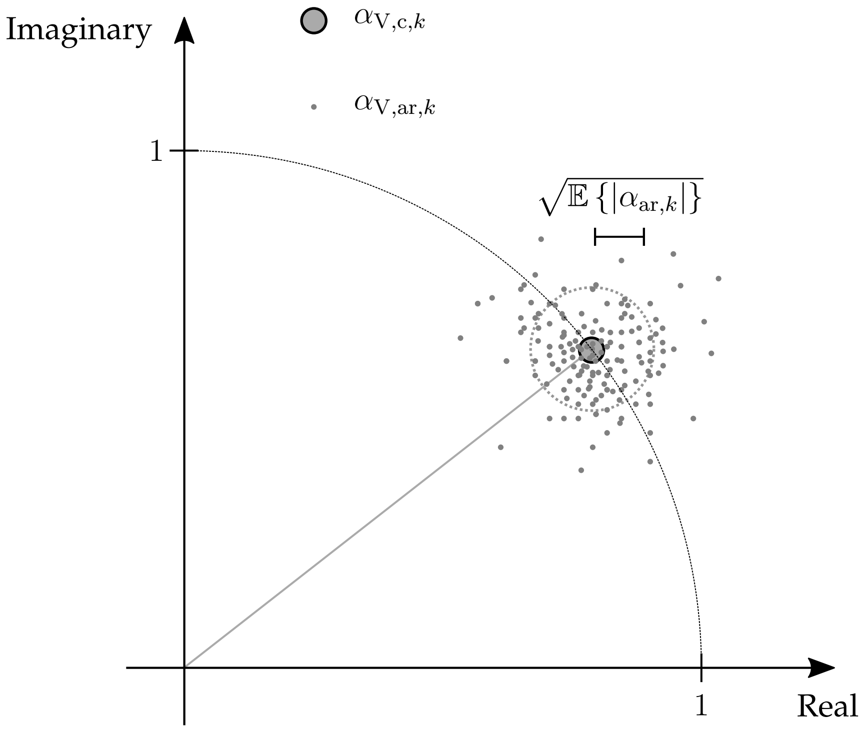

Figure 7.14. *Proposed modeling approach for the variation of the complex weight.*

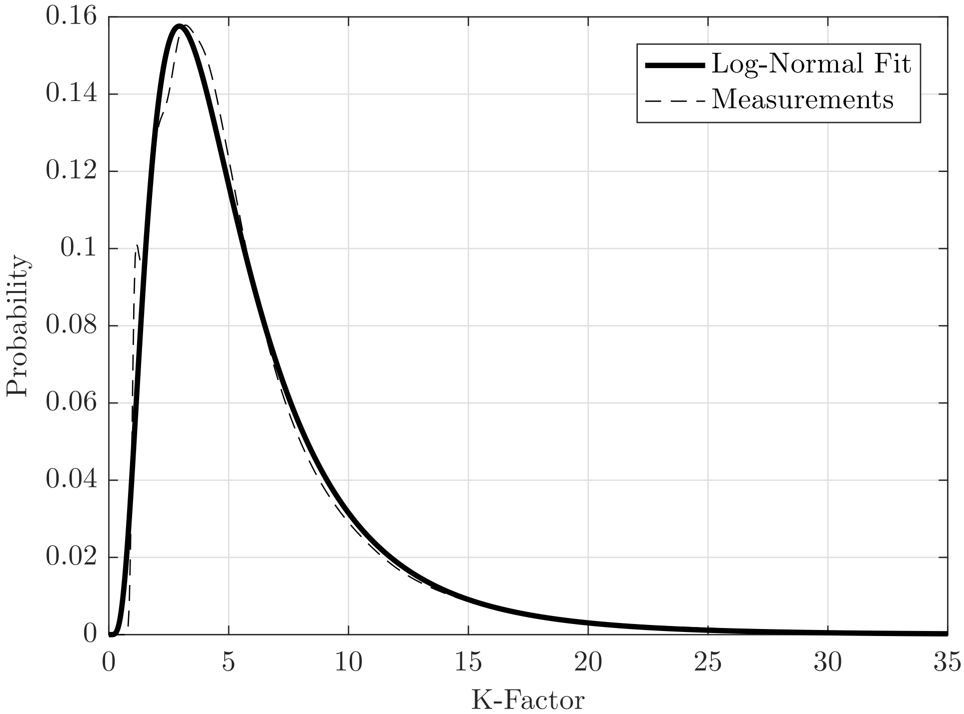

Figure 7.15. *Distribution of the K-factor used to model the complex weight variation.*

- The K-factor, i.e., the inverse power $\alpha_{\mathrm{V,ar},k}^{-2}$ of the AR process[2].
- The model order and pole(s) of the AR process describing $\alpha_{\mathrm{V,ar},k}$.

***K*-factor** The K-factor is calculated as the inverse variance of the normalized complex weight $\hat{\boldsymbol{\alpha}}_{\mathrm{V},k}$, i.e.

$$\begin{aligned}\hat{\mathcal{K}}_{\alpha,k} &= \frac{1}{\mathrm{var}\{\hat{\boldsymbol{\alpha}}_{\mathrm{V},k}\}}\\ &= \|\hat{\boldsymbol{\alpha}}_{\mathrm{V},k} - \sum_{m=1}^{M_k} \hat{\alpha}_{\mathrm{V},k,m}\|^{-2}.\end{aligned} \tag{7.33}$$

The distribution of the K-factor $p\left(\hat{\mathcal{K}}_\alpha\right)$ is shown in Fig. 7.15. We model the distribution of the K-factor $p\left(\hat{\mathcal{K}}_\alpha\right)$ using a log-normal distribution

$$p\left(\hat{\mathcal{K}}_\alpha\right) = \log\mathcal{N}\left(\zeta_{\alpha_{\mathrm{V},K},\mu} = 1.83, \zeta_{\alpha_{\mathrm{V},K},\sigma} = 0.68\right). \tag{7.34}$$

[2] The K-factor is defined as the ratio between the power of $\alpha_{\mathrm{V,c},k}$ and the power of the AR process $\alpha_{\mathrm{V,ar},k}$. As the power of $\alpha_{\mathrm{V,c},k}$ is equal to '1' we only need to consider the inverse power of the AR process $\alpha_{\mathrm{V,ar},k}$.

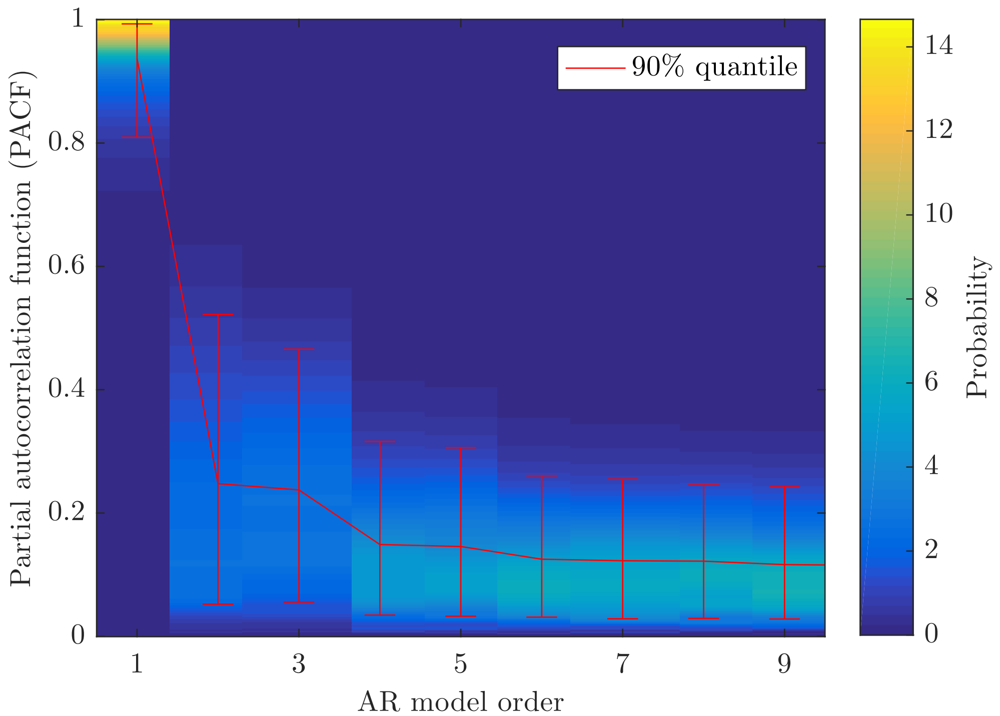

Figure 7.16. *Distribution of the PACF.*

AR Process Order and Poles To select the model order of the AR process we inspect the distribuation of the partial autocorrelation function (PACF) shown in Fig. 7.16 [111]: for every reflector we calculate the PACF and use a Gaussian kernel smoother to estimate the distribution over the reflectors. We observe that for most reflectors the majority of the power is expressed by the first AR coefficient. Therefore, in order to limit the complexity of the channel model, we use an order of '1' for the AR process.

We calculate variable $\hat{\boldsymbol{\alpha}}_{\mathrm{V,ar},k}$ to be modeled by the AR process as

$$\hat{\boldsymbol{\alpha}}_{\mathrm{V,ar},k} = \hat{\boldsymbol{\alpha}}_{\mathrm{V},k} - \sum_{m=1}^{M_k} \hat{\alpha}_{\mathrm{V},k,m}. \tag{7.35}$$

Note however that the vector $\hat{\boldsymbol{\alpha}}_{\mathrm{V,ar},k}$ describes measurements of a time series. As we want to model the correlation between two elements in $\boldsymbol{\alpha}_{\mathrm{V,ar},k}$ as a function of one-dimensional angle ϵ, rather than the time, we resample $\hat{\boldsymbol{\alpha}}_{\mathrm{V,ar},k}$ to an angular grid. The resampled vector of complex weights is denoted as $\hat{\boldsymbol{\alpha}}_{\mathrm{V,ar}\epsilon,k}$. Resampling all complex weights to a grid with the same grid spacing ϵ_Δ allows the comparison of the AR parameters between the detected MPCs. The pole of the AR process $\hat{\gamma_{\mathrm{ar}}}_k$ is estimated based on $\hat{\boldsymbol{\alpha}}_{\mathrm{V,ar}\epsilon,k}$ using the Vieira-Morf algorithm [112].

Fig. 7.17 shows the distribution of the absolute value of pole $p\left(|\hat{\gamma_{\mathrm{ar}}}|\right)$. For the generation of Fig. 7.17 we use a grid spacing $\epsilon_\Delta = 0.05°$. As the imaginary part of

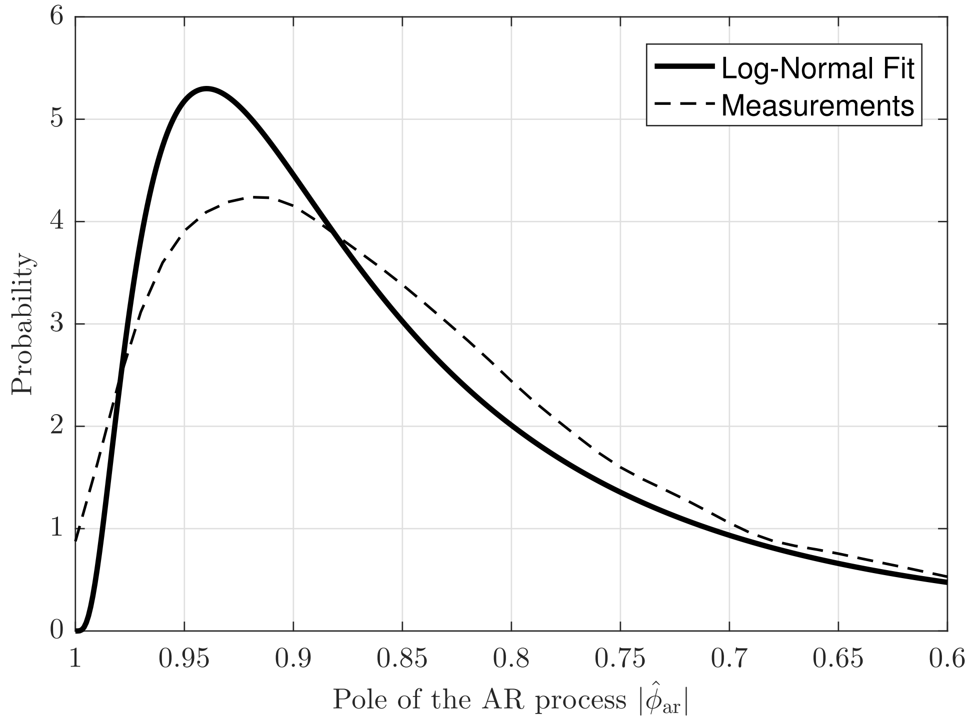

Figure 7.17. *Distribution of the pole $p\left(|\hat{\gamma_{\mathrm{ar}}}|\right)$ of the AR process used to model the complex weight variation.*

the pole $\mathrm{Im}\left\{|\hat{\gamma_{\mathrm{ar}}}|\right\}$ is typically negligible we assume the pole to be only real. We model the distribution of $p\left(1-\gamma_{\mathrm{ar}}\right)$ using an log-normal distribution

$$p\left(1-\gamma_{\mathrm{ar}}\right) = \log\mathcal{N}\left(\zeta_{\alpha_{\mathrm{V},\varphi,\mu}} = -2.07, \zeta_{\alpha_{\mathrm{V},\varphi,\sigma}} = 0.86\right). \tag{7.36}$$

Note that distribution of the pole $p\left(1-\gamma_{\mathrm{ar}}\right)$ has to be truncated at 2 to avoid non-stable AR processes.

Window Function The window function takes into account the physical requirement that the MPC amplitudes are time-continuous. In Fig. 7.18 we show the MPC amplitude distribution at the edges of the cone representing a reflector. We observe a decrease of the amplitude of $\hat{\alpha}_{\mathrm{A}}$ before the signal vanishes. The window function is modeled as

$$\alpha_{\mathrm{W}}\left(\epsilon|\omega\right) = \begin{cases} 1-\exp\left\{-\zeta_{\alpha_{\mathrm{W}},1}\left(\left(\omega-\epsilon\right)-\zeta_{\alpha_{\mathrm{W}},2}\right)\right\} & \text{for } \omega_k-\epsilon>0, \\ 0 & \text{else.} \end{cases} \tag{7.37}$$

The coefficients in (7.37) are LS estimated based on the measured data as $\zeta_{\alpha_{\mathrm{W}},1} = 3\cdot 10^3$ and $\zeta_{\alpha_{\mathrm{W}},2} = 0.89$.

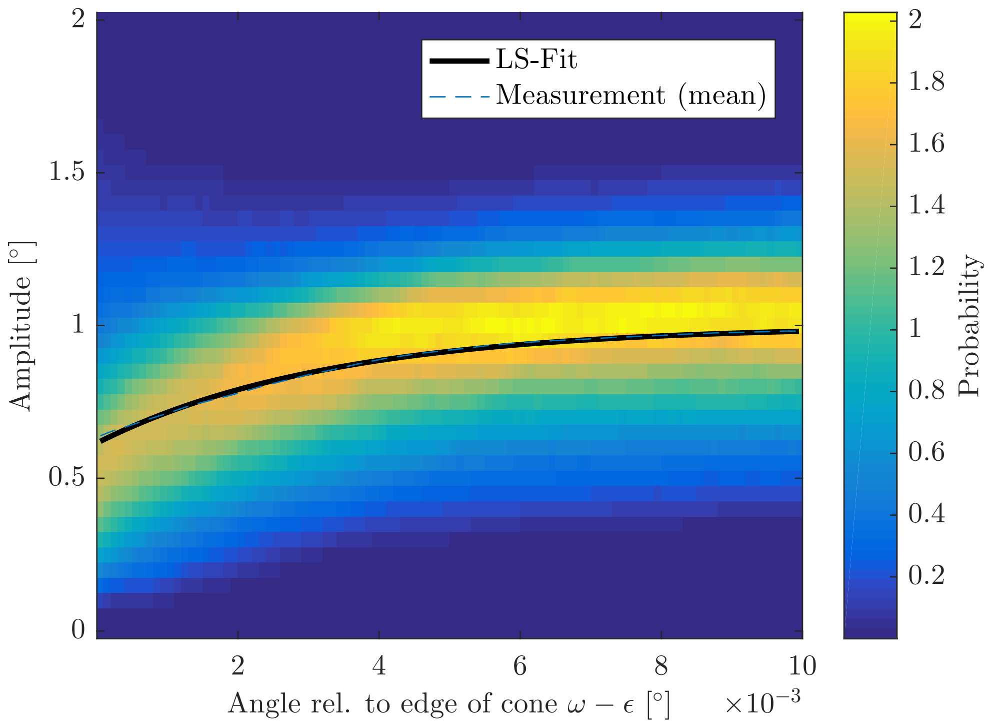

Figure 7.18. *Distribution of the MPC amplitude close to the edges of the cone representing a reflector.*

7.2.4 Ground Shadowing

In this section, we investigate the effect of ground shadowing. To this end, we analyze Fig. 6.4 from the previous section: the figure shows the LoS signal power versus the aircraft position as seen from the ground station. If ground shadowing occurs during the flight the effects of ground shadowing would visible in Fig. 6.4: first, by a drop of the LoS signal power and second by a "disappearing" of the aircraft, e.g., behind a building.

We observe that due to the antenna being located on a high building, ground shadowing generally does not arise for the investigated flight trajectories: ground shadowing would only be observed for an extremely low flying aircraft. The channel model parameterization presented in this dissertation is aimed at normal aircraft flying typical trajectories, i.e., it does not cover aircraft on the ground. Thus, we do not consider ground shadowing by buildings in the following. Note however that if the antenna height was lower ground shadowing would become relevant.

The only instance where the signal is shadowed is when the aircraft disappears behind the radio horizon (marked with an 'H' in Fig. 6.4). However, the channel model parameterization proposed in this dissertation does not consider the aircraft flying behind the radio horizon.

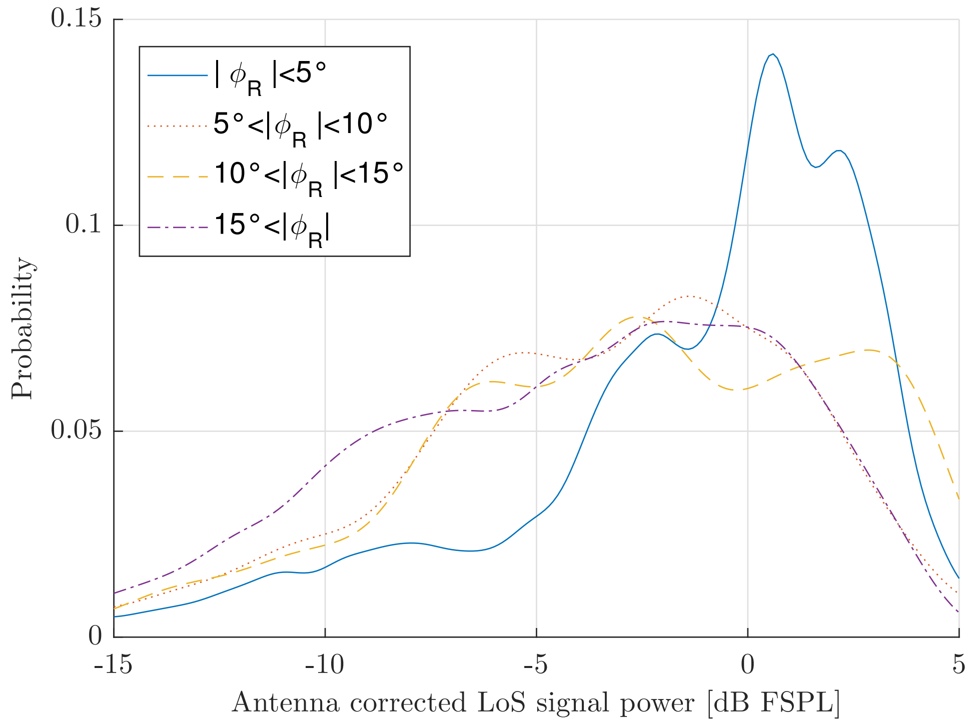

Figure 7.19. *Influence of the airframe on the LoS signal power as a function of the roll angle.*

7.2.5 Antennas

In this section we investigate the effects of the ground and airborne antennas on the channel. For the inclusion of the antennas we rely on the antenna radiation patterns measured in an anechoic chamber (the antenna is mounted on a ground plane of $30\,\mathrm{cm}$ diameter).

In the following, we analyze how well the antenna radiation patterns are able to predict the measured LoS signal power. To this end, we normalize the measured LoS signal power by the gain of ground and aircraft antennas given aircraft position and attitude. We term the resulting power as the antenna corrected LoS signal power.

Fig. 7.19 shows the distribution of the antenna corrected LoS signal power for different (absolute) aircraft roll angles $|\varphi_\mathrm{R}|$.

For small roll angles, i.e., $|\varphi_\mathrm{R}| < 5°$, the antenna corrected LoS signal power is distributed equally around $0\,\mathrm{dB}$ (relative to FSPL): the mean is $0.1\,\mathrm{dB}$. Therefore, for $|\varphi_\mathrm{R}| < 5°$ we are able to successfully compensate the gain introduced by the ground and airborne antennas. The wide distribution of the antenna corrected LoS signal power around $0\,\mathrm{dB}$ is attributed to ground multipath propagation. Note that ground multipath propagation on average does not change the mean LoS signal power but only causes a spreading of the LoS signal power distribution.

For increasing roll angles $|\varphi_\mathrm{R}|$ we observe the increasing influence of the airframe. Less power is received than expected as the LoS is shadowed, e.g., by the wings or the tail. We conclude that the proposed modeling approach is very precise for roll angles below $5°$.

For larger roll angles an error is introduced. This error could be compensated if the aircraft pattern, i.e., airborne antenna plus airframe, was available: the aircraft pattern could either be measured in an anechoic chamber or estimated based on simulations [107]. However, both techniques require a large amount of resources. Therefore, modeling the influence of the airframe is beyond the scope of this dissertation: we treat the effects of the airframe as part of the channel.

7.2.6 Diffuse Multipath Components

The diffuse MPCs represent both clusters of reflectors and the effect of scattering. Due to the limited resolution of the MPC parameter estimation objects causing these diffuse MPCs can generally not be located. Diffuse MPCs manifest themselves as a colored noise component in the measured signal. Note however that the influence of the diffuse MPCs on an application system is very minor as its typical power is usually below $-20\,\mathrm{dB}$ (relative to FSPL). Thus, for most applications the diffuse MPCs may be omitted to save simulation time.

In order to model the diffuse MPCs we propose a geometry-based stochastic approach: we describe the decay of the power over the delay, i.e., the power delay profile (PDP), by an exponential function [84], [86]. The spread of the power over the Doppler frequency is a function of aircraft position and speed vector.

Modeling of the PDP

We model the decay of the diffuse MPCs' PDP (relative to FSPL) using an exponential function

$$\sigma^2_{\mathrm{CN}}(\tau) = \zeta_{\mathrm{CN,y}} e^{-\tau\zeta_{\mathrm{CN,s}}}. \tag{7.38}$$

The exponential function is defined by the y-intersection point $\zeta_{\mathrm{CN,y}}$ and slope $\zeta_{\mathrm{CN,s}}$. We estimate the two parameters describing the diffuse MPCs for every channel sounding block based on the residual signal, i.e., the signal minus the detected MPCs. An analysis of the measured data shows that the y-intersection point $\zeta_{\mathrm{CN,y}}$ can be modeled as an exponential function of the link distance d

$$\zeta_{\mathrm{CN,y}}(d) = e^{\zeta_{\mathrm{CN,y,1}} + d\zeta_{\mathrm{CN,y,2}}} \tag{7.39}$$

with $\zeta_{\mathrm{CN,y,1}} = -6.21$ and $\zeta_{\mathrm{CN,y,2}} = -0.06\,\mathrm{km}^{-1}$. The slope is modeled constant as $\zeta_{\mathrm{CN,s}} = 1.07\,/\mathrm{\mu s}$.

Modeling of the Scattering Function

To model the spread of the diffuse MPCs power over the Doppler frequency we make the following assumption: the colored noise is caused by a cloud of $\zeta_{\mathrm{CN,N}} = 200$ scatterers located around the ground station. All scatterers are located in the ground plane. Their east and north coordinates follow a normal distribution, i.e.,

$$p\left([d_{\mathrm{CN,E}}, d_{\mathrm{CN,N}}]^{\mathrm{T}}\right) \sim \mathcal{N}\left(0, \mathbb{I}_2 \zeta^2_{\mathrm{CN},\sigma}\right). \tag{7.40}$$

We adopt the power of each scatterer as described in [113]: given the aircraft position and speed vector we calculate the delay associated which each scatterer. The power at delay τ' bin of the target PDP shown in Fig. 7.20 is equally distributed to all scatterers with a delay falling into the bin τ'. Each of the scatterers with the same delay τ' has a different Doppler frequency based on its location: thus, the power at the delay τ' is spread over the Doppler frequency as shown in Fig. 7.21. From Fig. 7.20 we observe that the target PDP is almost exactly replicated by the modeling approach.

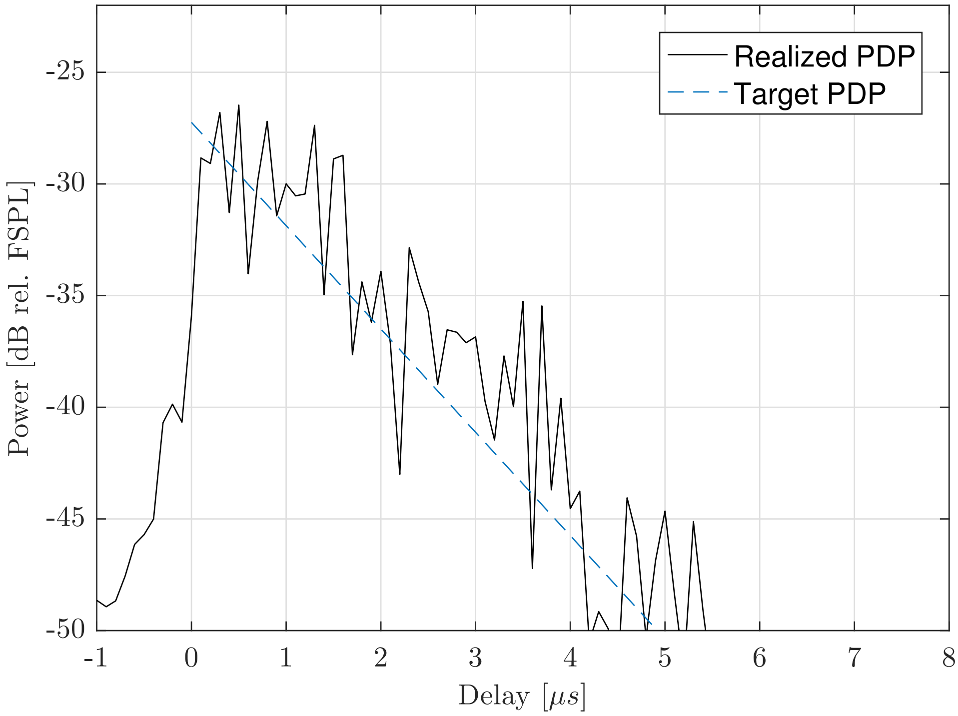

Figure 7.20. *Target PDP and realized PDP of the diffuse MPCs.*

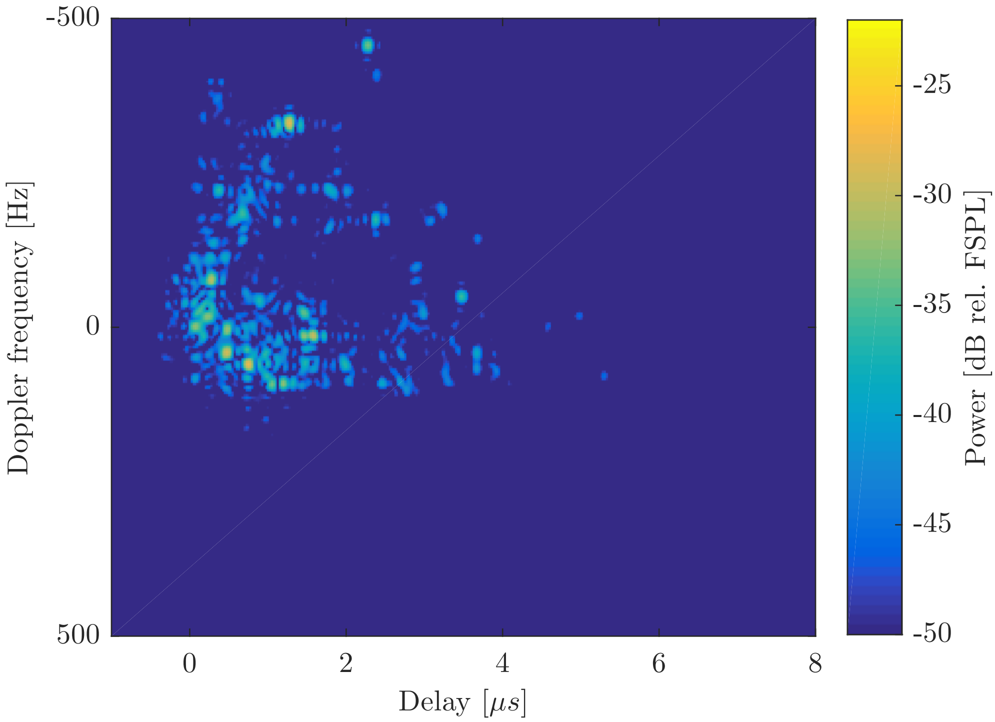

Figure 7.21. *Scattering function of the diffuse MPCs in a highly dynamic flight situation (TL scenario).*

7.3 Validation of the Parameterization

In the following, we validate the regional airport channel model parameterization presented in Sec. 7.2. The channel model parameterization is validated against the measured results presented in Chapter 6.

For the validation we use the simulation chain as described in Sec. 3.3.2: the channel model realization is first initialized, e.g., reflector locations and ground reflecting areas are drawn from the associated distributions. Given the aircraft trajectory and attitude we use the channel model to calculate the channel impulse response (CIR) for each aircraft position. Each CIR is then convoluted with the desired transmit signal. The resulting signal, in the following referred to as the modeled signal, is compared with the measured signal.

Note that it is not the goal of the validation to exactly reproduce the measured signal with the channel model - the proposed geometry-based stochastic channel model (GBSCM) is not a ray tracer. Rather, we aim to generate a signal with the same properties relevant for a typical communication, navigation, and surveillance (CNS) system: as measurements using different aircraft trajectories lead to different results, also different channel model realizations of the channel model lead to a different signal. This effect is desired as it allows to simulate the behavior of CNS systems for different propagation conditions likely to exist in a regional airport environment.

For the validation we rely on three methods:

Quantitative validation: In Sec. 7.3.1 we compare the statistical characteristics, e.g., PDP and Doppler power profile (DPP), of the measured and modeled channel.

Qualitative validation: We investigate how well the channel can represent the non-stationarity of the channel. To this end, we first analyze the LoS signal power against the aircraft position. Furthermore, we apply the MPC parameter estimation algorithm presented in Sec. 4.5 to both measured and modeled channel sounding data.

Application: We use the channel model to investigate the ranging performance of the L-band Digital Aeronautical Communication System (LDACS). In Sec. 7.3.3 these ranging results are compared with the results from the flight trial ranging experiments described in [101].

For the validation we often refer to the three scenarios described in Sec. 6.4: we use the same flight trajectories, i.e., aircraft position and attitude, as conducted during the 2013 flight trials as input to the channel model.

7.3.1 Quantitative Validation

The quantitative validation consists of comparison of the measured and modeled channel's key statistical parameters: the evaluated parameters are the distribution of the LoS signal power, the distribution of the PDP and DPP and, and the distribution of the delay spread.

Line of Sight Signal Power

The most important channel characteristic defining the coverage of a terrestrial CNS system is the LoS signal power[3].

In Fig. 7.22 we compare the distributions of the measured and the modeled LoS signal power for the three scenarios. To this end, we show the 90% quantile of the LoS signal power distribution based on 50 channel model realizations.

Overall we can conclude that in all scenarios the measured distribution fits well between the model's LoS signal power quantiles: apart from the tails, the measured distribution could very well originate from a realization of the channel model. The difference of mean LoS signal power between channel model and measurements is relatively small: in the TL scenario $0.6\,\mathrm{dB}$, in the CD scenario $1.9\,\mathrm{dB}$, and in the EC scenario $1.1\,\mathrm{dB}$.

One reason for the slightly lower measured LoS signal power becomes apparent when analyzing the distributions' tails: especially in the TL and CD scenarios the measured distribution has wider tails at low power levels. Further analysis shows that the low LoS signal power levels are mostly associated with the aircraft either performing steep turns or flying on an orbit around the ground station. Thus, the attenuation is most likely caused by the aircraft pattern. As effects caused by the airframe are not modeled a slight mismatch between measurements and channel model remains.

Another noticeable effect is the peak of the measured distribution in the EC scenario at $-4\,\mathrm{dB}$ relative to FSPL: a further analysis shows that the corresponding LoS signal fade is most likely caused by airframe shadowing. Due to the slight pitch of the aircraft during flight and the low elevation angle to the ground station, the rear part of the fuselage is likely to shadow the signal. This assumption is very reasonable when visually inspecting the aircraft. Furthermore, the attenuation appears only while the aircraft is flying north. When returning a similar effect cannot be observed.

[3] By the LoS signal power we understand the power contained in the first delay bin.

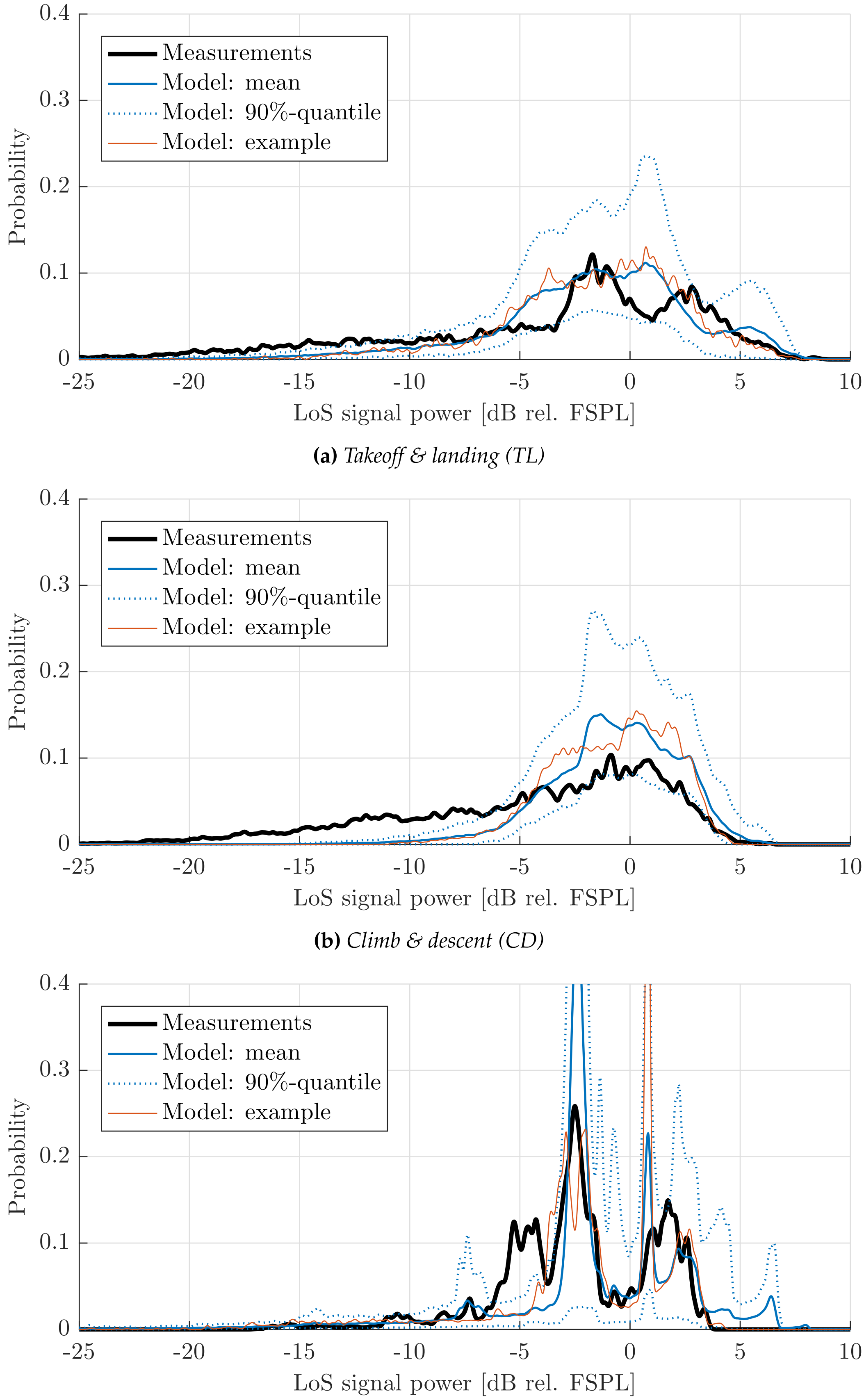

(a) *Takeoff & landing (TL)*

(b) *Climb & descent (CD)*

(c) *Enroute cruise (EC)*

Figure 7.22. *Measured and modeled LoS signal power distributions for the investigated scenarios.*

Power Delay Profile

The PDP describes the received power over the delay.

In Fig. 7.23 we show the distribution of the measured and modeled (one realization) PDPs for the three scenarios. The delay is taken relative to the LoS signal delay, i.e., we show the excess delay. The mean power is visualized by the dashed black line.

The most evident observation is that for each scenario the measured and modeled PDPs distribution look similar in shape: the overall decay of power over the delay is approximately the same: in both the measured and modeled PDP clusters of MPC are visible.

When comparing the two PDPs' distributions of each scenario we observe that the dominant MPCs appear at different delays. However, this behavior is both expected and desired: as we statistically distribute the reflector locations in each channel model realization the MPCs caused by those reflectors have different delays. Nevertheless, the channel model realizations all exhibit the same characteristics relevant for a terrestrial CNS system: the power decays in an almost identical fashion and we observe approximately the same number of MPC clusters.

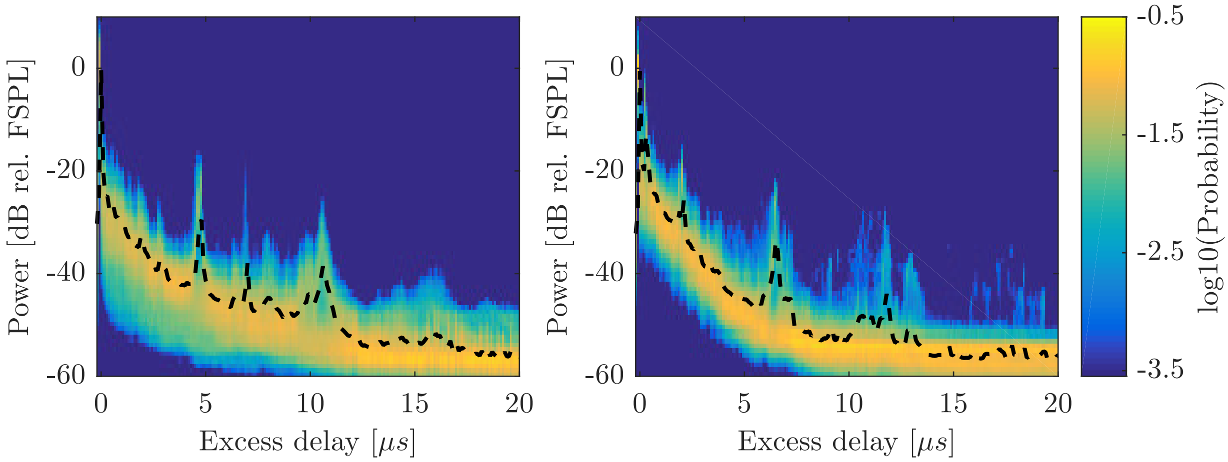

(a) *Takeoff & landing (TL)*

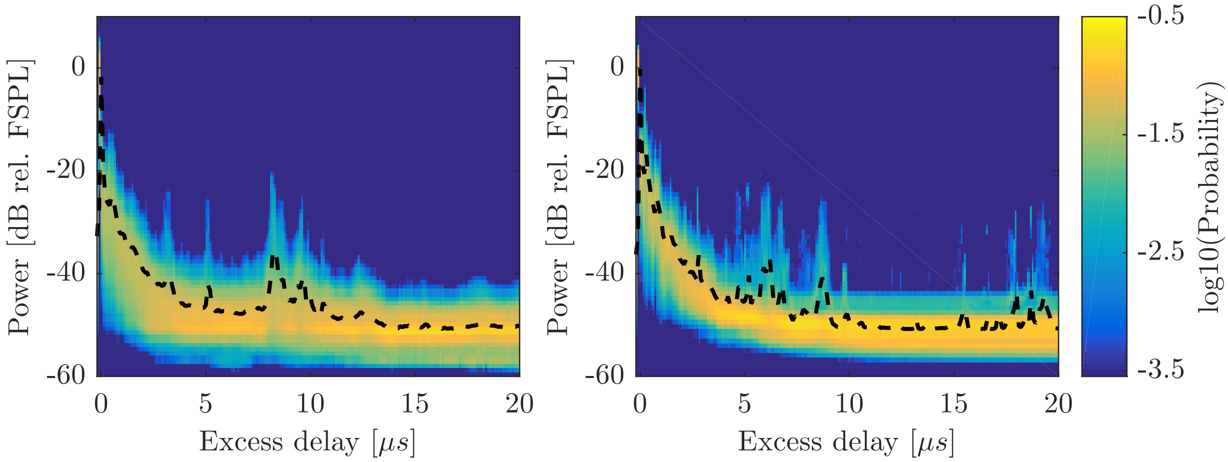

(b) *Climb & descent (CD)*

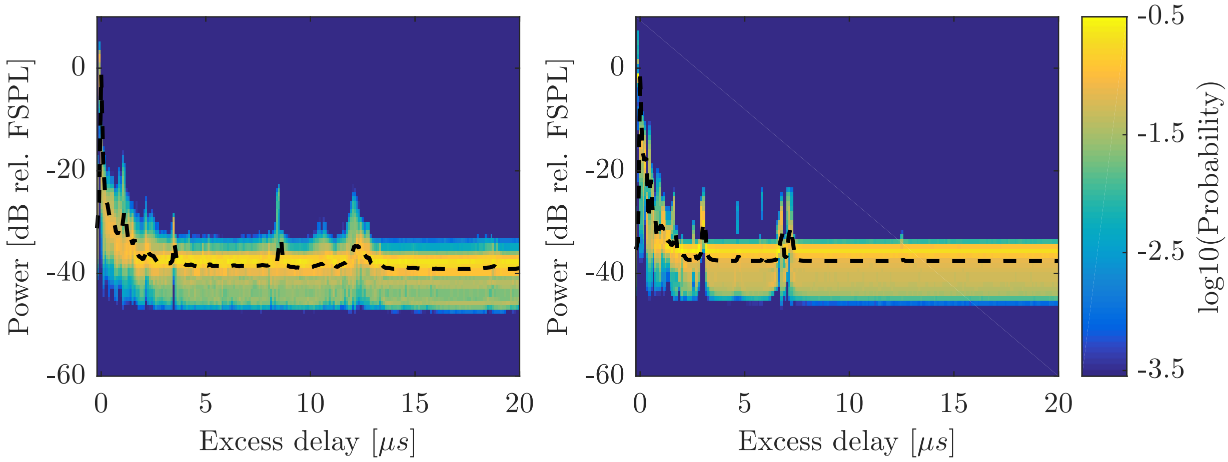

(c) *Enroute cruise (EC)*

Figure 7.23. *Measured (left) and modeled (right) PDP distribution.*

Doppler Power Profile

The DPP describes the received power over the Doppler frequency.

The distribution of the measured and modeled DPP is shown in Fig. 7.24. The Doppler frequency is taken relative to the LoS signal Doppler frequency, i.e., we show the excess Doppler frequency. The mean power is visualized by the dashed black line.

We observe that for all three scenarios the measured and modeled DPP distributions are approximately the same.

In the TL scenario the spread of the power over the Doppler frequencies from approximately $-150\,\mathrm{Hz}$ to $150\,\mathrm{Hz}$ directly around the maximum is well reproduced by the channel model. The wider spread of the power from $-600\,\mathrm{Hz}$ to $600\,\mathrm{Hz}$ - defined by the maximum aircraft speed - is also represented.

The slight spread of the power over the Doppler frequencies from $-30\,\mathrm{Hz}$ to $30\,\mathrm{Hz}$ in the CD scenario is also well reproduced by the channel model.

For an increasing link distance all power is exclusively received on the LoS Doppler frequency ν_{LoS}. This effect is well represented in the channel model.

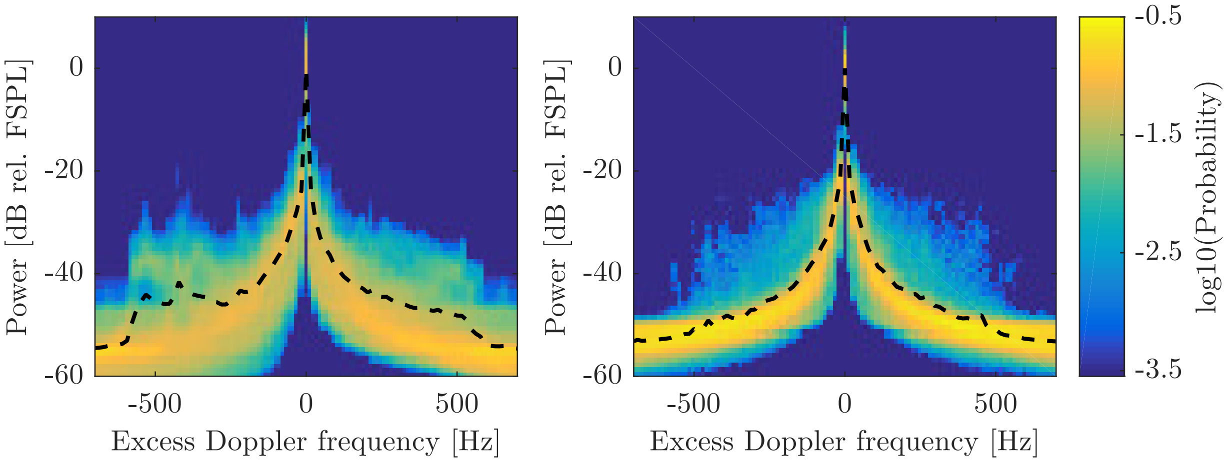

(a) *Takeoff & landing (TL)*

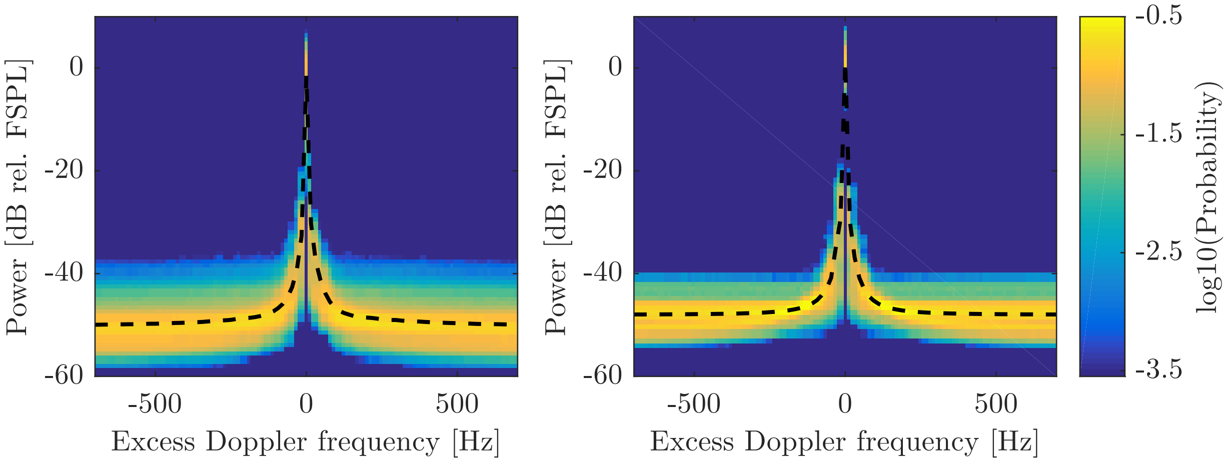

(b) *Climb & descent (CD)*

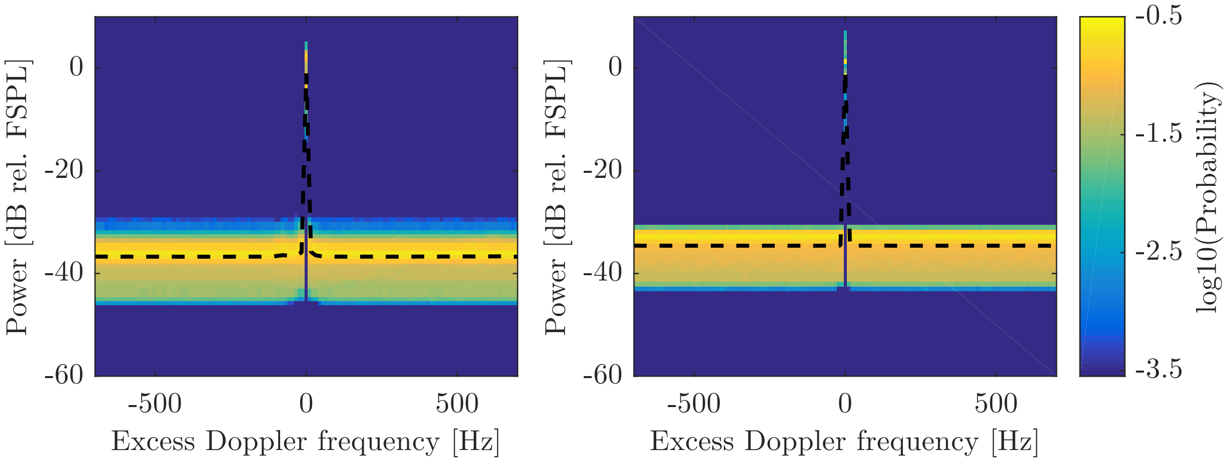

(c) *Enroute cruise (EC)*

Figure 7.24. *Measured (left) and modeled (right) DPP distribution.*

Rms Delay Spread

The root-mean-square (rms) delay spread describes the dispersiveness of the channel. For the calculation of the rms delay spread we only consider signal components whose power is at least above the 99%-quantile of the noise power - see Sec. 4.4

In Fig. 7.25 we show the distribution of the rms delay spreads for the three scenarios. The x-axis represents the delay and uses a logarithmic scaling. We compare the measured rms delay spread with the 90% quantile based on 50 channel model realizations. Additionally, for each scenario as an example we show a distribution based on one realization.

We observe that the rms delay spread distributions from measurements usually fall well within 90% quantile from the channel model. The example distributions are generally very similar to the measured distributions.

For the EC we discover that the measured distribution has a tail at rms delay spreads below $70\,\mathrm{ns}$. This tail is not reproduced by the channel model. We attribute this effect to shadowing of all signals by the rear part of the fuselage during one segment of the flight. The shadowing decreases the signal-to-noise-ratio (SNR): weaker signal components vanish in the noise floor and are not considered for the calculation of the rms delay spread.

In the EC scenario the channel model realizations differ from each other the most, visible by the larger quantiles. This effect is expected and desired in the model. The variation is attributed to the large link distance: MPCs are received from a smaller number of reflectors: the channel becomes less “statistical” and the rms delay spread distributions less “smooth”.

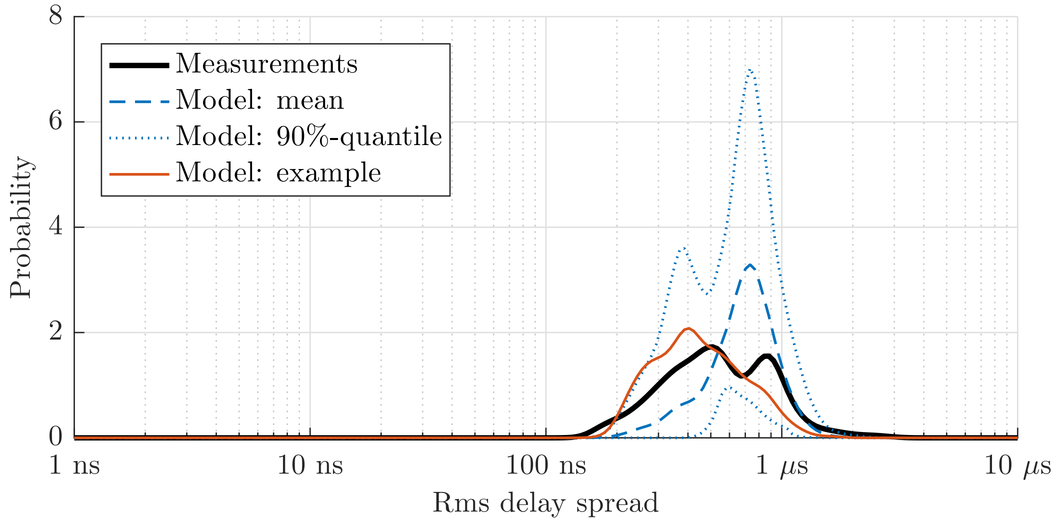

(a) *Takeoff & landing (TL)*

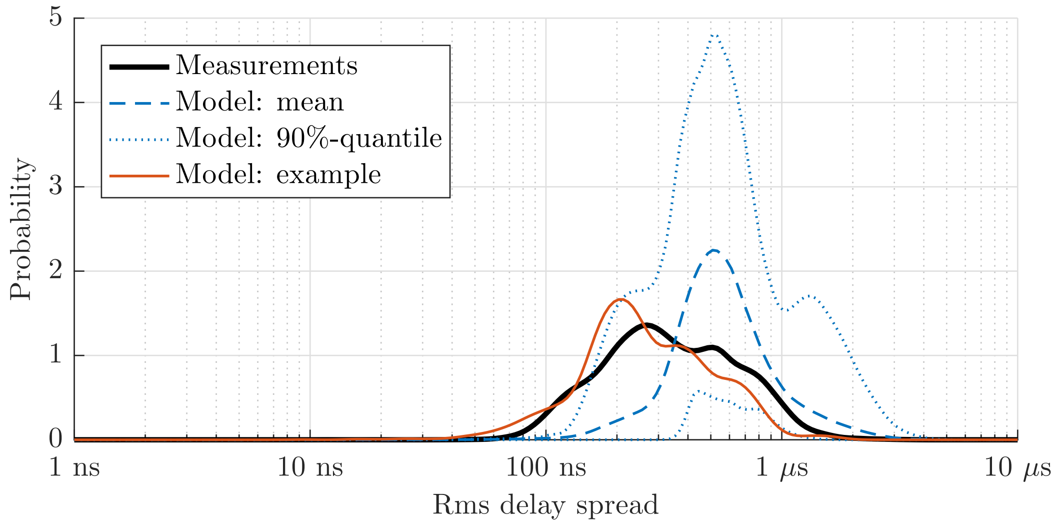

(b) *Climb & descent (CD)*

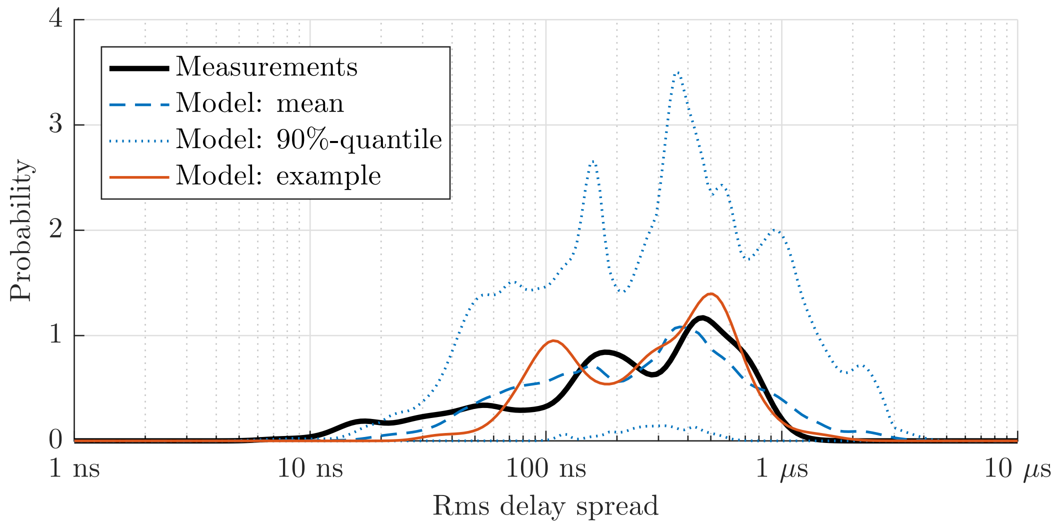

(c) *Enroute cruise (EC)*

Figure 7.25. *RMS Delay Spread.*

7.3.2 Qualitative Validation

In this section we show qualitative results to validate the channel model parameterization. We choose two approaches: first, we analyze the LoS signal power against the aircraft position. Second, we present results of the parameter estimation and tracking algorithm applied to the channel model data.

LoS Signal Power

In the following, we validate that the effect of the ground MPC is accurately reproduced by the channel model. We are especially interested in how well the chosen approach is able to represent the non-stationarity of the air-ground (AG) channel. Analogously to Fig. 6.3, in Fig. 7.26 we plot the LoS signal power against the aircraft position for two channel model realizations. The results in Fig. 7.26a are generated using the same ground reflecting areas as in Fig. 7.2. To exclude effects by the aircraft pattern we only consider regions where die aircraft is banking less than $5°$.

We observe that both the periodic variation as well as the long fades of the LoS signal power are well reproduced by the channel model. However, we observe that the fades are generally not as deep when the aircraft is flying on an orbit around the ground station: an effect we attribute to the aircraft pattern which not considered in the model.

Due to the random distribution of reflecting areas on the ground, fades of the LoS signal appear at different locations as in Fig. 6.3. Nevertheless, this effect is desired: each realization of the channel model produces a different channel. However, the statistics and non-stationarity of the different channel model realizations are very similar.

The frequency of LoS signal fades in the model may also be slightly different compared to Fig. 6.3 as we assume a flat area surrounding the ground station: this constant ground altitude is clearly a simplification as the terrain height around the ground station strongly varies, e.g., due to buildings or hills. Although a non-constant ground plane altitude could be incorporated in the model, the consequence would be a significantly higher complexity. The slightly differing occurrences of the LoS signal fades are not expected to alter the performance of a CNS system.

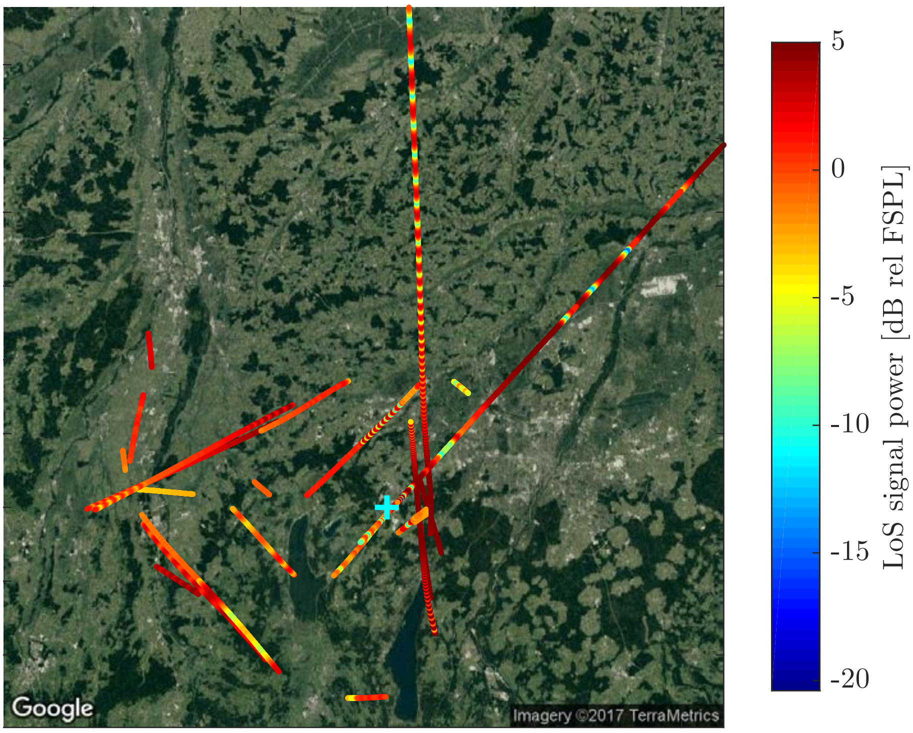

(a)

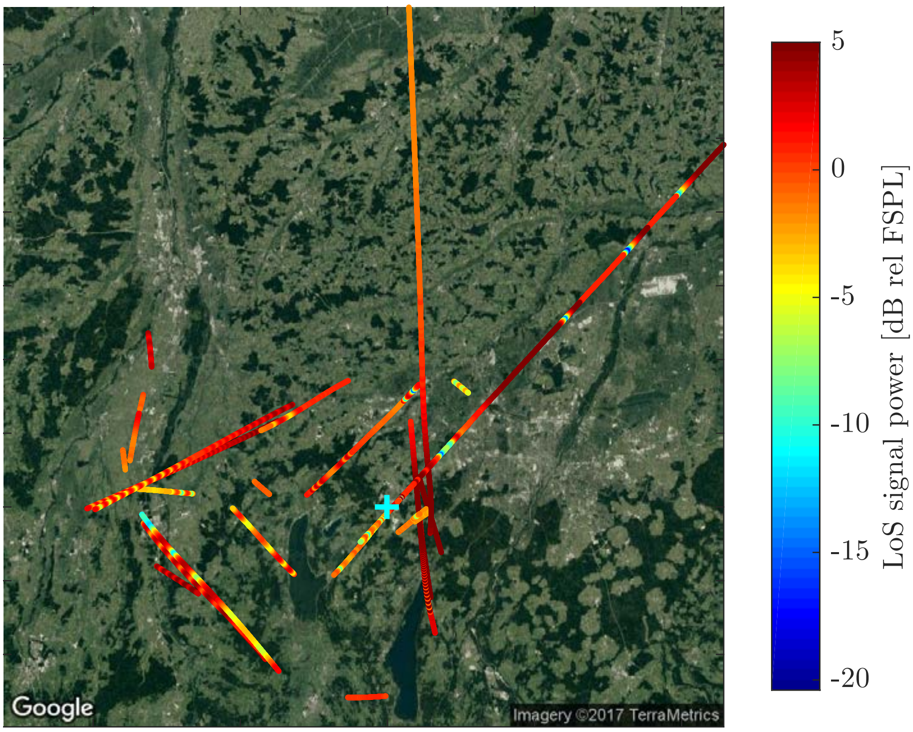

(b)

Figure 7.26. *LoS signal power against aircraft position for two channel model realizations.* ©*Google*

Multipath Component Parameters

In the following, we apply the MPC parameter estimation algorithm proposed in Sec. 4.5 to the modeled signal. In Fig. 7.27 we show the MPC parameter estimation results for the same flight segment investigated in Sec. 6.5 (Fig. 6.9 and Fig. 6.10) based on the modeled signal. The power of the MPCs is color coded. We plot both delay and Doppler frequency relative to the corresponding LoS signal parameter.

We observe that the detected MPCs in the modeled signal are distributed in a similar fashion over delay and Doppler frequency as for the measurements. The non-stationarity of the AG channel perceptible in the measured signal is reproduced by the channel model: the evolution of the individual MPCs over the time is well observable from Fig. 7.27. We also discover a similar Doppler frequency estimation variance as in the measured results shown in Fig. 6.10.

In Fig. 7.27c we compare the number of detected MPCs in the measured and modeled signal. We observe that both the average number of MPCs as well as the variation over time is approximately similar. The number of MPCs in the channel model is controlled by the number of reflectors $\zeta_{N_{\mathrm{ref}}}$ we distribute around the ground station in the channel model. Comparing measurements and channel model for other flight segments also shows a approximately similar numbers of MPC.

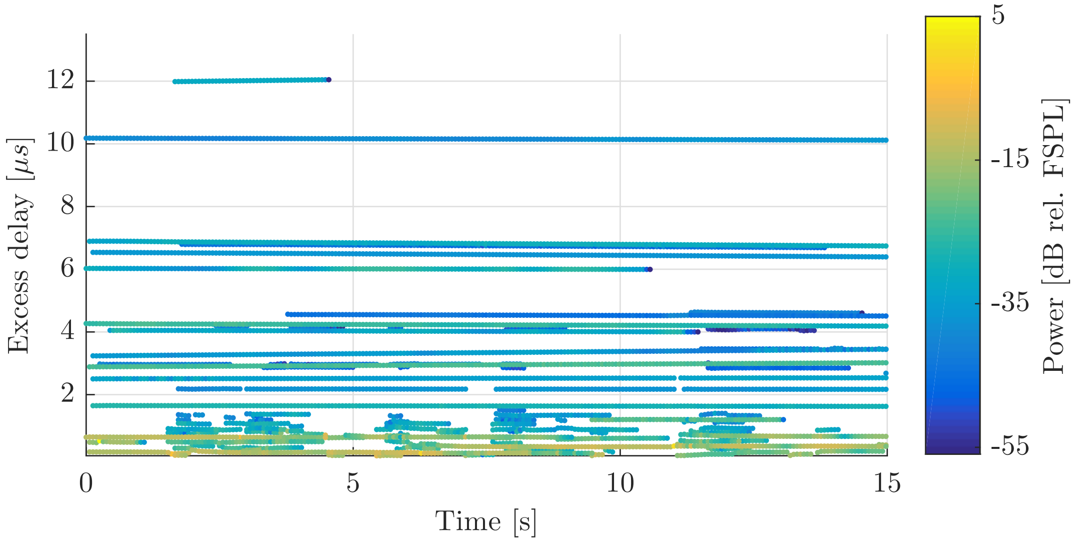

(a) *Delay*

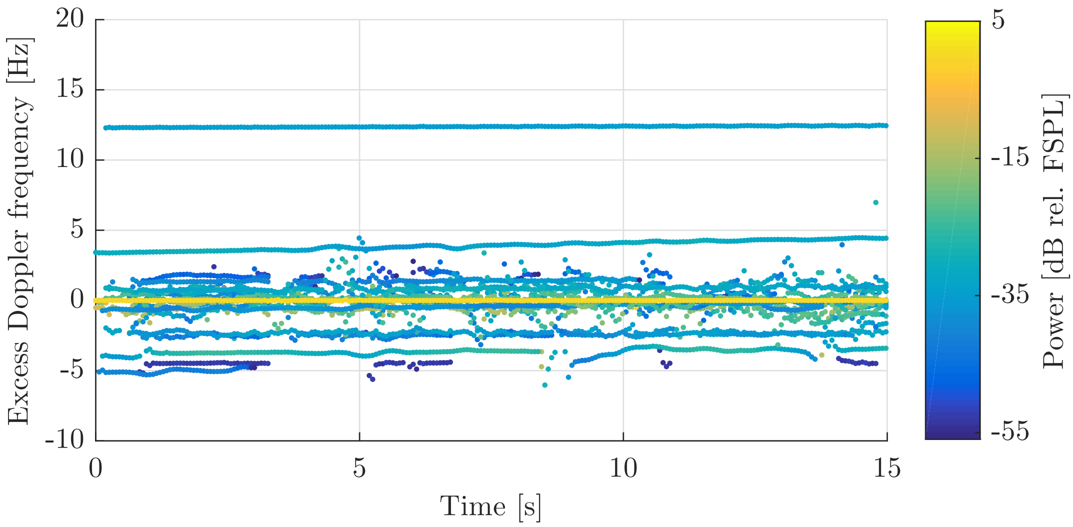

(b) *Doppler frequency*

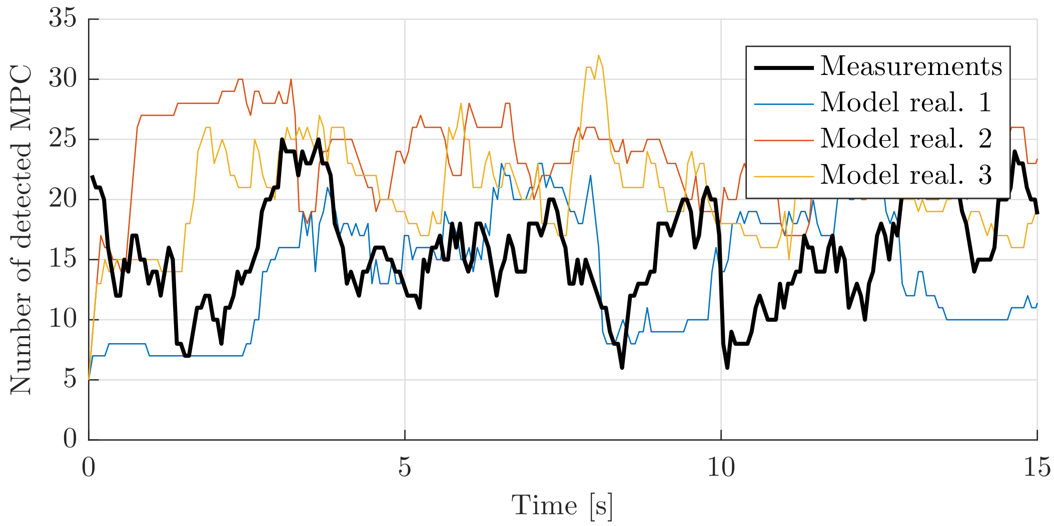

(c) *Number of detected MPC*

Figure 7.27. *Result of the MPC parameter estimation based on the modeled signal. The same flight segment is used as in Sec. 6.5 - see Fig. 6.8.*

7.3.3 Validation by Application

In the previous sections we validate the key channel parameters of the channel model against measurements. This validation is important as it verifies the similarity with respect to those key channel parameters. Nevertheless, the key performance indicator for a channel model is that the channel model can predict the performance of the systems it is intended for. Thus, in the following we validate the channel model using LDACS range measurements. We use data from the LDACS flight trials conducted the same year as the channel measurements [101].

For the validation by application we rely on two methods: first, an analysis of the statistical error distribution. Second, we analyze how well the model is able to reproduce the effects of the channel's non-stationarity on the ranging.

Statistical Analysis

In Fig. 7.28 we show both probability density function (PDF) and cumulative distribution function (CDF) of the LDACS ranging error. For the channel model we plot mean and 90% quantiles of the distributions based on 50 channel model realizations. We also present an example distribution based on one channel model realization.

From Fig. 7.28a we observe that the ranging error PDF from measurements and channel model approximately follow a normal distribution: compare the mean ranging error of $2.6\,\mathrm{m}$ from measurements with a mean of $1.1\,\mathrm{m}$ over all model realizations [4]. The RMSE of the measurements is $24\,\mathrm{m}$ and $22\,\mathrm{m}$ for the averaged channel model realizations.

In App. 7.28b we compare the absolute ranging error CDF based on measurements and channel model. A verification using the CDF is important as a mismatch of the two distributions tails becomes far more apparent as in the PDF. We again observe that the ranging error distributions based on measurements and channel model are almost identical.

For both PDF and CDF the measured distributions are well within the 90% quantile of the model; the example and measured distributions are almost identical. We conclude that the channel model is very well able to replicate the measured ranging error distributions. The ranging errors are not only very similar for the measurement flight shown in this dissertation but also for other flights.

[4]For both mean and root-mean-squared error (RMSE) we use the 99% quantile of the errors. This is done as a small number of errors in the measurements is caused by undetected distance measuring equipment (DME) interference - an effect we do not model in the channel model.

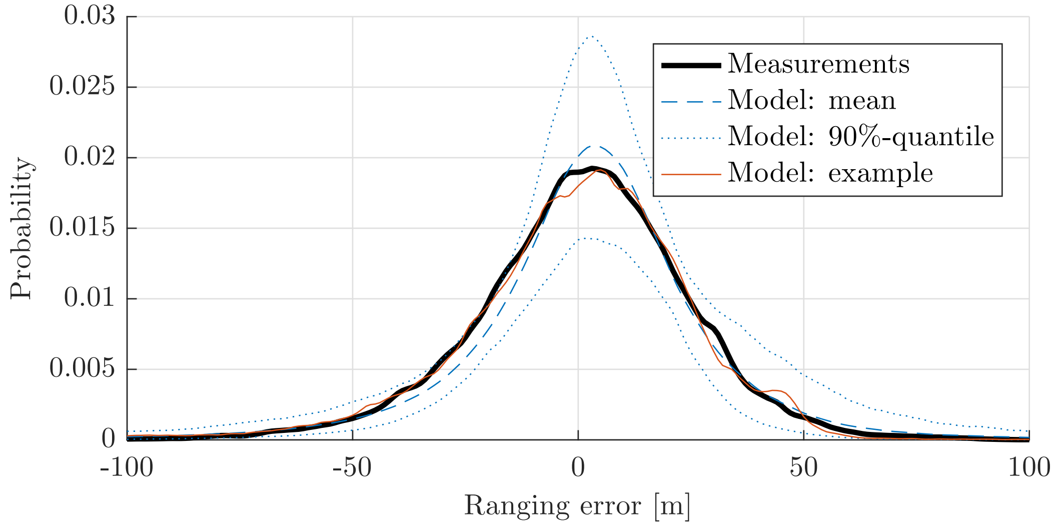

(a) *LDACS ranging error probability density function (PDF).*

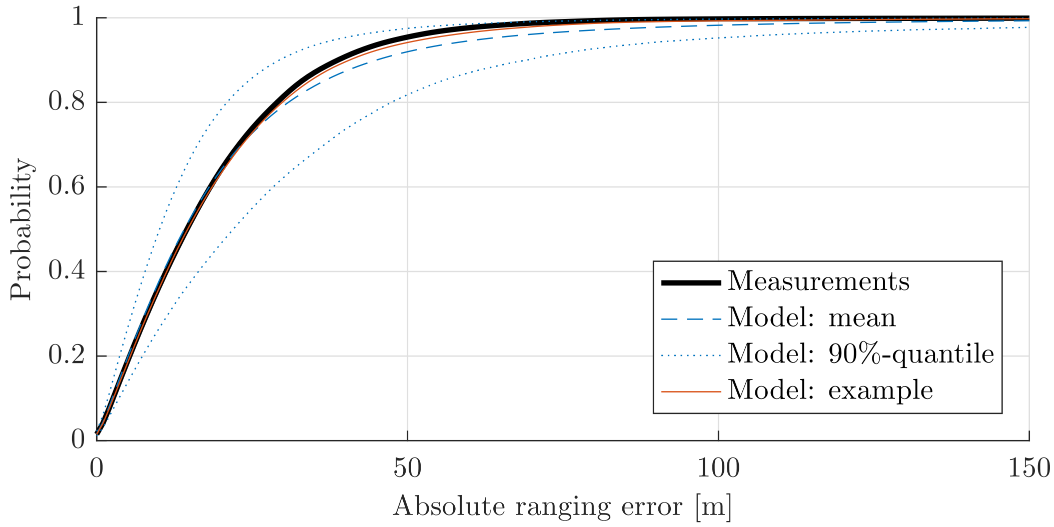

(b) *LDACS ranging error cumulative distribution function (CDF).*

Figure 7.28. *LDACS ranging errors based on measurements and channel model. The measured data was collected during the measurement flight conducted at 12th of November 2013 [101].*

Non-Stationarity

To this point we have only evaluated the statistical properties of the ranging errors. We have shown that the error statistics between measurements and model are almost identical. Nevertheless, this statistical validation gives no indication how well the effects of the channel's non-stationarity on the ranging performance is represented. This issue is investigated in the following.

As a qualitative analysis in Fig. 7.29a we plot the time series of the ranging error based on measurements and channel model. We observe that both in the measurements and channel model the ranging error for consecutive time instances is highly correlated. This correlation is caused by the fact that also the CIRs are also highly correlated. Due to the geometrical nature of the channel model these correlations can be well reproduced.

We now look at an characteristic of the ranging error of utmost importance in the context of navigation: the existence of slowly varying errors, e.g., an error exceeding $30\,\mathrm{m}$ and existing for a few seconds - an example is visible in Fig. 7.29a at a time of $1\,\mathrm{s}$. Such slowly varying errors cannot be mitigated by averaging, e.g., using a delay-locked loop (DLL). Thus the errors cause a severe integrity threat [24]. Note that a stationary statistical channel model is not able to reproduce these kind of errors.

Fig. 7.29b and Fig. 7.29c demonstrate the channel model's ability to reproduce slowly varying errors. The figures show how often such slowly varying errors of a given duration exceeding $10\,\mathrm{m}$ and $30\,\mathrm{m}$, respectively, occur during a $1\,\mathrm{h}$ flight. We observe that the channel model accurately reproduces the effect of slowly varying errors.

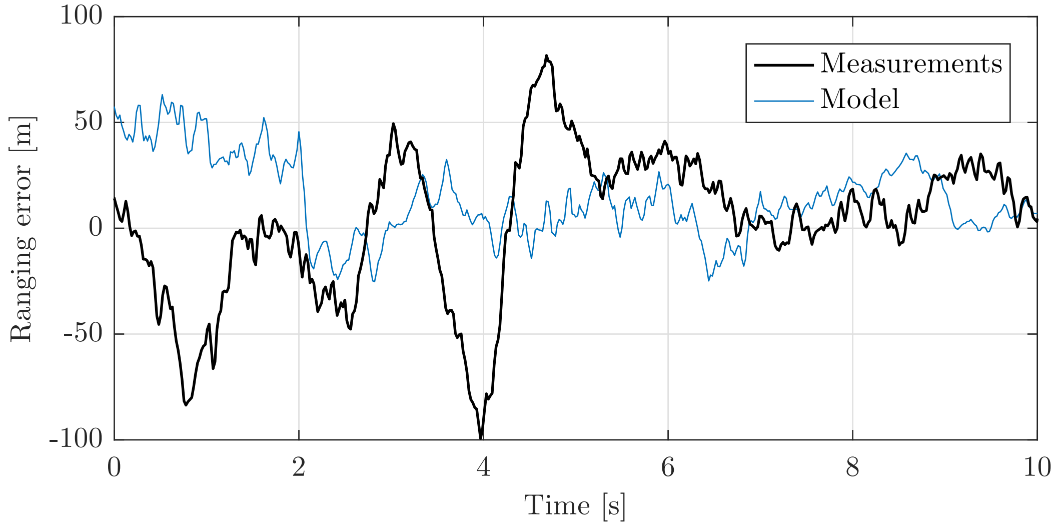

(a) *LDACS ranging error time series.*

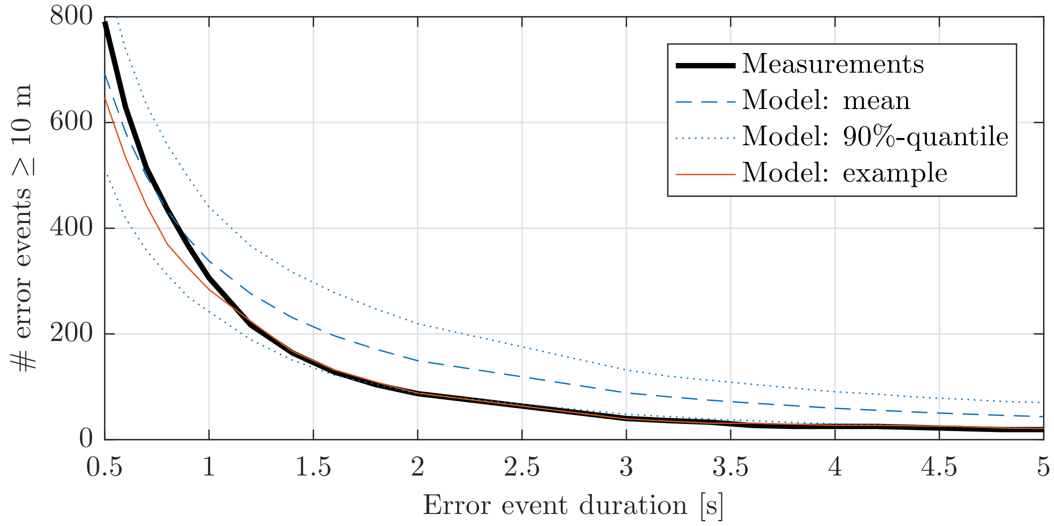

(b) *Occurence of slowly varying errors exceeding* 10 m.

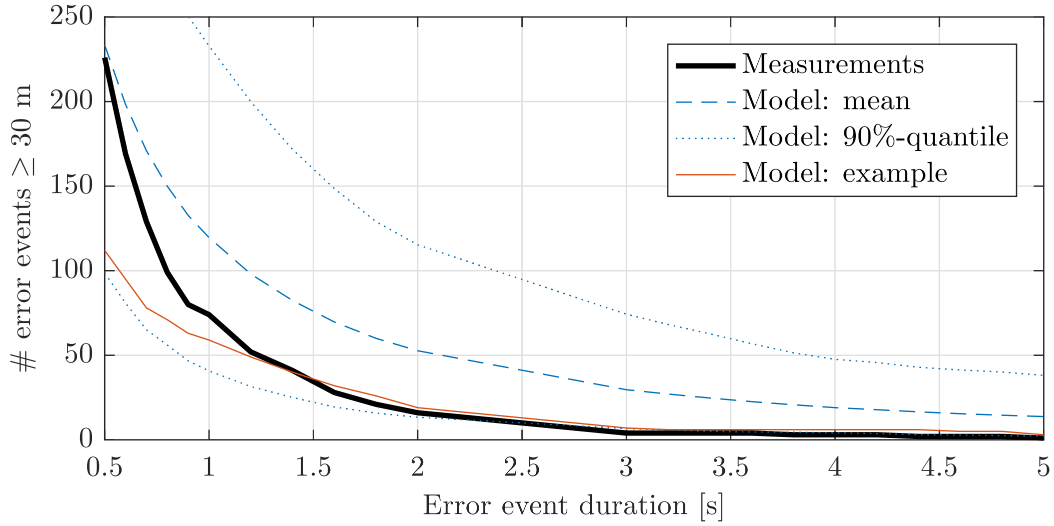

(c) *Occurence of slowly varying errors exceeding* 30 m.

Figure 7.29. *Number of events exceeding errors*

7.4 Summary

In this chapter we combine the findings from the previous chapters to derive a regional airport parameterization for the AG channel model architecture. The model uses a geometry-based stochastic modeling approach and is therefore able to accurately represent the non-stationarity of the AG channel.

The statistical distributions describing the different model element properties are derived from the flight measurement data collected for this dissertation. We successfully validate the channel model against measured data using three methods: a quantitative validation, a qualitative validation, and a validation by application. In the quantitative validation we show a good match between the statistical properties of the measured and the modeled channel. For the qualitative validation we compare time series of the channel model against measurements: thus, it is verified that the channel model is also able to capture the non-stationarity of the AG channel. Furthermore, we compare the ranging performance of LDACS using the channel model with results from the 2012/2013 LDACS flight trial ranging experiments. This validation by application is especially important as it verifies that - seen from the standpoint of the application system - both flight trial measurements and channel model lead to the same results.

The successful validation shows that, using the channel model presented in this chapter, we are able to assess the performance of different kinds of terrestrial CNS systems in the L-band. This ability is a significant improvement to the state of the art: previous channel models were usually only partly suitable to test the full range of terrestrial CNS systems in the L-band.

The main task for the future is to parameterize the channel model architecture to both additional environments and frequency bands. Apart from measurements, methods to to derive new parameterizations from publicly available data could turn out very useful: for example, the distributions of reflectors causing lateral MPCs could be derived from satellite imagery or building maps. This approach would also be advantageous in the context of ground multipath propagation as the extraction of ground surface information from channel sounding experiments is very complex. The inclusion of the aircraft patterns, i.e., the radiation pattern of the antenna on the aircraft, may further improve the channel model.

CHAPTER 8

CONCLUDING REMARKS

Past analyses of terrestrial communication, navigation, and surveillance (CNS) systems showed that the air-ground (AG) channel can have a strong negative impact on the quality of service. Two main factors for this effect can be identified: first, the AG channel features strong multipath components (MPCs); second, the AG channel is highly non-stationary.

Previously, the testing of terrestrial CNS systems using computer simulations was only possible to a limited extent: in fact most past channel models use a stationary statistical approach and thus do not sufficiently address the non-stationarity of the AG channel. Capturing the channel's non-stationarity with a fully statistical channel model is hardly feasible, especially under the constraint of keeping an acceptable model complexity. This dissertation proposes a realistic and comprehensive model of the AG channel by employing a general geometry-based stochastic channel model (GBSCM) architecture. This architecture comprises several model elements covering all relevant propagation effects. The geometrical-based stochastic approach is chosen as it allows to model non-stationary propagation effects accurately. Nevertheless, using a GBSCM we are able to maintain both an acceptable model complexity as well as an appropriate degree of randomness.

A major challenge when designing a GBSCM is the derivation of the statistical distributions describing the model elements: the required geometrical information, e.g., locations of reflectors, is generally not trivial to derive from measured data. To estimate this information we propose two algorithms. The first algorithm allows the robust detection of MPCs in the measured signal as well as the accurate estimation and tracking of the MPC parameters. The second algorithm provides an accurate estimate of the reflector location for each MPC using a Bayesian method.

We demonstrate the correctness and applicability of both algorithms based on the measured data collected during flight trials. Localizing reflectors causing MPCs provides previously unavailable understanding of the propagation effects in the AG channel. The scope of the proposed algorithms goes even far beyond the application of AG channel measurements: the algorithms may be used in any scenario were a precise MPC parameter estimation and reflector localization is required.

Using the GBSCM architecture and the measured data this dissertation presents a parameterization for a regional airport environment: this parameterization is successfully validated against measured data from channel sounding and ranging experiments; we demonstrate a very good match between channel model and measured channel.

With the proposed channel model it is now possible to perform realistic, rapid, and cost effective evaluations of the effect of the channel on the full range of terrestrial CNS systems. Such system evaluations are mandatory for the transition of the CNS infrastructure to new or improved systems.

APPENDIX A

REGIONAL AIRPORT CHANNEL MODEL SUMMARY

In the following we provide an overview of the regional airport channel model parameterization:

Tab. A.1 summarizes the distributions describing three model elements for the L-band regional airport environment:

- **ground multipath component (MPC)**,
- **lateral MPCs**, and
- **diffuse MPCs**.

All parameters for the angular distributions are expressed in radians.

For the **ground** and **airborne antenna** we use the radiation patterns measured in an anechoic chamber - see Fig. 3.5.

We assume that - due to the elevated ground antenna - the effect of **ground shadowing** does not appear at the regional airport environment.

Parameter	**Symbol**	**Distribution**	**Symbol**	**Parameter**
Ground MPC				
Coverage ratio	$r_{\mathrm{G,cov}}$	Constant	0.5	
Aspect ratio	$p\left(\log \frac{l_{\mathrm{G},1}}{l_{\mathrm{G},2}}\right)$	Normal	$\mathcal{N}\left(0, \zeta_{\mathrm{G,AR}}\right)$	$\zeta_{\mathrm{G,AR}} = 0.1$
Size	$p\left(l_{\mathrm{G},1} l_{\mathrm{G},1}\right)$	Exponential	$\mathcal{E}\left(\zeta_{\mathrm{G},s}\right)$	$\zeta_{\mathrm{G},s} = 0.01\,\mathrm{km}^2$
Roughness	$p\left(\sigma_{\mathrm{G,r}}\right)$	Exponential	$\mathcal{E}\left(\zeta_{\mathrm{G,r}}\right)$	$\zeta_{\mathrm{G,r}} = 0.1\,\mathrm{m}$
Lateral MPCs				
# reflectors	$\zeta_{N_{\mathrm{ref}}}$	Constant	$3.8 \cdot 10^5$	
Open dir. (az)	$p\left(\phi_{\mathrm{rd}}\right)$	Exponential	$\mathcal{E}\left(0, \zeta_{\phi_{\mathrm{rd}},\mathrm{b}}\right)$	$\zeta_{\phi_{\mathrm{rd}},\mathrm{b}} = 0.57$
Open dir. (el)	$p\left(\theta_{\mathrm{d}}\right)$	Uniform	$\mathcal{U}\left(\zeta_{\theta_{\mathrm{d}},\mathrm{l}}, \zeta_{\theta_{\mathrm{d}},\mathrm{u}}\right)$	$\zeta_{\theta_{\mathrm{d}},\mathrm{l}} = 0$ $\zeta_{\theta_{\mathrm{d}},\mathrm{u}} = \frac{\pi}{2}$
Open width	$p\left(\omega\right)$	Log-normal	$\log\mathcal{N}\left(\zeta_{\omega,\mu}, \zeta_{\omega,\sigma}\right)$	$\zeta_{\omega,\mu} = -7.15$ $\zeta_{\omega,\sigma} = 1.77$
Position (1D)	$p\left(\lvert \boldsymbol{r} \rvert\right)$	*Mixed*	-	$\zeta_{r,w1} = 0.65$ $\zeta_{r,w2} = 0.25$ $\zeta_{r,w3} = 0.1$
	$p_1\left(\lvert \boldsymbol{r} \rvert\right)$	Half-norm.	$\lvert\mathcal{N}\rvert\left(\zeta_{r,1,\sigma}\right)$	$\zeta_{r,1,\sigma} = 213\,\mathrm{m}$
	$p_2\left(\lvert \boldsymbol{r} \rvert\right)$	Gaussian-mixture	$\sum\mathcal{N}\left(\zeta_{r,2,\mu}, \zeta_{r,2,\sigma}\right)$	$\zeta_{r,2,N} = 6$ $\zeta_{r,2,\mu} \sim \mathcal{U}\left(500, 2\,\mathrm{km}\right)$ $\zeta_{r,2,\sigma} \sim \mathcal{U}\left(1, 50\,\mathrm{m}\right)$
	$p_3\left(\lvert \boldsymbol{r} \rvert\right)$	Uniform	$\mathcal{U}\left(\zeta_{r,3,\mathrm{l}}, \zeta_{r,3,\mathrm{u}}\right)$	$\zeta_{r,3,\mathrm{l}} = 0\,\mathrm{m}$ $\zeta_{r,3,\mathrm{u}} = 4\,\mathrm{km}$
Average amp.	$p\left(\alpha_{\mathrm{A}} \vert r\right)$			
Mean	$\bar{\alpha}_{\mathrm{A}}\left(r\right)$	*function*	-	$\zeta_{\bar{\alpha}_{\mathrm{A}},1} = 0.017$ $\zeta_{\bar{\alpha}_{\mathrm{A}},2} = 0.148$ $\zeta_{\bar{\alpha}_{\mathrm{A}},3} = 61.1\,\mathrm{m}$
Distr.	$p\left(\alpha_{\mathrm{An}}\right)$	Log-normal	$\log\mathcal{N}\left(\zeta_{\alpha_{\mathrm{An}},\mu},\right.$ $\left.(.\zeta_{\alpha_{\mathrm{An}},\sigma}\right)$	$\zeta_{\alpha_{\mathrm{An}},\mu} = -0.23$ $\zeta_{\alpha_{\mathrm{An}},\sigma} = 0.69$
Compl. weight variation	$p\left(\alpha_{\mathrm{V}}\right)$			
K-Factor	$p\left(\hat{\mathcal{K}}_{\alpha}\right)$	Log-normal	$\log\mathcal{N}\left(\zeta_{\alpha_{\mathrm{V},K},\mu},\right.$ $\left.\zeta_{\alpha_{\mathrm{V},K},\sigma}\right)$	$\zeta_{\alpha_{\mathrm{V},K},\mu} = 1.83$ $\zeta_{\alpha_{\mathrm{V},K},\sigma} = 0.68$
AR Pole	$p\left(1 - \gamma_{\mathrm{ar}}\right)$	Log-normal	$\log\mathcal{N}\left(\zeta_{\alpha_{\mathrm{V},\varphi},\mu},\right.$ $\left.\left(\zeta_{\alpha_{\mathrm{V},\varphi},\sigma}\right)\right.$	$\zeta_{\alpha_{\mathrm{V},\varphi},\mu} = -2.07$ $\zeta_{\alpha_{\mathrm{V},\varphi},\sigma} = 0.86$
Window function	$\alpha_{\mathrm{W}}\left(\epsilon, \omega\right)$	*function*	-	$\zeta_{\alpha_{\mathrm{W}},1} = 3 \cdot 10^3$ $\zeta_{\alpha_{\mathrm{W}},2} = 0.89$

Diffuse MPCs				
PDP	$\sigma^2_{\mathrm{CN}}\left(d,\tau\right)$	*function.*	-	$\zeta_{\mathrm{CN,y,1}} = -6.21$ $\zeta_{\mathrm{CN,y,2}} = -0.06\,\mathrm{km}^{-1}$ $\zeta_{\mathrm{CN,s}} = 1.07\,\mathrm{\mu s}^{-1}$
Scatterer location	$p\left(\boldsymbol{r}_{\mathrm{CN}}\right)$	Normal	$\mathcal{N}\left(0, \mathbb{I}_2\zeta^2_{\mathrm{CN},\sigma}\right)$	$\zeta_{\mathrm{CN},\sigma} = 700\,\mathrm{m}$ $\zeta_{\mathrm{CN,N}} = 200$

Table A.1. *Summary of the distributions describing the model element properties for the regional airport parameterization.*

APPENDIX **B**

INFLUENCE OF THE AIRCRAFT PATTERN

In Sec. 7.26 we show the measured line-of-sight (LoS) signal power against the aircraft position: the results shown in Fig. 7.26 suggest a significant drop of the power when the ground station is seen at $\pm 90°$, i.e., at either side of the aircraft. In the following we investigate this effect in more detail.

In Fig. B.1 we show the distribution of the LoS signal power against the angle the LoS signal is received from relative to the aircraft. The power is corrected using the antenna radiation patterns measured in an anechoic chamber for the ground and airborne antennas: neglecting effects by the airframe, we would expect on average a mean of $0\,\mathrm{dB}$ (rel. to FSPL).

From Fig. B.1 we observe that significantly less power is received if the ground station is seen at either side of the aircraft. One explanation is the existence of a ground multipath component (MPC) causing a long fade of the LoS signal: if the ground station is seen at $\pm 90°$ the aircraft is usually traveling on a circular trajectory around the ground station. Fades of the LoS signal power may last for a significant duration - see Sec. 2.3.1. Nevertheless, on average a ground MPC does not change the LoS signal power. Thus, it is unlikely that all fades can be attributed to ground multipath propagation.

Instead the accumulation of low LoS signal power levels at $\pm 90°$ suggests some influence of the aircraft fuselage on the overall aircraft radiation pattern. A likely explanation can be found when analyzing the attachment of the antenna on the aircraft. As shown in Fig. B.2 the antenna is mounted in a compartment under the fuselage: the antenna itself is recessed by roughly $6\,\mathrm{cm}$ between two guide rails (these guide rails allow for an closing the compartment if no antenna is attached). Thus, looking at the aircraft from one side only the lower half of the antenna is visible; the upper half is shadowed by the guide rails. Although part of signal may diffracted over the guide rails we expect that a part of the signal is shadowed. The shadowing intuitively explains the phenomena visible in Fig. B.1.

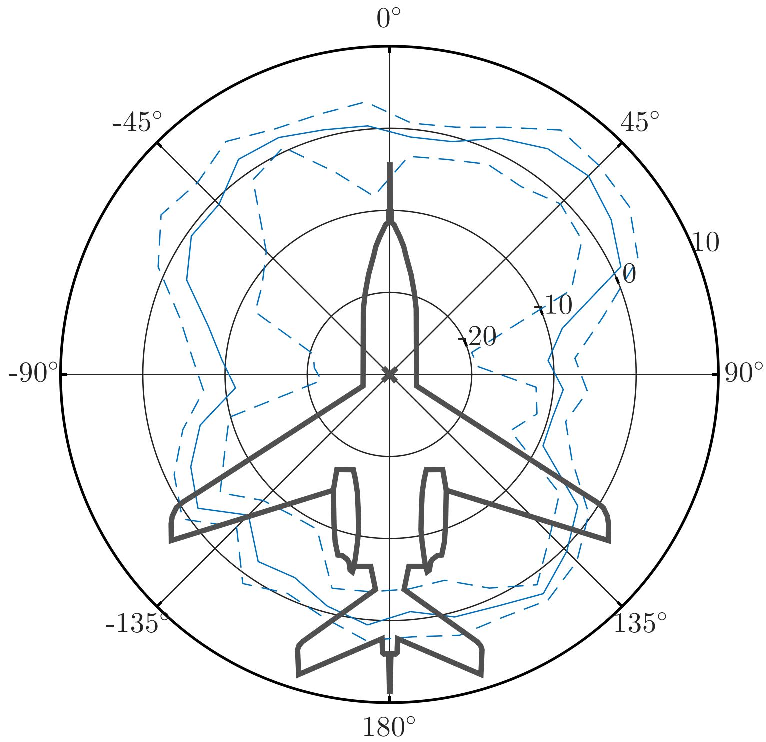

Figure B.1. *Mean LoS signal power (in dB FSPL) against the direction ground station is seen from the aircraft. The dashed lines represent the 90% quantile. The antenna position on the aircraft is marked by a cross.*

Figure B.2. *Mounting of the airborne antenna on the aircraft.*

Nevertheless, a more thorough investigation of the topic is required to separate the effects of ground multipath propagation and aircraft pattern on the LoS signal power. Such an investigation requires further measurements as well and/or simulations. Due to the involved complexity, such an investigation is left as an open topic for future work.

APPENDIX **C**

POINTS OF IDENTICAL DELAY AND DOPPLER FREQUENCY

To understand the propagation characteristics of the channel in more detail, we are interested in the reflector points causing a multipath component (MPC). In the following we assume an local east-north-up (ENU) coordinate system centered at the transmit antenna position. Hereby, the transmit antenna has the location $[0, 0, 0]^{\mathrm{T}}$ and the aircraft the position $\boldsymbol{d}$ with a speed vector $\boldsymbol{v}$.

Definition of the Three Dimensional Shapes

Delay

Under the assumption of a single bounce reflection, points with constant delay τ lie on an ellipsoid with the transmit and receive antenna as focal points as depicted in Fig. C.1. The ellipse is rotation symmetric towards its longest axis, its general equation is given as

$$\frac{x^2}{e_{\tau,a}^2} + \frac{y^2}{e_{\tau,b}^2} + \frac{z^2}{e_{\tau,b}^2} = 1 \tag{C.1}$$

$$\tag{C.2}$$

The parameters $e_{\tau,a}$ and $e_{\tau,b}$ of the ellipse can be directly calculated using the propagation delay of the line-of-sight (LoS) τ_{L} and the MPC τ_{M} as well as the speed of light in air c_{a} as

$$e_{\tau,a} = \frac{\tau_{\mathrm{M}}}{2} c_{\mathrm{a}} \quad \text{and} \tag{C.3}$$

$$e_{\tau,b} = \sqrt{\left(\frac{\tau_{\mathrm{M}}}{2}\right)^2 - \left(\frac{\tau_{\mathrm{L}}}{2}\right)^2} c_{\mathrm{a}}. \tag{C.4}$$

The center of the ellipsoid is given as $\frac{\boldsymbol{d}}{2}$.

However, due the second focal point lying arbitrarily in space, the ellipsoid has to be rotated around the N and U axis in order to align with the local ENU coordinate

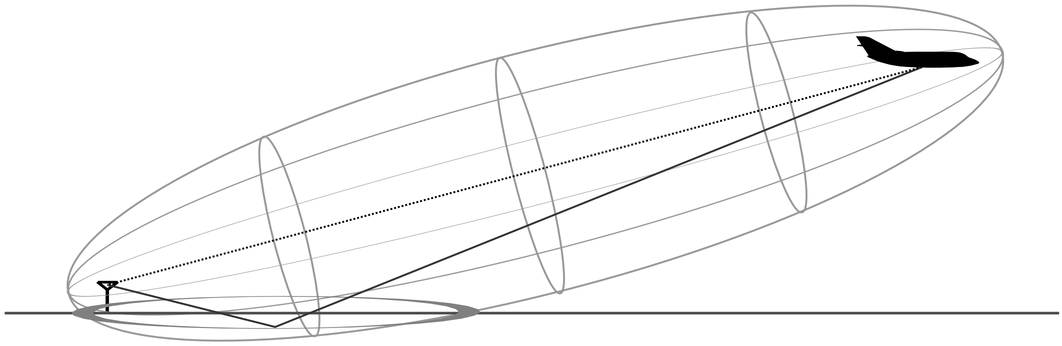

Figure C.1. *Illustration of ellipsoid defining points with equivalent delay τ.*

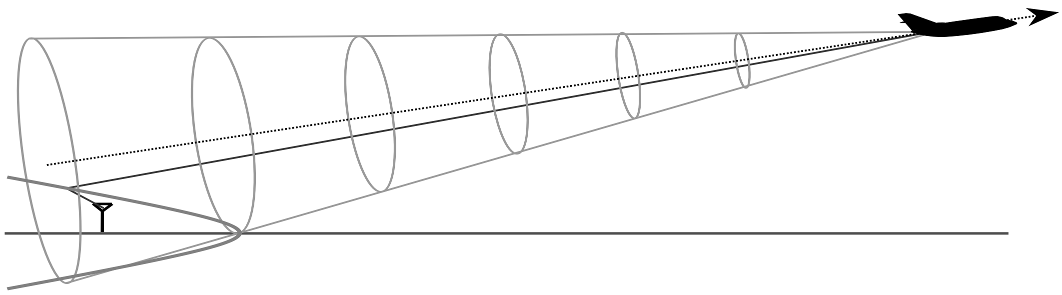

Figure C.2. *Illustration of cone defining points with equivalent Doppler frequency ν.*

system. Additionally, its center has to be shifted to $\frac{\boldsymbol{d}}{2}$. The equation for a point on the surface $\boldsymbol{g} = [x, y, z]^{\mathrm{T}}$ on the surface of the ellipse has to satisfy

$$\left(\underline{\boldsymbol{R}}_{\mathrm{U},\tau}\underline{\boldsymbol{R}}_{\mathrm{N},\tau}(\boldsymbol{g} - \frac{\boldsymbol{d}}{2})\right)^{\mathrm{T}} \begin{bmatrix} \frac{1}{e^2_{\tau,a}} & 0 & 0 \\ 0 & \frac{1}{e^2_{\tau,b}} & 0 \\ 0 & 0 & \frac{1}{e^2_{\tau,b}} \end{bmatrix} \underline{\boldsymbol{R}}_{\mathrm{U},\tau}\underline{\boldsymbol{R}}_{\tau,N}(\boldsymbol{g} - \frac{\boldsymbol{d}}{2}) = 1 \tag{C.5}$$

The rotation angles around the axis can be calculated as

$$\varphi_{\mathrm{N},\tau} = \arg\left(d_{\mathrm{E}} + \mathrm{j}d_{\mathrm{N}}\right) \quad \text{and} \tag{C.6}$$

$$\varphi_{\mathrm{U},\tau} = \arg\left(\sqrt{{d_{\mathrm{E}}}^2 + {d_{\mathrm{N}}}^2} + \mathrm{j}d_{\mathrm{U}}\right). \tag{C.7}$$

Doppler Frequency

Under the assumption of a single bounce reflection, points with constant Doppler frequency ν lie on an cone centered on the aircraft position $\boldsymbol{d}$ and opening in the direction of the aircraft movement vector $\boldsymbol{v}$. The resulting cone is illustrated in Fig. C.2. The cone is rotation symmetric towards its z-axis, its general equation is given as

$$\frac{x^2}{e^2_{\nu,h}} + \frac{y^2}{e^2_{\nu,h}} - z^2 = 0 \tag{C.8}$$

$$\tag{C.9}$$

The parameter $e_{\nu,h}$ depends on the Doppler frequency ν, the carrier frequency f_c, and the absolute speed of the aircraft $\|\boldsymbol{v}\|$ and is given as

$$e_{\nu,h} = \tan\left(\cos^{-1}\frac{\nu c_\mathrm{a}}{\|\boldsymbol{v}\| f_\mathrm{c}}\right). \tag{C.10}$$

To align the cone with the local ENU coordinate system, has to be rotated around the N and U axis and its center has to be shifted. In vector notation, the general equation can be written as

$$\left(\underline{\boldsymbol{R}}_{\mathrm{U},\nu}\underline{\boldsymbol{R}}_{\mathrm{N},\nu}(\boldsymbol{g}-\boldsymbol{d})\right)^\mathrm{T}\begin{bmatrix}\frac{1}{e_{\nu,h}^2} & 0 & 0\\ 0 & \frac{1}{e_{\nu,h}^2} & 0\\ 0 & 0 & 1\end{bmatrix}\underline{\boldsymbol{R}}_{\mathrm{U},\nu}\underline{\boldsymbol{R}}_{\mathrm{N},\nu}(\boldsymbol{g}-\boldsymbol{d}) = 0 \tag{C.11}$$

The rotation angles around the axis can be calculated as

$$\varphi_{\mathrm{N},\nu} = \arg\left(v_\mathrm{E} + \mathrm{j}v_\mathrm{N}\right) \quad \text{and} \tag{C.12}$$

$$\varphi_{\mathrm{U},\nu} = \arg\left(\sqrt{{v_\mathrm{E}}^2 + {v_\mathrm{N}}^2} + \mathrm{j}v_\mathrm{U}\right). \tag{C.13}$$

Reflector Locations on the Ground

To obtain the locations of the reflector points on the ground, we intersect the ellipsoid or cone, defined by (C.5) and (C.11) with the ground surface, i.e., set $z = 0$. Using simple but tedious math, in both cases the result can be converted into the general scalar form of a quadric curve [114], [115]. It can then be simply parametrized by the coefficient vector $\mathfrak{q}$

$$\mathfrak{q}_1 x^2 + 2\mathfrak{q}_2 xy + \mathfrak{q}_3 y^2 + 2\mathfrak{q}_4 x + 2\mathfrak{q}_5 y + \mathfrak{q}_6 = 0 \tag{C.14}$$

The intersection of an ellipsoid with the ground plane always results in an ellipse. In contrast to that, intersecting a the cone plane can result in either a hyperbola or an ellipsoid[1]. Using the definition

$$q = \det\begin{pmatrix}\mathfrak{q}_1 & \mathfrak{q}_2\\ \mathfrak{q}_2 & \mathfrak{q}_3\end{pmatrix} \tag{C.15}$$

the shape of the intersecting line can be determined. For $q > 0$ the intersection results in an ellipse and for $q < 0$ in a hyperbola.

The intersection of the two lines on the ground defined by the delay τ and Doppler frequency ν is the estimated position of the reflector. A closed solution for the intersection point can be found using computer algebra programs, e.g., Mathematica.

[1] In theory, a hyperbola can also be viewed as an ellipse with one focal point in infinity.

APPENDIX D

NORMALIZATION OF PROBABILITY DENSITY FUNCTION

The Jacobian $\Upsilon(\boldsymbol{g})$ which normalizes (4.46) to be a true probability density function (PDF) is calculated as

$$\begin{aligned}\Upsilon(\boldsymbol{g}) &= \operatorname{jac}(\boldsymbol{\mu}(\boldsymbol{g})) \\ &= \begin{vmatrix} \frac{\partial\tau(\boldsymbol{g})}{\partial g_{\mathrm{E}}} & \frac{\partial\tau(\boldsymbol{g})}{\partial g_{\mathrm{N}}} \\ \frac{\partial\nu(\boldsymbol{g})}{\partial g_{\mathrm{E}}} & \frac{\partial\nu(\boldsymbol{g})}{\partial g_{\mathrm{N}}} \end{vmatrix}. \end{aligned} \tag{D.1}$$

The partial derivatives of $\tau(\boldsymbol{g})$ are calculated as

$$\frac{\partial\tau(\boldsymbol{g})}{\partial g_{\mathrm{E}}} = \frac{1}{c_{\mathrm{a}}}\left(\frac{g_{\mathrm{E}}}{\|\boldsymbol{g}\|} + \frac{g_{\mathrm{E}} - d_{\mathrm{E}}}{\|\boldsymbol{g}-\boldsymbol{d}\|}\right) \tag{D.2}$$

and

$$\frac{\partial\tau(\boldsymbol{g})}{\partial g_{\mathrm{N}}} = \frac{1}{c_{\mathrm{a}}}\left(\frac{g_{\mathrm{N}}}{\|\boldsymbol{g}\|} + \frac{g_{\mathrm{N}} - d_{\mathrm{N}}}{\|\boldsymbol{g}-\boldsymbol{d}\|}\right). \tag{D.3}$$

The partial derivatives of $\nu(\boldsymbol{g})$ can be expressed as

$$\frac{\partial\nu(\boldsymbol{g})}{\partial g_{\mathrm{E}}} = \frac{f_{\mathrm{c}}}{c_{\mathrm{a}}}\left(\frac{v_{\mathrm{E}}}{\|\boldsymbol{g}-\boldsymbol{d}\|} - \frac{(\boldsymbol{g}-\boldsymbol{d})\cdot\boldsymbol{v}\,(g_{\mathrm{E}} - d_{\mathrm{E}})}{\|\boldsymbol{g}-\boldsymbol{d}\|^3}\right) \tag{D.4}$$

and

$$\frac{\partial\nu(\boldsymbol{g})}{\partial g_{\mathrm{N}}} = \frac{f_{\mathrm{c}}}{c_{\mathrm{a}}}\left(\frac{v_{\mathrm{N}}}{\|\boldsymbol{g}-\boldsymbol{d}\|} - \frac{(\boldsymbol{g}-\boldsymbol{d})\cdot\boldsymbol{v}\,(g_{\mathrm{N}} - d_{\mathrm{N}})}{\|\boldsymbol{g}-\boldsymbol{d}\|^3}\right). \tag{D.5}$$

After some simplifications, the closed form solution for the Jacobian can be found as

$$\begin{aligned}\Upsilon(\boldsymbol{g}) = |\frac{f_{\mathrm{c}}}{c_{\mathrm{a}}^2\|\boldsymbol{g}\|\|\boldsymbol{g}-\boldsymbol{d}\|^3} &\left\{\|\boldsymbol{g}-\boldsymbol{d}\|^2\,(g_{\mathrm{E}}v_{\mathrm{N}} - g_{\mathrm{N}}v_{\mathrm{E}})\right. \\ &+ \|\boldsymbol{g}\|\|\boldsymbol{g}-\boldsymbol{d}\|\,((g_{\mathrm{E}} - d_{\mathrm{E}})\,v_{\mathrm{N}} - (g_{\mathrm{N}} - d_{\mathrm{N}})\,v_{\mathrm{E}}) \\ &\left. + (\boldsymbol{g}-\boldsymbol{d})\cdot\boldsymbol{v}\,(g_{\mathrm{E}}d_{\mathrm{N}} - g_{\mathrm{N}}d_{\mathrm{E}})\right\}| \end{aligned} \tag{D.6}$$

Appendix E

Calibration of the 360° Panorama

In the following we describe how we generate and calibrate a panoramic image of the area surrounding the ground station: by calibration we understand the ability to map an aircraft position to a pixel in the image. We first take multiple images from the position of the transmit antenna and combine them into a single 360° panorama. The images are taken using a tripod.

For the calibration of the image, a set of reference points is required. We choose optically prominent reference points, e.g., the top of a church tower, and measure their azimuth angle ϕ and elevation angle θ using a Leica TPS1200 surveying Tachymeter. The pixel positions of the reference points are taken from the panorama image. Using the reference points the image is calibrated. Let $[\mathfrak{p}_x \mathfrak{p}_y]$ define the position of a pixel in the panorama image. We assume a linear mapping between a pixel location $\mathfrak{p}_x$ and azimuth angle ϕ:

$$\mathfrak{p}_x = a_x \phi + b_x. \tag{E.1}$$

As the camera can not be setup in a way such that it always points at the same elevation angle, for the mapping between $\mathfrak{p}_x$ and the elevation angle θ we assume the model

$$\mathfrak{p}_y = a_y \theta + b_y + c_y sin(d_y \phi + e_y). \tag{E.2}$$

The coefficients of the mapping function are least squares (LS) estimated using the reference points. A qualitative analysis using highly precise Global Positioning System (GPS) reference points to test the mapping shows, that a location at the relevant elevation angles can usually be mapped to a pixel with an accuracy of around 15 pixels.

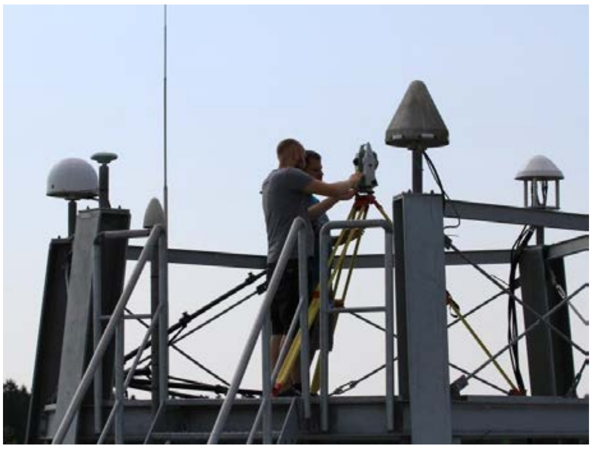

Figure E.1. *Measurement of the reference points at the transmit antenna position.*

APPENDIX **F**

AZIMUTHAL OPENING DIRECTION OF REFLECTORS

In the following we use simple ray-tracing simulations to briefly analyze the narrowness of the distribution of the azimuthal relative opening direction (arod) - see Fig. 7.4.

In Fig. F.2 we illustrate the setup of the simulations: we assume reflectors (modeled as lines of length $l_\mathrm{r} = 10\,\mathrm{m}$) are located around the ground station. The distance between reflectors and ground station r is distributed according to the measurements shown in Fig. 7.8. The reflectors are randomly rotated around their center. For each reflector we calculate whether an multipath component (MPC) would be received at the aircraft. The distance d between aircraft and ground station is distributed according to the trajectory during the flight trials.

The resulting distribution of the reflector's arod is shown in Fig. F.2. We observe that in both the simulations and measurements the distribution of the arod is narrowly centered around zero degrees. The simulations also show that more MPCs originating from reflectors associated with small (absolute) arods are received at the aircraft.

Nevertheless, we observe that the distribution derived from measurements is narrower compared to the distribution derived from simulations. Two reasons for that effect may be identified:

Specific ground station geometry: The aircraft often flies west of the ground station. This position favors the large hangar buildings directly east of the ground station to act as reflectors: due to the geometry, the arod associated with those hangar buildings is small.

To investigate the assumption we group the estimated arods into segments according to the angular position of the aircraft - see Fig. F.3 for an illustration. The marginal distributions of the arod for the eight angular segments are shown in Fig. F.2 (dotted lines): we observe that, depending on the angular segment, the distributions significantly differ. For example if an aircraft flies in the segment associ-

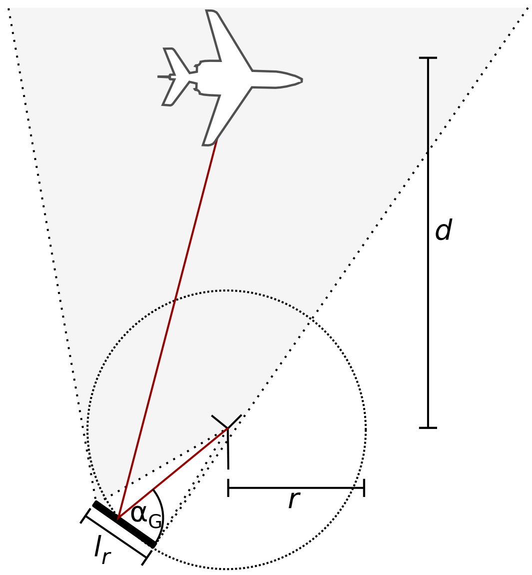

Figure F.1. *Illustration of the simulation scenario.*

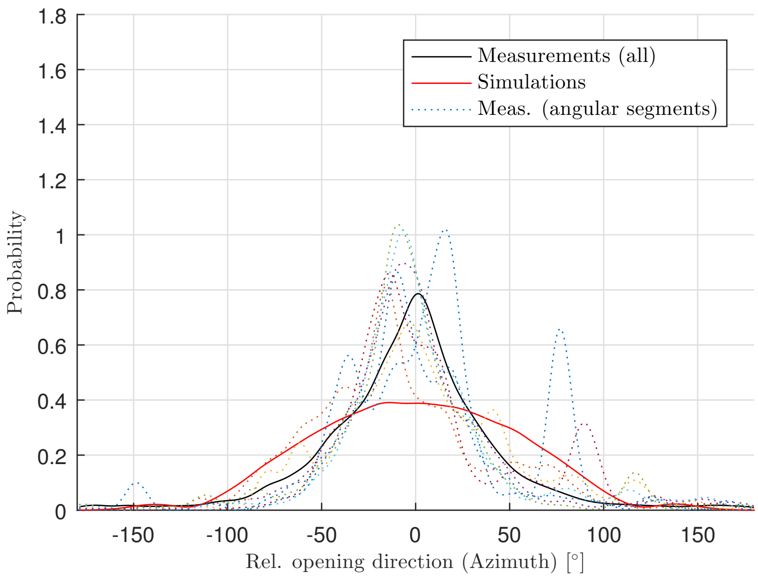

Figure F.2. *Measured and simulated azimuthal relative opening direction (arod).*

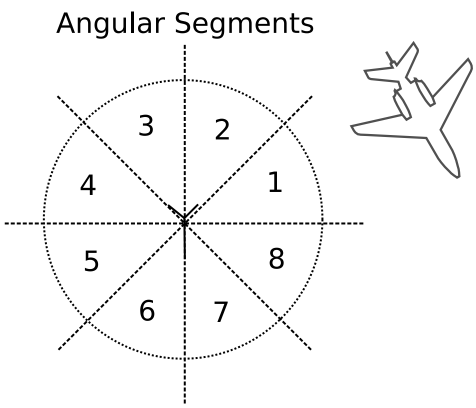

Figure F.3. *Illustration of the angular segments the aircraft is seen under from the ground station.*

ated with the green distribution it would experience reflectors with very different arods than in a different segment: the distribution of the arod strongly depends on the underlying geometry.

The second reason for the narrow distribution may be attributed to the **parameter estimation**: due to the diffuse MPCs usually observed at low delays the MPC parameter estimation may detect fewer MPC with short delays. Therefore, fewer reflectors associated with a large arod may be detected.

Acronyms

ADC analogue-to-digital-converter

ADS-B automatic dependent surveillance - broadcast

AG air-ground

AGL above ground level

AMSL above mean sea level

APNT alternative positioning, navigation, and timing

AR autoregressive

arod azimuthal relative opening direction

ATM air traffic management

AWG arbitrary waveform generator

BER bit error ratio

BOBYQA bound optimization by quadratic approximation

CD climb & descent

CDF cumulative distribution function

CIR channel impulse response

CNS communication, navigation, and surveillance

Cs cesium

CW continuous wave

DEM digital elevation model

DFT discrete Fourier transform

DLL delay-locked loop

DMC dense multipath component

DME distance measuring equipment

DPP Doppler power profile

EC enroute cruise

ECEF earth-centered earth-fixed

ENU east-north-up

FSPL free space path loss

GBSCM geometry-based stochastic channel model

GNSS global navigation satellite system

GPS Global Positioning System

GTD geometrical theory of diffraction

HPA high power amplifier

IDFT inverse discrete Fourier transform

INS inertial navigation system

LDACS L-band Digital Aeronautical Communication System

LNA low noise amplifier

LoS line-of-sight

LS least squares

MIMO multiple input multiple output

ML maximum likelihood

MPC multipath component

MSE mean squared error

NED north-east-down

NextGen Next Generation Air Transportation System

OFDM orthogonal frequency division multiplexing

PACF partial autocorrelation function

PAPR peak-to-average-power-ratio

PDF probability density function

PDP power delay profile

PPM pulse position modulation

PPS pulse per second

PSR primary surveillance radar

RAIM receiver autonomous integrity monitoring

Rb rubidium

rms root-mean-square

RMSE root-mean-squared error

RTK real time kinematic

SESAR Single European Sky ATM Research

SIMO single input multiple output

SISO single input single output

SNR signal-to-noise-ratio

SSD solid state drive

SSR secondary surveillance radar

TL takeoff & landing

UAV unmanned aerial vehicle

US uncorrelated scattering

VHF very high frequency

VOR VHF omnidirectional range

WSS wide-sense stationary

WSSUS wide-sense stationary uncorrelated scattering

List of Symbols

Scalars are denoted by Roman, vectors by bold, and matrices by underlined uppercase bold symbols, e.g., x, $\boldsymbol{x}$, and $\underline{\boldsymbol{X}}$.

Symbols

$(\cdot)^*$	Complex conjugate
$(\cdot)^{\mathrm{H}}$	Hermitian of a matrix
$(\cdot)^{\mathrm{T}}$	Transpose of a matrix
$\lvert\cdot\rvert$	Absolute value of a complex number
$\lVert \cdot \rVert$	L2 (Eucledian) norm
$\langle\cdot\rangle$	Cardinality of a set
$\lceil\cdot\rceil$	Ceiling function
$\odot$	Element-wise multiplication (Hadamard product)
$\oslash$	Element-wise division
$\otimes$	Kronecker product
$\cdot$	scalar product
$*$	Circular convolution
$\mathbb{1}_{(\cdot)}$	Vector of ones of length $(\cdot)$

Greek letters

$\alpha, \boldsymbol{\alpha}$	Complex weight(s) of MPC(s)
γ_{ar}	Pole of AR process
Γ_{τ}	Set of interference free channel sounding sequence instances
Γ_n	Set of delay indices for noise power calculation
Δ_{BM}	Blackman Window badwidth
ϵ	Angle the aircraft is seen from the reflector
$\zeta_{N_{\mathrm{ref}}}$	Lat. MPCs: number of refl.

$\zeta_{\theta_{\mathrm{d}},\mathrm{l}}, \zeta_{\theta_{\mathrm{d}},\mathrm{u}}$	Lat. MPCs (el. opening dir.): upper and lower limit of uniform distr.
$\zeta_{\phi_{\mathrm{rd}},\mathrm{b}}$	Lat. MPCs (az. opening dir.): scale param. of Laplacian distr.
$\zeta_{\omega,\mu}, \zeta_{\omega,\sigma}$	Lat. MPCs (opening width): mean and std. dev. of log-normal distr.
$\zeta_{\bar{\alpha}_{\mathrm{A}},1}, \zeta_{\bar{\alpha}_{\mathrm{A}},2}, \zeta_{\bar{\alpha}_{\mathrm{A}},3}$	Lat. MPCs (weight - avg.): coefficients of of distance dep. mean of avg. amplitude
$\zeta_{\alpha_{\mathrm{An}},\mu}, \zeta_{\alpha_{\mathrm{An}},\sigma}$	Lat. MPCs (weight - avg.): mean and std. dev. of log-normal distr.
$\zeta_{\alpha_{\mathrm{V},\varphi},\mu}, \zeta_{\alpha_{\mathrm{V},\varphi},\sigma}$	Lat. MPCs (weight - variation): mean and std. dev. of log-normal distr. describing AR-pole
$\zeta_{\alpha_{\mathrm{V},K},\mu}, \zeta_{\alpha_{\mathrm{V},K},\sigma}$	Lat. MPCs (weight - variation): mean and std. dev. of log-normal distr. describing K-factor
$\zeta_{\alpha_{\mathrm{W}},1}, \zeta_{\alpha_{\mathrm{W}},2}$	Lat. MPCs (weight - window): coefficients of window function
$\zeta_{r,w1}, \zeta_{r,w2}, \zeta_{r,w3}$	Lat. MPCs (pos.): weights of different reflectors classes
$\zeta_{r,1,\sigma}$	Lat. MPCs (pos. - close refl.): scale parameter of half-normal distr.
$\zeta_{r,2,N}$	Lat. MPCs (pos. - cluster refl.): number of components in Gaussian mixture
$\zeta_{r,2,\mu}, \zeta_{r,2,\sigma}$	Lat. MPCs (pos. - cluster refl.): mean and std. dev. of components in Gaussian mixture
$\zeta_{r,3,\mathrm{l}}, \zeta_{r,3,\mathrm{u}}$	Lat. MPCs (pos. - isolated refl.): lower and upper bound of uniform distr.
$\zeta_{\mathrm{CN,y}}, \zeta_{\mathrm{CN,s}}$	Diffuse MPCs: y-intersection and slope of exponential function
$\zeta_{\mathrm{CN},\sigma}$	Diffuse MPCs: std. dev. of normal distribution describing scatterer location
$\zeta_{\mathrm{G,AR}}$	Ground refl. area (aspect ratio): std. dev. of normal distr.
$\zeta_{\mathrm{G,r}}$	Ground refl. area (roughtness): mean of exponential distr.
$\zeta_{\mathrm{G},s}$	Ground refl. area (size): mean of exponential distr.
θ	Elevation angle (as seen from reflector)
$\kappa, \tilde{\boldsymbol{\kappa}}$	Impulse response of a propagation path
$\boldsymbol{\mu} = [\tau, \nu]^{\mathrm{T}}$	MPC parameter vector
$\nu, \boldsymbol{\nu}$	Doppler frequency(ies) of MPC(s)
ν_{LoS}	Doppler frequency of the LoS signal
$\boldsymbol{\xi} = [\tau, \nu, ..$ $\log\lvert\alpha\rvert, \arg(\alpha)]^{\mathrm{T}}$	MPC parameter vector

Π	Number of intersections between the shapes defined by delay and Doppler frequency
σ_ν^2	Doppler frequency spread
σ_τ^2	Delay spread
σ_{CN}^2	Diffuse MPCs: power as function of delay
$\sigma_{\mathrm{G,r}}$	Std. dev. of surface height about the local mean value (surface roughness)
σ_{n}	Noise std. dev.
$\underline{\boldsymbol{\Sigma}}$	Noise covariance
$\tau, \boldsymbol{\tau}$	Delay(s) of MPC(s)
τ_{LoS}	Delay of the LoS signal
Υ	Normalization factor of the reflector location PDF
ϕ	Azimuth angle (as seen from reflector)
φ_ω	Angle defining chord of a circle
$\varphi_{\mathrm{N},}, \varphi_{\mathrm{U},}$	Rotation angle around N/U-axis
$\varphi_{\mathrm{Y}}, \varphi_{\mathrm{P}}, \varphi_{\mathrm{R}}$	Yaw, pitch, and roll angle
χ^2	Chi-squared distribution (param.: degrees of freedom)
$\psi, \boldsymbol{\psi}, \underline{\boldsymbol{\Psi}}$	Colored noise at receiver
ω	Opening width (of reflector)

Latin letters

$\arg(\cdot)$	Phase of complex number
b	Block identifier
c_{a}	Speeed of light in air
$\boldsymbol{c}$	Calibration signal (includes hardware non-linearities)
$\mathrm{crd}(\cdot)$	Chord of a circle defined by angle $(\cdot)$
$\mathcal{CN}$	Complex normal distribution (param.: mean and covariance)
d	Link distance $\lVert\boldsymbol{d}\rVert$ (distance between aircraft and ground station)
$\boldsymbol{d} = [d_{\mathrm{E}}, d_{\mathrm{N}}, d_{\mathrm{U}}]^{\mathrm{T}}$	Position of aircraft in ENU
$\det(\cdot)$	Determinant of matrix
$\underline{\boldsymbol{D}}$	Path detection matrix
$e_{\nu,h}$	Cone parameter h
$e_{\tau,a}, e_{\tau,b}$	Ellipse parameters
$\mathbb{E}$	Expectation operator
$\mathcal{E}$	Exponential distribution (param.: mean)
f	Continuous frequency
f_{c}	Carrier frequency

$\underline{\boldsymbol{F}}$	Transition matrix(information filter)
$\underline{\mathfrak{F}}_{\cdot}$	DFT Matrix of dimension $(\cdot)$
$\underline{\mathfrak{F}}_{\cdot}^{\mathrm{H}}$	IDFT Matrix of dimension $(\cdot)$
$\boldsymbol{g} = [g_{\mathrm{E}}, g_{\mathrm{N}}, g_{\mathrm{U}}]^{\mathrm{T}}$	Point on the ground in ENU
$h, \underline{\boldsymbol{H}}$	Channel description function
h_{AC}	Altitude of aircraft
h_{GS}	Height of ground antenna over ground
$i \in [0, .., I-1]$	Index of a channel sounding sequence instance in a block
$\mathrm{Im}\left\{\cdot\right\}$	Imaginary part of a complex number
$\underline{\mathbb{I}}_{(\cdot)}$	Identity matrix of size $(\cdot)$
$\underline{\mathfrak{I}}$	Fisher information matrix
j	Imaginary unit
$\mathrm{jac}\left(\cdot\right)$	Jacobian of matrix
k	Reflector index
$\underline{\boldsymbol{K}}$	Kalman gain (information filter)
$\mathcal{K}$	K-Factor
$l \in [0, .., L-1]$	MPC index
$l_{\mathrm{G},1}, l_{\mathrm{G},2}$	Dimension of a ground reflecting area
$\log \mathcal{N}$	Log-normal distribution (param.: mean and std. dev.)
$\mathcal{L}$	Laplace distribution (param: scale)
$m \in [0, .., M-1]$	Measurement index associated with reflector / MPC
m_{τ}	Mean delay
m_{ν}	Mean Doppler frequency for block b
$\underline{\boldsymbol{M}}$	Measurement matrix (information filter)
$n \in [0, .., N-1]$	Index of channel sounding sequence sample
n_{BM}	Blackman Window length
$\mathcal{N}$	Normal distribution (param.: mean and std. dev.)
$\lvert\mathcal{N}\rvert$	Half-normal distribution (param.: scale)
p_{C}	Probability in Cartesian space
p_{P}	Probability in MPC parameter space
$\mathfrak{p}_x, \mathfrak{p}_y$	Location of a pixel in an image
P	Channel correlation function
$\mathfrak{q}, \boldsymbol{\mathfrak{q}}$	Coefficients of quadric curve
Q_{add}	Noise quantile for adding an MPC
Q_{rm}	Noise quantile for removing an MPC
$\underline{\boldsymbol{Q}}$	System / state noise (information filter)
r	Distance between reflector location and ground station $\lVert\boldsymbol{r}\rVert$

$\boldsymbol{r} = [r_{\mathrm{E}}, r_{\mathrm{N}}, r_{\mathrm{U}}]^{\mathrm{T}}$	Reflector location in ENU
$r_{\mathrm{G,cov}}$	coverage ratio of round refl. area
$\boldsymbol{r}_{\mathrm{CN}} = [d_{\mathrm{CN,E}}, .. \; d_{\mathrm{CN,N}}]^{\mathrm{T}}$	Location of scatterer
$\underline{\boldsymbol{R}}_{(\cdot)}$	Rotation matrix around axis $(\cdot)$
$\mathrm{Re}\{\cdot\}$	Real part of a complex number
$\boldsymbol{s}$	Transmitted signal
t	Continuous time
t_{cal}	Time of calibration
$\tan_2^{-1}(\cdot,\cdot)$	Four-quadrant inverse tangent
$\mathsf{t}_{\mathrm{add}}, \mathsf{t}_{\mathrm{rm}}$	Threshold to add/remove a path
T_{sym}	Duration of the channel sounding sequence
T_{s}	Sampling period
$\mathcal{U}$	Uniform distribution (param.: lower and upper limit)
$\boldsymbol{v} = [v_{\mathrm{E}}, v_{\mathrm{N}}, v_{\mathrm{U}}]^{\mathrm{T}}$	Speed vector of aircraft in ENU
$\mathrm{vec}_{\cdot}^{-1}\{\cdot\}$	Inverse Vector operator
$\underline{\boldsymbol{V}}$	State covariance (information filter)
$\mathcal{W}$	Weibull distribution (param.: scale and shape)
$\boldsymbol{w}_{\mathrm{BM}}, \tilde{\boldsymbol{w}}_{\mathrm{BM}}$	Blackman window (with/without padded zeros)
$\boldsymbol{x}_{(\cdot)}$	Indicator vector of set $(\cdot)$
$\boldsymbol{y}$	Receive signal

Bibliography

[1] R. Schaufele, K. Lizotte, N. Miller, A. Barlett, M. Lukacs, and M. Becker, "FAA aerospace forecast: fiscal years 2016-2036", Federal Aviation Administration, Tech. Rep.

[2] European Commission, "SESAR 2020: developing the next generation of european air traffic management", SESAR Joint Undertaking, Tech. Rep., 2016.

[3] FAA, *NextGen: https://www.faa.gov/nextgen/*.

[4] European Commission, "SESAR 2020 multi-annual work programme", SESAR Joint Undertaking, Tech. Rep. July, 2015.

[5] M. Schnell, U. Epple, D. Shutin, and N. Schneckenburger, "LDACS: future aeronautical communications for air-traffic management", *IEEE Commun. Mag.*, vol. 52, no. 5, pp. 104–110, 2014.

[6] L. Eldredge, P. Enge, M. Harrison, R. Kenagy, S. Lo, R. Loh, R. Lilley, M. Narins, and R. Niles, "Alternative positioning, navigation and timing (PNT) study", in *International Civil Aviation Organisation Navigation Systems Panel (NSP)*, Montreal, Canada, 2010.

[7] W. E. Jackson, *The Federal Airways System*. Washington DC: The Institute of Electrical and Electronic Engineers, 1970.

[8] N. Schneckenburger, T. Jost, U.-C. Fiebig, G. Del Galdo, H. Jamal, D. W. Matolak, and R. Sun, "Modeling the air-ground multipath channel", in *Proc. EuCAP, ©IEEE*, Paris, France: ©IEEE, 2017.

[9] N. Schneckenburger, S. Lo, R. Lilley, U.-C. Fiebig, and P. Enge, "Characterization and Mitigation of Multipath for Terrestrial based Aviation Radionavigation", *Navigation (submitted for publication)*, 2016.

[10] N. Schneckenburger, T. Jost, D. Shutin, M. Walter, U.-C. Fiebig, and G. Del Galdo, "Reflector localization for geometrical modeling the air-ground channel", *IEEE Trans. Veh. Technol. (submitted for publication)*, 2017.

[11] N. Schneckenburger, T. Jost, D. Shutin, M. Walter, T. Thiasiriphet, M. Schnell, and U.-C. Fiebig, "Measurement of the L-band air-to-ground channel for positioning applications", ©*IEEE Trans. Aerosp. Electron. Syst.*, vol. 52, no. 5, pp. 2281–2297, 2016.

[12] N. Schneckenburger, D. Matolak, T. Jost, U.-C. Fiebig, and G. Del Galdo, "A geometrical-statistical model for the air-ground channel", in *Proc. DASC*, St. Petersburg, FL, 2017.

[13] J. B. Keller, "Geometrical theory of diffraction", *J. Opt. Soc. Am.*, vol. 52, no. 2, pp. 116–130, 1962.

[14] J. D. Parsons, *The Mobile Radio Propagation Channel*, 2nd. West Sussex, United Kingdom: Wiley, 2000.

[15] ITU-R, "P.527-3: Electrical characteristics of the surface of the earth", Tech. Rep., 1992.

[16] G. H. Millman, "Atmospheric effects on VHF and UHF propagation", in *IEEERE International Convention*, vol. 46, 1958, pp. 1492–1501.

[17] P. Beckman and A. Spizzichino, *The Scattering of Electromagnetic Waves from Rough Surfaces*. Norwood, MA: Artech House, 1987.

[18] T. Jost, W. Wang, U.-C. Fiebig, and F. Pérez-Fontán, "Comparison of L-and C-band satellite-to-indoor broadband wave propagation for navigation applications", *IEEE Trans. Antennas Propag.*, vol. 59, no. 10, pp. 3899–3909, 2011.

[19] ITU-R, "P.1008-1: Reflection from the surface of the Earth", Tech. Rep., 1990.

[20] N. Schneckenburger, T. Jost, D. Shutin, and U.-C. Fiebig, "Line of sight power variation in the air to ground channel", in *Proc. EuCAP*, Davos, Switzerland, 2016.

[21] J. Proakis, *Digital Communications*, 4th. Boston, MA: McGraw-Hill, 2010.

[22] M. Kayton and W. R. Fried, *Avionics Navigation Systems*, 2nd. New York, NY: John Wiley & Sons, Inc., 1997, pp. 127–132, 284–286.

[23] P. Misra and P. Enge, *Global Positioning System: Signals, Measurements, and Performance*, 2nd. Lincoln, MA: Ganga-Jamuna Press, 2011.

[24] S. Lo, Y.-H. Chen, B. Segal, B. Peterson, P. Enge, R. Erikson, and R. Lilley, "Containing a difficult target: techniques for mitigating DME multipath to alternative position navigation and timing (APNT)", in *Proc. ION ITM*, San Diego, CA, 2014.

[25] W. Pelgrum, K. Li, M. Smearcheck, and F. van Graas, "eDME architecture development and flight-test evaluation", in *Proc. ION GNSS+*, Nashville, TN, 2012, pp. 812–825.

[26] N. Schneckenburger, S. Lo, M. Walter, and U.-C. Fiebig, "Geometric rules for terrestrial radionavigation multipath mitigation by averaging", *Navigation*, vol. 64, no. 2, pp. 231–236, 2017.

[27] International Civil Aviation Organization (ICAO), "Guidance material on comparison of surveillance technologies (GMST)", Tech. Rep., 2007.

[28] P. Almers, E. Bonek, A. Burr, N. Czink, V. Debbah M. Degli-Esposti, H. Hofstetter, P. Kyosti, D. Laurenson, G. Matz, A. Molisch, C. Osteges, and H. Ozcelik, "Survey of channel and radio propagation models for wireless mimo systems", *EURASIP Journal on Wireless Communications and Networking*, vol. 2007, no. 1, pp. 1–19, 2007.

[29] G. Del Galdo, "Geometry based channel modeling for multi-user MIMO systems and applications", PhD thesis, Ilmenau University of Technology, 2007.

[30] M. Walter, D. Shutin, and U.-C. Fiebig, "Delay-dependent doppler probability density functions for vehicle-to-vehicle scatter channels", *IEEE Trans. Antennas Propagat.*, vol. 62, no. 4, pp. 2238–2249, 2014.

[31] G. Matz, "On non-WSSUS wireless fading channels", *IEEE Trans. Wireless Commun.*, vol. 4, no. 5, pp. 2465–2478, 2005.

[32] A. Molisch, A. Kuchar, J. Laurila, K. Hugl, and R. Schmalenberger, "Geometry-based directional model for mobile radio channels - principles and implementation", *European Transactions on Telecommunications*, vol. 14, no. 4, pp. 351–359, 2003.

[33] T. Jost, W. Wang, U.-C. Fiebig, and F. Pérez-Fontán, "A wideband satellite-to-indoor channel model for navigation applications", *IEEE Trans. Antennas Propag.*, vol. 62, no. 10, pp. 5307–5320, 2014.

[34] P. Bello, "Characterization of randomly time-variant linear channels", *IEEE Trans. Commun.*, vol. 11, no. 4, pp. 360–393, 1963.

[35] R. Kattenbach, "Charakterisierung zeitvarianter indoor-funkkanäle anhand ihrer system- und korrelationsfunktionen", PhD thesis, Univ. Kassel, 1997.

[36] A. Papoulis and S.-U. Pillai, *Probabilities, Random Variables, and Stochastic Processes*, 3rd. New York, NY: McGraw-Hill, 1991.

[37] R. Sun, “Dual-band non-stationary channel modeling for the air-ground channel”, PhD thesis, College of Engineering and Computing,University of South Carolina, 2015.

[38] D. W. Matolak, “Air-ground channels and models: comprehensive review and considerations for unmanned aircraft systems”, in *Proc. IEEE Aerospace Conference*, Big Sky, MT, 2012, pp. 1–17.

[39] W. Vergara, J. Levatich, and T. Carroll, “VHF air-ground propagation far beyond the horizon and tropospheric stability”, *IRE Trans. Antennas Propag.*, vol. 10, no. 5, pp. 608–621, 1962.

[40] K. Chamberlin, “The effect of tree cover on air-ground, VHF propagation path loss”, *IEEE Trans. Commun.*, vol. 34, no. 9, pp. 958–962, 1986.

[41] S. Elnoubi, “A simplified stochastic model for the aeronautical mobile radio channel”, in *Proc. IEEE Vehicular Techn. Conf.*, vol. 2, Denver, CO, 1992, pp. 960–963.

[42] G. Dyer, T. G. Gilbert, S. Hendriksen, and E. Sayadlan, “Mobile propagation measurements using CW and sliding correlator techniques”, in *Proc. IEEE Ant. Propagation Symposium*, vol. 4, Atlanta, GA, 1998, pp. 1896–1899.

[43] Q. Feng and J. McGeehan, “Path loss models for air-to-ground radio channels in urban environments”, in *Proc. IEEE Vehicular Techn. Conf.*, Melbourne, Australia, 2006, pp. 2901–2905.

[44] Q. Lei and M. Rice, “Multipath channel model for over-water aeronautical telemetry”, *IEEE Trans. Aerosp. Electron. Syst.*, vol. 45, no. 2, pp. 735–742, 2009.

[45] J. Kunisch, I. D. L. Torre, A. Winkelmann, M. Eube, and T. Fuss, “Wideband time-variant air-to-ground radio channel measurements at 5 GHz”, in *Proc. EuCAP*, Rome, Italy, 2011, pp. 1386–1390.

[46] Y. S. Meng and Y. H. Lee, “Measurements and characterizations of air-to-ground channel over sea surface at C-band with low airborne altitudes”, *IEEE Trans. Veh. Technol.*, vol. 60, no. 4, pp. 1943–1948, 2011.

[47] Y. S. Meng and Y. H. Lee, “Study of shadowing effect by aircraft maneuvering for air-to-ground communication”, *International Journal of Electronics and Communications (AEÜ)*, vol. 66, no. 1, pp. 7–11, 2012.

[48] C. Bluemm, C. Heller, B. Fourestie, and R. Weigel, "Wideband aeronautical channel sounding and modeling for c-band telemetry", in *Proc. PMIRC*, London, United Kingdom, 2013.

[49] C. Heller, C. Blumm, and B. Fourestie, "On the characterization of the wireless channel for aeronautic mobile telemetry in C-band", in *Proc. IEEE/AIAA DASC*, East Syracuse, NY, 2013.

[50] Y. H. Lee and Y. S. Meng, "Key considerations in the modeling of tropical maritime microwave attenuations", *International Journal of Antennas and Propagation*, vol. 2015, pp. 1–7, 2015.

[51] J. H. Painter, S. C. Gupta, and L. R. Wilson, "Multipath modeling for aeronautical communications", *IEEE Trans. Commun.*, vol. 21, no. 5, pp. 658–662, 1973.

[52] J. R. Child, "Air-to-ground propagation at 900 MHz", in *Proc. IEEE Vehicular Techn. Conf.*, Falls Church, VA, 1985, pp. 73–80.

[53] M. Rice, A. Davis, and C. Bettweiser, "Wideband channel model for aeronautical telemetry", *IEEE Trans. Aerosp. Electron. Syst.*, vol. 40, no. 1, pp. 57–69, 2004.

[54] M. Rice and A. Davis, "A multipath channel model for wideband aeronautical telemetry", in *Proc. IEEE MILCOM*, Anaheim, CA, 2002.

[55] W. G. Newhall, R. Mostafa, C. Dietrich, C. R. Anderson, G. Joshi, and J. H. Reed, "Wideband air-to-ground radio channel measurements using an antenna array at 2 GHz for low-altitude operations", in *Proc. IEEE MILCOM*, vol. 2, Baltimore, MD, 2003, pp. 1422–1427.

[56] M. Rice and M. Jensen, "Multipath propagation for helicopter-to-ground MIMO links", in *Proc. IEEE MILCOM*, Baltimore, MD, 2011.

[57] M. Simunek, P. Pechac, and F. P. Fontan, "Excess loss model for low elevation links in urban areas for uavs", *Radioengineering*, vol. 20, no. 3, pp. 561–568, 2011.

[58] K. Li and W. Pelgrum, "Flight test evaluation of enhanced DME (eDME) performance enhancements", in *Proc. ION GNSS+*, Nashville, TN, 2012.

[59] K. Li, W. Pelgrum, and A. Naab-Levy, "Impact of ground multipath on terrestrial radio navigation performance", in *Proc. ION GNSS+*, Nashville, TN, 2013, pp. 722–736.

[60] W. Pelgrum and K. Li, "An investigation on the contributing factors of enhanced DME ranging errors", in *Proc. ION GNSS+*, Tampa, FL, 2015.

[61] S. Lo, Y. H. Chen, P. Enge, and M. Narins, “Techniques to provide resilient alternative positioning, navigation, and timing (APNT) using automatic dependent surveillance - broadcast (ADS-B) ground stations”, in *Proc. ION ITM*, Monterey, CA, 2015.

[62] M. Simunek, P. Pechac, and F. P. Fontan, “Feasibility of UAV link space diversity in wooded areas”, *International Journal of Antennas and Propagation*, vol. 2013, pp. 1–5, 2013.

[63] M. Simunek, P. Pechac, and F. Perez-Fontan, “Space diversity analysis for low elevation links in urban areas”, in *Proc. EuCAP*, Prague, Czech Republic, 2012.

[64] T. J. Willink, C. C. Squires, G. W. Colman, and M. Muccio, “Measurement and characterization of low-altitude air-to-ground MIMO channels”, *IEEE Trans. Veh. Technol.*, vol. 65, no. 4, pp. 2637–2648, 2016.

[65] D. W. Matolak and R. Sun, “Air-ground channel characterization for unmanned aircraft systems - part I: methods, measurements, and models for over-water settings”, *IEEE Trans. Veh. Technol.*, vol. 66, no. 1, pp. 26–44, 2016.

[66] R. Sun and D. W. Matolak, “Air-ground channel characterization for unmanned aircraft systems - part II: hilly & mountainous settings”, *IEEE Trans. Veh. Technol.*, vol. 66, no. 3, pp. 1913–1925, 2017.

[67] D. W. Matolak and R. Sun, “Air-ground channel characterization for unmanned aircraft systems - part III: the suburban and near-urban environments”, *IEEE Trans. Veh. Technol.*, vol. PP, no. 8, pp. 6607–6618, 2017.

[68] ——, “AG channel measurement and modeling results for over-water and hilly terrain conditions”, NASA Glenn Research Center, Tech. Rep., 2015.

[69] ——, “AG channel measurement and modeling results for over-sea conditions”, NASA Glenn Research Center, Tech. Rep., 2015.

[70] P. Bello, “Aeronautical Channel Characterization”, *IEEE Trans. Commun.*, vol. 21, no. 5, pp. 548–563, 1973.

[71] E. Haas, “Aeronautical Channel Modeling”, *IEEE Trans. Veh. Technol.*, vol. 51, no. 2, pp. 254–264, 2002.

[72] S. Brandes, S. Gligorevic, M. Ehammer, T. Gräupl, R. Dittrich, M. Schnell, and C. Rihacek, “Expected B-AMC system performance”, Eurocontrol, Tech. Rep., 2007.

[73] W. G. Newhall and J. H. Reed, “A geometric air-to-ground radio channel model”, in *Proc. IEEE MILCOM*, Anaheim, CA, 2002.

[74] S. M. Gulfam, S. J. Nawaz, A. Ahmed, M. N. Patwary, and Q. Ni, "A novel 3d analytical scattering model for air-to-ground fading channels", *Applied Sciences*, vol. 6, no. 8, 2016.

[75] M. Ibrahim and H. Arslan, "Air-ground doppler-delay spread spectrum for dense scattering environments", in *Proc. MILCOM*, Tampa, FL, 2015.

[76] Q. Feng, E. K. Tameh, A. R. Nix, and J. McGeehan, "Modelling the likelihood of line-of-sight for air-to-ground radio propagation in urban environments", in *Proc. IEEE Globecom 2006*, San Francisco, CA, 2006.

[77] A. Al-Hourani, S. Kandeepan, and A. Jamalipour, "Modeling air-to-ground path loss for low altitude platforms in urban environments", in *Proc. IEEE Globecom 2006*, Austin, TX, 2014.

[78] M. Steinbauer, A. Molisch, and E. Bonek, "The double-directional radio channel", *IEEE Antennas and Propagation Magazine*, vol. 43, no. 4, pp. 51–63, 2001.

[79] ITU-R, "P.528-3: Propagation curves for aeronautical mobile and radionavigation services using the VHF, UHF and SHF bands", Tech. Rep., 2012.

[80] O. Osechas and N. Schneckenburger, "Modeling ground-to-air ranging errors using a local elevation mask", in *Proc. DASC*, IEEE, 2016.

[81] A. Molisch, "Ultra-wide-band propagation channels", *Proceedings of the IEEE*, vol. 97, no. 2, pp. 353–371, 2009.

[82] R. S. Thomä, M. Landmann, A. Richter, and U. Trautwein, "Smart Antennas - State of the Art", in, T. Kaiser, A. Bourdoux, H. Boche, J. Rodríguez Fonollosa, J. Bach Andersen, and W. Utschick, Eds., ser. EURASIP Book Series on SP&C. Hindawi Publishing Corporation, 2005, ch. II-13, pp. 211–240.

[83] N. Schneckenburger, D. Shutin, T. Jost, M. Schnell, and U.-C. Fiebig, "Super-resolution Analysis of the L-band Air-to-ground Radio Channel", in *Proc. ION GNSS+*, Tampa, FL, 2015.

[84] J. Salmi, A. Richter, and V. Koivunen, "Detection and Tracking of MIMO Propagation Path Parameters Using State-Space Approach", *IEEE Trans. Signal Process.*, vol. 57, no. 4, pp. 1538–1550, 2009.

[85] T. Jost, W. Wang, U.-C. Fiebig, and F. Pérez-Fontán, "Detection and tracking of mobile propagation channel paths", *IEEE Trans. Antennas Propag.*, vol. 60, no. 10, pp. 4875–4883, 2012.

[86] A. Richter, "Estimation of radio channel parameters: Models and algorithms", PhD Thesis, TU Ilmenau, Ilmenau, Germany, 2005.

[87] R. Brown and P. Hwang, *Introduction to Random Signals and Applied Kalman Filtering*, 3rd. New York, NY: John Wiley & Sons, Inc., 1997.

[88] M. J. Powell, “The BOBYQA algorithm for bound constrained optimization without derivatives”, Department of Applied Mathematics and Theoretical Physics, Cambridge University, Tech. Rep., 2009.

[89] S. Kay, *Modern Spectral Estimation: Theory and Application*. Upper Saddle River, NJ: Prentice Hall, 1999.

[90] E. Gumbel, “The Return Period of Flood Flows”, *The Annals of Mathematical Statistics*, vol. 12, pp. 163–190, 1941.

[91] S. M. Kay, *Fundamentals of statistical signal processing, volume 1: estimation theory*. Upper Saddle River, NJ: Prentice Hall PTR, 1993.

[92] L. Scharf, *Statistical Signal Processing*. Pearson, 1991.

[93] S. S. Abhyankar, *Algebraic Geometry for Scientists and Engineers*, ser. Mathematical Surveys and Monographs. Amer Mathematical Society, 1990.

[94] M. Pätzold, *Mobile Fading Channels*, 1st. West Sussex, United Kingdom: John Wiley & Sons, Ltd, 2002.

[95] N. Schneckenburger, D. Shutin, T. Jost, M. Walter, T. Thiasiriphet, A. Filip, and M. Schnell, “From L-band measurements to a preliminary channel model for APNT”, in *Proc. ION GNSS+*, Tampa, FL, 2014, pp. 3009–3015.

[96] NovAtel, *GrafNav GNSS post-processing software manual*, 2015.

[97] National Instruments, *PXI description*, 2015.

[98] S. Boyd, “Multitone signals with low crest factor”, *IEEE Trans. Circuits Syst.*, vol. 33, no. 10, pp. 1018–1022, 1986.

[99] F. v. Graas, S. Craig, W. Pelgrum, and S. Ugazio, “Laboratory and Flight Test Analysis of Rubidium Frequency Reference Performance under Dynamics”, *Navigation*, vol. 60, no. 2, pp. 123–131, 2013.

[100] A. Leick, *GPS Satellite Surveying*, 3rd. New York, NY: John Wiley & Sons, Inc., 2004.

[101] T. Thiasiriphet, N. Schneckenburger, and M. Schnell, “Ranging with LDACS: results from measurement campaign”, in *Proc. ICNS*, Herndon, VA, 2016.

[102] D. Shutin, N. Schneckenburger, M. Walter, T. Thiasiriphet, N. Franzen, A. Filip, and M. Schnell, “LDACS1 ranging results with doppler smoothing from new flight experiments”, in *Proc. DASC*, Colorado Springs (CO), 2014.

[103] N. Schneckenburger, B. P. B. Elwischger, B. Belabbas, D. Shutin, M. S. Circiu, M. Suess, M. Schnell, J. Furthner, and M. Meurer, "LDACS1 navigation performance assessment by flight trials", in *Proc. ENC*, Vienna, Austria, 2013.

[104] N. Schneckenburger, B. Elwischger, D. Shutin, M. Suess, B. Belabbas, and M.-S. Circiu, "Positioning results for LDACS1 based navigation with measurement data", in *Proc. ION GNSS+*, Nashville, TN, 2013.

[105] "A Report from the Portable Electronic Devices (PED) Aviation Rule Making Committee (ARC) to the Federal Aviation Administration (FAA)", Tech. Rep., 2013.

[106] M. Schwinzerl, T. Jost, F. Pérez-Fontán, M. Schoenhuber, W. Wang, M. Walter, and T. Pelzmann, "Wide-Band Characterization of Antennae Plus Aircraft Platform Patterns in L- and Ka-Band", in *Proc. EuCAP*, Lisbon, Portugal, 2015, pp. 1–5.

[107] K. J. Keeping and J. C. Sureau, "Scale model pattern measurements of aircraft l-band beacon antennas", Lincoln Laboratory, Tech. Rep., 1975.

[108] B. W. Silverman, *Density Estimation for Statistic and Data Analysis*. London, United Kingdom: Chapman and Hall, 1986.

[109] A. Lehner, "Multipath channel modelling for satellite navigation systems", PhD thesis, Universität Erlangen-Nürnberg, 2007.

[110] M. Ait Ighil, "Enhanced physical-statistical simulator of the land mobile satellite channel for multipath modelling applied to satellite navigation systems", PhD thesis, Université de Toulouse, 2013.

[111] G. E. P. Box, G. M. Jenkins, and G. C. Reinsel, *Time Series Analysis: Forecasting and Control*. Wiley, 2008.

[112] S. L. Marple, *Digital Spectral Analysis: With Applications (Prentice-Hall Series in Signal Processing)*. Prentice Hall, 1987.

[113] T. Jost, W. Wang, and M. Walter, "A geometry-based channel model to simulate an averaged power delay profile", *IEEE Trans. Antennas Propag.*, no. 99, 2017.

[114] J. Casey, "The General Equation of the Second Degree", in *A Treatise on the Analytical Geometry of the Point, Line, Circle, and Conic Sections, Containing an Account of Its Most Recent Extensions, with Numerous Examples*, 2nd ed., Dublin: Hodges, Figgis, & Co, 1893, ch. 4, pp. 151–172.

[115] W. Beyer, *CRC Standard Mathematical Tables and Formulae*, 28th ed. Boca Raton, FL: CRC Press, 1987, pp. 200–201.

Alphabetical Index